4-21-2022 10:00 AM

Humid Air Corrosion of Carbon Steel and Stainless Steels under Gamma Radiation: The Role of Solution Volume and Radiolysis Products

Masoud Zakeri, *The University of Western Ontario*

Supervisor: Wren, Jungsook C., *The University of Western Ontario*

A thesis submitted in partial fulfillment of the requirements for the Doctor of Philosophy degree in Chemistry

ABSTRACT

As nuclear power plants age and their lifetimes are extended, it is critical to be able to accurately assess the long-term integrity of the reactor structural materials. A current investigation into a leak in the End Shield Cooling (ESC) System in Ontario Power Generation's Pickering Unit 6 reactor has raised a potential issue. The corrosion of the supporting structural materials (carbon steel (CS) and stainless steel (SS)) in the presence of ionizing radiation in small stagnant solutions and humid air conditions therefore needs careful evaluation.

This project investigates the effect of water radiolysis and humid air radiolysis products (H_2O_2 and HNO_3) on the corrosion of CS and SS under different conditions. The parameters studied in this thesis include the concentration of HNO_3 and H_2O_2, solution pH, and the presence or absence of γ-radiation. A series of electrochemical techniques and coupon exposure tests were employed to measure the corrosion rates of different steels. Post-test surface and solution analyses were performed to understand the oxides formed on the corroded surfaces and to determine the amounts of metal ions dissolved in the solution.

This study has shown that CS corrosion involves several elementary reactions and transport processes that determine the overall corrosion rate. The presence of H_2O_2 and nitrate affect the corrosion rate by providing a more oxidizing solution environment that increases the charge transfer rate via increasing the mass transport rate of metal cations. At relatively high concentrations (≥10 mM) of H_2O_2 and in neutral pHs, the redox reactions of hydrogen peroxide can couple strongly with metal redox reactions. High

H_2O_2 concentration can provide the conditions for the formation of a protective oxide and increase the corrosion potential to values at which the redox reactions of hydrogen peroxide can be strongly coupled with the metal oxidation. This study has highlighted the strong feedback that can occur between different processes involved in corrosion. Ignoring this feedback and the effect of nitrate and other solution parameters on the mass transfer process of metal cations could result in inaccurate predictions of the long-term integrity of structural alloys.

The results of this study have improved the mechanistic understanding of the effect of these redox-active species on the corrosion pathways of carbon steel and stainless steels, and will contribute to the development of a corrosion model that can be used to assess the long-term integrity of the CANDU reactor structural materials with confidence.

KEYWORDS

Carbon Steel, Stainless Steel, Humid Air Corrosion, Gamma Radiation, Water Radiolysis, Electrochemical Reactions, Nitrate, Hydrogen Peroxide, Nitric Acid

SUMMARY FOR LAY AUDIENCE

Because of the possibility of a water leak in Canada Deuterium Uranium (CANDU) nuclear reactors, corrosion is a potential issue for the supporting structure materials, carbon steel (CS) and stainless steel (SS).

Ionizing radiation creates a more oxidizing environment and lowers the pH of solutions. The work presented here investigates the effects of water radiolysis and humid air radiolysis products (most notably, HNO_3 and H_2O_2), on the corrosion of CS and SS under different conditions. The results of this study will be used to build a better understanding of the effect of the key redox-active species on corrosion pathways and will contribute to the development of a CS and SS corrosion model that can be used to assess the long-term integrity of the CANDU reactor structural materials with confidence.

The studied parameters were concentration of nitrate and hydrogen peroxide, solution pH, the presence of additional oxidants, and the presence or absence of γ-radiation. A series of electrochemical techniques were employed to measure the corrosion rates of different steels. Post-test surface and solution analyses were performed to understand oxide formation on the corroded surfaces and to determine the amount of dissolved metal ions in the solution.

The work presented in this thesis has demonstrated that disregarding the strong feedback between the different processes involved in corrosion and ignoring the effect of solution parameters on the mass transfer of metal cations could result in an inaccurate prediction of the corrosion rate.

To my parents

and

To my wonderful wife, Masi,

for making everything possible

CO-AUTHORSHIP STATEMENT

I was the main author for all chapters, and Prof. J.C. Wren provided invaluable comments.

Mr. G. Whitaker provided valuable comments and helped with editing.

Dr. J. Joseph helped with the post-test solution analyses and provided valuable comments.

Dr. M. Naghizadeh helped with the interpretation of the data in all the chapters.

Dr. M. Momeni and Dr. R. Karimihaghighi provided valuable comments and helped with editing.

ACKNOWLEDGEMENTS

I would like to thank all those who have provided steady encouragement throughout my doctoral journey. I would like to express my sincere gratitude to the following people:

First of all, I would like to thank Prof. Clara Wren, my supervisor, for her guidance. I appreciate all her advice and encouragement and that she always helped push me to become an independent scientist. I would like to extend my thanks to my committee members Prof. Dave Shoesmith and Dr. Jamie Noel. I owe thanks to Dr. Jiju Joseph for always being incredibly supportive. I am immensely grateful for the aid of Giles Whitaker in improving my writing skills. I would like to thank my friends, both past and present, in the Wren lab. I would like to thank Dr. Ryan Morco for his friendship and all the encouragement and mental support. I also would like to thank Dr. Razieh KarimiHaghighi for her valuable friendship and also providing constructive comments. Special thanks to Dr. Mojtaba Momeni for a long-term true friendship, for all the support he provided and for sharing knowledge and resources. I also would like to thank my dear friends Nasrin, Milad, Nasim and all others in front of whom I could talk freely without the fear of being judged.

I also would like to thank my parents and all my family members. Your help throughout my life has been invaluable. Words cannot express the full extent of my appreciation.

I would like to offer my special thanks to my beloved dear wife, Masi, who stood by me and supported me in the most challenging time of my life. I discussed all my

scientific interpretations and also personal ideas with her, and she helped prevent several wrong turns.

TABLE OF CONTENTS

LIST OF TABLES

LIST OF FIGURES

LIST OF ABBREVIATIONS

BCC	Body-Centred Cubic
CANDU	Canada Deuterium Uranium
CE	Counter Electrode
CS	Carbon Steel
CV	Cyclic Voltammetry
DR	Dose Rate
EDX	Energy Dispersive X-Ray
FCC	Face-Centred Cubic
FIB	Focused-Ion Beam
Gy	Gray
ICP	Inductively Coupled Plasma
ICP-OES	Inductively Coupled Plasma-Optical Emission Spectroscopy
LPR	Linear Polarization Resistance
OPG	Ontario Power Generation
ORR	Oxygen Reduction Reaction
PD	Potentiodynamic Polarization
PPB (ppb)	Parts Per Billion
RDS	Rate-Determining Step
RE	Reference Electrode
RHE	Reversible Hydrogen Electrode
SCE	Saturated Calomel Electrode

SEM	Scanning Electron Microscopy
SHE	Standard Hydrogen Electrode
SS	Stainless Steel
304L SS	Stainless Steel (Type 304L)
309 SS	Stainless Steel (Type 309)
UV-Vis	Ultraviolet and Visible
WE	Working Electrode
WT	Wagner-Traud
XRD	X-Ray Diffraction Spectroscopy

LIST OF SYMBOLS

A	Surface area of electrode
$(a_A)_{int}$	Interfacial activity of ion A
C	Concentration
C_{sat}	Saturation concentration
D_R	Dose rate
E^0	Standard potential
E_{app}	Applied potential
E_{eq}	Equilibrium potential
E_{rxn}^{eq}	Difference between the equilibrium potential for a redox half-reaction
E_{elec}	Electrode potential
E_{corr}	Corrosion potential
$E_{i=0}$	Potential of zero current density
F	Faraday constant
Fe_m	Iron atom
Fe_{sol}^{2+}	Fully solvated Fe^{2+}
$[Fe^{2+}]_{int}$	Concentration of Fe^{2+} at the interface
$[Fe^{2+}]_{bulk}$	Concentration of Fe^{2+} in bulk solution
$[HNO_3]_0$	Initial concentration of HNO_3 in the solution
$[H_2O_2]_0$	Initial concentration of H_2O_2 in the solution
I_s	Ionic strength

i	Current density
i_a	Anodic current density
i_c	Cathodic current density
i_{corr}	Corrosion current density
$i_{corr,a}$	Corrosion current density obtained from the intersection of anodic Tafel extrapolation with E_{corr}
$i_{corr,c}$	Corrosion current density obtained from the intersection of cathodic Tafel extrapolation with E_{corr}
i_{meas}	Measured current density
i^0	Exchange current density
i_{ox}^0	Exchange current of the metal oxidation half-reaction
i_{red}^0	Exchange current of the solution reduction half-reaction
i_{ox}	Oxidation current density
i_{red}	Reduction current density
i_{ox}^{eq}	Oxidation current density at equilibrium
i_{red}^{eq}	Reduction current density at equilibrium
i_L	Limiting current density
i_k	Kinetic current density
J_x	Flux of species (mol cm^{-2}) at distance x
k	Rate constant
L	Length
n	Stoichiometric number of electrons involved in an electrode reaction

Q	Accumulated charge
R	Ideal gas constant
R_P	Charge transfer resistance
R_S	Solution resistance
t	Time
t_{corr}	Time of corrosion
α	Charge transfer coefficient
β	Tafel slope
β_a	Anodic Tafel slope
β_c	Cathodic Tafel slope
ΔG	Gibbs free energy of reaction
$\Delta_{ox}G$	Gibbs free energy change for the solution species oxidation half-reaction
$\Delta_{red}G$	Gibbs free energy change for the solution species reduction half-reaction
ε	Extinction coefficient
η	Overpotential
ν_{Gel}	Rate of hydrogel formation
ν_{Hyd}	Rate of hydrolysis Process
ν_{M1}	Metal oxidation rate ($Fe \leftrightarrows Fe^{2+}$)
ν_{M2}	Metal oxidation rate ($Fe^{2+} \leftrightarrows Fe^{3+}$)
ν_{Ox}	Rate of oxide formation
ν_{trans}	Ion transfer rate

CHAPTER 1
INTRODUCTION

1.1 BACKGROUND AND MOTIVATION

Nuclear power reactors offer a long term, cost-efficient and sustainable method for producing electricity with very low greenhouse gas emissions [1]. Accurate assessment of the long-term integrity of reactor structural materials is vital for assuring the safe operation of aging nuclear power plants.

A current investigation into a leak in the end shield cooling (ESC) system in Ontario Power Generation's Pickering Unit 6 reactor has indicated that moisture from this leak could possibly reach a location in the annular air gap which exists around the periphery of the calandria tank assembly and its supporting structures. In particular, the potential for corrosion attack on carbon steel (CS) adjacent to the dissimilar metal weld (W, type 309 SS) between CS (SA36) and stainless steel (SS, Type 304L) at the periphery of the annular air gap must be evaluated. Schematics of the calandria tank assembly, its supporting structures and the location of the CS and stainless steel weld

joint are shown in **Figure 1-1**.

The reactor structures will be exposed to very different environments from those commonly seen in previously published corrosion studies. The water volume per unit surface area would be small (water droplets), and the water would be stagnant. The pH of the ESC water is adjusted to around 10.4, but after condensing onto the weld region, the pH might be different, altering the dissolution rate. In addition, the oxygen level, humidity, and many other factors are expected to evolve with time. The ESC system and its components will also be exposed to a continuous flux of γ-radiation emitted from the reactor core. Hence, any air or water trapped in the annular gap will undergo radiolysis producing redox-active species (most notably, HNO_3 and H_2O_2) [2], producing potentially corrosive conditions in the weld region.

$$H_2O \xrightarrow{\gamma} \bullet e_{aq}^-,\ \bullet O_2^-,\ H^+,\ H_2,\ O_2,\ H_2O_2$$

$$\text{Humid air } (N_2,\ O_2,\ H_2O) \xrightarrow{\gamma} NO_x,\ HNO_3,\ H_2O_2$$

Furthermore, dissolved HNO_3 lowers the pH, which can affect the solubility of any metal cations produced by metal oxidation, and consequently, can alter the corrosion behaviours of carbon steel and stainless steel.

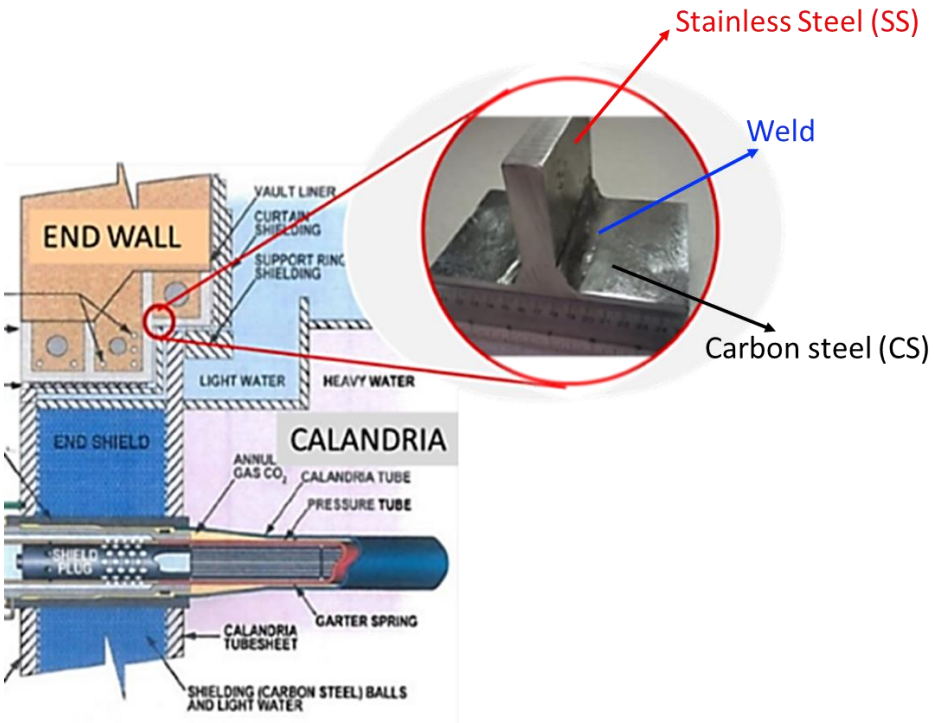

Figure 1-1: Schematic representation of the calandria tank assembly and its supporting structures in a CANDU reactor and the carbon steel-stainless steel weld joint block provided by Ontario Power Generation

The effects of γ-radiation, solution pH, and temperature on the independent corrosion of carbon steel (CS), 304L SS (SS) and the 309 SS filler material (W) and the galvanic corrosion between these dissimilar metals have already been investigated using both electrochemical and coupon immersion experiments [3]. This study showed that 304L SS and 309 SS have similar corrosion behaviours, and their corrosion rates remain low at both pH 6.0 and 10.6 due to the presence of protective chromium oxide layers on the surface. For CS, the major corrosion pathway was found to be metal dissolution at pH 6.0, whereas at pH 10.6, it was oxide formation due to the much lower solubility of Fe^{II} at this pH. Increasing temperature or applying γ-irradiation increases the corrosion rates of the alloys initially, but it also accelerates the formation and growth of protective

oxides on CS, suppressing subsequent metal oxidation. Therefore, the acceleration of CS corrosion due to galvanic coupling diminishes with increasing temperature and the presence of radiation.

As mentioned before, any trapped air or water in the annular gap will undergo radiolysis, producing redox-active species (HNO_3 and H_2O_2) that can affect the corrosion. Therefore, it is important to understand the effect of these redox-active species on the corrosion behaviours of CS and SS. Even though the corrosion of carbon steel and different types of stainless steels has been studied in different environments [4–12], the effects of nitrate ions and hydrogen peroxide on the corrosion of CS and SS, particularly at lower pHs, require further study. In order to better understand the corrosion of CS and SS in the presence of γ-radiation and under humid air, it is essential to understand the effect of nitrate ions and hydrogen peroxide on the electrochemical behaviours of CS and SS in solutions of different pHs and also to study the effect of γ-radiation, nitrate and hydrogen peroxide on the corrosion evolution of alloys in small volume solutions.

1.2 THESIS OBJECTIVES AND APPROACHES

The main objective of this thesis is to determine the effects of γ-radiation on the corrosion of CS and SS. This will contribute to the development of a mechanism that can explain how nitric acid and hydrogen peroxide (the main radiolytic products in humid air) impact CS corrosion under the conditions anticipated inside the calandria tank and adjacent to its supporting structures.

To develop a corrosion dynamic model, it is important to identify how the key elementary processes that control the overall corrosion rate are affected by radiolysis

products and how the kinetics of reactions change in the presence of nitric acid and hydrogen peroxide. The elementary processes considered in the study were electrochemical reactions, solution reactions, transport processes, and oxide particle nucleation and growth on each steel under study.

In this thesis, the corrosion dynamics of carbon steel and SS were investigated in a series of electrochemical measurements and droplet studies. The parameters studied were the concentration of nitrate and hydrogen peroxide, the initial pH of the solution, and the effect of other oxidants in the presence of nitrate ions. The electrochemical methods used were corrosion potential measurements, potentiodynamic polarization, and linear polarization resistance. The corrosion pathways are discussed based on the post-test surface and solution analysis results. The surface analysis techniques used were optical microscopy, scanning electron microscopy (SEM) combined with energy dispersive X-Ray spectroscopy (EDS), and Raman spectroscopy. The dissolved metals (Fe, Ni, and Cr) were measured using inductively coupled plasma optical emission spectrometry (ICP-OES).

1.3 THESIS OUTLINE

Chapter 1: Thesis motivation, thesis objectives, and thesis outline.

Chapter 2: Literature review and theoretical background for the experimental results presented in Chapters 4-8.

Chapter 3: Description of the experimental techniques used in this thesis.

Chapter 4: Corrosion Behaviour of Carbon Steel in Nitrate Solutions

This chapter investigates the effect of nitrate on the corrosion behaviour of CS by

performing electrochemical experiments (corrosion potential measurements and potentiodynamic polarization experiments). In this chapter, the electrochemical behaviour of CS (CS Type SA36) was studied in pH 6.0 buffered solutions in the presence of different concentrations of chemically added $NaNO_3$. Additionally, the electrochemical behaviour of CS in $NaNO_3$ solutions was compared with that in $Fe(NO_3)_3$ solutions, to study the effect of nitrate in the presence of ferric ions.

Chapter 5: Corrosion Behaviour of Carbon Steel and Stainless Steels in Nitric Acid Solutions

This chapter studies the corrosion behaviours of carbon steel (CS Type SA36) and stainless steels (304L SS and 309 SS) in nitric acid solutions. In this chapter, the effect of different concentrations of nitrate in acidic solution (pH 2.0) on the independent corrosion of CS and stainless steels was investigated using electrochemical techniques (corrosion potential measurements, linear polarization resistance, and potentiodynamic polarization). The amounts of dissolved metal ions (Fe, Ni, Cr) measured using ICP-OES were used to better understand the mechanism of the effect of nitrate on the corrosion behaviour of the studied alloys.

Chapter 6: Corrosion Behaviour of Carbon Steel and Stainless Steels in Hydrogen Peroxide Solution

In this chapter, the effect of chemically added H_2O_2 on the corrosion behaviour of carbon steel is investigated using electrochemical experiments and solution analysis techniques. In this chapter, the electrochemical behaviour of CS was studied in pH 6.0 buffered solutions in the presence of different concentrations of chemically added H_2O_2 using potentiodynamic polarization, linear polarization, and corrosion potential

measurement experiments. Additionally, the effect of H_2O_2 on the corrosion of CS, 304L SS and 309 SS was investigated in solutions of pH 2 with different H_2O_2 concentrations. The amounts of dissolved metal ions (Fe, Ni, Cr) measured using ICP-OES were used to better understand the mechanism of the effect of H_2O_2 on the corrosion behaviour of the studied alloys.

Chapter 7: Corrosion Dynamics of Carbon Steel in Small Volume Solutions

In this chapter, the effect of chemically added radiolytic products on the corrosion of CS was studied by performing droplet studies in small volume solutions (150 µL) of nitric acid with different initial pHs and chemically added hydrogen peroxide. In this chapter, the evolution of oxide formation and the changes in dissolved Fe concentration were evaluated using solution and surface analysis techniques to understand the effect of nitric acid and hydrogen peroxide on the different dynamic stages of corrosion.

Chapter 8: Gamma Radiation-Influenced Corrosion of Carbon Steel and Stainless Steel

This chapter studies the effect of different cover gases and γ-radiation on the corrosion of CS in small-volume solutions and under humid air. The different cover gases tested were Ar, hydrocarbon-free air, and 21% O_2+79% Ar. In the first section of this chapter, the evolution of the surface and the solution were investigated after corrosion of CS in a small volume solution (150 µL) under different cover gases in the presence and absence of γ-radiation. In the second section of this chapter, the humid air corrosion of joint of carbon steel and 309 SS (CS-W) was studied by the evaluation of surfaces corroded under 100% humidity and different cover gases in the presence of γ-radiation.

Chapter 9: Thesis summary and a brief discussion of potential future work.

1.4 REFERENCES

[1] F. Cattant, D. Crusset, D. Féron, Corrosion issues in nuclear industry today, Mater. Today. 11 (2008) 32–37.

[2] R.P. Morco, J.M. Joseph, D.S. Hall, C. Medri, D.W. Shoesmith, J.C. Wren, Modelling of radiolytic production of HNO_3 relevant to corrosion of a used fuel container in deep geologic repository environments, Corros. Eng. Sci. Technol. 52 (2017) 141–147.

[3] M. Li, Galvanic Corrosion of Carbon Steel-Stainless Steel Welds, PhD Thesis, The University of Western Ontario, 2020.

[4] C.M. Abreu, M.J. Cristóbal, M.F. Montemor, X.R. Nóvoa, G. Pena, M.C. Pérez, Galvanic coupling between carbon steel and austenitic stainless steel in alkaline media, Electrochim. Acta. 47 (2002) 2271–2279.

[5] M.L. Schlegel, S. Necib, S. Daumas, C. Blanc, E. Foy, N. Trcera, A. Romaine, Microstructural characterization of carbon steel corrosion in clay borehole water under anoxic and transient acidic conditions, Corros. Sci. 109 (2016) 126–144.

[6] R. Jia, D. Yang, J. Xu, D. Xu, T. Gu, Microbiologically influenced corrosion of C1018 carbon steel by nitrate reducing Pseudomonas aeruginosa biofilm under organic carbon starvation, Corros. Sci. 127 (2017) 1–9.

[7] D. Dwivedi, K. Lepkova, T. Becker, Emerging surface characterization techniques for carbon steel corrosion: a critical brief review, Proc. R. Soc. A Math. Phys. Eng. Sci. 473 (2017) 20160852.

[8] Y. Xiang, W. Xie, S. Ni, X. He, Comparative study of A106 steel corrosion in fresh and dirty MEA solutions during the CO_2 capture process: Effect of NO_3^-, Corros. Sci. 167 (2020) 108521.

[9] J. Vandenborre, F. Crumière, G. Blain, R. Essehli, B. Humbert, M. Fattahi, Alpha localized radiolysis and corrosion mechanisms at the iron/water interface: Role of molecular species, J. Nucl. Mater. 433 (2013) 124–131.

[10] K. Daub, A Study of Gamma Radiation Induced Carbon Steel Corrosion, PhD Thesis, The University of Western Ontario, 2013.

[11] K. Daub, X. Zhang, J.J. Noël, J.C. Wren, Effects of γ-radiation versus H_2O_2 on carbon steel corrosion, Electrochim. Acta. 55 (2010) 2767–2776.

[12] C. Pillay, J. Lin, The impact of additional nitrates in mild steel corrosion in a seawater/sediment system, Corros. Sci. 80 (2014) 416–426.

Chapter 2
Technical Background and Literature Review

2.1 MATERIALS BACKGROUND

2.1.1 Microstructure of Carbon Steel

The stable form of pure iron at room temperature is known as alpha ferrite (α-Fe) and has a body-centred cubic (BCC) structure. Pure iron is soft and is not used in structural applications. When a small amount of carbon (up to 2 wt %) is mixed with iron, it becomes an alloy known as carbon steel and its mechanical properties, e.g., the hardness and strength, are improved [1].

The three main distinct solid phases normally present in carbon steels are ferrite, austenite, and cementite (Fe_3C) [2]. The iron-carbon phase diagram is shown in **Figure 2-1**. The horizontal axis of the Fe-C diagram shows the percentage of carbon inside the Fe-C system. The fields (ranges of temperatures and carbon content) for the three basic phases of steel can be found in this diagram.

Cementite (Fe_3C) contains 6.67 wt% carbon by mass and is a hard and brittle interstitial compound with an orthorhombic crystal structure. The dissolved content of carbon in the ferrite (α-Fe) phase (body-centred cubic [BCC] crystal structure) at room temperature is 0.008 wt% or less. Austenite (γ-Fe) is an interstitial solid solution of C dissolved in Fe with a face-centred cubic (FCC) crystal structure and a maximum carbon content of 2 wt%. Finally, pearlite is a mixture of ferrite and cementite, with the ferrite sandwiched between an array of thin plates of cementite [3,4].

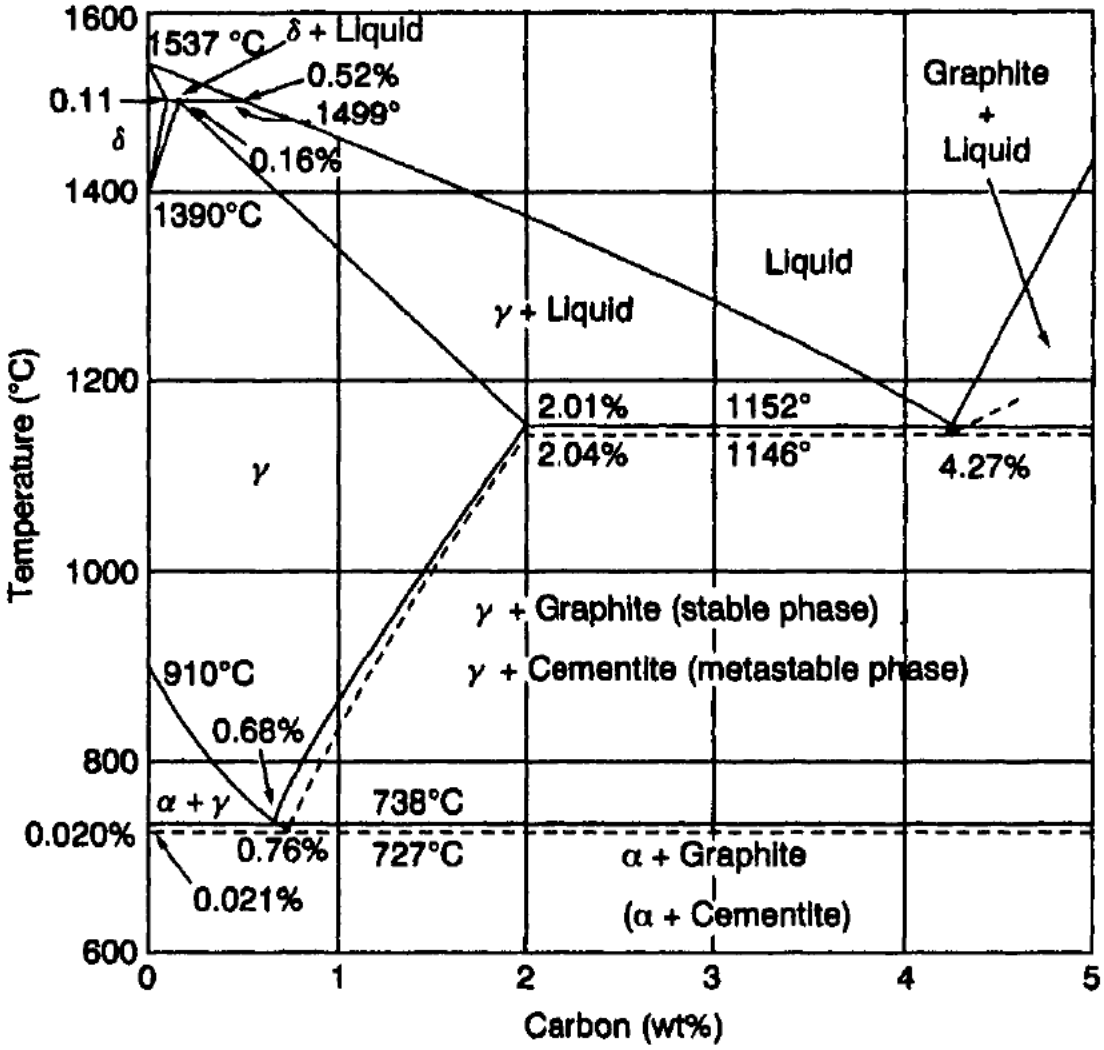

Figure 2-1: The iron-iron carbide (Fe-Fe_3C) phase diagram [2] (reprinted with permission from Ref. [2], © 1998 Elsevier Ltd.)

During the steelmaking process, due to the presence of sulfur as a common impurity in coal and coke and also the use of oxygen as the refining agent, secondary phases can also form in CS [5–7]. These secondary phases are non-metallic inclusions categorized into two main types based on the composition: oxide (CaO, Al_2O_3, SiO_2) and sulfide (CaS, MnS) [5–8]. Both oxygen and sulfur are soluble in liquid iron but have minimal solubility in the solid phase iron (α-Fe) [5,7]. To decrease the oxygen and sulfur content, elements with high affinity for oxygen (such as Si, Mn and Al) or sulfur (such as Ca and Mg) and with low solubility in liquid iron are added into liquid iron. However, these elements convert dissolved oxygen and sulfur into oxides and sulfides (the inclusions) [5,8]. While most inclusions can be removed, it is impossible to produce steels completely free of inclusions in industrial steelmaking processes [5].

2.1.2 Microstructure of Stainless Steel

Steels can contain a range of impurities such as Si, Al, S and P and can be alloyed with elements such as Cr, V, Mo, and Mn. Stainless steels are types of Fe-based alloys that contain a minimum of approximately 11 wt% Cr. Stainless steels offer high corrosion resistance due to a protective Cr-rich oxide layer.

The Fe-Fe_3C phase diagram for stainless steel is different from that of carbon steel due to the different stabilities of alloying elements in the BCC and FCC structures. Chromium and nickel are important alloying elements and affect the BCC to FCC phase transition. Chromium is a ferrite-stabilizing element, and Ni, N and Mn are austenite-stabilizing elements [9,10].

With the addition of a sufficient amount of Ni, the austenite phase stability range is extended to room temperature [2,11]. Austenitic stainless steels have excellent

formability and weldability and can be easily identified, as they are not ferromagnetic [12]. The most common stainless steel is 304 stainless steel, which is widely used in various household and industrial applications due to its high ductility, resulting in excellent drawing, forming, and spinning properties. It is an austenitic stainless steel with Ni content of approximately 8 wt% and Cr content of approximately 18 wt%.

2.2 PRINCIPLES OF AQUEOUS CORROSION

2.2.1 Electrochemical Reactions on Bare Metal

During corrosion, metal is oxidized to produce metal cations. This oxidation is coupled to the reduction of a water-soluble oxidant. For example, iron corrosion in an acidic environment in deaerated solution occurs via the following oxidation (**Eq. 2-1**) and reduction half-reactions (**Eq. 2-2**):

Oxidation Reaction: $Fe_{(m)} \rightarrow Fe^{2+} + 2\ e^-$ (**Eq. 2-1**)

Reduction Reaction: $2\ H^+ + 2\ e^- \rightarrow H_2$ (**Eq. 2-2)**

Overall Reaction: $Fe_{(m)} + 2\ H^+ \rightarrow Fe^{2+} + H_2$ **(Eq. 2-3)**

Under naturally corroding conditions, the rates of the oxidation and reduction half-reactions are equal and the same as the rate of the overall corrosion reaction. Electrochemical reactions take place at the electrode/electrolyte interface and are therefore heterogeneous in nature and strongly affected by the mass transfer of redox pairs (i.e., H^+ and H_2 in **Eq. 2-2** and Fe^{2+} in **Eq. 2-1**) towards and away from the interfacial region. In this section, the kinetics of electron transfer reactions are presented, and the effect of mass transfer is discussed in **Section 2.2.2.**

When metal is exposed to the solution, the metal/solution system starts to move

towards chemical equilibrium. The equilibrium potentials of the redox half-reactions are expressed by the Nernst equations [13]:

$$E_{ox}^{eq} = E_{(Fe^{2+}/Fe)}^{0} + \frac{RT}{nF} \ln \left(\frac{a_{eq}^{Fe^{2+}}}{a_{eq}^{Fe}}\right) \quad \textbf{(Eq. 2-4)}$$

$$E_{red}^{eq} = E_{(H^{+}/H^{2})}^{0} + \frac{RT}{nF} \ln \left(\frac{a_{eq}^{H^{+}}}{a_{eq}^{H^{2}}}\right) \quad \textbf{(Eq. 2-5)}$$

where E_{ox}^{eq} and E_{red}^{eq} are the equilibrium potentials for the oxidation half-reaction (Fe/Fe^{2+}) and solution reduction half-reaction (H^{+}/H_2), n is the number of electrons, F is Faraday's constant (96485 C/mol), R is the gas constant (8.314 J/K.mol), and T is the temperature (in Kelvin). In **Eq. 2-4** and **Eq. 2-5**, $E_{(Fe^{2+}/Fe)}^{0}$ and $E_{(H^{+}/H^{2})}^{0}$ represent the standard potentials for the oxidation half-reaction and the reduction half-reaction, respectively. The standard potentials of reactions are relative to the reference potential of hydrogen reduction ("standard" conditions are 1 M concentration of both oxidizing and reducing species and a gas pressure of 1.00 atm.), and $a_{eq}^{Fe^{2+}}$, a_{eq}^{Fe}, $a_{eq}^{H^{2}}$, $a_{eq}^{H^{+}}$, are the chemical activities of the redox species involved in the reactions. The activity of a pure solid metal is 1.0 by definition [14].

The thermodynamic driving forces for the oxidation and reduction half-reactions are the Gibbs free energy change for the metal oxidation half-reaction ($\Delta_{ox}G$) and the Gibbs free energy change for the solution species reduction half-reaction ($\Delta_{red}G$), respectively [13,15,16]. The difference between the electrode potential (E_{elec}) and the equilibrium potential for a redox half-reaction (E_{rxn}^{eq}) is called overpotential (η).

$$-\Delta_{ox}G = nF\left(E_{elec} - E_{ox}^{eq}\right) = nF\eta_{ox} \quad \textbf{(Eq. 2-6)}$$

$$-\Delta_{red}G = nF\left(E_{elec} - E_{red}^{eq}\right) = nF\eta_{red} \quad \textbf{(Eq. 2-7)}$$

An overpotential is required to drive a half-reaction proceeding at a certain rate. When the rates of the half-reactions are controlled by interfacial charge transfer, the rate of electron transfer is expressed by the Butler-Volmer equation [17,18]:

$$i_{ox} = i_{ox}^{0}\left\{exp\left(\frac{\alpha_{ox}\,nF\,\eta_{ox}}{RT}\right) - exp\left(-\frac{(1-\alpha_{ox})nF\,\eta_{ox}}{RT}\right)\right\} \quad \textbf{(Eq. 2-8a)}$$

$$i_{red} = i_{red}^{0}\left\{exp\left(\frac{\alpha_{red}\,nF\,\eta_{red}}{RT}\right) - exp\left(-\frac{(1-\alpha_{red})nF\,\eta_{red}}{RT}\right)\right\} \quad \textbf{(Eq. 2-8b)}$$

where (i_{red}^{0}), (i_{ox}^{0}) are the exchange currents of the metal oxidation half-reaction and the solution reduction half-reaction, and α_{ox} and α_{red} are transfer coefficients that represent the relative dependence of the forward and reverse reaction rates on their overpotentials. The transfer coefficients are typically assumed to be 0.5 and indicate the fraction of the electrostatic potential energy that affects oxidation. The Butler-Volmer relationships are schematically presented in **Figure 2-2.**

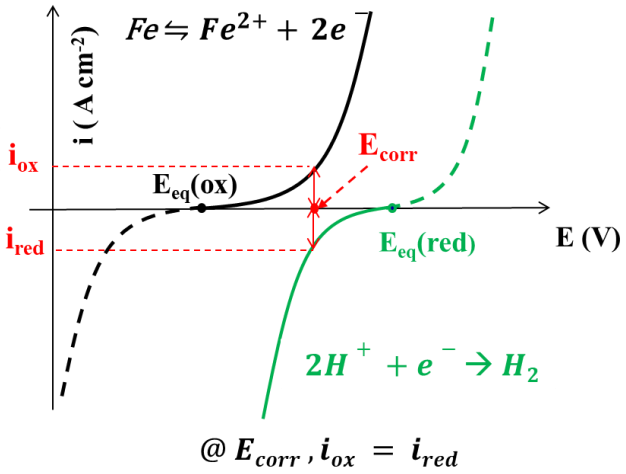

Figure 2-2: Illustration of the Butler-Volmer relationships for metal oxidation and solution reduction half-reactions.

With the assumption that E_{elec} is sufficiently far away from the equilibrium potentials of the two half-reactions, the anodic (oxidation) and cathodic (reduction) current densities can be approximated by **Eq. 2-9a** and **Eq. 2-9b**.

$$i_{ox} \approx i_{ox}^{0} \left(exp(\frac{\alpha_{ox}\, nF(E_{elec}-E_{ox}^{eq})}{RT})\right) \quad \textbf{(Eq. 2-9a)}$$

$$i_{red} \approx i_{red}^{0} \left(exp(-\frac{(1-\alpha_{red})\, nF(E_{elec}-E_{red}^{eq})}{RT})\right) \quad \textbf{(Eq. 2-9b)}$$

Due to charge and mass balance requirements, the oxidation and reduction rates at the corrosion potential must be the same. To obtain the corrosion current density (i.e., the current density at E_{corr}), the system is often polarized by applying an external voltage. The net current under polarization can be determined by the Wagner-Traud equation (**Eq. 2-10**), derived from the Butler-Volmer equations [19,20]:

$$i \approx i_{corr} \left(exp(\frac{\alpha_{ox}\, nF\, (E_{elec}-E_{corr})}{RT}) - exp\,(-\frac{(1-\alpha_{red})\, nF(E_{elec}-E_{corr})}{RT})\right) \quad \textbf{(Eq. 2-10)}$$

For high negative overpotentials, the term $exp(\frac{\alpha_{ox}\, nF\, (E_{elec}-E_{corr})}{RT})$ can be neglected, and for high positive overpotentials, the term $exp(-\frac{(1-\alpha_{red})\, nF\, (E_{elec}-E_{corr})}{RT})$ in **Eq. 2-10** can be neglected, and **Eq. 2-11a** and **Eq. 2-11b** can be derived:

$$i_{ox} \approx i_{corr}\, exp(\frac{\alpha_{ox}\, nF\, (E_{elec}-E_{corr})}{RT}) \quad \textbf{(Eq. 2-11a)}$$

$$i_{red} \approx -i_{corr}\; exp(-\frac{(1-\alpha_{red})\, nF(E_{elec}-E_{corr})}{RT}) \quad \textbf{(Eq. 2-11b)}$$

For potentials sufficiently far from E_{corr} and in the absence of mass-transport effects, the anodic or cathodic branches normally exhibit linear behaviour on a logarithmic scale. The experimental Tafel slopes, β_a and β_c in volts per current decade unit, can be expressed using the following equations (**Eq. 2-12a** and **Eq. 2-12b**) [17,18]:

$$\beta_a = \frac{2.3RT}{\alpha_{ox} nF} \quad \textbf{(Eq. 2-12a)}$$

$$\beta_c = \frac{2.3RT}{(1-\alpha_{red}) nF} \quad \textbf{(Eq. 2-12b)}$$

The i_{corr} can be estimated by extrapolation of these Tafel lines to E_{corr}.

2.2.2 Effect of Mass Transport on the Corrosion Process

The overall electrochemical reaction consists of multiple steps that can contribute to the overall rate. These include electron transfer via a conducting electrode between the redox pairs and transport of the redox species towards and away from the interfacial region [21–23].

The Butler-Volmer equation assumes that the rates of the oxidation and reduction reactions are controlled by electron transfer. However, the redox species may, in some cases, undergo a chemical reaction in the interfacial region. In this case, the Tafel slopes will contain a contribution from chemical processes other than interfacial electron transfer, which means that using the Tafel extrapolation method will give an incorrect value for the corrosion rate.

In electrochemical reactions, the electron transfer rate is influenced by the mass transport of redox-active species [24–26]. Mass transport of redox-active species may occur via diffusion (i.e., the movement of species due to a concentration gradient), migration (i.e., movement of charged species due to an electric field gradient), or convection (i.e., solution flow due to a pressure gradient or stirring) or a combination of these modes. The mass transport of ions is described by the Nernst-Planck equation (**Eq. 2-13**) [13].

$$J_j(x) = -D_j \frac{\partial C_j(x)}{\partial x} - \frac{m_j F}{RT} . D_j C_j . \frac{\partial \phi(x)}{\partial x} + C_j \nu(x) \quad \textbf{(Eq. 2-13)}$$

where $J_j(x)$ is the flux of species (mol cm^{-2}) at distance x, D_j is the diffusion coefficient (cm^2 s^{-1}), $\frac{\partial C_j(x)}{\partial x}$ is the concentration gradient at distance x, m_j is the charge of species j, C_j is the concentration (mol cm^{-3}), $\frac{\partial \phi(x)}{\partial x}$ is the potential gradient at a given distance x, and $\nu(x)$ is the rate (cm s^{-1}) of the solution flux in the x-direction.

The movement of ions by convection is minimal in the absence of stirring or vibration in an electrochemical cell, and it can thus be ignored [13]. In the bulk solution, at a distance from the surface where the concentration gradients are small, the diffusion component is negligible, and the total current is carried by migration. Migration plays a critical role in mass transport processes in low ionic strength solutions. Near the electrode surface, the concentration gradient is significant, and thus ions are transported to and from of the surface by both migration and diffusion processes.

The contribution of mass transport to the oxidation and reduction current densities can be determined by performing polarization tests under various mass transfer conditions (e.g., polarization tests using a rotating disk electrode). The current density (i) is related to the mass-transport-limiting current density (i_L), which is obtained from Levich equation ($i_L = B\omega^{0.5}$), by the Koutecky-Levich equation (**Eq. 2-14**).

$$\frac{1}{i} = \frac{1}{i_k} + \frac{1}{B\omega^{0.5}} \quad \textbf{(Eq. 2-14)}$$

where i_k is the kinetic current density, B is the Levich constant and ω is the angular rotation rate of the electrode (rad s^{-1}) [27,28].

In the interfacial region (x = 0), convection does not occur (i.e., the boundary layer), and the solution can be treated as stagnant. As stated earlier in **Section 2.2.1,** the equilibrium potential of half-reactions is governed by the Nernst equation. The changes in the concentration of oxidant and reductant ions at the electrode interface can affect the steady-state equilibrium potential of the half-reactions and consequently affect the rate of charge transfer [29]. In addition, the potential at which the rate-determining step changes from interfacial electron transfer to mass transport is different for metal oxidation and oxidant reduction. Thus, using a linear dynamic approach such as that of the Koutecky-Levich equation may lead to an incorrect value of i_{corr}.

2.2.3 Effect of an Oxide Layer on the Corrosion Rate

An oxide layer can affect both the electron transfer and the mass transfer processes by changing the potential gradient and limiting ion transport, respectively.

As explained below, the overall corrosion process involves more than two major phases and also involves more than one interface. In order for a corrosion reaction to proceed, metal cations must transfer through the oxide phase and reach the oxide/solution interface to dissolve into the solution phase or be incorporated into the oxide phase. A net flux of positive charge (metal cations, holes) must take place from the metal/oxide interface to the oxide/solution interface. At the same time, a net flux of negative charge (electrons, oxygen anions) must transfer from the oxide/solution interface to the metal/oxide interface [14,16,30]. These processes are schematically presented in the mass and charge balance model shown in **Figure 2.3.**

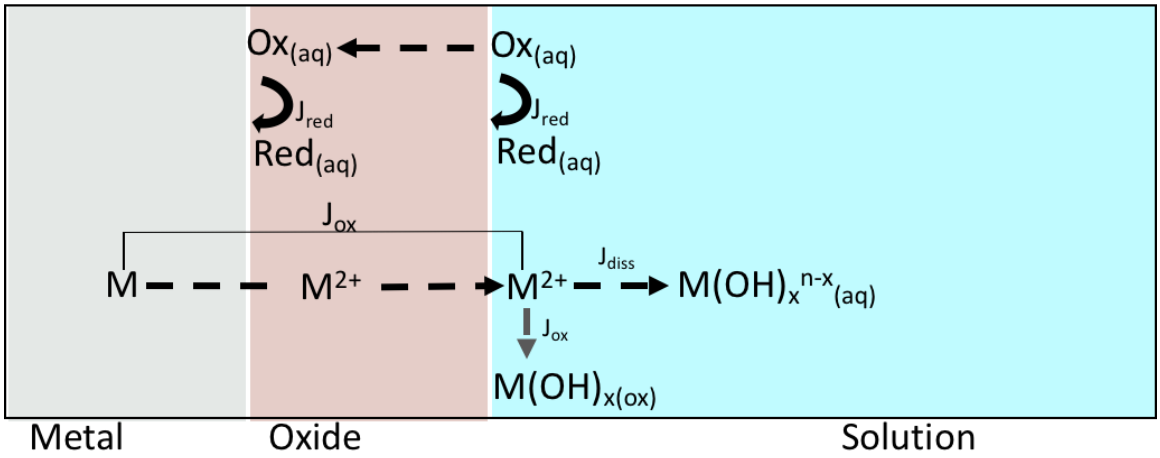

Figure 2-3: Illustration of Mass and Charge Balance (MCB) model for the corrosion in the presence of an oxide layer [27,41,42].

In addition to the effect on mass transport, an oxide layer can create a potential barrier and reduce the effective overpotential ($\eta_{ox(eff)}$) for metal oxidation [16], which depends on the physical and electrochemical nature of the oxide layer. A decrease in the effective overpotential for metal oxidation results in a decrease in the corrosion rate.

2.3 CORROSION OF CARBON STEEL AND STAINLESS STEELS

2.3.1 Main Oxides and Oxyhydroxides on Steels

The main oxides and oxyhydroxides that can be formed during corrosion of carbon steels are iron(II) hydroxide ($Fe(OH)_2$), magnetite (Fe_3O_4), lepidocrocite (γ-FeOOH), maghemite (γ-Fe_2O_3), hematite (α-Fe_2O_3), and goethite (α-FeOOH).

Magnetite is a black oxide with a bandgap of only 0.1 eV, and is therefore conductive. Magnetite contains both Fe^{II} and Fe^{III} with a crystal structure of an FCC arrangement of O^{2-} anions with Fe^{III} cations filling the octahedral sites and Fe^{II} cations

occupying the octahedral and tetrahedral interstitial sites.

Lepidocrocite is an oxyhydroxide with an orthorhombic structure consisting of layers of Fe^{III} oxide octahedra linked by hydrogen bonding via hydroxide ligands. The colour of lepidocrocite ranges from yellow to reddish-brown, and it has a band gap of 2.06 eV.

Maghemite has a band gap of 2.03 eV, which is very close to that of lepidocrocite (2.06 eV). The structure is similar to magnetite, with the difference being that almost all the interstitial sites are occupied by Fe^{III}. Because of the structural similarity of magnetite and maghemite, phase transformation between the two is facile.

Hematite appears red to black in colour and has a band gap of 2.2 eV. Hematite has the sapphire structure, with a hexagonal close-packed array of O^{2-} and 2/3 of the octahedral sites filled with Fe^{III}, and is exceptionally stable.

Finally, the colour of goethite ranges from yellow to red to black. This oxyhydroxide consists of a hexagonal (hcp) array of OH^{-} and O^{2-} ions with Fe^{III} ions occupying ½ of the octahedral sites [31]. α-FeOOH is thermodynamically more stable than γ-FeOOH. Thus, γ-FeOOH gradually transforms into α-FeOOH once it has formed [32]. β-FeOOH is another type of ferric oxyhydroxide that is only observed in chloride-containing environments [33,34].

2.3.2 Solubility of Iron

The oxidation states of Fe are Fe^{II} and Fe^{III}. In acidic solution, Fe^{2+} is the predominant form of Fe^{II}, and undergoes hydrolysis to $FeOH^{+}$ and $Fe(OH)_{2(aq)}$ in neutral solutions and precipitates as $Fe(OH)_{2(s)}$. For Fe^{III}, the aqueous species Fe^{3+} is

formed in very acidic solutions, and as pH increases, it is hydrolyzed to $Fe(OH)^{2+}$, $Fe(OH)_2^+$ and $Fe(OH)_{3(aq)}$. Iron (III) hydroxide ($Fe(OH)_3(s)$) precipitates in neutral solutions, but the solubility increases again in very alkaline solutions via the formation of $Fe(OH)_4^-$ [16]. **Figure 2-4** shows the solubility plot for Fe (II) and Fe (III) species. At any given time, the total amount of dissolved iron is the sum of the dissolved ferrous and ferric species present in the solution. In general, the solubility of Fe^{III} oxides is low, and Fe^{II} oxides are sparingly soluble. This means that the concentration of Fe in the solution is very low, except at extreme pH values. Iron oxides dissolve slowly over a wide pH range [35–37].

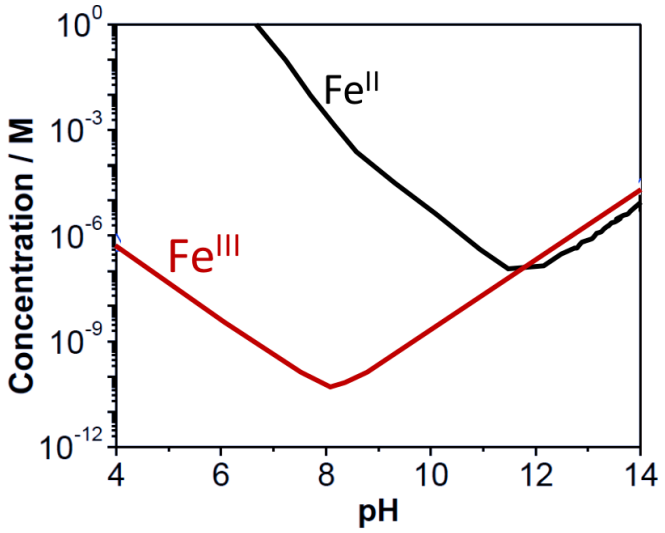

Figure 2-4: pH-dependent solubility of Fe^{II}, Fe^{III} at 25 °C [37].

The minimum solubilities of the total ferrous (Fe^{2+}) and ferric (Fe^{3+}) species occur at pH 12 and 8.4, respectively. An increase in temperature increases the solubility by less than an order of magnitude, and shifts the solubility minima to lower pHs [7,29].

2.3.3 Pourbaix Diagram for CS and Stainless Steel Systems

Corrosion can occur over a wide range of both pH and potential. A valuable tool for studying corrosion is the potential-pH diagram (Pourbaix diagram), which was first developed by Pourbaix to show the stability regions of the most thermodynamically favourable corrosion products as a function of pH and electrode potential [19,20,35]. The diagrams are plotted using thermodynamic equilibrium values for reactions between the metal and aqueous electrolyte. The stability regions of the species and corrosion products depend on the concentrations of dissolved species considered to be at equilibrium with the solid compounds [17]. Each Pourbaix diagram consists of three types of electrochemical equilibrium for a metal–water system: those (i) depending only on the electrochemical potential; (ii) depending only on the pH; and (iii) depending on both potential and pH [17,19,35,38]. **Figure 2-5** shows the Pourbaix diagram for the iron-water system [38].

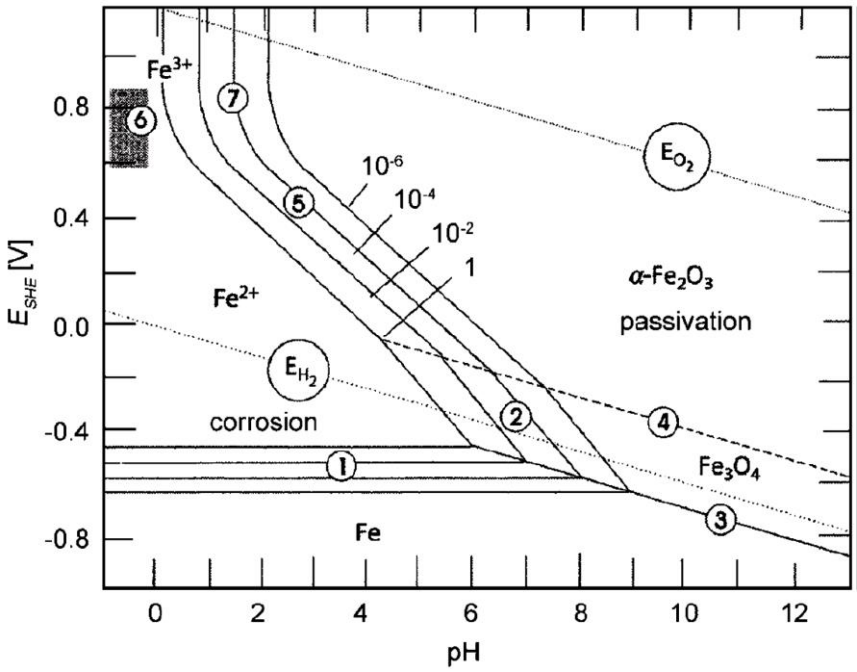

Figure 2-5: Pourbaix diagram of the iron-water system at 25 °C [38] (reprinted with permission from Ref. [38], © 2003, Springer-Verlag.)

Extensive work has been performed to improve the iron-water Pourbaix diagram to include different alloying elements [39], higher temperatures [36,40], different anions [41,42], or revised thermodynamic data for different oxides/hydroxides [33,43,44].

The Pourbaix diagram for the Fe-Cr-Ni system (three main elements found in stainless steels) has also been studied, and the stability regions for spinels and oxide layers calculated [39]. However, among these phases, only one (Cr_2O_3 or a Cr-rich oxide layer) is capable of forming a barrier conferring corrosion resistance. Consequently, from the corrosion point of view, displaying all of the other phases is an unnecessary complication that adds little to the understanding of the corrosion process [45].

When discussing Pourbaix diagrams, it should be noted that these diagrams are based purely on thermodynamic data and do not provide any information on the kinetics

and therefore the rates of the reactions involved [46].

2.3.4 Mechanism of Evolution of CS Corrosion

The mechanism of carbon steel corrosion determined by Guo et al. [7] is presented below in detail.

The initial electrochemical oxidation requires interfacial electron transfer between metal and solution species:

$$Fe_m \left\{\rightarrow Fe^{I}_{(m)} + e^{-}\right\} \rightarrow Fe^{II}_{(m)} + 2\ e^{-} \qquad \textbf{(Eq. 2-15)}$$

$$2\ H_2O + 2\ e^{-} \rightarrow 2\ OH^{-} + H_2 \qquad \textbf{(Eq. 2-16)}$$

In order for corrosion to proceed, this electron transfer must be accompanied by metal cation transfer from the metal to the solution phase, to satisfy charge conservation. The metal cation transfer process includes lattice-bond breaking followed by solvation (or hydration) of the cation:

$$Fe^{II}_{(m)} + n\ H_2O \rightarrow Fe^{II}_{(hyd)} \qquad \textbf{(Eq. 2-17)}$$

where $Fe^{II}_{(hyd)}$ represents the hydrated ferrous ion on the metal surface, and the overall rate of reaction is controlled by whichever is slowest between charge transfer and mass transfer processes.

The overall interfacial charge transfer process that produces $Fe^{II}_{(hyd)}$ in water is:

$$Fe_m + 2\ H_2O \rightarrow Fe^{II}_{(hyd)} + 2\ OH^{-} + H_2 \qquad \textbf{(Eq. 2-18)}$$

The hydrated ferrous ion can now diffuse from the surface into the bulk solution phase. As ferrous ions are hydrated and diffuse into solution, they also undergo hydrolysis:

$$Fe^{2+} + 2\ H_2O \rightleftarrows Fe(OH)^{+} + H^{+} + H_2O \rightleftarrows Fe(OH)_2 + 2\ H^{+} \quad \textbf{(Eq. 2-19)}$$

The dissolved ferrous species will henceforth be collectively referred to as $Fe^{II}_{(aq)}$. The relative concentrations of the different solvated ferrous species depend on pH. Initially, the concentration of Fe^{II} near the surface will be zero and hence the oxidation of Fe^0 to Fe^{II} coupled with solution reduction proceeds immediately, irrespective of solution conditions. The predominant corrosion pathway immediately following the oxidation of Fe^0 to Fe^{II} is the diffusion of Fe^{II} into the bulk solution. However, as corrosion progresses, $[Fe^{II}_{(aq)}]$ will increase and approach its saturation limit, and at that point, the predominant corrosion pathway switches from dissolution to the formation of $Fe(OH)_{2(s)}$. The time to reach this kinetic stage depends on the solution environment parameters.

The Fe^{II} formed on the metal surface by the reaction will end up either in the solution as dissolved ferrous ions ($Fe^{II}_{(aq)}$) or in the solid hydroxide phase as $Fe(OH)_{2(s)}$.

In the presence of O_2, as $Fe(OH)_{2(s)}$ is growing, some of the Fe^{II} present on the surface of the $Fe(OH)_{2(s)}$ particles can further oxidize to Fe^{III}. The ferric ion produced from $Fe(OH)_{2(s)}$ also undergoes hydration and may precipitate as hydroxides which then grow into an oxyhydroxide or oxide of a specific phase such as γ-FeOOH (lepidocrocite) or α-Fe_2O_3 (maghemite).

$$4\ Fe(OH)_2 + O_2 + 2\ H_2O \rightleftarrows 4\ Fe^{III}_{(hyd)} + 12\ OH^{-} \quad \textbf{(Eq. 2-20)}$$

Mixed Fe^{II} and Fe^{III} hydroxides can dehydrate and transform to the thermodynamically more stable oxide magnetite (Fe_3O_4):

$$Fe^{II}Fe^{III}{}_2(OH)_8 \rightarrow Fe_3O_4 + 4\,H_2O \qquad \textbf{(Eq. 2-21)}$$

The possible iron oxidation reactions, dissolution processes, and formation of the hydroxide/oxide oxidation products that can occur during CS corrosion are identified and schematically presented in **Figure 2-6**.

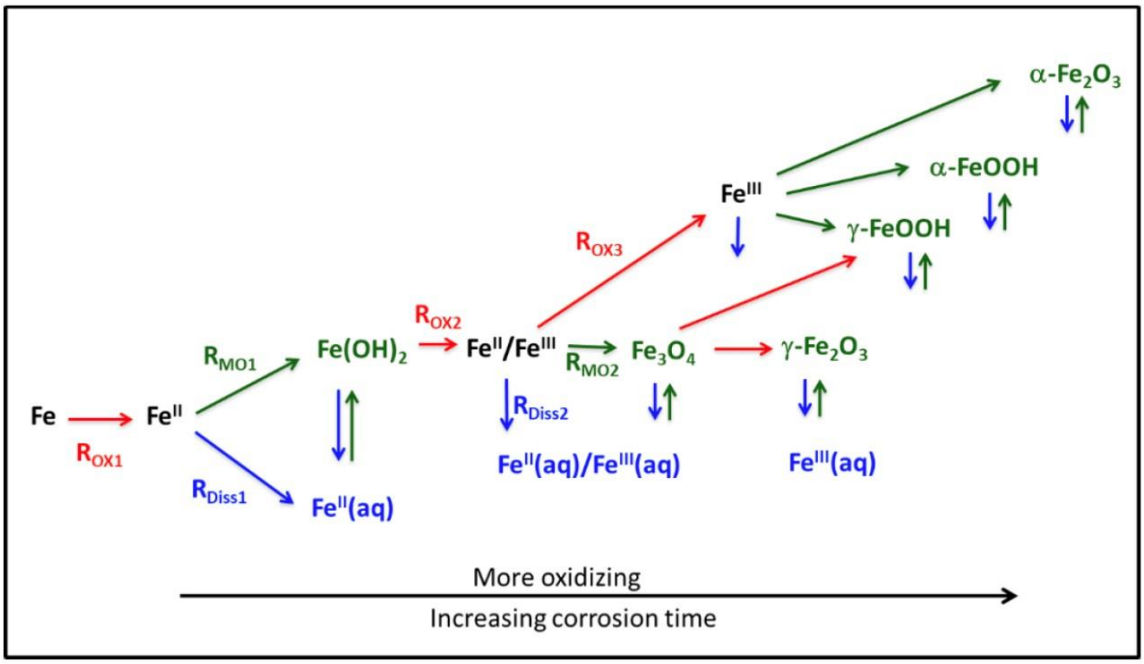

Figure 2-6: CS corrosion reaction pathways. The red arrows represent interfacial charge transfer steps (with R_{OX} being the oxidation rate), the blue arrows represent metal cation- dissolution steps at rates of R_{Diss} (dissolution rate), and the green arrows represent metal hydroxide/oxide formation steps at rates of R_{MO} (mixed oxide formation). The large black arrow at the bottom of the schematic indicates that corrosion progresses further along the corrosion pathway and faster in a more oxidizing solution environment [7].

Other existing mechanisms describe the charge transport processes but ignore the changes in oxide composition and structure during corrosion and the dependence of this on the solution environment [47–50]. However, the time-dependence of corrosion has been considered in some models, such as point defect models [45,51–55]. In these

models, the potential drop depends linearly on the oxide thickness:

$$\Delta E_{oxide} = \varepsilon . L \quad \textbf{(Eq. 2-22)}$$

where ΔE_{oxide} is the potential drop across the oxide layer, ε is the oxide's field strength and L is the thickness of the oxide. The oxide thickness changes logarithmically with time and eventually reaches a steady state [54]:

$$L = A + B . ln(t) \quad \textbf{(Eq. 2-23)}$$

where A and B are constants and *t* is time.

2.3.5 Humid Air Corrosion of Carbon Steel

Humid air corrosion occurs when a thin water layer can form on a metal surface under high relative humidity conditions. Humid air corrosion, usually referred to as atmospheric corrosion, is mechanistically similar to aqueous corrosion [56,57]. In this type of corrosion, the solution volume is very small, and even using specially adapted designs, the three-electrode experimental method cannot provide accurate results [58–63]. Different electrochemical approaches such as zero resistance ammeter (ZRA), electrochemical noise (EN), Kelvin probe, and wire beam electrode (also referred to as multi-electrode array) have previously been adopted in environments with different %RH to study the humid air corrosion of carbon steel [57,64–67].

A droplet can be created on a metal surface by placing different volumes of solution on the surface to simulate the water layer produced in humid air. Droplet studies using NaCl-containing solutions have been employed extensively in the study of humid air corrosion [61,62,68–75]. Nishikata et al. [61] showed that the maximum corrosion rate for iron occurs for an electrolyte layer thickness of 20 to 30 μm. They also showed

that the corrosion rate of iron would be affected by the solution pH only under a very thick electrolyte layer (layer thickness > 1 mm) for a short exposure period (<1 h). For longer exposure (> 1 h), the effect of pH was negligible, probably due to neutralization. Weissenriederz and Leygraf [72] showed that corrosion spreads at the edge of a 2 μg cm^{-2} sodium chloride solution droplet and attributed this phenomenon to the adsorption of water by corrosion products formed at the edges of the droplet. In another study, the formation of microdroplets adjacent to the main droplet was also explained based on the spreading of the main droplet [68]. In this study, they found that when a solution droplet contains a salt (e.g. NaCl), corrosion under the droplet progresses via the formation of wet areas and micro-droplets around the initial droplet. The propagation of the droplet to the coupon surface edges happens because the local pH increases due to cathodic polarization in the droplet edge region, and consequently, adsorption of water from the air and mass transport of water and cations from the droplet centre to the edge [68], which is in agreement with what Wang et al. [75] reported when studying the corrosion characteristics of carbon steel using a wire beam electrode. Based on the study of Chen and Mansfeld [73], galvanic corrosion at the edges, due to the difference in oxygen concentration, is the reason why oxide forms at the edges of the coupon. They claimed that the oxygen concentration at the edge of the droplet was higher than in its interior. This concentration difference, they claimed, in this classic "Evans drop" experiment [76], results in localized galvanic corrosion, with the centre acting as the anode and the edge as the cathode.

The probability of initiation of CS corrosion was found to be dependent on the size of the NaCl droplet. Li and Hihara [77,78] showed that, under certain conditions,

there is a minimum droplet size below which corrosion cannot initiate due to the low probability of the droplet covering an inclusion site. They speculated that the small droplets (< ~45 μm dia.) may contain oxygen above the critical level necessary to passivate the steel surface. Although the initiation sites for the initiation of corrosion on steels are inclusions (most importantly MnS), the initiation sites on pure iron have been reported to be surface heterogeneities caused by grinding [78].

2.4 RADIATION CHEMISTRY AND IONIZING RADIATION

When a metal is exposed to γ-radiation, the radiation energy it absorbs is dissipated mainly as heat. However, the water redox chemistry can be dramatically affected because ionizing radiation decomposes water into a range of redox active species. A brief overview of radiation chemistry and water radiolysis is presented below.

Radiation chemistry deals with the chemical effects produced in a system when exposed to high-energy ionizing radiation. Ionizing radiation includes electromagnetic radiation (X- and γ-rays) and charged particles (α- and β-particles) that can cause ionization (along with some excitation) of molecules in a medium. Ionizing radiation transfers its energy to an interacting medium by colliding non-discriminately with the electrons bound to atoms and molecules in the medium. Due to its high kinetic energy, each radiation particle undergoes a series of collisions before it loses most of its kinetic energy. In assessing the chemical effects produced in the interacting medium upon interaction with radiation, the rate of radiation-energy transfer per unit length or the rate of linear energy transfer, LET, is a useful parameter. The LET depends on the mass of the

radiation particle and is higher for α-particles than for β-particles or γ-photons. The changes observed in matter following exposure to radiation vary depending on the type of radiation [79–83].

Heavy particles, such as α-particles, lose their energy mainly through inelastic collisions with electrons located along the radiation path. Due to their large mass compared with the electrons they perturb, only small amounts of energy are lost with each collision, and the large α-particles are not easily deflected from their paths. The large collision cross section of α-particles with electrons prevents these particles from penetrating deeply into a medium and therefore, they have a very short penetration depth (10-100 μm) in water. This results in a very dense collection of excited and ionized particles along a short stretch of the radiation track [79,80].

For low-mass particles (e.g. β-particles), energy loss also occurs mainly through inelastic collisions, but in contrast, β-particles have a larger penetration depth. Since β-particles share the same mass as the electrons with which they interact, the particles can lose up to half of their energy with each collision and can be deflected through large angles. β-particles can interact with additional electrons to lose their remaining energy. The penetration range for β-particles is 1 to 2 cm in water, and these particles create a low-density collection of ions or excited molecules along their radiation track [79,80].

Gamma-rays transfer most of their energy by Compton scattering if their energy exceeds 0.01 MeV [79,81,83,84] and is less than about 20 MeV. Compton scattering is a phenomenon in which the γ-ray interaction with matter causes electron ejection from the molecule and the resulting γ-ray photon emerges with a reduced energy. Each ejected electron from a high-energy collision acts similarly to a β-particle and produces a

characteristic ionization cascade. The most probable Compton scatterings are either near 100% energy transfer or near 0% energy transfer. Due to the low probability of inelastic Compton scattering, the penetration depth of γ-radiation is large relative to all other radiation forms. The ejected electrons from Compton scattering with near 100% energy transfer are referred to as primary electrons. These primary electrons have similar energies to β-particles. Thus, the collision cross section, the collision frequency, and the mean free path energy of primary electrons are similar to those of β-particles. Therefore, the chemical effects such as primary radiolysis product yields per unit of absorbed energy (g-values) are essentially the same for both β- and γ-radiation. The difference between β- and γ-radiation lies primarily in the energy transfer rate. The penetration depth of γ-radiation is the largest relative to other radiation forms. Each ejected electron from these high-energy collisions acts similarly to a β-particle and prolongs the collision effect by transferring its kinetic energy [79,81,83,84].

In radiation chemistry, the energy absorption mechanisms are insensitive to molecular structure and are almost entirely dependent on atomic composition. Because all molecules are equally likely to interact with the radiation, the effect on the bulk solution predominates over the effect on solute molecules. Hence, the radiation chemistry of solutions is described as a solvent-oriented process [79–83].

2.4.1 Principles of Water Radiolysis

When passing through liquid water, a gamma photon will undergo collisions with water molecules. The average energy transferred, per collision, typically ranges from 60 to 100 eV [79,83]. This amount of energy is only a very small fraction of the initial energy of the radiation particle (of the order of 1 MeV), so the collisions do not slow the

radiation particle or change the radiation path appreciably (except at the very end of the track). The radiation particle moves in a straight line that is referred to as a radiation track. The initial consequence of each energy transfer collision is the ionization or electronic excitation of a water molecule. This creates ion pairs ($H_2O^{\bullet+}$ and e^-_{hot}) or electronically excited water molecules (H_2O^*) along the radiation track. The electron of this ion pair is labelled as a 'hot' electron because it has sufficiently high kinetic energy to excite or ionize one or more neighbouring water molecules (the 60– 100 eV transferred in a collision is well in excess of the ionization energy of a water molecule: 12.6 eV). Secondary (or subsequent) ionizations caused by this 'hot' electron will occur very near the first ionization that created the 'hot' electron, resulting in a cluster of 2-3 ion pairs (or excited water molecules) near the radiation track. This cluster is referred to as a "spur" [79,83].

Following ion pair production, the electrons formed in a spur can have sufficiently high kinetic energy to move away from their H_2O^+ counter cations. This process is referred to as expansion of the spur. As the spur expands, the 'dry' electrons that arose from the water molecule ionization will be solvated and become hydrated electrons ($\bullet e^-_{aq}$). The water cations and any excited water molecules in the spur will interact with other solvent water molecules. Various intra- and inter-molecular energy transfer processes will occur that can lead to bond formation and bond breaking as illustrated in **Figure 2-7**. The Coulombic attraction of the counter ions diminishes as the spur expands and the counter ions and radicals become no longer distinguishable from other ions and radicals formed in other neighbouring spurs or already present in the bulk phase. Once the system reaches this stage, the subsequent physical and chemical processes of these

'free' species can be treated as ordinary bulk phase chemistry. The time frame during which spur expansion occurs is approximately 100 ns in liquid water at 25 °C, as shown in **Figure 2-7**. The species present at this stage are normally referred to as 'primary' radiolysis products and their concentrations per unit of absorbed energy are referred to as primary radiolysis yields, or G-values. For a specific type of radiation and a given absorbing medium, the primary radiolysis yield depends on the amount of energy absorbed by the medium. Hence, the G-values are expressed per unit of absorbed energy (in units of amounts of species produced per 100 eV absorbed energy, or $\mu molJ^{-1}$ in SI units) [79,83].

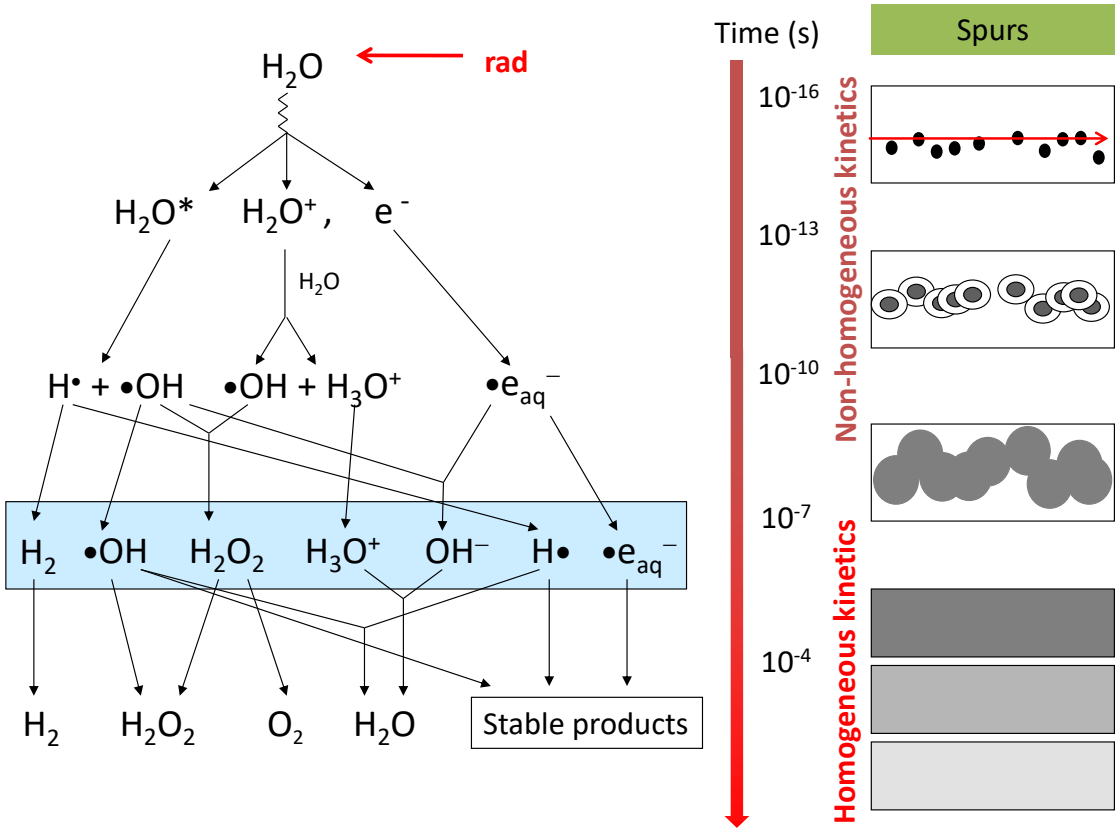

Figure 2-7: Water radiolysis as a function of time following absorption of radiation energy as a pulse. The right-hand panel shows the expansion of spurs with time.

The distribution of spurs along a radiation track is an important parameter in determining the chemical yields of radiolysis products. The spur density along the track mainly depends on the collision rate of the radiation particles with the bound electrons in the water molecules. If the spur density is sufficiently high, as for high LET α-radiation, the ions and radicals in a spur can interact with those of an adjacent spur before they diffuse into the bulk water phase. This can lead to a higher ratio of molecular to radical primary radiolysis products. In the case of low LET radiation like X-rays or γ-rays the spurs are spread out along the radiation track. This relatively large distance between adjacent spurs allows the reactive species to diffuse more easily away from the radiation track and avoid recombination to molecular products. This results in a higher ratio of radical to molecular radiolysis products.

Under a continuous, steady-state flux of radiation, water molecules are continuously interacting with radiation particles to form primary radiolysis products. After the start of irradiation, the concentrations of water radiolysis products increase rapidly. However, these species very rapidly begin to react with each other and other species in the system and the chemical kinetics reach a pseudo-steady state on a time scale that is on the order of minutes. It is the pseudo-steady-state concentrations of reactive species and not the primary radiolytic yields of reactive species that are crucial in evaluating the corrosion of reactor materials [79,83].

2.4.2 Humid Air Radiolysis

In a humid environment, the absorption of radiation energy by the three main components of air (N_2, O_2 and H_2O) results in the formation of primary radiolysis products and subsequent stable products (NO_x and HNO_3) [83].

$$N_2, O_2, H_2O \xrightarrow{\gamma} \bullet H, \bullet OH, \bullet N, \bullet O, H_2, O_2, H_2O_2, O_3, NO_x, HNO_3 \qquad \textbf{(Eq. 2.24)}$$

To study humid air radiolysis kinetics, a humid-air radiolysis model (HARM) [85,86] was developed in our research group and was used to calculate the time-dependent concentrations of radiolysis products. The model calculations were performed as a function of temperature, air relative humidity and radiation dose rate. The results showed that HNO_3 is the dominant oxidizing species formed during humid air radiolysis that is capable of affecting corrosion. The HNO_3 formed in the gas phase will be continually absorbed in the condensed water droplets in contact with the humid air. This will lower the pH of the water in the droplet in contact with the surface and increase the concentration of nitrate, a potential oxidant for CS.

The concentrations of nitrogen species produced by irradiation of 0% RH (dry air), 10% RH, and 85% RH air at 75 ˚C and a dose rate of 1 kGy·h^{-1} were calculated in a study by Morco et al. and are shown in **Figure 2-8** [86].

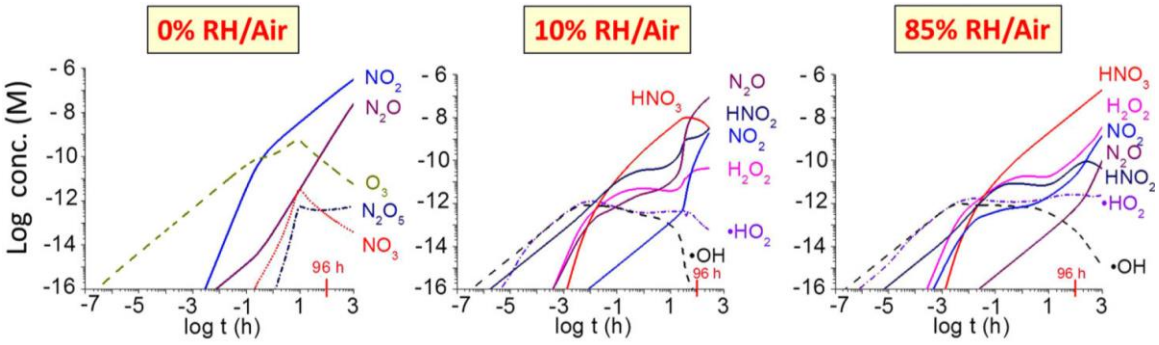

Figure 2-8: Concentrations of nitrogen species calculated using the humid air radiolysis model for different relative humidities in air at 75 ºC and at a dose rate of 1 kGy·h^{-1} [86] (reprinted with permission from Ref. [86], © 2017, Taylor & Francis, www.tandfonline.com)

Morco's study [85,86] indicated that nitric acid is not produced via irradiation of dry air; the main products of the irradiation of dry air are NO_x species (N_2O_5, NO_2, N_2O) and O_3. In humid air, in contrast, HNO_3 production becomes significant. The other significant product of humid air radiolysis is H_2O_2.

The HNO_3 formed in the gas phase will be continually absorbed into water droplets on the metal surface, lowering their pH and increasing the nitrate concentration.

2.5 CORROSION OF CARBON STEEL AND STAINLESS STEEL IN REACTOR ENVIRONMENTS

A current investigation into a leak in the end shield cooling (ESC) system in Ontario Power Generation's Pickering Unit 6 reactor has indicated that moisture from this leak could possibly reach a location in the annular air gap which exists around the periphery of the calandria tank assembly and its supporting structures. The possibility of the corrosion attack on carbon steel (CS) adjacent to the dissimilar metal weld (type 309 SS) between CS (SA36) and stainless steel (SS) (Type 304L SS) at the periphery of the annular air gap must be evaluated (shown in **Figure 2-9).**

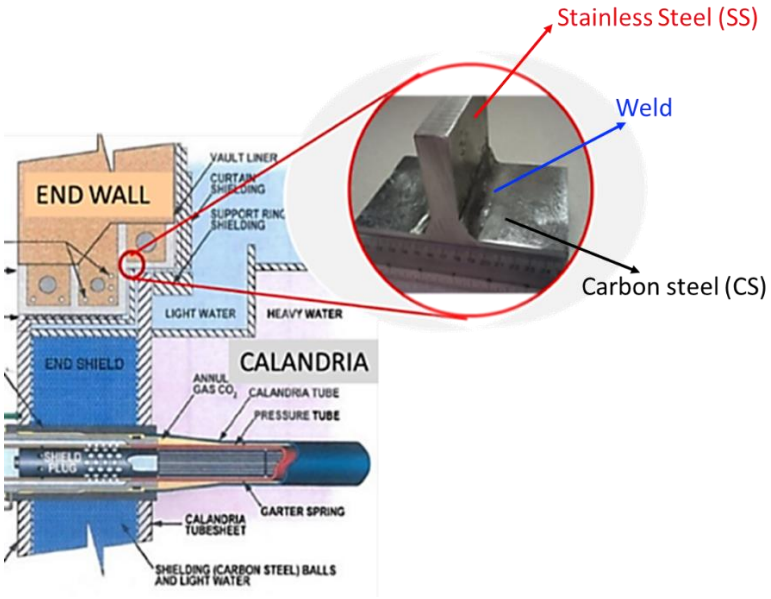

Figure 2-9: Schematic of the calandria tank assembly and its supporting structures in a CANDU reactor. The red circle indicates the location of the carbon steel (CS) and stainless steel (SS) weld joint (b) a SS-CS weld block supplied by Ontario Power Generation (OPG).

Corrosion in the vicinity of a nuclear reactor core happens in the presence of high-energy ionizing radiation. Nuclear fission and the decay of fission products produce different forms of ionizing radiation. The primary shield system that protects workers by absorbing radiation from the reactor core is called the end shield, and is filled with neutron-absorbing light water. Alpha and beta radiation from fission and radionuclide decay have very short penetration depths and will therefore be blocked by all the materials between the fuel channels and the weld region. Neutron radiation will not be of concern either because the weld is behind the end-shield. Thus, for the CS/SS/weld in question, only γ-radiation needs to be considered.

In the presence of radiation, the most important oxidizing species (due to water radiolysis) are H_2O_2 [87–89], O_2 [90,91], or •OH [89,92]. Studies on the corrosion of CS

under γ-radiation are limited, and those that do exist can be categorized as either corrosion in nuclear waste disposal environments, focusing on groundwater conditions [93,94] or corrosion in nuclear reactor environments, focusing on high temperature circulating water conditions [95–97]. In the latter, studies showed that H_2O_2 is the key radiolysis product controlling CS corrosion [96]. Another study examined the Fe_3O_4/ γ-Fe_2O_3 film formed on a CS surface after corrosion at 150 °C at pH 7.0 and 10.6 under γ-radiation [97] and concluded that the presence of γ-radiation does not necessarily increase the corrosion rate.

Ishigure et al. [98] showed that, under irradiation, the amount of iron oxide on the metal surface increases while the dissolved iron in the solution decreases. Based on this finding, they concluded that γ-radiation does not have an overall marked influence on carbon steel corrosion. In contrast, the work of Fujita et al. [99] showed that exposure to radiation increases the rate of CS corrosion six times. Daub et al. [96] studied the CS corrosion behaviour following the chemical addition of H_2O_2 at pH 10.6. They compared the corrosion behaviour in the absence of radiation with that under γ-radiation and observed a significant increase in the corrosion potential under γ-radiation, which was comparable to that of chemically added H_2O_2 solution in the absence of radiation. They concluded that hydrogen peroxide is the key radiolysis product controlling the corrosion of CS.

When H_2O_2 is used as a solution additive to simulate water under gamma irradiation, the measured corrosion potential of stainless steel does not change considerably when it is removed from the hydrogen peroxide solution and, after ultrasonic cleaning in acetone solution, placed in a solution without hydrogen peroxide,

suggesting that H_2O_2 makes permanent changes to the oxide layer [100]. The same observation was reported upon the removal of stainless steel from the presence of radiation [89].

2.5.1 Corrosion of Carbon Steel and Stainless Steel in Nitrate Solution

The results of previous studies on the effect of nitrate on carbon steel and stainless steel corrosion are inconsistent and contentious, leaving some issues unclear. The studies on adsorption and reduction mechanisms are in separate publications and the results regarding how different conditions affect corrosion are not consistent [101].

Sridhar et al. [102] studied the effect of nitrate on the stress corrosion cracking of carbon steel in radioactive waste storage systems. Their analysis concluded that nitrate is an aggressive agent for the localized corrosion of carbon steel and the role of nitrate and nitrite in localized corrosion is mostly through active dissolution and passivity rather than effect on corrosion potential. They also concluded that the pH controls the long-term corrosion potential of carbon steel in a nitrate-containing environment.

Pillay and Lin [103] studied the effect of nitrate on the corrosion of carbon steel in sea water. Their analysis concluded that the addition of nitrate significantly increases the corrosion rate after 20 weeks, mostly because of microbial corrosion.

Kolman et al. [104] examined the effect of nitrate and chloride on the corrosion of 304 stainless steel using electrochemical methods. Their analysis revealed that the corrosion of 304 SS exhibits two distinct behaviours. The stainless steel samples were either continuously passive or there was passivity following active dissolution. They also found that the active dissolution process was autocatalytic, with the corrosion rate

increasing exponentially with time and potential. They reported that the length of the active corrosion period was a function of the solution volume to surface area ratio. Their analysis suggested that spontaneous passivation was a consequence of a change in solution chemistry with time as opposed to changes in surface oxide composition.

2.5.2 Effect of Hydrogen Peroxide on Corrosion of Carbon Steel and Stainless Steel

The effect of hydrogen peroxide on the corrosion of carbon steel and stainless steels has been investigated over the past few decades. Most of the studies emphasised the oxidative role of hydrogen peroxide in the corrosion process.

Bellanger studied the effect of radiolytic hydrogen peroxide on the passivity of a carbon steel. The analysis results revealed the importance of hydrogen peroxide acting as an oxidant, on the corrosion potential, passivity, and oxide thickness.

Anzai et al. [105] studied the effect of hydrogen peroxide and oxygen on the intergranular stress corrosion cracking of 304 stainless steel. Their analysis results revealed that hydrogen peroxide accelerated crack growth, irrespective of the oxygen concentration.

Toijer and Jonsson [106] investigated the effect of hydrogen peroxide on the corrosion of 304 stainless steel. They concluded that catalytic decomposition of hydrogen peroxide resulting in hydroxyl radical formation is the main pathway for corrosion. They also claimed that the main effect of hydrogen peroxide on stainless steel corrosion is on the inner layer oxide (chromium-rich oxide) rather than the outer layer (iron-nickel rich oxide).

In another study in 2019, Makjan et al. [107] examined the effect of hydrogen peroxide on the corrosion of 304 stainless steel at temperatures below 80 °C using SEM/EDX analysis. Their analysis concluded that an increase in hydrogen peroxide concentration mostly results in the depletion of Fe and Ni rather than Cr and the most likely stable corrosion products are chromium oxides. This is in contrast with the study by Toijer and Jonsson [106], which showed that dissolution of chromium occurs in the presence of hydrogen peroxide. They also stated that an increase in hydrogen peroxide concentration and temperature accelerates pitting corrosion.

Satoh et al. [108] investigated the effect of hydrogen peroxide concentration at high temperature and high pressure on the corrosion of 304 SS. The corrosion potential measurements and their impedance spectroscopy analysis demonstrated that the corrosion potential in the presence of hydrogen peroxide is mainly determined by the electric resistance of a hematite-rich layer on the surface. In another (2005) study [109,110], it was found that oxide dissolution resistance and oxide film resistance were affected by the presence of hydrogen peroxide. In the presence of 100 ppb hydrogen peroxide, the dissolution resistance decreased, and the oxide film resistance increased, causing an increase in corrosion potential. They also attributed this to the presence of two oxide layers (an outer layer with a high dissolution rate and an inner layer with high electric resistance) on the surface. In an article published by the same authors in 2006 [111], they studied the oxide film on the surface and observed that the oxide thickness decreased in the presence of hydrogen peroxide and increased in the presence of oxygen. Also, they noted that the higher dissolution rate and oxide growth rate with high hydrogen peroxide concentrations result in the formation of a thin oxide film and small oxide particles. In

another work (in 2007) [112], they reported that anodic and cathodic polarizations of samples exposed to hydrogen peroxide changed with the concentration of hydrogen peroxide. It was found that the cathodic current was limited by the diffusion of hydrogen peroxide through the boundary layer on the metal surface, while the anodic current increased as a result of a hydrogen peroxide oxidation reaction. The contribution of metallic cations to the anodic current was minor. They also found that the corrosion potential was affected by hydrogen peroxide concentration, resulting from the dependence of both the anodic and cathodic current densities on the hydrogen peroxide concentration.

2.6 REFERENCES

[1] H. Chandler, Heat Treater's Guide, Practices and Procedures for Irons and Steels, ASM International, 1995.

[2] D.T. Llewellyn, R.C. Hudd, Steels: Metallurgy & Applications, 3rd ed., Elsevier, 1998.

[3] Y. Li, J.A. Wilson, D.N. Crowther, P.S. Mitchell, A.J. Craven, T.N. Baker, The Effects of Vanadium, Niobium, Titanium and Zirconium on the Microstructure and Mechanical Properties of Thin Slab Cast Steels, ISIJ Int. 44 (2004) 1093–1102.

[4] F.G. Caballero, M.K. Miller, S.S. Babu, C. Garcia-Mateo, Atomic scale observations of bainite transformation in a high carbon high silicon steel, Acta Mater. 55 (2007) 381–390.

[5] A.L.V. da Costa e Silva, Non-metallic inclusions in steels – origin and control, J. Mater. Res. Technol. 7 (2018) 283–299.

[6] J. Poirier, A review: Influence of refractories on steel quality, Metall. Res. Technol. 112 (2015).

[7] D. Guo, Corrosion Dynamics of Carbon Steel in Used Fuel Container Environments, PhD Thesis, The University of Western University, 2018.

[8] H. Esaka, Continuous casting of steels, in: B. Cantor, K. O'Reilly (Eds.), Solidif. Cast., 1st ed., CRC Press, 2002.

[9] H. Berns, W. Theisen, Ferrous Materials: Steel and Cast Iron, 1st ed., Springer-Verlag Berlin Heidelberg, 2008.

[10] M. Durand-Charre, Microstructure of Steels and Cast Irons, Springer, 2004.

[11] S. Seetharaman, ed., Fundamentals of metallurgy, CRC Press, 2005.

[12] H.K.D.H. Bhadeshia, R.W.K. Honeycombe, Steels: Microstructure and Properties, 4th ed., Elsevier, 2017.

[13] A. J. Bard Larry R., Faulkner, Electrochemical Methods Fundamentals and Applications, second, JOHN WILEY & SONS, INC., Austin, 2001.

[14] A.Y. Musa, J.C. Wren, Combined effect of gamma-radiation and pH on corrosion of Ni-Cr-Fe alloy inconel 600, Corros. Sci. 109 (2016) 1–12.

[15] M. Momeni, Gamma-Radiation Induced Corrosion of Alloy 800, PhD Thesis, The University of Western Ontario, 2017.

[16] M. Momeni, J.C. Wren, A mechanistic model for oxide growth and dissolution during corrosion of Cr-containing alloys, Faraday Discuss. 180 (2015) 113–135.

[17] B. Cottis, M. Graham, R. Lindsay, S. Lyon, T. Richardson, D. Scantlebury, S. Howard, eds., Shreir's Corrosion, Elsevier, 2010.

[18] K. Kakaei, M.D. Esrafili, A. Ehsani, Graphene and Anticorrosive Properties, Interface Sci. Technol. 27 (2019) 303–337.

[19] W. Plieth, Electrochemistry for Materials Science, Elsevier Science, 2008.

[20] V.S. Bagotsky, Fundamentals of electrochemistry, 2nd ed., John Wiley & Sons, Inc, 2006.

[21] D. Guo, M. Li, J.M. Joseph, J.C. Wren, A New Method for Corrosion Current Measurement: the Dual-Electrochemical Cell (DEC), J. Electrochem. Soc. 167 (2020) 111505.

[22] J.O.M. Bockris, L.F. Oldfield, The oxidation-reduction reactions of hydrogen peroxide at inert metal electrodes and mercury cathodes, Trans. Faraday Soc. 51 (1955) 249–259.

[23] R.G. Kelly, J.R. Scully, D. Shoesmith, R.G. Buchheit, Electrochemical Techniques in Corrosion Science and Engineering, CRC Press, 1st ed., CRC Press, 2002.

[24] Z. Nagy, D.A. Thomas, Effect of Mass Transport on the Determination of Corrosion Rates from Polarization Measurements, J. Electrochem. Soc. 133 (1986) 2013.

[25] A.H. Fakeeha, F.A. Abdelaleem, The Interaction between Corrosion Processes and Mass Transfer at Rough Surfaces, J. King Saud Univ. - Eng. Sci. 8 (1996) 51–69.

[26] R. Oltra, Mass transport control of localised corrosion processes: in situ local probing and modelling, Corros. Eng. Sci. Technol. 53 (2018) 2–8.

[27] V. Jovancicevic, J.O. Bockris, The Mechanism of Oxygen Reduction on Iron in Neutral Solutions, J. Electrochem. Soc. 133 (1986) 1797.

[28] V.G. Levich, Physicochemical Hydrodynamics. Translated by Scripta Technica, Inc., Englewood Cliffs, N.J., Prentice-Hall, 1962.

[29] Y.G. Shin, Nonlinear Dynamics of Carbon Steel Corrosion under Gamma Radiation, PhD Thesis, The University of Western Ontario, 2020.

[30] M. Behazin, J.J. Noël, J.C. Wren, Combined effects of pH and γ-irradiation on the corrosion of Co-Cr alloy stellite-6, Electrochim. Acta. 134 (2014) 399–410.

[31] R.M. Cornell, U. Schwertmann, The Iron Oxides, Wiley-VCH Verlag GmbH & Co. KGaA, Weinheim, FRG, 2003.

[32] T. Misawa, K. Asami, K. Hashimoto, S. Shimodaira, The mechanism of atmospheric rusting and the protective amorphous rust on low alloy steel, Corros. Sci. 14 (1974) 279–289.

[33] T. Misawa, K. Hashimoto, S. Shimodaira, The mechanism of formation of iron oxide and oxyhydroxides in aqueous solutions at room temperature, Corros. Sci. 14 (1974) 131–149.

[34] C. Rémazeilles, P. Refait, On the formation of β-FeOOH (akaganéite) in chloride-containing environments, Corros. Sci. 49 (2007) 844–857.

[35] M. Pourbaix, Atlas of chemical and electrochemical equilibria in Aqueous Solutions, Second ed, NACE International Cebelcor, 1974.

[36] B. Beverskog, I. Puigdomenech, Revised Pourbaix diagrams for iron at 25-300°C, Corros. Sci. 38 (1996) 2121–2135.

[37] C.F. Baes Jr., R.E. Mesmer, The Hydrolysis of Cations, John Wiley & Sons, Inc, 1976.

[38] H. Kaesche, Corrosion of Metals, Springer Berlin Heidelberg, 2003.

[39] B. Beverskog, I. Puigdomenech, Pourbaix Diagrams for the Ternary System of Iron-Chromium-Nickel, Corrosion. 55 (1999) 1077–1087.

[40] H.E. Townsend, Potential-pH diagrams at elevated temperature for the system Fe-H_2O, Corros. Sci. 10 (1970) 343–358.

[41] A. Groß, Computational modeling of electrocatalytic reactions, in: Encycl. Interfacial Chem. Surf. Sci. Electrochem., Elsevier, 2018: pp. 455–465.

[42] J.A. Richardson, A.A. Abdullahi, Corrosion in Alkalis, Ref. Modul. Mater. Sci. Mater. Eng. (2018).

[43] B.N. Popov, Thermodynamics in the Electrochemical Reactions of Corrosion, in: Corros. Eng. Princ. Solved Probl., Elsevier, 2015: pp. 29–92.

[44] T. Misawa, The thermodynamic consideration for Fe-H_2O system at 25°C, Corros. Sci. 13 (1973) 659–676.

[45] D.D. MacDonald, The history of the Point Defect Model for the passive state: A brief review of film growth aspects, Electrochim. Acta. 56 (2011) 1761–1772.

[46] A. Zaki, Principles of Corrosion Engineering and Corrosion Control, Elsevier Ltd, 2006.

[47] D.D. Macdonald, The Point Defect Model for the Passive State, J. Electrochem. Soc. 139 (1992) 3434.

[48] L. Zhang, D.D. Macdonald, E. Sikora, J. Sikora, On the Kinetics of Growth of Anodic Oxide Films, J. Electrochem. Soc. 145 (1998) 898–905.

[49] D.D. Macdonald, M. Urquidi-Macdonald, Theory of Steady-State Passive Films, J. Electrochem. Soc. 137 (1990) 2395–2402.

[50] B. Krishnamurthy, R.E. White, H.J. Ploehn, Simplified point defect model for growth of anodic passive films on iron, Electrochim. Acta. 47 (2002) 3375–3381.

[51] C.Y. Chao, L.F. Lin, D.D. Macdonald, A Point Defect Model for Anodic Passive Films: I . Film Growth Kinetics, J. Electrochem. Soc. 128 (1981) 1187–1194.

[52] L.F. Lin, C.Y. Chao, D.D. Macdonald, A Point Defect Model for Anodic Passive Films, J. Electrochem. Soc. 128 (1981) 1194.

[53] D.D. Macdonald, The Point Defect Model for the Passive State, J. Electrochem. Soc. 139 (1992) 3434–3449.

[54] A. Seyeux, V. Maurice, P. Marcus, Oxide Film Growth Kinetics on Metals and Alloys: I. Physical Model, J. Electrochem. Soc. 160 (2013) C189.

[55] K. Leistner, C. Toulemonde, B. Diawara, A. Seyeux, P. Marcus, Oxide Film Growth Kinetics on Metals and Alloys: II. Numerical Simulation of Transient Behavior, J. Electrochem. Soc. 160 (2013) C197–C205.

[56] N.D. Tomashov, Development of the Electrochemical Theory of Metallic Corrosion, Corrosion. 20 (1964) 7t-14t.

[57] S. Hœrlé, F. Mazaudier, P. Dillmann, G. Santarini, Advances in understanding atmospheric corrosion of iron. II. Mechanistic modelling of wet–dry cycles, Corros. Sci. 46 (2004) 1431–1465.

[58] G. Inzelt, A. Lewenstam, F. Scholz, eds., Handbook of reference electrodes, Springer, 2013.

[59] A. Cox, S.B. Lyon, An electrochemical study of the atmospheric corrosion of mild steel-I. Experimental method, Corros. Sci. 36 (1994) 1167–1176.

[60] M. Stratmann, H. Streckel, On the atmospheric corrosion of metals which are covered with thin electrolyte layers-I. Verification of the experimental technique, Corros. Sci. 30 (1990) 681–696.

[61] A. Nishikata, Y. Ichihara, Y. Hayashi, T. Tsuru, Influence of Electrolyte Layer Thickness and pH on the Initial Stage of the Atmospheric Corrosion of Iron, J. Electrochem. Soc. 144 (1997) 1244–1252.

[62] T. Tsuru, A. Nishikata, J. Wang, Electrochemical studies on corrosion under a water film, Mater. Sci. Eng. A. 198 (1995) 161–168.

[63] S.G. Fishman, C.R. Crowe, The application of potentiostatic polarization techniques to corrosion under thin condensed moisture layers, Corros. Sci. 17 (1977) 27–33.

[64] F. Mansfeld, S. Tsai, Laboratory studies of atmospheric corrosion-I. Weight loss and electrochemical measurements, Corros. Sci. 20 (1980) 853–872.

[65] F. Mansfeld, J. V. Kenkel, Electrochemical monitoring of atmospheric corrosion phenomena, Corros. Sci. 16 (1976) 111–122.

[66] Z. Liu, W. Wang, J. Wang, X. Peng, Y. Wang, P. Zhang, H. Wang, C. Gao, Study of corrosion behavior of carbon steel under seawater film using the wire beam electrode method, Corros. Sci. 80 (2014) 523–527.

[67] D. Xia, S. Song, W. Jin, J. Li, Z. Gao, J. Wang, W. Hu, Atmospheric corrosion monitoring of field-exposed Q235B and T91 steels in Zhoushan offshore environment using electrochemical probes, J. Wuhan Univ. Technol. Mater. Sci. Ed. 32 (2017) 1433–1440.

[68] T. Tsuru, K.I. Tamiya, A. Nishikata, Formation and growth of micro-droplets during the initial stage of atmospheric corrosion, Electrochim. Acta. 49 (2004) 2709–2715.

[69] B.E. Risteen, E. Schindelholz, R.G. Kelly, Marine Aerosol Drop Size Effects on the Corrosion Behavior of Low Carbon Steel and High Purity Iron, J. Electrochem. Soc. 161 (2014) C580–C586.

[70] E. Schindelholz, B.E. Risteen, R.G. Kelly, Effect of Relative Humidity on Corrosion of Steel under Sea Salt Aerosol Proxies, J. Electrochem. Soc. 161 (2014) C450–C459.

[71] S. Li, L.H. Hihara, Atmospheric-Corrosion Electrochemistry of NaCl Droplets on Carbon Steel, J. Electrochem. Soc. 159 (2012) C461–C468.

[72] J. Weissenrieder, C. Leygraf, In Situ Studies of Filiform Corrosion of Iron, J. Electrochem. Soc. 151 (2004) B165.

[73] C. Chen, F. Mansfeld, Potential distribution in the Evans drop experiment, Corros. Sci. 39 (1997) 409–413.

[74] A. Esayah, M. Kelley, A. Howell, S.J. Shulder, B. Mishra, D. Olson, J. Porter, Flow Accelerated Corrosion of Carbon Steel with Droplet Impingement Using a Modified Rotating Cylinder Electrode Experiment, Corrosion. 76 (2020) 202–209.

[75] Y.H. Wang, Y.Y. Liu, W. Wang, L. Zhong, J. Wang, Influences of the three-phase boundary on the electrochemical corrosion characteristics of carbon steel under droplets, Mater. Corros. 64 (2013) 309–313.

[76] E. McCafferty, Introduction to corrosion science, Springer, New York, 2010.

[77] S.X. Li, L.H. Hihara, Atmospheric corrosion initiation on steel from predeposited NaCl salt particles in high humidity atmospheres, Corros. Eng. Sci. Technol. 45 (2010) 49–56.

[78] S. Li, L.H. Hihara, The comparison of the corrosion of ultrapure iron and low-carbon steel under NaCl-electrolyte droplets, Corros. Sci. 108 (2016) 200–204.

[79] J.W.T. Spinks, R.J. Woods, An introduction to radiation chemistry, John Wiley and Sons Inc, United States, 1990.

[80] Farhataziz, M.A.J. Rodgers, eds., Radiation chemistry: principles and applications, VCH Publishers, United States, 1987.

[81] J.H. O'Donnell, D.F. Sangster, Principles of Radiation Chemistry, American Elsevier Publishing Company, 1970.

[82] I.C. Draganic, Z.D. Draganic, The Radiation Chemistry of Water, Academic Press, 1971.

[83] J.C. Wren, Steady-State Radiolysis: Effects of Dissolved Additives, in: C.M. Wai1, B.J. Mincher (Eds.), Nucl. Energy Environ., American Chemical Society, 2010: pp. 271–295.

[84] L. Grandy, Effects of Gamma-Radiation on the Evolution of Copper Corrosion Dynamics in Deep Geological Repository Solution Environments, PhD Thesis, The University of Western Ontario, 2021.

[85] R.P. Morco, Gamma-Radiolysis Kinetics and Its Role in the Overall Dynamics of Materials Degradation, PhD Thesis, The University of Western Ontario, 2020.

[86] R.P. Morco, J.M. Joseph, D.S. Hall, C. Medri, D.W. Shoesmith, J.C. Wren, Modelling of radiolytic production of HNO_3 relevant to corrosion of a used fuel container in deep geologic repository environments, Corros. Eng. Sci. Technol. 52 (2017) 141–147.

[87] G. Bellanger, Effect of pH and hydrogen peroxide in radioactive water on the passivity of 1018 carbon steel, J. Mater. Sci. 30 (1995) 1259–1265.

[88] S. Sunder, N.H. Miller, D.W. Shoesmith, Corrosion of uranium dioxide in hydrogen peroxide solutions, Corros. Sci. 46 (2004) 1095–1111.

[89] R.S. Glass, G.E. Overturf, R.A. Van Konynenburg, R.D. McCright, Gamma radiation effects on corrosion-I. Electrochemical mechanisms for the aqueous corrosion processes of austenitic stainless steels relevant to nuclear waste disposal in tuff, Corros. Sci. 26 (1986) 577–590.

[90] R.H. Lamoreaux, D. Cubicciotti, Contributions of the Oxide Layer to the Corrosion Potential of Stainless Steel under Nuclear Reactor Conditions, J. Electrochem. Soc. 140 (1993) 2197–2205.

[91] A.N. Scott, W.R. Mawhinney, Electrochemical corrosion potential of carbon steel feeder pipes in a Canadian deuterium uranium reactor generating station under return-to-service conditions, Corrosion. 65 (2009) 49–60.

[92] E. Leoni, C. Corbel, V. Cobut, D. Simon, D. Féron, M. Roy, O. Raquet, Electrochemical behaviour of gold and stainless steel under proton irradiation and active RedOx couples, Electrochim. Acta. 53 (2007) 495–510.

[93] D. Crusset, V. Deydier, S. Necib, J.-M. Gras, P. Combrade, D. Féron, E. Burger, Corrosion of carbon steel components in the French high-level waste programme: evolution of disposal concept and selection of materials, Corros. Eng. Sci. Technol. 52 (2017) 17–24.

[94] C. Liu, J. Wang, Z. Zhang, E.-H. Han, Studies on corrosion behaviour of low carbon steel canister with and without γ-irradiation in China's HLW disposal repository, Corros. Eng. Sci. Technol. 52 (2017) 136–140.

[95] Q.W. Knapp, J.C. Wren, Film formation on type-316L stainless steel as a function of potential: Probing the role of gamma-radiation, Electrochim. Acta. 80 (2012) 90–99.

[96] K. Daub, X. Zhang, J.J. Noël, J.C. Wren, Effects of γ-radiation versus H_2O_2 on carbon steel corrosion, Electrochim. Acta. 55 (2010) 2767–2776.

[97] K. Daub, X. Zhang, J.J. Noël, J.C. Wren, Gamma-radiation-induced corrosion of carbon steel in neutral and mildly basic water at 150 °C, Corros. Sci. 53 (2011) 11–16.

[98] K. Ishigure, N. Fujita, T. Tamura, K. Oshima, Effect of Gamma Radiation on the Release of Corrosion Products From Carbon Steel and Stainless Steel in High Temperature Water., Nucl. Technol. 50 (1980) 169–177.

[99] N. Fujita, C. Matsuura, K. Saigo, Radiation-induced preferential dissolution of specific planes of carbon steel in high-temperature water, Radiat. Phys. Chem. 60 (2001) 53–60.

[100] T.H. Song, I.S. Kim, S.K. Rho, Effect of H_2O_2 on the Corrosion Behavior of 304L Stainless Steel, J. Korean Nucl. Soc. 27 (1995) 453–462.

[101] W. Xu, B. Zhang, Y. Deng, L. Yang, J. Zhang, Nitrate on localized corrosion of carbon steel and stainless steel in aqueous solutions, Electrochim. Acta. 369 (2021) 137660.

[102] N. Sridhar, J.A. Beavers, B. Rollins, S. Chawla, K. Evans, X. Li, Stress Corrosion Cracking and Localized Corrosion of Carbon Steel in Nitrate Solutions, Corrosion. 72 (2016) 927–942.

[103] C. Pillay, J. Lin, The impact of additional nitrates in mild steel corrosion in a seawater/sediment system, Corros. Sci. 80 (2014) 416–426.

[104] D.G. Kolman, D.K. Ford, D.P. Butt, T.O. Nelson, Corrosion of 304 stainless steel exposed to nitric acid-chloride environments, Corros. Sci. 39 (1997) 2067–2093.

[105] H. Anzai, K. Nakata, J. Kuniya, S. Hattori, The effect of hydrogen peroxide on the stress corrosion cracking of 304 stainless steel in high temperature water, Corros. Sci. 36 (1994) 1201–1207.

[106] E. Toijer, M. Jonsson, H_2O_2 and γ-radiation induced corrosion of 304L stainless steel in aqueous systems, Radiat. Phys. Chem. 159 (2019) 159–165.

[107] S. Makjan, P. Boonsri, J. Channuie, K. Kanjana, Effects of hydrogen peroxide on 304 stainless steel in high temperature water, J. Phys. (2019).

[108] T. Satoh, S. Uchida, J.-I. Sugama, N. Yamashiro, T. Hirose, Y. Morishima, Y. Satoh, K. Iinuma, Effects of Hydrogen Peroxide on Corrosion of Stainless Steel, (I), J. Nucl. Sci. Technol. 41 (2004) 610–618.

[109] S. Uchida, T. Satoh, J. Sugama, N. Yamashiro, Y. Morishima, T. Hirose, T. Miyazawa, Y. Satoh, K. Iinuma, Y. Wada, M. Tachibana, Effects of Hydrogen Peroxide on Corrosion of Stainless Steel, (III), J. Nucl. Sci. Technol. 42 (2005) 66–74.

[110] T. Miyazawa, S. Uchida, T. Satoh, Y. Morishima, T. Hirose, Y. Satoh, K. Iinuma, Y. Wada, H. Hosokawa, N. Usui, Effects of Hydrogen Peroxide on Corrosion of Stainless Steel, (IV), J. Nucl. Sci. Technol. 42 (2005) 233–241.

[111] T. Miyazawa, T. Terachi, S. Uchida, T. Satoh, T. Tsukada, Y. Satoh, Y. Wada, H. Hosokawa, Effects of Hydrogen Peroxide on Corrosion of Stainless Steel, (V), J. Nucl. Sci. Technol. 43 (2006) 884–895.

[112] S. Uchida, Y. Morishima, T. Hirose, T. Miyazawa, T. Satoh, Y. Satoh, Y. Wada, Effects of Hydrogen Peroxide on Corrosion of Stainless Steel, (VI), J. Nucl. Sci. Technol. 44 (2007) 758–766.

CHAPTER 3
EXPERIMENTAL TECHNIQUES

In this chapter, the principles of the electrochemical techniques and post-analysis methods used in this thesis are reviewed. Detailed information about the experimental parameters and methods used in each chapter is provided in the experimental sections of those chapters.

3.1 ELECTROCHEMICAL TECHNIQUES

3.1.1 Electrochemical Cell

All electrochemical measurements were performed using a typical three-electrode cell arrangement. The cell (see the schematic in **Figure 3-1**) consists of a working electrode (WE), a reference electrode (RE), and a counter electrode (CE). The reference electrode used was a saturated calomel electrode (SCE, Fisher Scientific). The CE was a 99.9% pure platinum mesh with a large surface area (5 cm^2). The working

electrode was the carbon steel (CS) or stainless steel (304L SS, or 309 SS) 1 cm diameter coupon under study.

To avoid side product contamination, the solution in the WE compartment was separated from those in the RE and CE compartments using porous glass frits.

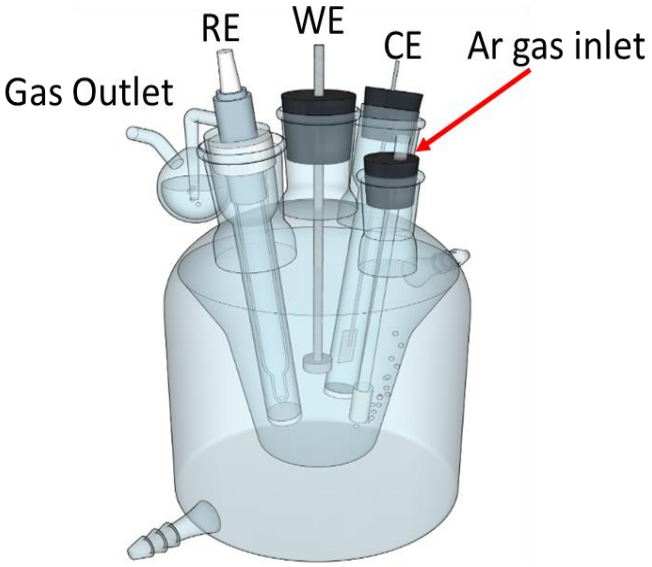

Figure 3-1: Schematic of a three-electrode electrochemical cell. Schematic courtesy of Giles Whitaker.

A potentiostat was connected to the cell to control and/or monitor the current and potential during electrochemical tests. The potential difference between the WE and RE is measured in this setup. The measured current is the current flow between the WE and the CE, while the current flow between the WE and RE is prevented by a high impedance voltammeter [1,2].

3.1.2 Potentiodynamic Polarization (PD) and Cyclic Voltammetry (CV)

Potentiodynamic polarization (PD) and cyclic voltammetry (CV) are the most widely used techniques for studying the anodic and cathodic processes that occur on an

electrode surface as a function of an applied potential. In both methods, the potential is applied over a wide range (≥ ±30 mV) with a constant scanning rate, and the resulting current is recorded. In PD, the potential is scanned in a single direction, whereas for CV, the potential is scanned up and down sometimes in multiple cycles. At a given point in a scan, the measured current density shows the net charge transfer occurring on the working electrode at the applied potential. The overall potential-current relationship provides information about the electrochemical oxidation and reduction reactions occurring on the WE. The scan rate may also affect the current response and using different scan rates may provide information on the relative contribution to the current of different reactions [2]. Also, varying the final potential can provide information on the coupling of oxidation and reduction processes. In other words, it is a way to check on the presence of a reduction peak that corresponds to a specific oxidation peak.

3.1.3 Linear Polarization Resistance (LPR)

The Wagner-Traud equation describes the relationship between the applied potential and the corrosion current density (i_{corr}):

$$i = i_{CORR}\left[exp\left(\frac{2.3\ (E - E_{CORR})}{\beta_a}\right) - exp\left(\frac{-2.3\ (E - E_{CORR})}{\beta_c}\right)\right] \qquad \textbf{(Eq. 3-1)}$$

where b_a and b_c are the anodic and cathodic Tafel constants, respectively.

In **Eq. 3-1**, in a very small potential range around E_{corr} (±10 mV), an approximately linear relationship between the applied potential and current density can be demonstrated mathematically. This linear relationship has also been observed by many investigators [3], and its slope is called the polarization resistance (R_p) [2,4], which is defined mathematically as:

$$R_P = \left[\frac{\Delta E}{\Delta i}\right]_{(E_{app}-E_{corr})\to 0} (\Omega.cm^2) \qquad \textbf{(Eq. 3-2)}$$

R_p is related to the corrosion current density (i_{corr}) thus:

$$i_{corr} = \frac{B}{R_p} \quad (A.cm^{-2}) \qquad \textbf{(Eq. 3-3)}$$

where the constant *B* is defined thus:

$$B = \frac{\beta_a.\beta_c}{2.3\,(\beta_a + \beta_c)} \qquad \textbf{(Eq. 3-4)}$$

Figure 3-2 shows the potential range in which the above equations are applicable [5]:

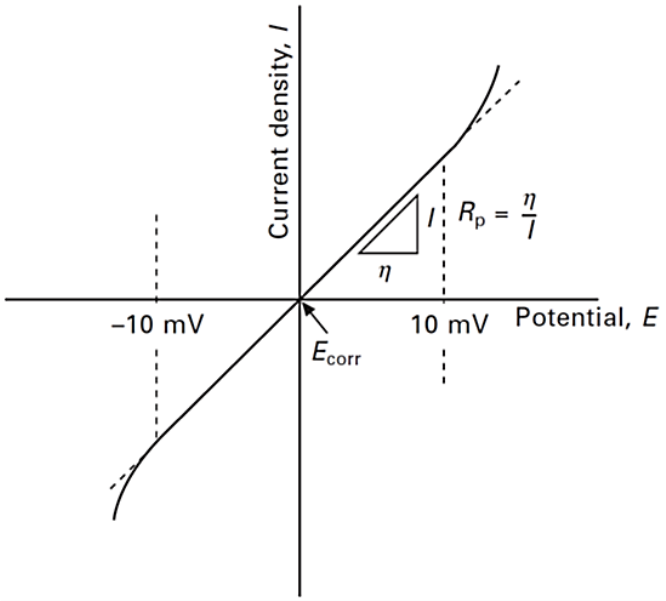

Figure 3-2: Schematic illustration of linear polarization test (η = Over potential, I = Current density) [5] (reprinted with permission from Ref. [5], © 2010 Woodhead Publishing Limited.)

Rearranging gives:

$$i_{CORR} = \left(\frac{1}{2.3R_p}\right)\left(\frac{\beta_a.\beta_c}{(\beta_a + \beta_c)}\right) \quad (A.cm^{-2}) \qquad \textbf{(Eq. 3-5)}$$

3.2 SURFACE ANALYSIS TECHNIQUES

The morphology and composition of the oxides formed on the corroded CS surface were examined using a combination of microscopic (optical microscope and scanning electron microscope (SEM)) and spectroscopic (Raman scattering) techniques. The principles behind these techniques are described below.

3.2.1 Optical Microscopy

In the work carried out in this thesis, a digital microscope (a Leica DVM6A digital microscope) was used to examine the morphology and topography of the corrosion products formed on corroded CS coupons (**Figure 3-5**). A digital microscope uses optics to produce an image and outputs the image using software to a monitor. In an optical (i.e. visible light) microscope, a pair of convex lenses is used to generate the images. The resolution (i.e., the shortest distance between two points on a specimen that still allows two distinct entities to be identified) of optical microscopes is lower than that of SEM. However, this surface analysis method is preferable to SEM imaging, as corrosion products with different compositions and morphologies can be distinguished via their colour under an optical microscope. Also, optical microscopy is very convenient to use and does not require the use of a vacuum, preventing dehydration and other forms of degradation that can occur under vacuum.

Figure 3-3: Leica DVM6A digital microscope used for optical microscopy. Photo copied from RAMPS group website (https://www.rampsgroup.org/members), Photo taken by Giles Whitaker.

3.2.2 Scanning Electron Microscopy/ Energy Dispersive X-ray Spectroscopy (SEM/EDX)

Scanning electron microscopy (SEM) combined with energy dispersive X-ray spectroscopy (EDX) was used to provide information about the surface morphology and the quantitative elemental composition of surface oxides. A schematic of the components of a standard SEM instrument is shown in **Figure 3-4**.

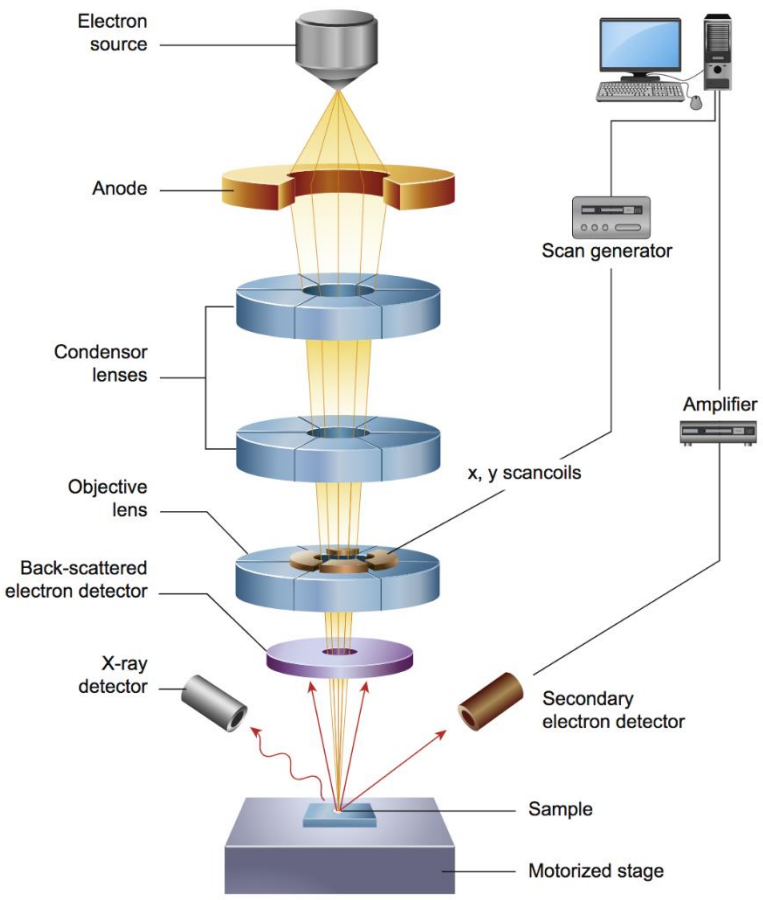

Figure 3-4: Schematic of a scanning electron microscope [6]. (reprinted with permission from Ref. [6], © 2016 Elsevier Ltd.)

In this method, samples are placed in a high vacuum chamber to provide an absorption-free path for the electron beam. A primary electron beam (200 eV–30 keV) is produced via an electron gun and focused onto the surface. The electrons in the beam interact with the sample, producing various signals such as secondary electrons, backscattered electrons, characteristic X-rays, and continuum X-rays. The low energy secondary electrons (< 50 eV) provide information about the surface topography of a sample. Even though secondary electrons do not suffer from inelastic scattering, due to their low kinetic energy, they suffer rapid energy losses with distance travelled, thus

limiting their escape depth to a few nanometers [7]. This results in a greater emission of secondary electrons at non-normal incidence of the probe than at normal incidence. The surface topography of the sample primarily governs the intensity of the secondary electrons. An image of a sample surface can be created by measuring the intensity of these secondary electrons as a function of the position of the primary electron beam.

Backscattered electrons are reflected back after elastic interactions between the beam and the sample. The intensity of backscattered electrons can be correlated to the atomic number of the element within the sampling volume and thus provides some qualitative elemental information. The analysis of characteristic X-rays gives quantitative elemental details and can be obtained by employing EDX combined with SEM. In EDX, when the primary electron beam bombards the sample, electrons are ejected from the atoms. Electrons from a higher state fill the resulting electron vacancies and an X-ray of corresponding energy is emitted. The wavelength of the X-ray is characteristic of a particular element, and its relative intensity gives quantitative information on the composition of the sampled volume. In this project, SEM analysis was carried out using a LEO (Zeiss) 1540XB FIB/SEM microscope at the Western Nanofabrication Facility.

3.2.3 Focused Ion Beam Cross Section

This technique was used for visualization of cross-sections of cuts made into the coupon surfaces. FIB-cutting was carried out using a gallium ion (Ga^+) beam. The ions of the beam collide with a solid sample's surface and lose energy to the surface electrons. The consequent physical effects of the collisions of beam ions cause substrate milling through the sputtering of neutral and ionized substrate atoms. The cross-sections were examined using SEM.

3.2.4 Raman Spectroscopy

Raman spectroscopy was used to characterize the chemical composition of oxides formed on CS surfaces during corrosion experiments. Raman spectroscopy is an analytical technique that studies the vibrational modes of a molecule [8,9].

A narrow wavelength laser with a monochromatic frequency in the visible or near-infrared distorts the electron cloud of a molecule. The induced changes in the polarizability of the electron cloud after interaction with light are determined. The majority of the scattered light has the same frequency as the incident beam, which is referred to as Rayleigh scattering. Raman scattering, by contrast, is an inelastic process, is very weak (low probability), and produces light that is shifted in wavelength compared to the source.

The vibrational transitions of a chemical compound are characteristic of that compound, and Raman shifts, which correspond to these transitions, can be used to identify the compounds [9,10]. For a vibrational mode of a molecule to be Raman active, it must have a non-zero derivative of its polarizability [9,10].

3.3 SOLUTION ANALYSIS TECHNIQUES

3.3.1 Inductively Coupled Plasma-Optical Emission Spectrometry (ICP-OES)

The concentrations of iron and other elements in solution after electrochemical tests and coupon exposure studies were determined using ICP-OES. The ICP-OES technique is based upon the spontaneous emission of photons from excited ions and atoms. A schematic of a typical ICP-OES instrument is presented in **Figure 3-5**. Prior to

the analysis, the liquid samples were digested using trace analytical grade nitric acid solution (Fisher Scientific) to dissolve any solid particles present in the solution. The sample solution first converted to an aerosol (nebulization) and then injected into the plasma. Inductively coupled plasma (ICP) is performed at a temperature high enough (between 8000 and 10000 K) to vaporize the aerosol and convert it to a plasma, in which all the solution elements are present as free atoms in the gaseous state [11]. Atoms are promoted to excited states through further collisions within the plasma. Atoms may also be ionized and subsequently excited. The photons emitted via the relaxation from the excited state to the ground state have characteristic energies, depending on the element. The wavelengths of the detected photons can therefore be used to identify the elements. The intensity at this wavelength is proportional to the concentration of the element in the sample, so the concentrations of elements in samples can be determined using a calibration curve made with solutions of known concentrations [11].

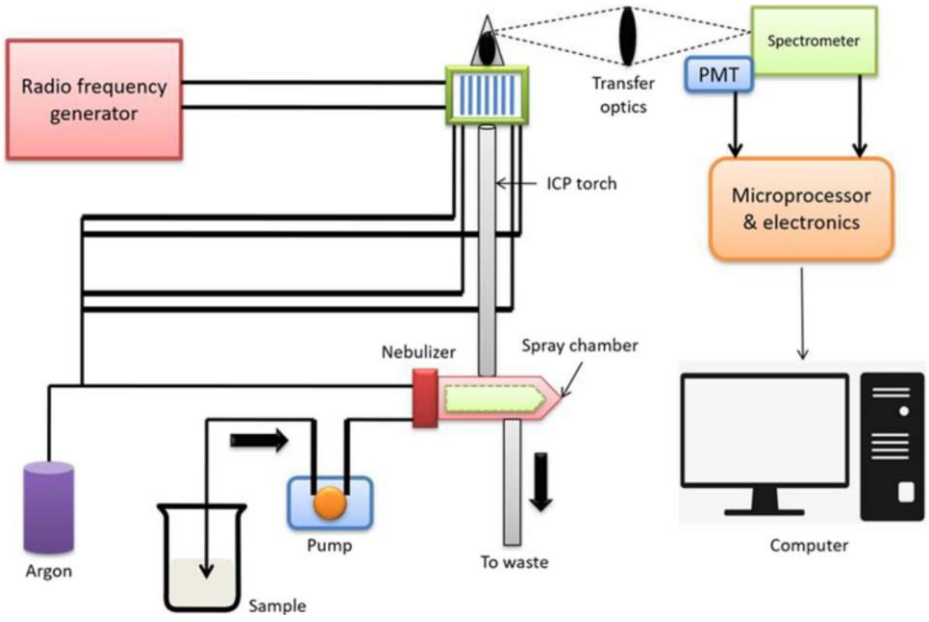

Figure 3-5: Schematic of an Inductively Coupled Plasma-Optical Emission Spectrometry (ICP-OES) instrument [10] (reprinted with permission from Ref. [11], © 2021 Springer Nature.)

3.3.2 UV-Vis Spectrophotometry

Ultraviolet-visible spectroscopy (UV-Vis) was employed to determine the concentration of H_2O_2 in test solutions using the Ghormley tri-iodide method [12]. In the presence of an ammonium molybdate catalyst, I^- is oxidized to I_3^- by H_2O_2. The I_3^- formed has a maximum absorption at 350 nm with a molar extinction coefficient of 25,500 $M^{-1} \cdot cm^{-1}$ [13]. Using this method, the detection limit for [H_2O_2] was determined to be 3×10^{-6} M.

The UV-Vis studies were carried out using a diode array UV spectrometer (BioLogic Science Instruments). The wavelength and amount of light that compounds absorb depend on their molecular structure and their concentration [8].

3.4 SAMPLE IRRADIATION

All radiation experiments were performed using an MDS Nordion 220 Excel gamma cell, as shown in **Figure 3-6**.

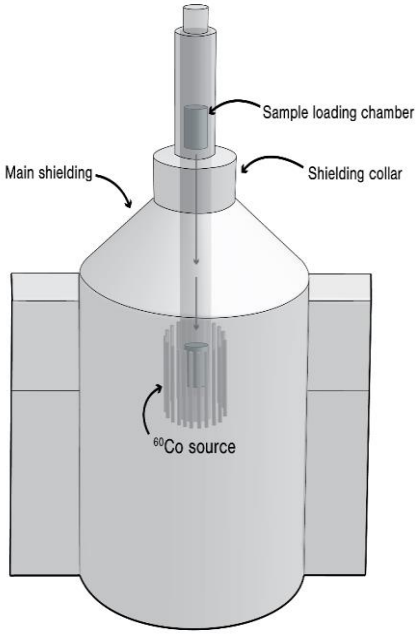

Figure 3-6: Photograph of the ^{60}Co irradiator (220 Excel, MDS Nordion)

The gamma cell uses radioactive ^{60}Co to produce gamma rays through a process of radioactive decay:

$$^{60}Co \rightarrow {}^{60}Ni + \beta + 2\gamma \qquad \textbf{(Eq- 3-6)}$$

Both gamma rays (γ) and beta particles (β) are emitted, but the beta particles are blocked from entering the sample by the metal shielding around the sample container, and thus the sample is irradiated only by γ-rays. The two γ-rays emitted have different energies, 1.332 MeV and 1.173 MeV. The dose rate of the gamma cell during the time when these experiments were performed was 2.0 kGy· h^{-1} (1 Gy is 1 J/kg). Test vials were placed in a circular sample holder to ensure they all received the same radiation dose during the irradiation period.

3.5 REFERENCES

[1] K.J. Vetter, Electrochemical Kinetics: Theoretical and Experimental Aspects, Academic Press, (1967).

[2] R.G. Kelly, J.R. Scully, D. Shoesmith, R.G. Buchheit, Electrochemical Techniques in Corrosion Science and Engineering, CRC Press, 1st ed., CRC Press, 2002.

[3] M. Stern, A.L. Geaby, Electrochemical Polarization, J. Electrochem. Soc. 104 (1957) 56.

[4] S. Papavinasam, Electrochemical polarization techniques for corrosion monitoring, in: L. Yang (Ed.), Tech. Corros. Monit., Woodhead Publishing, 2008: pp. 49–85.

[5] S. Hiromoto, Corrosion of metallic biomaterials, in: S. Hiromoto (Ed.), Woodhead Publ. Ser. Biomater. Met. Biomed. Devices (First Ed., Woodhead Publishing, 2010: pp. 99–121.

[6] B.J. Inkson, Scanning Electron Microscopy (SEM) and Transmission Electron Microscopy (TEM) for Materials Characterization, in: Mater. Charact. Using Nondestruct. Eval. Methods, Elsevier Inc., 2016: pp. 17–43.

[7] J.I. Goldstein, D.E. Newbury, J.R. Michael, N.W.M. Ritchie, J.H.J. Scott, D.C. Joy, Secondary Electrons, in: Scanning Electron Microsc. X-Ray Microanal., Springer, New York, NY, 2018: pp. 29–37.

[8] D.A. Skoog, F.J. Holler, T.A. Nieman, Principles of Instrumental Analysis,Brooks/Cole, Belmont, 1998.

[9] J.R. Ferraro, R. Island, C.W. Brown, Introductory Raman Spectroscopy, 2nd Editio, Elsevier, 2003.

[10] E. Smith, G. Dent, Modern Raman Spectroscopy: A Practical Approach, John Wiley, Hoboken, NJ; Chichester, UK. (2005). (accessed November 16, 2020).

[11] S.R. Khan, B. Sharma, P.A. Chawla, R. Bhatia, Inductively Coupled Plasma

Optical Emission Spectrometry (ICP-OES): a Powerful Analytical Technique for Elemental Analysis, Food Anal. Methods. 15 (2022) 666–688.

[12] C.J. Hochanadel, Effects Of Cobalt γ-Radiation On Water And Aqueous Solutions, J. Phys. Chem. 56 (1952) 587–594.

[13] I. Štefanić, J.A. LaVerne, Temperature Dependence of the Hydrogen Peroxide Production in the γ-Radiolysis of Water, J. Phys. Chem. A. 106 (2002) 447–452.

CHAPTER 4
CORROSION BEHAVIOUR OF CARBON STEEL IN NITRATE SOLUTIONS

4.1 INTRODUCTION

Carbon steel (CS), because of its low processing cost, low production cost, and high strength, is the material of choice for many structures [1,2], including for many components of nuclear power plants.

Reactor structural materials are exposed to a continuous flux of ionizing radiation, such as α-, β- and γ-radiation. The energy of the ionizing radiation particles or photons these materials are exposed to is less than 10 MeV, which is not large enough to induce nuclear reactions or atomic displacement in a solid interacting medium. However, the energy of each particle or photon is still large enough to indiscriminately ionize tens of thousands of atoms and molecules on its path [3,4]. Because of its indiscriminate nature, radiation-induced processes are often referred to as solvent-oriented processes, as opposed to solute-oriented processes (a process in which the bulk solution remains

largely unaffected by the presence of the radiation [4–10]) induced by, for example, UV photolysis [3–6,9,11–13]. In a low dielectric constant medium such as a metal, the ions and electrons quickly recombine, and the radiation energy transferred to the interacting medium quickly dissipates as heat. In a high dielectric constant medium such as water, the ions and excited species continue to undergo chemical processes such as decomposition to reactive species, which can significantly affect the chemical kinetics of aqueous solution reactions and the degradation dynamics of materials exposed to the aqueous solution and/or humid air. Of the types of ionizing radiation, a- and b-particles significantly affect only the corrosion of nuclear fuel and/or fuel cladding materials, and not that of out-of-core reactor materials, because of their short penetration depths. Because each radiation particle or photon undergoes tens of thousands of collisions with atoms and molecules on its path, ionizing radiation affects materials degradation by producing reactive species not directly at a solid-liquid or solid-gas interface but homogeneously in a bulk solution phase. The radiolysis products that are formed within a time scale less than 100 ns upon collision with radiation are referred to as the primary radiolysis products. In a continuous flux of ionizing γ-radiation, water decomposes to yield a range of chemically reactive species [4,14].

$$H_2O \rightarrow \bullet OH, e_{aq}^-, H\bullet, HO_2\bullet, H_2, H_2O_2, H^+ \qquad \textbf{(Eq. 4-1)}$$

While the concentrations of these primary radiolysis products may be limited by their rapid recombination, low steady-state concentrations are rapidly achieved [15–19]. Gamma-radiation excites the ions and molecules of water and humid air and can decompose solvent molecules (water and humid air), resulting in redox-active species

such as H_2O_2 and HNO_3.

Aqueous corrosion is an electrochemical process, which involves a metal oxidation half-reaction coupled with a reduction half-reaction of a dissolved oxidant by exchanging electrons via the conducting medium of the metal. The overall corrosion process occurs in multiple elementary steps, including (i) interfacial electron transfer between the redox pairs involved in the half-reactions at the metal-solution interface (or metal-oxide and oxide-solution interfaces, if an oxide layer is present between the metal and solution phases); (ii) solution transport of the redox pair to and from the interfacial region to the bulk solution; and (iii) solution reactions (hydrolysis) [20,21]. However, corrosion differs from typical electrochemical processes occurring on inert (conducting or semi-conducting) electrodes in one key aspect: the metal oxidation half-reaction involves the interfacial transfer of not only electrons but also metal atoms.

The concentrations of redox-active species can control the corrosion rates of metals. Because these radiolysis products can affect corrosion kinetics, it is important to study the effect of γ-radiation on the corrosion performance of structural materials. The kinetics of water radiolysis have been well studied under a wide range of solution conditions using both radiolysis kinetics modelling and experimental data [19,22–27]. There has also been extensive research on the corrosion of carbon steel and stainless steels in the presence of γ-radiation [28–35]. A humid-air radiolysis model (HARM) [10,24] was developed in our group and was used to calculate time-dependent concentrations of radiolysis products. These calculations were performed as a function of temperature, relative humidity in air and radiation dose rate. The results showed that HNO_3 is the dominant oxidizing species formed during humid air radiolysis. These

results were analyzed to formulate the overall radiolytic production rate of nitric acid absorbed in the water that the supporting structure steels may come into contact with.

Nitric acid is a powerful oxidant, and its formation makes the solution system complex [24]. The continuous addition of nitric acid not only can affect the metal solution redox reactions but also changes the solution pH and hence the solubility of iron and other metals [5]. Nitrate ions also affect the solubility of Fe^{3+} ions and hinder the precipitation of Fe^{3+} oxides via the formation of soluble Fe^{3+}-NO_3^- complexes [36].

The corrosion of CS and other transition metals (Cu and Ni) in different solution environments has been studied in our group [5,6,9,33,37]. These studies have shown that the corrosion of CS and transition metals evolves through different dynamic stages. In this study, the effects of Fe^{3+} and NO_3^- concentration on CS oxidation were investigated using electrochemical techniques.

In the absence of Fe^{3+} and NO_3^-, $[H^+]$ determines the proton reduction electron transfer rate, which is coupled with metal oxidation. It can also affect the rate of metal ion solvation, hydrolysis, and metal hydroxide precipitation. The presence of redox-active species affects the evolution of interfacial electron transfer, interfacial mass (metal atom) transfer and solution-phase processes.

The evolution of the elementary steps and the rate-determining steps that control the overall metal oxidation rate were investigated by measurements of corrosion potential as a function of time ($E_{corr}(t)$) and the current vs potential relationships under potentiodynamic conditions. The key elementary steps involved in the corrosion of CS and how the solution environment affects these elementary steps have previously been

identified and are summarized below [5,33]. The main elementary steps are also included in **Table 4-1**.

Table 4-1: Elementary reactions involved in the overall oxidation of pure Fe. Adapted from [6,9,38].

Rxn ID	Reaction Type	Equation	Rate ID
M1	**Electron transfer**	$Fe^{0}_{(m)\|int} \rightleftharpoons Fe^{2+}_{(aq)\|int} + 2\,e^{-}$	$\boldsymbol{\upsilon_{M1}}$ $\boldsymbol{i_{M1}}$**=nF.** $\boldsymbol{\upsilon_{M1}}$
	This is a reversible process, consisting of two reaction steps ($\upsilon_{M1} = \upsilon_{M1f} - \upsilon_{M1r}$): $(M1f)$: $Fe^{0}_{(m)\|int}$ ® $Fe^{2+}_{(aq)\|int} + 2e^{-}$ $\quad \upsilon_{M1f} = k_{M1f}.(\alpha_{Fe^0})_{int} \approx k_{M1f}$ $(M1r)$: $Fe^{2+}_{(aq)\|int} + 2\,e^{-}$® $Fe^{0}_{(m)\|int}$ $\quad \upsilon_{M1r} = k_{M1r}.(\alpha_{Fe^{II}})_{int}$ Where $(\alpha_{Fe^{II}})_{int}$ represents the overall redox activities of Fe^{2+} in the interfacial region.		
Trans	**Ion diffusion**	$Fe^{2+}_{(aq)\|int}$ ⇝ $Fe^{2+}_{(aq)\|bulk}$	$\boldsymbol{\upsilon_{Trans}}$
Hyd	**Hydrolysis**	$Fe^{2+} + n\ OH^{-} \rightleftharpoons Fe(OH)_m^{2-m} + (n-m)\ OH^{-}$	$\boldsymbol{\upsilon_{Hyd}}$
Gel	**Hydrogel formation**	$Fe(OH)_2/Fe(OH)_3$ ⇝ $Fe^{II}_x Fe^{III}_y (OH)_{2z\ (gel)}$	$\boldsymbol{\upsilon_{Gel}}$
M2	**Electron transfer**	$\{Fe^{2+}_{(aq)\|int} \rightleftharpoons Fe(OH)_2\} \rightleftharpoons \{Fe^{3+}_{(aq)\|int} \rightleftharpoons Fe(OH)_3\} + e^{-}$	$\boldsymbol{\upsilon_{M2}}$ $\boldsymbol{i_{M2}}$**=nF.** $\boldsymbol{\upsilon_{M2}}$
	This is a reversible process, consisting of two reaction steps ($\upsilon_{M2} = \upsilon_{M2f} - \upsilon_{M2r}$): $(M2f)$: $\{Fe^{2+}_{(aq)\|int} \rightleftharpoons Fe(OH)_2\}$®$\{Fe^{3+}_{(aq)\|int} \rightleftharpoons Fe(OH)_3\} + e^{-}$ $\upsilon_{M2f} \approx k_{M2f}.(\alpha_{Fe^{II}})_{int}$ $(M2r)$: $\{Fe^{3+}_{(aq)\|int} \rightleftharpoons Fe(OH)_3\} + e^{-}$®$\{Fe^{2+}_{(aq)\|int} \rightleftharpoons Fe(OH)_2\}$ $\upsilon_{M2r} = k_{M2r}.(\alpha_{Fe^{III}})_{int}$ Where $(\alpha_{Fe^{II}})_{int}$ and $(\alpha_{Fe^{III}})_{int}$ represent the overall redox activities of Fe^{II} and Fe^{III} species (dissolved and colloidal) in the interfacial region.		
Oxd	**Oxide crystal growth**	$Fe(OH)_2 + 2\ Fe(OH)_3$ ®® $Fe_3O_4 + 4\ H_2O$ $Fe(OH)_3$ ®® $FeOOH + H_2O$	$\boldsymbol{\upsilon_{ox}}$

In **Stage 1**, the oxidation of iron is accompanied by the production of OH^- (or consumption of H^+) by solution reduction reactions. The oxidation reaction is followed by the transport of metal cations from the surface to the bulk solution. In the absence of dissolved oxygen:

Interfacial charge transfer reactions at the metal surface:

Metal oxidation reaction: $Fe_{(m)} \rightleftharpoons Fe^{2+} + 2\ e^-$ (**Eq. 4-2a**)

Oxidant reduction: Hydrogen reaction: $2\ H^+ + 2\ e^- \rightleftharpoons H_2$ (**Eq. 4-2b**)

Overall charge transfer reaction: $2\ Fe_{(m)} + 2\ H^+ \rightarrow 2\ Fe^{2+} + 2\ H_2$ (**Eq. 4-2c**)

where the subscript (m) denotes the solid metal.

The interfacial mass transfer reactions and the transport of solution oxidants to the surface:

Mass transport of metal cations: $Fe^{2+}|_{x=0} \longrightarrow\!\!\!\!\!\!\rightarrow Fe^{2+}|_{x=sol}$ **(Eq. 4-3a)**

Mass transport of oxygen: $O_2|_{x=sol} \longrightarrow\!\!\!\!\!\!\rightarrow O_2|_{x=0}$ **(Eq. 4-3b)**

Mass transport of hydroxide ions: $OH^-|_{x=0} \longrightarrow\!\!\!\!\!\!\rightarrow OH^-|_{x=sol}$ **(Eq. 4-3c)**

where x represents the distance of species from the surface, and sol denotes the solution phase.

The formation of an $Fe(OH)_2$ gel layer starts at the surface once the interfacial region is saturated with Fe^{2+} ions.

The formation of a viscous Fe^{II} hydroxide layer (the greenish gel) through hydrolysis and hydrogel formation:

$Fe^{2+} + n\ OH^- \rightleftharpoons Fe(OH)_m^{2-m} + (n-m)\ OH^-$ where $n \geq m = 1, 2, \text{or } 3$ **(Eq. 4-4a)**

$n\ Fe(OH)_2 + m\ H_2O \rightleftarrows Fe_m(OH)_{2n}(H_2O)_{m(gel)}$ **(Eq. 4-4b)**

Redox reactions in the hydrogel network:

Oxidation half-reaction of Fe^{II}: $2\ Fe(OH)_2 + 2\ OH^- \rightleftarrows 2\ Fe(OH)_3 + 2\ e^-$ **(Eq. 4-5)**

With time, the transport of metal ions from the metal/solution interface to the bulk solution slows down, once the non-dispersible gelatinous layer has formed. The formation of hydrogel as a slow transport medium promotes systemic feedback between chemical reactions and mass transport processes. In the **Transition stage** (the end of **Stage 2**), the formation of iron oxide occurs via the reactions below:

Magnetite Formation: $Fe(OH)_2 + 2\ Fe(OH)_3 \rightarrow\rightarrow Fe_3O_4 + 4\ H_2O$ **(Eq. 4-6a)**

γ-FeOOH Formation: $Fe(OH)_3 \rightarrow\rightarrow FeOOH + H_2O$ **(Eq. 4-6b)**

Electron transfer between Fe^{II} and Fe^{III} is faster in the hydrogel than in the aqueous solution [5,39–41].

When nitrate is present in the solution, $[Fe^{3+}]$ and $[NO_2^-]$ are initially both zero. The coupling between the reduction half-reaction of ferric ion to ferrous ion with the oxidation half-reaction of hydroxide ions to oxygen is not as effective as that involving nitrite/nitrate due to the very high activation energy of oxidation of OH^- to O_2 [5]. Thus, although $[OH^-]$ also increases with time in the interfacial region, it diffuses out into the bulk solution rather than reducing ferric ions. Depending on the steady-state concentration of Fe^{II} and Fe^{III} and also on the concentration of oxygen or other oxidants in the interfacial region, the oxidation rate of Fe^{II} to Fe^{III} will be different.

This chapter investigates the effect of nitrate ions on the corrosion of CS by performing electrochemical experiments. First, a corrosion potential (E_{corr}) experiment was carried out to determine how corrosion evolves with time. Then, potentiodynamic

experiments were performed, with the anodic and cathodic branches of potentiodynamic curves in pH 6.0 buffered solution with different concentrations of $NaNO_3$ being investigated. Additionally, the corrosion behaviour was studied by comparing the results in $NaNO_3$ solutions containing $Fe(NO_3)_3$ to investigate the effect of nitrate ions in the presence of Fe^{3+} ions to understand the effect of the presence of Fe^{III} in the solution. Understanding this is important when more oxidizing environments (i.e., in the presence of radiolysis products) and limited solution volumes (**Chapter 7** and **Chapter 8**) are being studied. The effect of nitric acid (effect of nitrate in acidic solutions) is discussed in **Chapter 5.**

4.2 EXPERIMENTAL PROCEDURES

4.2.1 Sample Preparation

ASTM A36 carbon steel (CS) (provided by Ontario Power Generation Inc. (OPG)) test coupons of 1 cm diameter and 1 cm thickness were used in this study. The composition of this alloy is listed in **Table 4-2**. The coupons were polished manually with a series of abrasive silicon carbide papers (80, 320, 400, 600, 1200, and 2500 grit). This was followed by polishing on a Texmet microcloth (Buehler) with a 1 μm MetaDi Supreme diamond paste suspension (Buehler) and, lastly, sonication in an acetone/methanol mixture for 5 min to remove polishing residues. The polished coupons were then rinsed with Type I water and dried in flowing argon.

In this chapter, the electrochemical tests were performed by exposing one face of the samples (1 cm dia.) to the 100 mL of test solution volume contained within the

electrochemical cell. All other surfaces were covered with Teflon tape to isolate the electrical connection (a metal rod, which screws into the back of the sample) and ensure that the exposed surface area remained the same in all experiments. After each experiment, the sample was inspected visually to ensure that the covered surfaces were not in contact with the test solution.

Table 4-2: Chemical composition of carbon steel ASTM A36 CS.

Element	C	Mn	P	Cr	Ni	S	Si	Cu	Mo	Fe
(wt. %)	0.15	0.84	0.024	0.16	0.23	0.03	0.24	0.23	0.03	Bal.

4.2.2 Solution Preparation

All solution conditions studied in this chapter are summarized in **Table 4-3**

Table 4-3: List of solution conditions presented in Chapter 4.

Solution Composition			$[NO_3^-]$ (M)
pH 6.0 buffered solution	+	$NaNO_3$	0 (Blank)
			10^{-4}
			10^{-3}
			10^{-2}
			0.1
			0.3
			1
		$Fe(NO_3)_3$	0
			0.1
			0.3
			1

All solutions were prepared with water purified with a NANO pure Diamond UV

ultrapure water system (Barnstead International) to give a resistivity of 18.2 MΩ.cm. The pH 6.0 buffered solutions were prepared using 0.01 M concentrations of sodium borate ($Na_2B_4O_7.10H_2O$), and then adjusted to pH 6.0 by adding boric acid (H_3BO_3, analytical grade, Caledon Laboratories Ltd.). The pH of the solution was measured using an Accumet^{Ò} Basic AB15 pH meter. Then, sodium nitrate was added to the buffered solution of pH 6.0 to make solutions with different nitrate concentrations. For comparison, the same electrochemical experiments were performed in $Fe(NO_3)_3$-containing solutions with the same concentrations of nitrate in pH 6.0 buffered solutions (0.1 M, 0.3 M, and 1 M), but the amount of Fe^{3+} was one-third of the nitrate concentration.

4.2.3 Electrochemical Tests

All electrochemical measurements were performed using a three-compartment cell with CS as the WE, a saturated calomel electrode (SCE, Fisher Scientific) as the reference electrode, and a platinum mesh as the CE. The electrochemical tests were conducted using a BioLogic VMP-300 multichannel potentiostat. All experiments in this chapter were performed in Ar-purged solutions. The deaeration process started with purging the solution with argon for 45 min prior to the test, and continued during the experiment.

Before each experiment, cathodic cleaning was conducted at -0.230 V_{RHE} for 5 min. Then the corrosion potential (E_{corr}) was measured for 8 h, and finally potentiodynamic polarization was performed by scanning the potential with a scan rate of 0.167 mV s^{-1} from -0.3 V to 0.2 V with respect to E_{corr}. All experiments were repeated at least three times to ensure reproducibility.

4.3 RESULTS AND DISCUSSION

A chemical reaction occurs in order to achieve chemical equilibrium (i.e., to minimize the free energy of the reacting system). When a chemically closed system reaches equilibrium (i.e., the state of minimum chemical potential), the net rate of reactions is zero. The corrosion potential (E_{corr}) is the potential at which the sum of the rates of the oxidation reactions i_{ox}, and the sum of the rates of the reduction reactions $|i_{red}|$are equal, but opposite in sign, adding up to zero [1,9,20,29,33,37,42]. However, determination of the redox equilibrium potential during the corrosion process is not possible using an E_{corr} measurement. Similarly, measurement of the rate of each redox reaction is also impossible. When the chemical reaction is a reversible process, and the redox pair is at chemical equilibrium, for an oxidation reaction to occur, the E_{corr} of the system must be higher than the E_{rxn}^{eq} of the oxidation reaction. In a corroding system, the comparison of E_{corr} with its E_{rxn}^{eq} value is not to determine whether the redox reaction can occur or not but to determine how the overall metal oxidation process evolves with time. Thus, a comparison of the equilibrium potential of redox reactions with the E_{corr} graph and analysis of the trend of changes in the E_{corr} can be employed to obtain mechanistic information on the evolution of the metal redox half-reaction(s) that may occur as corrosion progresses to understand the corrosion system. The parameter that controls the net reaction rate of an electrochemical half-reaction is the overpotential, $\eta_{rxn} = E_{elec} - E_{rxn}^{eq}$ [20,43,44]. The η_{rxn}, which is the difference between the electrode potential (E_{corr} under naturally corroding conditions or E_{app} applied during

polarization) and the E_{rxn}^{eq}, is what controls the net rate of that half-reaction [6,20,43]. The E_{rxn}^{eq} values for different metal oxidation reactions on CS at 25 °C are calculated from the standard redox potentials (E_{rxn}^{0}) [45] for the range of potentials tested in this study (See **Figure 4-1)**, and are also listed on the left side of the E_{corr} and PD graphs (**Figure 4-2**).

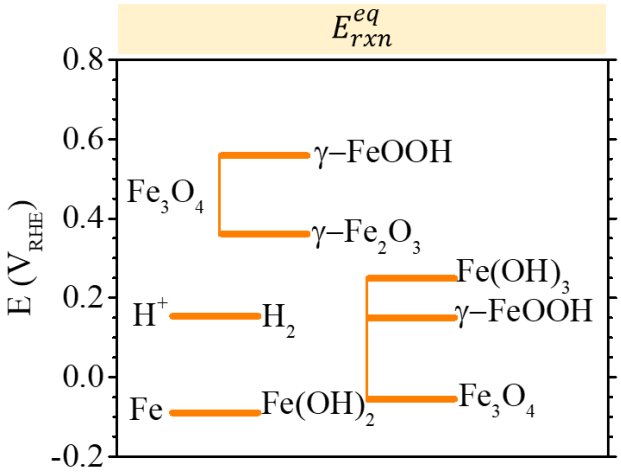

Figure 4-1: The diagram of E_{rxn}^{eq} of some of the redox reactions involved in CS corrosion.

The E_{rxn}^{eq} values of various redox half-reactions involving iron species were calculated from the reported standard Gibbs free energies of formation ($\Delta_f G^{\circ}$) of the chemical species involved in the redox reactions and their chemical activities in solution [33,46]. The chemical activities of H_2O and solid species are 1, and those of dissolved species such as metal cations are assumed to be the same as their concentrations. Oxidizing conditions and solution pH are key parameters that strongly control the CS corrosion path [30,33,35,47]. The E_{rxn}^{eq} values of the redox reactions involving solid metal and hydroxides/oxyhydroxides/oxides also decrease by 59 mV per pH-unit increase when the ratio of H^+:e^- transferred in these redox-reactions and the chemical activity of

solid species are one. Therefore, E_{rxn}^{eq} on the reversible hydrogen electrode (RHE) scale, in V_{RHE} units, is independent of pH. In this thesis, the E_{corr} and E_{rxn}^{eq} values are presented relative to the V_{RHE} scale to directly compare the overpotential for a redox reaction involved in corrosion at different pHs. The E_{RHE} on the standard hydrogen electrode (SHE) potential scale decreases by 59 mV_{SHE} per unit pH increase, but on the V_{RHE} scale $E_{\mathrm{RHE}} = 0.0\ V_{RHE}$ at all pHs:

$$H^+ + 2\ e^- \rightleftarrows H_2 \qquad E_{\mathrm{RHE}} = E_{H^+ \rightleftarrows H_2}^{eq} = 0.0\ V_{RHE} \text{ (at all pHs)} \qquad \textbf{(Eq. 4-7)}$$

An electrode potential on the RHE potential scale (E (V_{RHE})) is related to a potential on the standard hydrogen electrode (SHE) scale (E (V_{SHE})) by:

$$E(V_{RHE}) = E(V_{SHE}) + 0.059 \times pH \qquad \textbf{(Eq. 4-8)}$$

For the chemical activity of H_2 in its standard state, the RHE potential is 0.0 V_{RHE}. However, the dissolved H_2 is in partitioning equilibrium with gaseous H_2 at a partial pressure of 1 atm (the standard state of H_2). The fraction of gaseous H_2 in normal air is ~ 6×10^{-7} [6,9]; thus, the $E_{H^+ \rightleftarrows H_2}^{eq}$ value is 0.154 V_{RHE}. The fraction of H_2 in an Ar-purged environment (conditions of all experiments in this chapter) was unavailable, but we can assume that its fraction is below that in normal air. Thus, the $E_{H^+ \rightleftarrows H_2}^{eq}$ value under the conditions studied in this thesis should be > 0.154 V_{RHE}.

Nitrate, like other polyoxygenated anions, can be reduced in multiple steps (to NO_2^-, NO^-, N_2O, N_2, and NH_3/NH_4^+). Although the reduction of NO_3^- to N_2O and NH_4^+ is thermodynamically possible, for kinetic reasons only the first reduction step (NO_3^-/NO_2^-) can effectively couple with iron oxidation [6,48,49].

$NO_3^- + 2\,H^+ + 2\,e^- \rightarrow NO_2^- + H_2O$ **(Eq. 4-9)**

The equilibrium potential for the NO_3^-/NO_2^- half-reaction (**Eq. 4-9**) could not be defined accurately because the concentration of NO_2^- in the interfacial region is not known. The lower $[NO_3^-]/[NO_2^-]$ is, the lower the $E^{eq}_{NO_3^- \rightleftharpoons NO_2^-}$ value will be. The value of this equilibrium potential decreases from 1.022 V_{RHE} to 0.845 V_{RHE} when the ratio of $[NO_3^-]/[NO_2^-]$ decreases from 10^6 to 1.

Only the E^{eq}_{rxn} diagrams for redox half-reactions involving solid iron redox pairs are presented in the figures throughout this chapter. For the E^{eq}_{rxn} values presented in **Figure 4-1** and **Figure 4-2,** a chemical redox activity of 1.0 was used for the solid species, Fe^0, $Fe(OH)_2$, $Fe(OH)_3$ and Fe_3O_4.

$E^{eq}_{Fe^0 \rightleftarrows Fe^{2+}}$ (**Eq. 4-10**), and $E^{eq}_{Fe^{2+} \rightleftarrows Fe^{3+}}$ (**Eq. 4-11**) are not presented in the graph shown in **Figure 4-2**:

$Fe^{2+}_{(aq)} + 2\,e^- \rightleftarrows Fe^0_{(m)} \quad E^0_{Fe^{2+} \rightleftarrows Fe^0} = -0.44\ V_{RHE}$ **(Eq. 4-10)**

$Fe^{3+}_{(aq)} + e^- \rightleftarrows Fe^{2+}_{(aq)} \quad E^0_{Fe^{2+} \rightleftarrows Fe^0} = 0.77\ V_{RHE}$ **(Eq. 4-11)**

$E^{eq}_{Fe^0 \rightleftharpoons Fe^{2+}}$ and $E^{eq}_{Fe^{2+} \rightleftharpoons Fe^{3+}}$ depend on the chemical activity (~ concentration) of Fe^{2+} in the interfacial region $\left(\left(a_{Fe^{2+}}\right)_{int}\right)$ or Fe^{3+} in the interfacial region $\left(\left(a_{Fe^{3+}}\right)_{int}\right)$. As discussed in more detail later, $\left(a_{Fe^{2+}}\right)_{int}$ or $\left(a_{Fe^{3+}}\right)_{int}$ is determined not only by the net electron/metal atom transfer step but also by the transport of Fe^{2+} or Fe^{3+} from the interfacial region to the bulk solution and/or by other removal processes of Fe^{2+} or Fe^{3+}

from the interfacial region. There exists no true chemical equilibrium state for the interfacial mass transfer process; otherwise, the equilibrium potential of the reaction ($E^{eq}_{Fe^0 \rightleftharpoons Fe^{2+}}$ and $E^{eq}_{Fe^{2+} \rightleftharpoons Fe^{3+}}$) would be determined by $\left(a_{Fe^{2+}}\right)_{int}$ or $\left(a_{Fe^{3+}}\right)_{int}$.

When the steady-state concentrations of Fe^{2+} in the interfacial region are below their respective solubility limits,

$$E^0_{Fe^{2+} \rightleftarrows Fe^0} < E^0_{Fe^{2+}(sat'd) \rightleftarrows Fe^0} \quad \textbf{(Eq. 4-12)}$$

where $Fe^{2+}_{(sat'd)}$ represents $[Fe^{2+}_{(aq)}]$ at its saturation limit.

However, steady-state exists when the solution is saturated with metal cations. Metal cations dissolved in water are in hydrolysis equilibrium:

$$Fe^{2+} + n\ OH^- \rightleftharpoons Fe(OH)_x^{2-x} + (n-x)\ OH^- \text{ where } x = 1,2, \text{ or } 3 \quad \textbf{(Eq. 4-13)}$$

Due to the hydrolysis and solid-liquid equilibria, the redox half-reaction of Fe^0 to $Fe^{2+}_{(sat)}$ and Fe^{2+} to $Fe^{3+}_{(sat)}$ is also at equilibrium when the oxidation half-reaction of Fe^0 to amorphous $Fe(OH)_2$ is at equilibrium. Hence, the E^{eq}_{rxn} starts very low but increases until metal cation concentration reaches its saturation limit.

When the total concentration of dissolved metal cations (Fe^{2+} + $Fe(OH)^+$ + $Fe(OH)_2 \cdot nH_2O$ + $Fe(OH)_3^-$) exceeds its saturation limit, the dissolved species precipitate with OH^- as solid $Fe(OH)_2$ [46,50]:

$$Fe^{2+}_{(sat)} + 2\ OH^- \rightleftarrows Fe(OH)_{2(solid)} \quad \textbf{(Eq. 4-14)}$$

The chemical activities of metal hydroxides in colloidal form or in a hydrogel network will not be 1.0, because transition metal hydroxides are hygroscopic, and thus initially

condense as colloids in water and/or aggregate to form a hydrogel network [5,51,52].

$$E^{eq}_{Fe^0 \leftrightarrows Fe^{2+}_{(aq)}} < E^{eq}_{Fe^0 \leftrightarrows Fe^{2+}_{(aq\ at\ sat)}} = E^{eq}_{Fe^0 \leftrightarrows Fe(OH)_2} \quad \textbf{(Eq. 4-15)}$$

There are two possible pathways for forming solid $Fe(OH)_2$ from oxidation of $Fe_{(m)}$. One pathway involves the direct interfacial transfer of iron atoms from the solid metal to the solid hydroxide phase at the metal-hydroxide interface, coupled with the interfacial transfer of OH^- from the solution phase to the solid hydroxide at the hydroxide-solution interface via electron transfer through the solid hydroxide phase. In this pathway, the metal is not exposed to the aqueous solution. This is a very energetic process, not only thermodynamically (high Gibbs free energy of reaction, i.e., high $E^{eq}_{Fe \rightleftharpoons Fe(OH)_2}$) but also has a high activation energy [20–22].

$$Fe(OH)_{2(solid)} + 2\ H^+ + 2\ e^- \rightleftarrows Fe^0_{(m)} + 2\ H_2O \quad \textbf{(Eq. 4-16)}$$

The second pathway involves oxidation of $Fe^0_{(m)}$ to $Fe^{2+}_{(solv)}$ followed by precipitation of $Fe^{2+}_{(solv)}$ with OH^- when $\left(a_{Fe^{2+}}\right)_{int}$ is at or above its saturation limit. Due to the hydrolysis and solid-liquid equilibria, the redox half-reaction of $Fe^0_{(m)}$ to $Fe^{2+}_{(solv)}$, when the interfacial region is saturated with $Fe^{2+}_{(solv)}$, is also in equilibrium with the redox half-reaction of $Fe^0_{(m)}$ to $Fe(OH)_2$:

$$Fe^0_{(m)} + 2\ H_2O \rightleftarrows Fe^{2+}(sat'd) + 2\ H_2O + 2\ e^- \rightleftarrows Fe(OH)_{2(gel)} + 2\ H^+ + 2\ e^- \quad \textbf{(Eq. 4-17)}$$

Iron hydroxide is hygroscopic, and the $Fe(OH)_2$ precipitates initially as colloids, which can then aggregate to form a hydrogel network [5,33,38]. To differentiate from the solid layer of $Fe(OH)_2$ in contact with iron metal in reaction (**Eq. 4-16**), the $Fe(OH)_2$ formed by the precipitation of dissolved ferrous ion is represented by $Fe(OH)_{2(gel)}$ in the

above equation (**Eq. 4-17**). Hence, when both redox species, $Fe^0_{(m)}$ and $Fe(OH)_2$, are fully exposed to the aqueous solution,

$$E^{eq}_{Fe(OH)_{2(gel)} \rightleftarrows Fe^0} \approx E^{eq}_{Fe^{2+}(sat'd) \rightleftarrows Fe^0} = \text{-0.09 } V_{RHE} \qquad \textbf{(Eq. 4-18)}$$

4.3.1 The Evolution of E_{corr} as Function of Time

Figure 4-2 compares log $E_{corr}(t)$ as a function of time during corrosion of CS electrodes in pH 6.0 buffered solution in the presence of different concentrations of $NaNO_3$ or $Fe(NO_3)_3$.

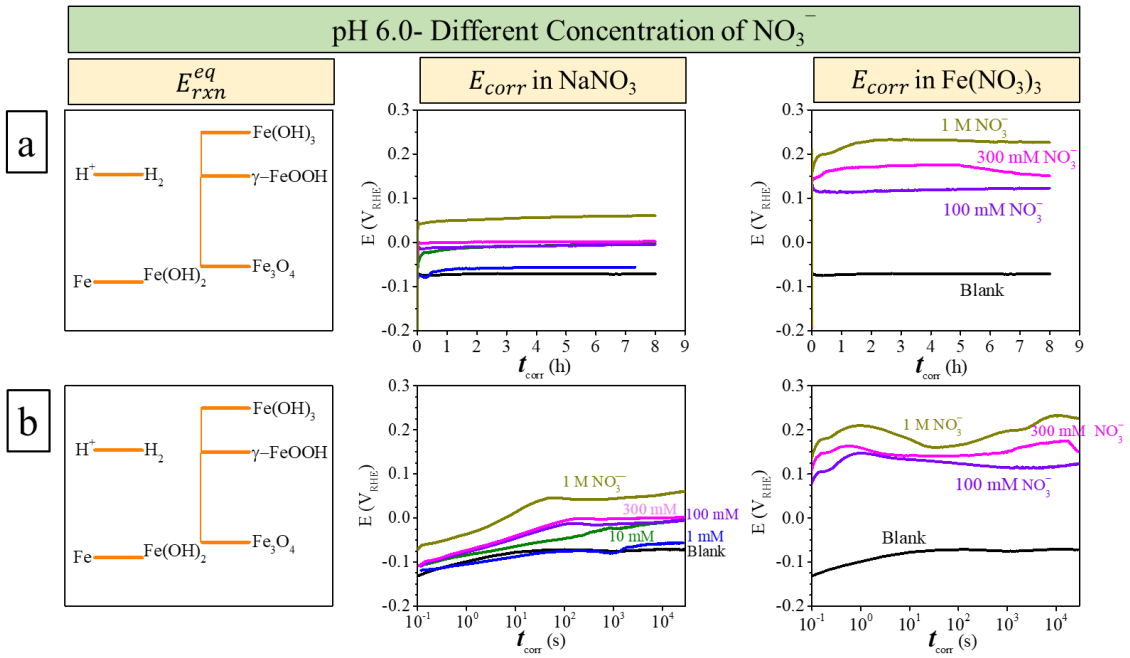

Figure 4-2: E_{corr} of CS as a) as a function of t_{corr} b) a function of $log\ (t_{corr})$ in buffered solutions of pH 6.0 containing different concentrations of $NaNO_3$ and $Fe(NO_3)_3$, taken immediately after cathodic cleaning. The diagram on the left indicates the E^{eq}_{rxn} of redox reactions that may be involved.

The evolution of E_{corr} as a function of time was studied in pH 6.0 $NaNO_3$ solutions and $Fe(NO_3)_3$ solutions. For all solutions containing $NaNO_3$ (+ any residual O_2

not removed by constant Ar-purging), except the one with 1 M $NaNO_3$, the initial E_{corr} values were similar to or higher than that of the blank ($[NO_3^-] = 0$), but were still close to $E^{eq}_{Fe^0 \rightleftharpoons Fe(OH)_2}$ and lower than $E^{eq}_{Fe(OH)_2(\text{sat'd}) \rightleftarrows Fe_3O_4}$. The initial E_{corr} in the presence of 1 M $NaNO_3$ was higher than $E^{eq}_{Fe(OH)_2(\text{sat'd}) \rightleftarrows Fe_3O_4}$. However, the E_{corr} increased with time (except in the case of 0.1 mM $NaNO_3$). Overall, the corrosion potential increased with time rapidly in the first few seconds and then remained constant or continued its upward trend at a lower rate. The final E_{corr} depended on the nitrate concentration and increased as $[NO_3^-]$ increased.

In $Fe(NO_3)_3$ solution, when the same amount of NO_3^- is initially present, the initial E_{corr} is significantly higher than observed in $NaNO_3$ solution, close to $E^{eq}_{Fe(OH)_2(\text{sat'd}) \rightleftarrows \gamma\text{-FeOOH}}$. Corrosion of CS in $NaNO_3$ and $Fe(NO_3)_3$ is discussed in detail below.

4.3.1.1 Effect of nitrate on Corrosion Dynamics of CS (pH 6.0)

The data presented in **Figure 4-2** are replotted in **Figure 4-3** to present the time-dependent behaviour of E_{corr} and assign different dynamic stages of CS corrosion to different steady-state E_{corr} values. The effect of nitrate on the duration of the dynamic stages is explained using **Figure 4-3**.

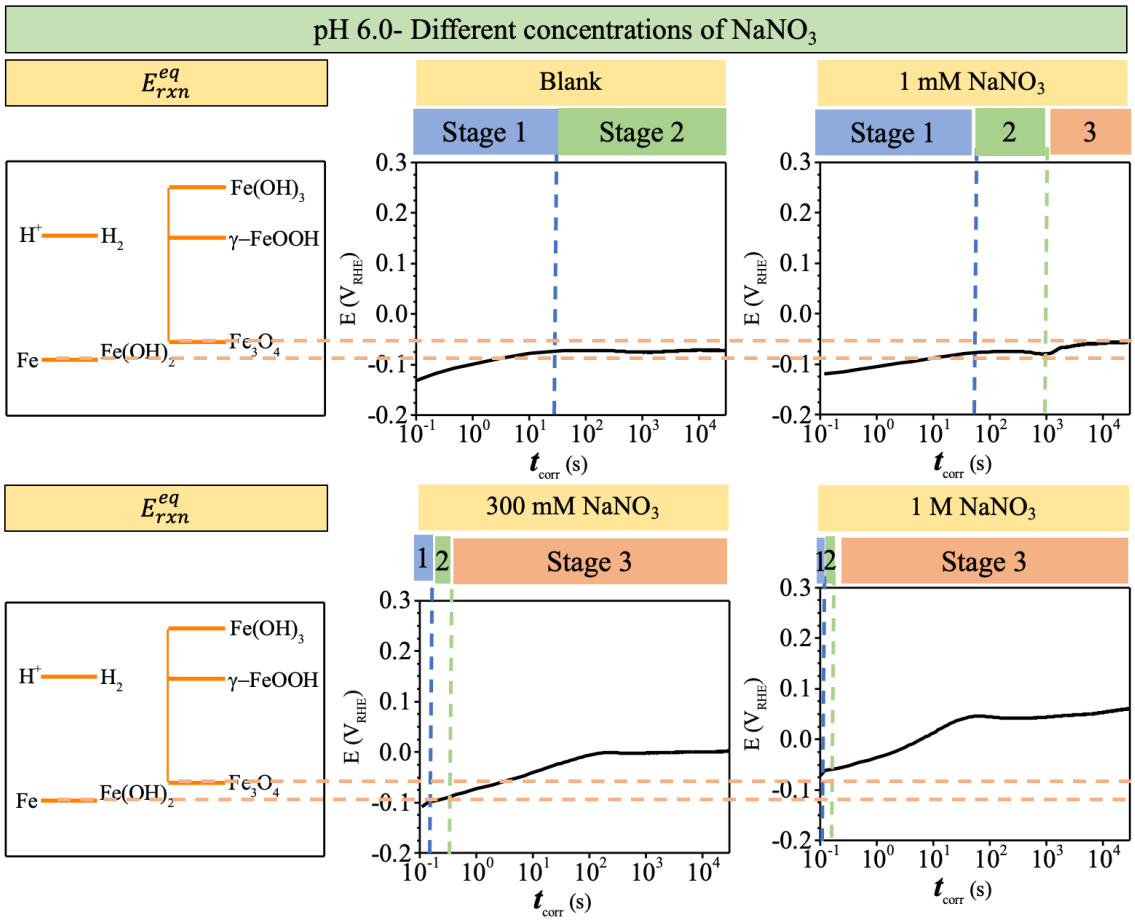

Figure 4-3: E_{corr} vs time behaviour of CS in pH 6.0 buffered solution in the presence of different concentrations of $NaNO_3$, replotted to show the stages.

For the blank and all solutions containing $NaNO_3$ (+ any residual O_2 not removed by constant Ar-purging), the key observations are as follows:

- The initial E_{corr} value increased with $NaNO_3$ concentration. Except for 1 M $NaNO_3$, the initial E_{corr} values were close in all solutions and higher than in the blank, but were still close to $E^{eq}_{Fe^0 \rightleftharpoons Fe(OH)_2}$ and lower than $E^{eq}_{Fe(OH)_2(\text{sat'd}) \rightleftarrows Fe_3O_4}$. The initial E_{corr} in the presence of 1 M $NaNO_3$ was higher than $E^{eq}_{Fe(OH)_2(\text{sat'd}) \rightleftarrows Fe_3O_4}$.

- The E_{corr} value in solutions with different concentrations of $NaNO_3$ approached different steady-state values. The final value of E_{corr} for the blank solution remained between $E^{eq}_{Fe^0 \rightleftharpoons Fe(OH)_2}$ and $E^{eq}_{Fe(OH)_2(\text{sat'd}) \rightleftarrows Fe_3O_4}$, but closer to the former; the E_{corr} in 100 mM $NaNO_3$ containing solution approached $E^{eq}_{Fe(OH)_2(\text{sat'd}) \rightleftarrows Fe_3O_4}$, and the final value of E_{corr} in solutions containing 300 mM and 1 M $NaNO_3$ was above $E^{eq}_{Fe(OH)_2(\text{sat'd}) \rightleftarrows Fe_3O_4}$ and below $E^{eq}_{Fe(OH)_2(\text{sat'd}) \rightleftarrows \gamma - FeOOH}$.

<u>Corrosion Dynamics of CS (pH 6.0) in Blank Solution:</u>

For CS in the blank solution, it took about 20 s for E_{corr} to reach its steady-state value. Once E_{corr} had reached this value, it remained there for the remainder of the test duration. The initial E_{corr} was below $E^{eq}_{Fe^0 \rightleftharpoons Fe(OH)_2}$ and the steady-state value was close to $E^{eq}_{Fe^0 \rightleftharpoons Fe(OH)_2}$ and lower than $E^{eq}_{Fe(OH)_2(\text{sat'd}) \rightleftarrows Fe_3O_4}$. The 1st region in the E_{corr} vs time graph corresponds to the 1st dynamic stage. The E_{corr}– log t_{corr} graph of the blank pH 6.0 solution showed an almost linear increase in E_{corr} with time. The E_{corr} changes with time and approaches a steady-state value by about 20 s. During this time, the concentration of Fe ions in the interfacial region increases via oxidation of iron. We attribute the initial linear change in E_{corr} to a change in $\left(a_{Fe^{II}}\right)_{int}$ as metal oxidation progresses, where $\left(a_{Fe^{II}}\right)_{int}$ is determined by the metal oxidation rate ($\boldsymbol{\nu_{M1}}$) and mass transfer rate ($\boldsymbol{\nu_{trans}}$) while ($\boldsymbol{\nu_{M1}}$) and ($\boldsymbol{\nu_{trans}}$) vary with $\left(a_{Fe^{II}}\right)_{int}$. In this stage, $\left(a_{Fe^{II}}\right)_{int}$ and $\left(a_{Fe^{III}}\right)_{int}$ are not constant (they are not at their saturation concentrations). Thus, E_{corr} increases with time until $\left(a_{Fe^{II}}\right)_{int}$ reaches saturation at $E^{eq}_{Fe^0 \rightleftharpoons Fe(OH)_2}$ ($\sim 20\ s$). $Fe^{II}_{(aq)}$ forms continuously via oxidation and Fe ions dissolve into the solution. The first

E_{corr} steady state is reached (in less than 20 s) when $\left(a_{Fe^{II}}\right)_{int}$ and $\left(a_{Fe^{III}}\right)_{int}$ no longer change with time, and the net rate of oxidation is equal to the rate of mass transport of Fe from the interfacial region into the bulk solution. For at least 8 h of E_{corr} measurement, no change in the E_{corr} value was observed and E_{corr} remained in the first steady-state, indicating that the concentrations of Fe^{II} and Fe^{III} in $Fe(OH)_2$ layer had not reached the saturation values that promote $Fe(OH)_2 \rightarrow Fe^{III}$ oxidation. Thus, in nitrate-free solution, the corrosion dynamics remained in **Stage 2** at least for 8 h.

Corrosion Dynamics of CS (pH 6.0) in $NaNO_3$ Solutions:

The effects of NO_3^- ions on the corrosion behaviour of CS were investigated by E_{corr} measurement during 8-h corrosion of CS in pH 6.0 solutions containing different concentrations of $NaNO_3$ (ranging from 0.1 mM to 1 M) (See **Figure 4-2**).

The equilibrium potential of the NO_3^-/NO_2^- redox reaction depends on the pH and the ratio of NO_3^- to NO_2^- ions. In a pH 6.0 solution, the $E^{eq}_{NO_2^-/NO_3^-}$ decreases from 1.022 V_{RHE} to 0.845 V_{RHE} when the ratio of NO_3^-:NO_2^- decreases from 10^6 to 1. $E^{eq}_{NO_3^-/NO_2^-}$ varies as follows:

$$E^{eq}_{NO_3^-\rightleftarrows NO_2^-} = 0.845 + 0.0295 \log\frac{[NO_3^-]}{[NO_2^-]} \ (V_{RHE}) \qquad \textbf{(Eq. 4-19)}$$

Also, an increase in the ionic strength affects the concentration gradient and consequently, affects the ion mobility [53-55]. The ion mobility is approximately the square root of the ionic strength. The ionic strengths of solutions were calculated using (**Eq. 4-20**):

$$\mu = 0.5 \sum_i c_i z_i^2 \qquad \textbf{(Eq. 4-20)}$$

where c_i is the concentration of anion (i), and z_i is the charge of species i.

In the presence of NO_3^-, an increase in the ionic strength of the solution facilitates the mass transport of cations away from the surface. It allows metal ions to leave the surface more rapidly, and thus the metal oxidation is less likely to become diffusion-limited.

In 1 mM $NaNO_3$ solution, similar to the results observed in the blank (nitrate free) solution, E_{corr} initially increased almost linearly with log t_{corr} (**Stage 1**) until it reached a steady-state value. The initial E_{corr} value (-0.12 V_{RHE}) was slightly higher than the initial E_{corr} observed in the blank solution (-0.13 V_{RHE}). The E_{corr} vs time slope remained unchanged, and **Stage 2** was reached after the same time as for the blank solution. Although the NO_3^-/NO_2^- redox reaction can couple with the oxidation of Fe and increase the rate at which iron is oxidized to Fe^{II}, the higher ionic strength in 1 mM $NaNO_3$ slightly increases the mass transport rate of Fe ions from the interfacial region into the solution phase. Thus, the potential at which the rate of Fe oxidation and nitrate reduction are equal remains the same as for the blank solution. The 2nd steady state E_{corr} was reached by 3 h. The second steady state corresponds to **Stage 3,** where Fe_3O_4 forms within the $Fe(OH)_2/Fe(OH)_3$ gelatinous layer. Formation of Fe_3O_4 implies that when a viscous hydroxide layer of $Fe(OH)_2$ has formed via $Fe(OH)_2$ colloid formation (**Eq. 4-4a**), NO_3^- promotes the oxidation of Fe^{II} to Fe^{III}. As a result, the formation of Fe_3O_4 is accelerated in the presence of 1 mM $NaNO_3$.

Redox reactions in the hydrogel network:

Oxidation half-reaction of Fe^{II}: $2\ Fe(OH)_2 + 2\ OH^- \rightarrow 2\ Fe(OH)_3 + 2\ e^-$ **(Eq. 4-21a)**

Reduction half-reaction of nitrate: $NO_3^- + 2\ H^+ + 2\ e^- \rightarrow NO_2^- + H_2O$ **(Eq. 4-21b)**

Overall charge transfer reaction:

$$2\,Fe(OH)_2 + NO_3^- + H_2O \rightarrow 2\,Fe(OH)_3 + NO_2^- \qquad \textbf{(Eq. 4-21c)}$$

In 300 mM $NaNO_3$ solution, the initial E_{corr} at 0.1 s was slightly (10 mV) higher than the E_{corr} observed in 1 mM $NaNO_3$ solution. As will be explained later in **Section 4-3-2**, 300 mM $NaNO_3$ is strong enough to effectively couple with the oxidation of Fe. In 300 mM $NaNO_3$ solution, a rapid increase in the $Fe^{II}_{(aq)}$ concentration occurs in the interfacial region. At the same time, hydrolysis reactions and hydroxide formation are also accelerated, as the rate at which Fe^{II} accumulates is faster. This provides the conditions for the precipitation of $Fe(OH)_2$ in less than 1 s, and results in the progression of corrosion to **Stage 2,** where mass transfer from the less soluble $Fe(OH)_2$ gel layer to the bulk solution controls the rate of oxidation. Once $Fe(OH)_2$ has formed at the surface, NO_3^- can effectively oxidize Fe^{II} to Fe^{III}. Thus, E_{corr} progresses from the 1st steady-state to the 2nd steady state. The second steady state E_{corr} was above $E^{eq}_{Fe(OH)_2(\text{sat'd})\rightleftarrows Fe_3O_4}$ and below $E^{eq}_{Fe(OH)_2(\text{sat'd})\rightleftarrows \gamma-FeOOH}$. During the transition to the second steady state, the oxide layer becomes thicker while the Fe^{II} cations continue to transfer to the solution phase. Ferrous ions can easily transfer to the solution phase in a high ionic strength solution.

In 1 M $NaNO_3$ solution, the initial E_{corr} was significantly higher than observed in other solutions. This indicates that due to the oxidative power that 1 M NO_3^- provides, the initial corrosion potential is higher than $E^{eq}_{Fe(OH)_2(\text{sat'd})\rightleftarrows Fe_3O_4}$. Immediately after cathodic cleaning, Fe cations accumulate at the interfacial region. The presence of a high nitrate concentration, which can act as a strong oxidant and couple with Fe oxidation, provides

the conditions for progression to **Stage 3**, as was previously observed for the solution containing 300 mM nitrate.

In summary, NO_3^- can affect the CS corrosion in large solution volumes via redox reactions of NO_3^-/NO_2^- that can be coupled with Fe/Fe^{II} and Fe^{II}/Fe^{III} oxidation reactions and increase the corrosion potential to a range where (hydr)oxides with higher oxidation states than in the blank solution can form.

Corrosion Dynamics of CS (pH 6.0) in $Fe(NO_3)_3$ Solutions:

In 100 mM $Fe(NO_3)_3$ solution buffered at pH 6.0 , the initial E_{corr} of CS was significantly higher than in the blank solution (see **Figure 4-2**). For higher concentrations of $Fe(NO_3)_3$, the initial E_{corr} increased even more. The E_{corr} of CS in all $Fe(NO_3)_3$ solutions remained almost unchanged with time and only fluctuated around a constant potential. When $Fe(NO_3)_3$ is present, reduction of Fe^{3+} to Fe^{2+} (**Eq. 4-22**) can occur (in addition to equation **(Eq 4-2b)**).

$$Fe^{3+} + e^- \leftrightarrows Fe^{2+} \quad E^0 = 0.77\ V_{RHE},\ E_{eq} = 0.77 + 0.059 \log \frac{[Fe^{3+}]}{[Fe^{2+}]}\ V_{RHE} \quad \textbf{(Eq. 4-22)}$$

Upon immersion in $Fe(NO_3)_3$, when the surface is free of oxide and hydroxide, the Fe^{3+} to Fe^{2+} reduction can couple with the oxidation of Fe to Fe^{2+}. Fe^{3+} can also reduced to Fe^{2+} **(Eq 4-23).** This reaction has been proposed for the use of $Fe^{(III)}$ as an oxidant for the leaching of metallic iron [36].

$$2\ Fe^{3+} + Fe^0 \leftrightarrows 3\ Fe^{2+} \quad \textbf{(Eq. 4-23)}$$

In addition, for the same concentration of nitrate, the ionic strength of $Fe(NO_3)_3$ solution is higher than for $NaNO_3$ solution. For a 1 M solution, for example, the ionic strength of $Fe(NO_3)_3$ is 4 times higher than for $NaNO_3$. The increase in mass transfer rate for solutions with higher ionic strength can increase the overall charge transfer rate. When an

iron hydroxide layer forms at the surface, not only is the transport of metal ions from the metal/solution interface to the bulk solution slowed down, but also the transport of Fe^{3+} from the solution toward the surface. Thus, the system approaches the 2nd steady-state involving the oxidation of Fe^{II} to Fe^{III} inside the gel layer via the reduction of NO_3^- ions. The formation of hydroxide (Fe^{II} hydroxide) occurs in a very short period of time (less than 1 s), and corrosion progresses to **Stage 2** (1st steady-state E_{corr}). In this stage, Fe^{3+} is not an effective oxidant for Fe oxidation. Instead, the formation of the hydrogel as a slow transport medium induces systemic feedback between chemical reactions and mass transport processes. In **Stage 3**, the formation of iron oxide results in the formation of magnetite and/or γ-FeOOH, depending on the concentration of Fe^{II} and Fe^{III} hydroxide, while iron ions can transfer easily from the interfacial region to the solution phase in a high ionic strength medium.

In summary, the addition of $Fe(NO_3)_3$ to the solution has two major effects. First, the introduction of another reduction reaction, which increases the oxidative power of the solution. Second, the increase in the ionic strength, which increases the mass transport rate. The combination of these two assisted in the formation of Fe^{III} at the interface, and consequently, the corrosion potential shifted to more positive values.

4.3.2 Potentiodynamic Polarization Results

The potentiodynamic polarization behaviours of CS after 8 h immersion in solutions with different NO_3^- concentrations were studied in $NaNO_3$ and in $Fe(NO_3)_3$ solutions to understand the effect of nitrate on the kinetics of chemical and electrochemical reactions involved in CS corrosion.

4.3.2.1 Potentiodynamic Polarization Behaviour in $NaNO_3$ Solutions

Figure 4-4 shows the potentiodynamic polarization data obtained in a pH 6.0 buffered solution with and without various concentrations of $NaNO_3$. A Tafel analysis was performed to understand the polarization behaviour at positive and negative overpotentials and the results are presented in **Figure 4-5** and

Table 4-4.

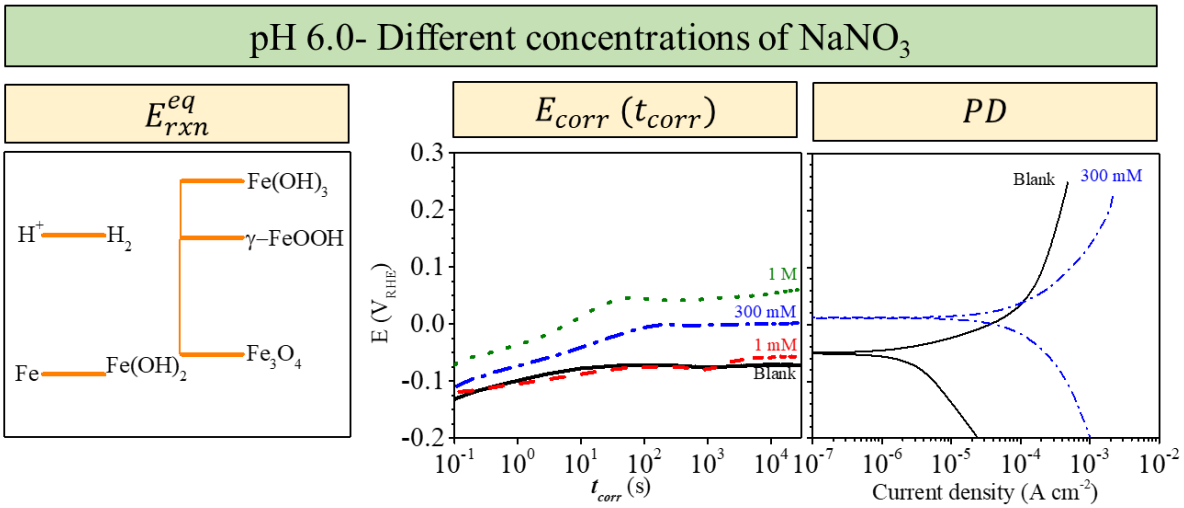

Figure 4-4: Potentiodynamic polarization curves for CS in pH 6.0 buffered solution containing different concentrations of $NaNO_3$.

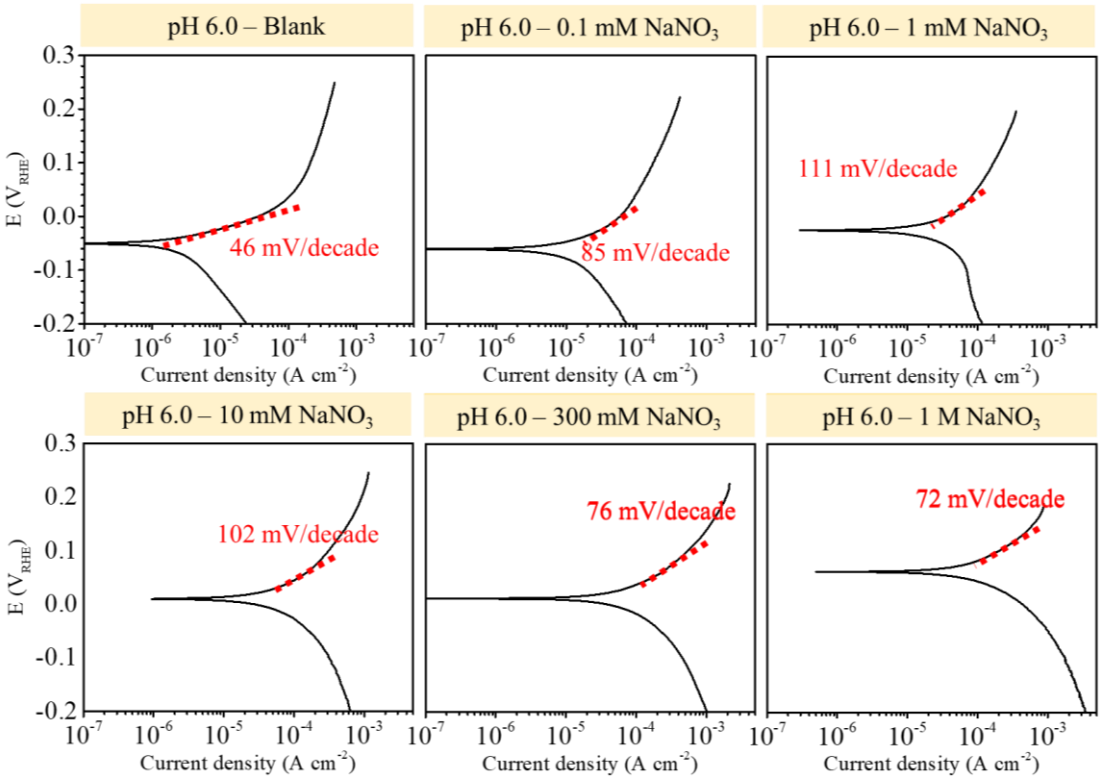

Figure 4-5: Anodic Tafel analysis for potentiodynamic polarization curves of CS in pH 6.0 buffered solution initially containing various $NaNO_3$ concentrations.

Table 4-4: The values for $E_{i=0}$, Tafel slopes, and corrosion current densities (i_{corr}) obtained from Tafel analysis of the PD results presented in Figure 4-5.

[$NaNO_3$] (mM)	**0**	**0.1**	**1**	**10**	**100**	**300**	**1000**
$E_{i=0}$ (mV_{RHE})	-50±2	-61±4	-24±4	15±1	10±8	12±2	62±7
b_a (mV/decade)	46±0	85±10	111±0	102±5	85±4	76±0	72±4
$\|b_c\|$ (mV/decade)	119±1	123±5	133±2	87±3	102±1	96±8	80±2
$i_{corr,a}$ ($\mu A\ cm^{-2}$)*	2.9	11	23	28	39	51	62
$i_{corr,c}$ ($\mu A\ cm^{-2}$)**	2.1	9.3	23	30	43	53	79
i_{corr} ($\mu A\ cm^{-2}$)	2.3	10	23	29	41	52	71

* $i_{corr,a}$ is the anodic current density when the anodic Tafel line is extrapolated to E_{corr}

** $i_{corr,c}$ is the cathodic current density when the cathodic Tafel line is extrapolated to E_{corr}

It should be mentioned that a prerequisite for an accurate Tafel slope measurement is finding a linear region (which should be present for at least one decade of current density) in a range of potentials far enough from the corrosion potential [42,56,57]. In this study, the reported Tafel slopes are based on the best fit for the most linear region within ±30 mV to ±60 mV around E_{corr}. The reason for choosing this lower limit for the range of overpotential (±30 mV) was that based on the WT equation (**Eq, 4-24**) for n = 2 and $\alpha = 0.5$, when $\eta > 30\,mV$, i_c is less than 10% of i_a and when $\eta < -30\,mV$, i_a is less than 10% of i_c. The upper limit for the range (±60 mV) was selected to ensure the same region of overpotential was studied in all conditions. It is also worth mentioning that, for obtaining Tafel slopes, the data in the desired potential range were extracted and then the slope of the best linear fit ($R^2 > 95\%$) for the $E - \log i$ curve was considered to be the Tafel slope [42]. One interesting observation in **Figure 4-5** was that the anodic Tafel region is over two decades long in the blank solution. However, when $NaNO_3$ is present in the solution, the region is less than one decade long. As a result, when $NaNO_3$ is initially present in the solution, it is not possible to make a reasonably accurate extrapolation to E_{corr} using Tafel extrapolation in the anodic region (to obtain the i_{corr}), which is one of the limitations of the Tafel extrapolation method. Although finding such a sizeable linear region was difficult, we believe that it is still worth reporting the values of these so-called Tafel slopes (hereafter referred to simply as Tafel slopes) because they can provide valuable information. Tafel slopes will be used for a comparison study on the polarizability (how easily current density changes with change in potential).

When $NaNO_3$ was present, both the anodic and cathodic branches of the

polarization curves generally shifted to the right (higher current densities), and the potential of zero current ($E_{i=0}$) shifted to higher values.

The cathodic current increased with nitrate concentration, which can be explained using the Wagner-Traud equation. The Wagner-Traud equation is the sum of two Butler-Volmer equations for the metal oxidation and solution reduction half-reactions. This equation is often used for extracting a corrosion rate from the overall current observed as a function of E_{elec} during polarization. The underlying assumption of the application of this equation is that E_{corr} is sufficiently far away from both E_{ox}^{eq} and E_{red}^{eq}, which means E_{elec} is beyond the potentials where either reaction could be considered to be reversible.

$$i \approx i_{corr}.\left[\exp\left(\left(\alpha_{ox}\cdot\frac{n_{ox}F}{RT}\right)\cdot\eta_{corr}\right)-\exp\left(\left(-\alpha_{red}\cdot\left(\frac{n_{red}F}{RT}\right)\right)\cdot\eta_{corr}\right)\right] \qquad \textbf{(Eq. 4-24)}$$

where $\eta_{corr} = E_{elec} - E_{corr}$, n is the number of electrons, F is Faraday's constant (96485 C/mol), R is the gas constant (8.314 J/K.mol), and T is temperature (in Kelvin).

This is shown schematically in **Figure 4-6**. When two anodic reactions exist (e.g., metal M and metal N), the total cathodic rate would be the sum of both rates at a given potential (shown as the dashed line).

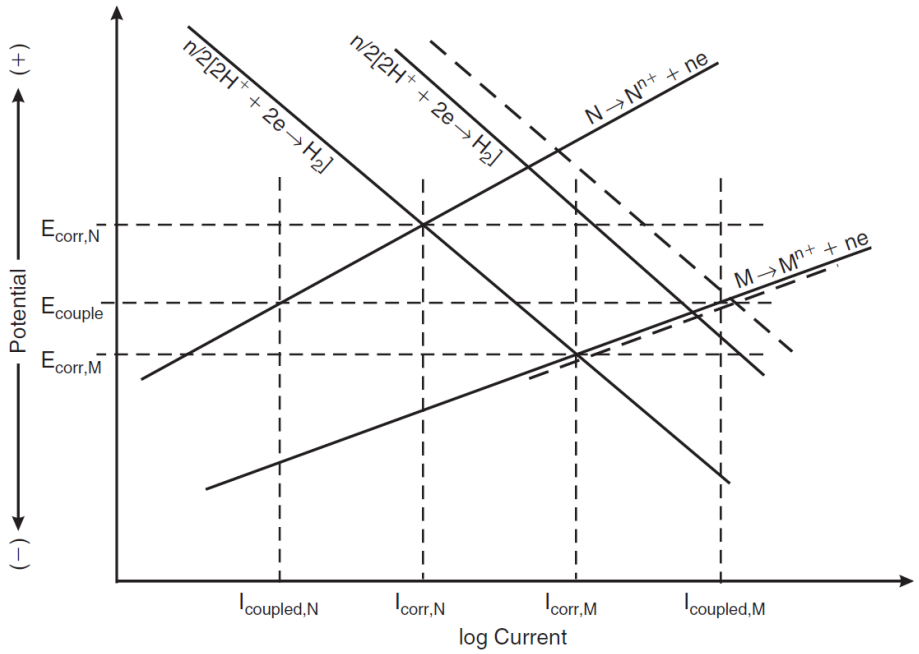

Figure 4-6: Evans diagram constructed from the oxidation reactions of metals M and N and two reduction reactions (dashed lines represent the sum of cathodic reactions and anodic reactions) [58] (reprinted with permission from Ref. [58], © 2004 Elsevier Ltd.)

The Wagner-Traud graph (identified by the dashed lines) could be constructed as the sum of the anodic and cathodic currents at each potential. It should be noted that the cathodic current is considered negative, and the anodic current is positive. At the E_{corr}, the sum of all cathodic rates equals those of anodic rates.

The cathodic current in blank (nitrate free) solution is due to water reduction. In the presence of nitrate ions, the current density increases significantly, indicating that nitrate is a good oxidant. In the presence of NO_3^- ions (assuming negligible contribution of oxygen reduction in the Ar-purged environment), the probable cathodic reactions are:

$$2\ H_2O + 2\ e^- \leftrightarrows 2\ OH^- + H_2 \qquad \textbf{(Eq. 4-25)}$$

$$NO_3^- + 2\,H^+ + 2\,e^- \leftrightarrows NO_2^- + H_2O \qquad \textbf{(Eq. 4-26)}$$

The measured current values in the potentiodynamic polarization graphs are the net current densities and contain both anodic and cathodic components.

$$i_{net} = \sum i_a + \sum i_c \qquad \textbf{(Eq. 4-27)}$$

For example, assuming the nitrate reduction reaction (n = 2 and $\alpha = 0.5$) to be the most effective reaction, the cathodic part of the W-T equation could be used to calculate the cathodic current density. For the solution containing 1 mM $NaNO_3$, the absolute value of the calculated current density was 7.9×10^{-3} A cm^{-2}, whereas the measured value in the potentiodynamic results was 2.3×10^{-5} A cm^{-2}. The main reason for the difference between the two values arises from the contribution of the oxidation reaction of Fe to Fe^{II}. Note that in this analysis, the contribution of water reduction and any metal cation reduction was ignored, and nitrate reduction reaction was considered to be the main reduction reaction.

One important observation was that as the concentration of the oxidants in the solution increased, and for a range of potential where nitrate reduction is theoretically possible, the net anodic current density increased with the concentration of nitrate. It was expected that an increase in the nitrate concentration would increase the cathodic current density, and if nitrate by itself had no effect on the anodic reaction, the net current density should have decreased for a given potential (constant anodic current and increase in the cathodic current). The reason for the increase in measured anodic current density in the potentiodynamic polarization measurements in the presence of nitrate is the increase in the ions' mobility, which directly depends on the ionic strength of the solution [132,159]

and increases with nitrate concentration. In a sodium nitrate solution, the ionic strength is equal to the molarity of the solution. As the nitrate concentration increases, the mass transfer rate increases, which results in a higher anodic current.

Increasing the nitrate concentration to 10 mM increased the anodic Tafel slope, while a further increase in the nitrate concentration from 10 mM to 1 M lowered the anodic slope.

Depending on the equilibrium potential of the nitrate to nitrite redox reaction and the effect of nitrate on the mass transport process, nitrate may affect the corrosion rate differently, which is discussed below.

In blank solution and 0.1 mM $NaNO_3$ solution, as explained earlier, the corrosion of CS in naturally corroding conditions had reached **Stage 2** after 8 h. This indicates that the concentration of Fe^{II} in the $Fe(OH)_2$ hydrogel was not sufficiently high to permit formation of Fe_3O_4. The anodic current is lowest in the blank solution. Note that the pH 6.0 blank solution is a low ionic strength solution compared to the other solutions tested in this chapter. The anodic Tafel slope is close to 2-e transfer, indicating that the process is under charge-transfer control. With a sufficiently high overpotential, accumulation of Fe^{II} at the interfacial region occurs, oxidation of Fe^{II} ® Fe_3O_4 occurs at higher overpotential, and the slope of E-log(i) increases, which will be discussed later.

For pH 6.0 buffered 1 mM $NaNO_3$, the slope was larger (0.111 V/decade) than for the blank. The E_{corr} measurements showed that corrosion had progressed to the second steady state after less than 1 h immersion (approaching the E_{eq} of Fe^{II} ® Fe_3O_4). When a small overpotential is applied, $Fe(OH)_2$ can reach saturation concentration in the interfacial solution, and charge transfer becomes limited by mass transfer of metal ions

via the formation of Fe_3O_4. Thus, while the corrosion progresses through the activation control region or is partially limited by mass transport of ions through a $Fe(OH)_2$ gel layer, the Tafel extrapolation showed a slope of 0.111 V/decade, which corresponds to close to 1-e^- charge transfer, which can be interpreted as the rate controlling step during corrosion of CS in 1 mM $NaNO_3$.

For higher nitrate concentrations (300 mM $NaNO_3$ and 1 M $NaNO_3$), the formation of $Fe(OH)_2$ occurs at a faster rate (in less than a second). Thus, in naturally corroding conditions, after 8 h of immersion, the corrosion had progressed to **Stage 3** (where the hydrogel layer is saturated with Fe^{II} and oxidation of Fe^{II} ® Fe_3O_4 may occur within it). However, the anodic Tafel slope was 0.076 V/decade in 300 mM and 0.072 V/decade in 1 M $NaNO_3$, which indicates a 2-electron charge transfer reaction. It was also observed that the anodic current densities in solutions with >10 mM $NaNO_3$ are almost one decade larger than those in lower $NaNO_3$ concentrations.

We can conclude that, although the interfacial region is saturated with Fe^{II} and the formation of Fe_3O_4 occurs at E_{corr}, under low positive overpotentials (in the Tafel region), the formation of Fe_3O_4 cannot limit the oxidation of Fe®Fe^{II} in such a high ionic strength medium. At sufficiently high overpotentials, the current densities were limited by the mass transfer of ions. The potential at which the current density reaches the mass transfer limit was higher in 10 mM $NaNO_3$ than that in 1 M $NaNO_3$. This indicates that, although the rate of charge transfer is faster in 1 M $NaNO_3$, supersaturation of iron at the surface can occur at a lower potential.

The values of E_{corr} and $E_{i=0}$ obtained after 8 h immersion of CS at pH 6.0 are plotted against [$NaNO_3$] in **Figure 4-7.**

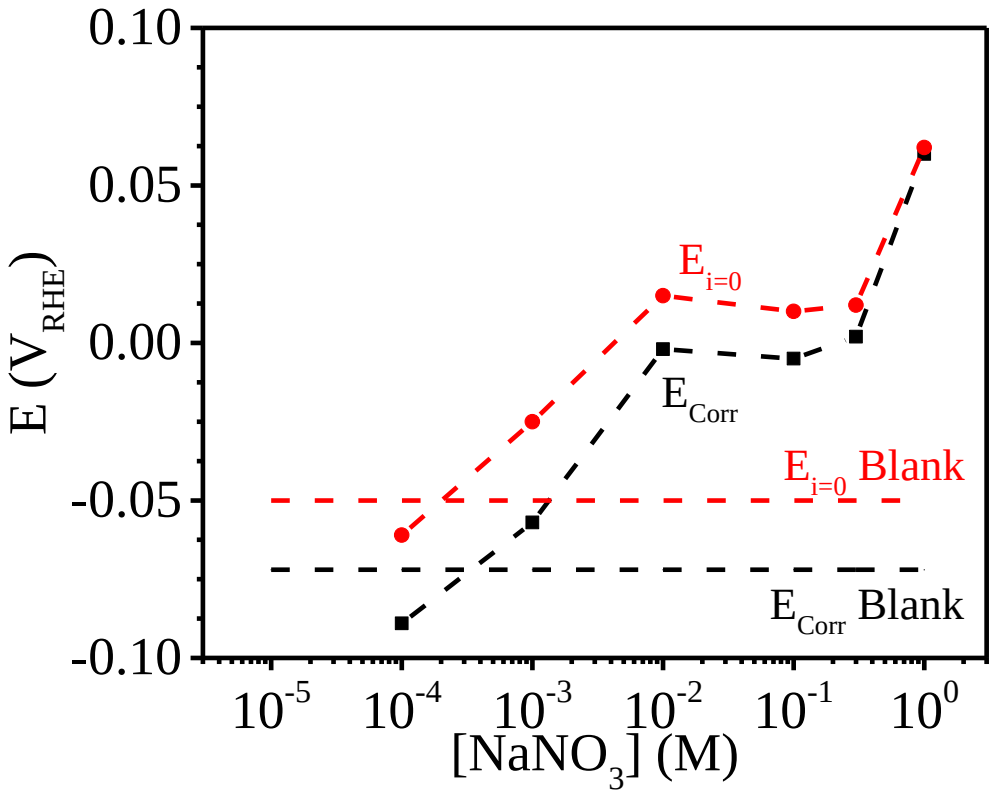

Figure 4-7: E_{corr} of CS in pH 6.0 $NaNO_3$ solutions as a function of [$NaNO_3$]. $E_{i=0}$ is the potential of zero current from potentiodynamic measurements after 8 h immersion, and E_{corr} is the E_{corr} after 8 h immersion.

As can be seen in **Figure 4-7**, the E_{corr} values after 8 h were generally lower than the $E_{i=0}$ values. This difference becomes smaller with nitrate addition, reaching almost zero in 1 M $NaNO_3$ solution. This observation could be explained based on the fact that the current density obtained from potentiodynamic polarization includes the charging process of the interfacial capacitance (i_{ct}) and Faradaic current (i_f) [20]; In a corrosion potential measurement experiment, the Faradaic current is zero. Thus, E_{corr} and $E_{i=0}$ (the potential at which anodic and cathodic current density is zero in the potentiodynamic experiment) could not be equal [20,59]. As stated before, addition of different concentrations of $NaNO_3$ increases the ionic strength of the solution (**Eq. 4-20**). It is also

well known that the relationship between ionic strength and interfacial capacitance thickness (δ_{dl}) is as follows [60–62]:

$$I_s \propto \delta_{dl}^{-0.5} \quad \textbf{(Eq. 4-28)}$$

Therefore, addition of $NaNO_3$ leads to a decrease in δ_{dl} and consequently, the difference between E_{corr} and $E_{i=0}$ decreases and becomes almost zero in the presence of 1 M $NaNO_3$. However, because in these sets of experiments the scan rate is low, the charging current should be very small, and so charging current is insufficient to explain this behaviour.

Later, we will see that in $Fe(NO_3)_3$ and HNO_3 solutions, the solubilities are high enough, even at lower concentrations of NO_3^-, for the values of E_{corr} and $E_{i=0}$ to be equal.

One important observation that can be also interpreted in relation to the change in the ionic strength in the presence of nitrate is the relationship between E_{corr} and log[$NaNO_3$]. For low [$NaNO_3$] (from 0.1 mM to 10 mM) the relationship between E_{corr} and log[$NaNO_3$] is linear with a slope of 0.04 V/decade. This increase is similar to the increase in equilibrium potential for the nitrate reduction redox reaction which shows a slope of 0.03 V/decade (**Eq. 4-29**). The similar slope for the increase in E_{corr} vs. log[$NaNO_3$] and that of the nitrate equilibrium potentials and nitrate concentration indicates that the main reason for the increase in corrosion potential is a change in the cathodic reaction and that the effect of ionic strength was small. After that, the E_{corr} remains constant for [$NaNO_3$] up to 300 mM, revealing that the E_{corr} is effectively independent of [$NaNO_3$], because the increase in the nitrate concentration affected the ionic strength and therefore the mass transfer. Thus, both anodic and cathodic reactions

were affected and there was no change in the corrosion potential. A further increase in [$NaNO_3$] to 1 M resulted in another linear increase with a slope of 23 mV/decade, resulting from the higher ionic strength and mass transport thus no longer being a limiting factor. The reduction reaction had the highest equilibrium potential and current density for this 1 M concentration of $NaNO_3$.

In order to further investigate the effect of nitrate, the potential was scanned up to 0.8 V_{RHE}. The PD curves are shown in **Figure 4-8.**

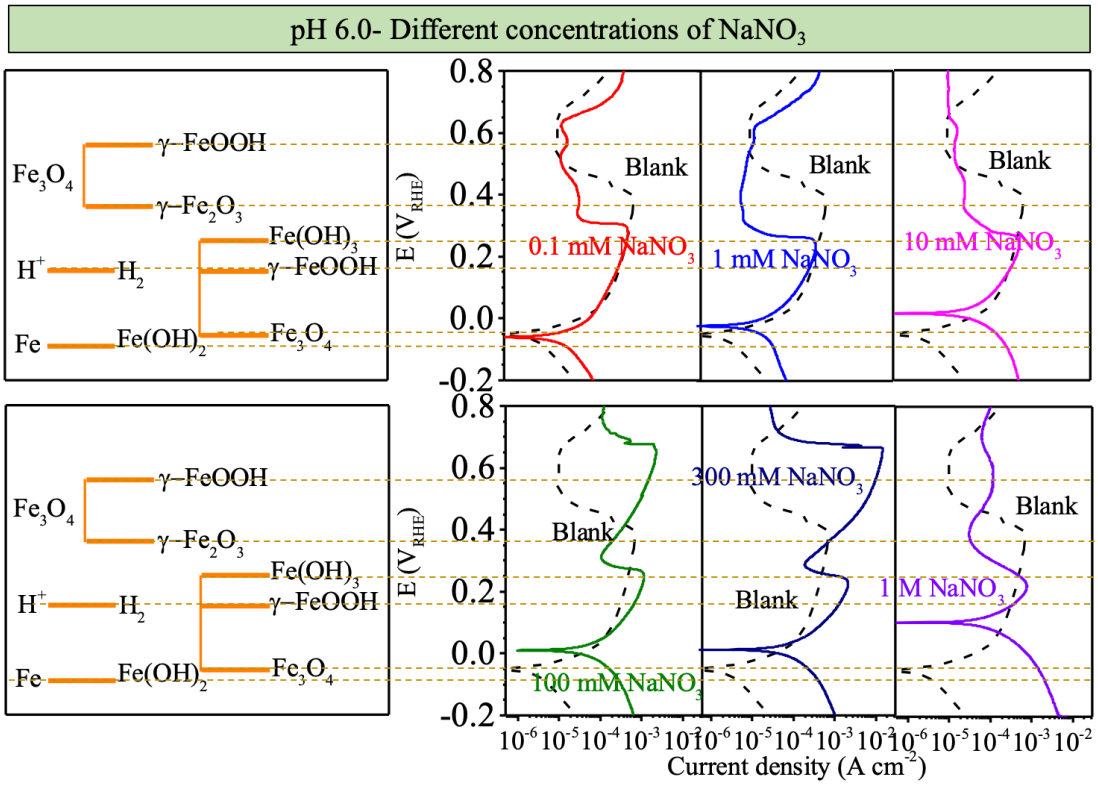

Figure 4-8: Potentiodynamic polarization curves for CS in pH 6.0 $NaNO_3$ solutions. The potential range was -0.2 V_{RHE} to 0.8 V_{RHE}.

In all solutions, when the potential was scanned toward positive potetials, above the E_{corr}, current density increased with increase in potential. This increase was followed by a sudden drop occurring at $E_{appl} > E^{eq}_{Fe_3O_4 \leftrightarrows \gamma-FeOOH}$ for blank solution, and

$E^{eq}_{Fe(OH)_2 \leftrightarrows Fe(OH)_3} < E_{appl} < E^{eq}_{Fe_3O_4 \leftrightarrows \gamma-FeOOH}$ for nitrate solutions. The potential at which this drop was observed was lower for higher concentrations of $NaNO_3$, while the maximum current density (the peak current) increased with nitrate concentration, with the exception being for [$NaNO_3$] = 1 M.

Over the 8 h of E_{corr} measurement, the [Fe^{II}] in the hydrogel in the interfacial region increases. In blank solution, the [Fe^{II}] near the interface during the E_{corr} measurement remains below $E^{eq}_{Fe \leftrightarrows Fe(OH)_2}$ indicating that the $Fe(OH)_2$ hydrogel layer was not saturated with Fe^{II}. During forward scanning to higher potentials, the solution near the surface becomes saturated with Fe^{II}, and $Fe^{II} \rightarrow Fe_3O_4$ oxidation occurs within the hydroxide layer, which finally results in a drop in the current density at about 0.4 V_{RHE}. When nitrate is present, Fe_3O_4 formation is fast, and the peak current is observed at a lower potential than in the blank solution. The greater the [$NaNO_3$], the higher the rate of Fe_3O_4 formation within the gelatinous hydroxide layer and the lower the potential of peak current density. Although Fe_3O_4 formation resulted in a drop in current, in 100 mM and 300 mM $NaNO_3$, at sufficiently high overpotentials (immediately above the current drop), the current density started to increase and continued to increase. This indicates that the oxide formed at about 0.2 V_{RHE} is not protective. Thus, the oxidation can continue at higher potentials through the oxide layer until the current decreases, at about 0.7 V_{RHE}, due to the formation of a protective layer such as Fe_2O_3. In 1 M $NaNO_3$, the formation of a sufficiently thick Fe_3O_4 prevents oxidation at higher overpotentials.

4.3.2.2 Potentiodynamic Polarization Behaviour in $Fe(NO_3)_3$ Solutions

To investigate the corrosion behaviour of CS in nitrate solutions, $Fe(NO_3)_3$ solution was used instead of $NaNO_3$. The results of the E_{corr} measurements and PD

experiments are shown in **Figure 4-9**. The Tafel slopes and other corrosion parameters are shown in **Figure 4-10** and are given in **Table 4-5.**

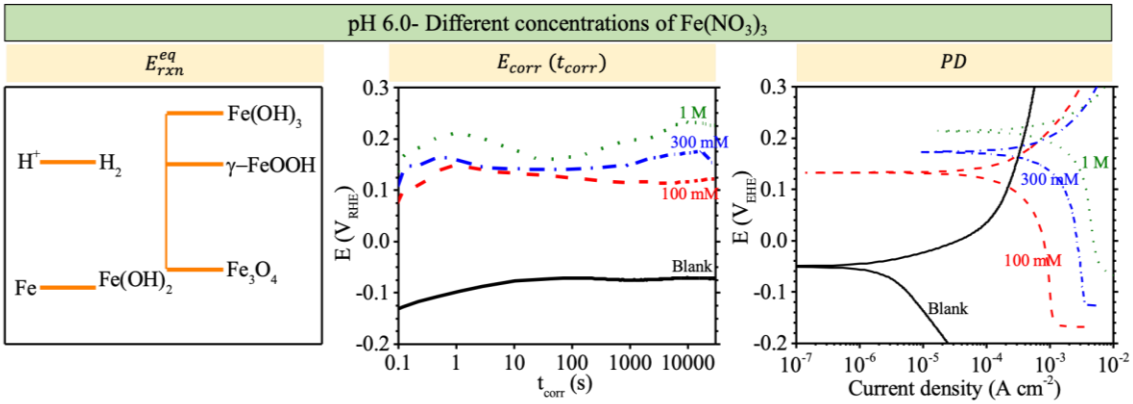

Figure 4-9: E_{corr} of CS as a function of t_{corr} (log scale) in pH 6.0 buffered solution, in the presence of different concentrations of ferric nitrate, taken immediately after cathodic cleaning, and potentiodynamic polarization measurements for different concentrations of $Fe(NO_3)_3$ taken after 8 h of immersion. The equilibrium potentials of reactions potentially involved are shown in the left panel.

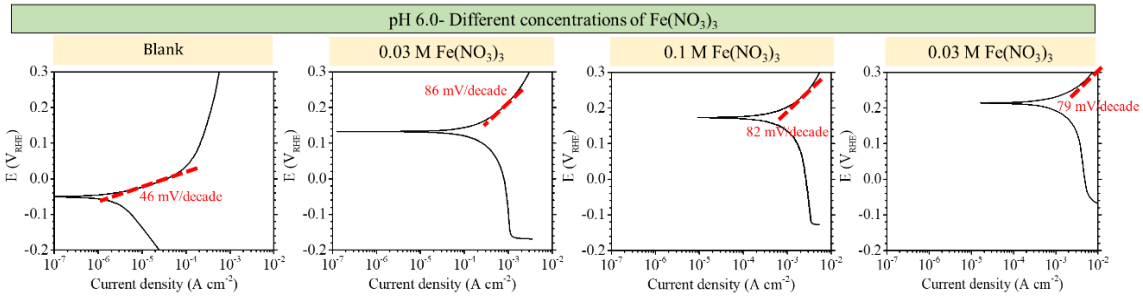

Figure 4-10: Potentiodynamic polarization measurements for CS in $Fe(NO_3)_3$ at pH 6.0.

Table 4-5: The values of $E_{i=0}$, Tafel slopes, and i_{corr} of CS in $Fe(NO_3)_3$ solutions of pH 6.0, obtained from the PD experiments presented in Figure 4-10.

$[NO_3^-]$ (mM)	Blank	100	300	1000
$E_{i=0}$ (V_{RHE})	-50	0.133	139	214
b_a (mV/decade)	46	86	82	79
$\|b_c\|$ (mV/decade)	118	112	134	115
$i_{corr,a}$ (μA cm^{-2})	2.9	130.0	314.0	840.0
$i_{corr,b}$ (μA cm^{-2})	2.1	130.0	360.0	780.0
i_{corr} (μA cm^{-2})	2.3	130.0	340.0	800.0

The key observations from the experiments in $Fe(NO_3)_3$ are as follows:

- Immediately after cathodic cleaning, the E_{corr} values in in the presence of 100 mM $Fe(NO_3)_3$ were 0.075V_{RHE} to 0.225 V_{RHE}. The E_{corr} values remained almost constant with time during 8 h immersion, except for fluctuations of about 50 mV. A further increase in $Fe(NO_3)_3$ concentration (0.1 M and 0.3 M $Fe(NO_3)_3$) resulted in a slight increase in E_{corr}. The initial E_{corr} in the presence of $Fe(NO_3)_3$ was slightly below $E^{eq}_{Fe(OH)_2 \leftrightarrows \gamma-FeOOH}$.
- Ferric nitrate shifted the polarization curves to higher current densities. The higher the concentration of $Fe(NO_3)_3$ was, the higher the corresponding cathodic current density. In $Fe(NO_3)_3$ solutions, cathodic Tafel slopes were about 115-140 mV/decade, close to those obtained for the blank solution. The current densities were almost constant, with potentials at negative overpotentials greater than 100 mV in $Fe(NO_3)_3$ solutions. The diffusion-controlled cathodic current density increased from 10^{-3} A cm^{-2} to $5´10^{-3}$ A cm^{-2} when the concentration of $Fe(NO_3)_3$ was increased from 0.03 to 0.3 M.

The anodic Tafel slope was about 80-85 mV/decade, and the anodic branch was shifted to higher current densities in the presence of $Fe(NO_3)_3$.

Ferric ion is a strong oxidant, and the large cathodic current in the presence of ferric nitrate is due to the reduction of Fe^{3+}. Because the reduction of Fe^{3+} happens at the carbon steel surface, it requires the mass transfer of Fe^{3+} cations from the solution phase toward the surface. Thus, the cathodic current could be controlled by diffusion of Fe^{3+} cations to the CS surface and remains almost constant at sufficiently negative overpotentials (about 100 mV below the $E_{i=0}$).

Although the high reduction rate of ferric ions explains the high cathodic current and the high E_{corr} values in $Fe(NO_3)_3$ solutions, the high anodic current densities and larger Tafel slopes in $Fe(NO_3)_3$ solutions require more detailed analysis. In order to investigate the anodic behaviour of CS in nitrate solutions, the PD results in a broader range of applied potentials (from -0.2 V_{RHE} to 1 V_{RHE}) in $Fe(NO_3)_3$ and in $NaNO_3$ solutions were evaluated. As shown in **Figure 4-11**, in Fe^{3+}-containing solution the cathodic current increased, with slopes of about 0.110 V/decade to 0.135 V/decade which indicates that the reaction was predominantly a single electron transfer reaction, up to a sufficiently high potential at which the current density is under complete mass transfer control.

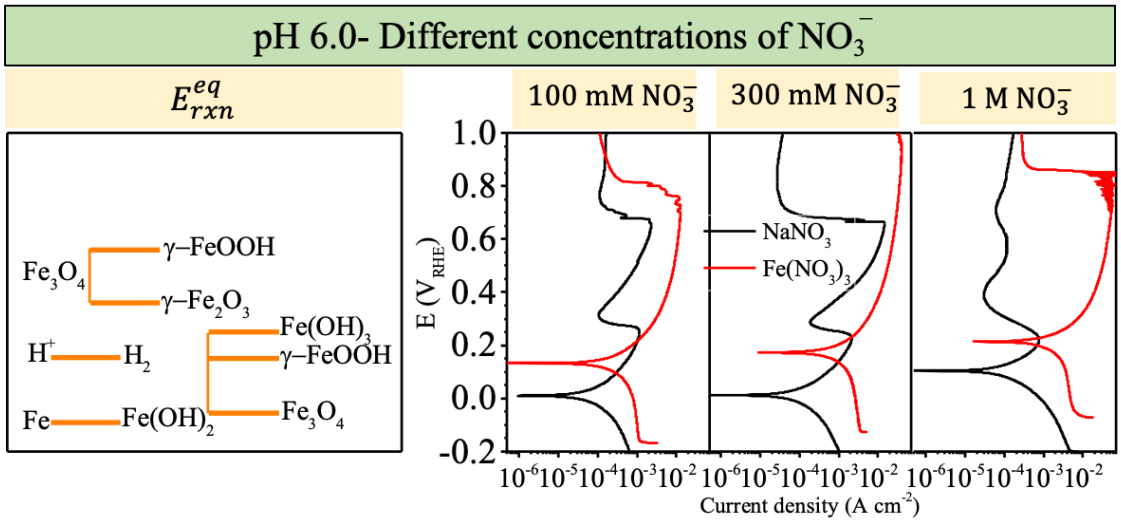

Figure 4-11: Potentiodynamic curves for CS in the presence of different NO_3^- solutions of pH 6.0.

It can be clearly seen in **Figure 4-11** that the drop in current density at about 0.3 V_{RHE}, which corresponds to the formation of a protective Fe_3O_4 oxide, was not observed in $Fe(NO_3)_3$ solutions. The maximum current density (the current density at

which the current is under complete mass transfer control) increased with [$Fe(NO_3)_3$]. The potential at which the current density reached its maximum was higher in 0.3 M than in 0.1 M $Fe(NO_3)_3$, whereas it was lower in 1 M than in 0.3 M. In all $Fe(NO_3)_3$ solutions, the current density dropped suddenly at slightly above the potential at which the maximum current was reached.

The solubility of $Fe^{2+}$and the ionic strength increase with [$Fe(NO_3)_3$]; thus, the solubility limit at which the rate of mass transfer of metal ions from the interfacial region becomes rate-controlling increases with [$Fe(NO_3)_3$]. Although the maximum current was higher in 1 M $Fe(NO_3)_3$ than observed in 300 mM $Fe(NO_3)_3$, the maximum current was reached at a lower potential. The supersaturation of the interfacial region with Fe^{II} ions results in a current drop at a lower potential than in 300 mM $Fe(NO_3)_3$, which could be due to the formation of a thick oxide.

These electrochemical studies in the presence of $Fe(NO_3)_3$ have revealed the significance of Fe^{III} cations for CS corrosion and their impact on the rate of the reactions. It should be noted that the electrochemical tests in this chapter were conducted in a large solution volume. However, in small solution volumes, where the surface area to solution volume ratio is large, the presence of oxidative agents like NO_3^- could lead to Fe^{III} cations building up in the interfacial region and the oxidative role of the ferric ions becoming important. Moreover, previous studies [37,63] have revealed that under radiation, the corrosion potential resides in a range of potentials where formation of Fe^{III} is possible. These observations will be presented in the coming chapters.

4.4 SUMMARY

In this chapter, the effect of NO_3^- ions on the corrosion of CS in Ar-purged pH 6.0 buffered $NaNO_3$ and $Fe(NO_3)_3$ solutions was studied using electrochemical techniques. This work provides new insights into the effect of NO_3^- ions on the corrosion behaviour of CS and discusses the limitations of the use of the Tafel method in corrosion rate determinations. It also provides a basis for studying CS corrosion in small volume solutions (discussed in **Chapter 7**) and when γ-radiation is present (**Chapter 8**).

Depending on the concentration of nitrate and ionic strength, nitrate can affect the dynamics of corrosion by either accelerating the rate of iron oxidation via NO_3^-/NO_2^- reduction reaction, or by influencing the rate of mass transport of metal ions.

The increase in the cathodic current densities with [$NaNO_3$] is due to the increase in the equilibrium potential of the nitrate reduction reaction with increase in nitrate concentration. The general increase in the anodic current was explained based on the increase in the mobility of ions, which depends directly on the ionic strength of the solution, which increases with [$NaNO_3$]. Mass transport of ions is faster for higher concentrations of nitrate; thus, in the presence of higher concentrations of $NaNO_3$ the polarizability of CS is increased. An increase in nitrate concentration up to 10 mM increased the anodic Tafel slope, while a further increase in the nitrate concentration from 10 mM to 1 M lowered the anodic slope. During PD tests (forward scanning of potential) in $NaNO_3$ solutions, the solution in the interfacial region becomes saturated at a different rate. In low concentrations of nitrate (0.1 mM), the rate of oxidation of iron, and the ionic strength of the solution are only slightly higher than in the blank. Thus, the time at which the interfacial solution becomes saturated with Fe^{II} is similar to what is observed in the

blank solution. When the $Fe(OH)_2$ hydrogel layer has become saturated with Fe^{II} (**Stage 2**), the NO_3^-/NO_2^- redox reaction can effectively couple with Fe^{II}/Fe^{III} oxidation in the hydrogel and corrosion progresses to **Stage 3** where oxide formation occurs. Because of the low rate of the oxidation of $Fe \rightarrow Fe^{II}$, scanning toward positive potentials cannot result in a fast saturation of $Fe(OH)_2$ in the interfacial region during scanning. Thus, mass transfer does not become rate-controlling at low overpotentials (within the anodic Tafel region) and the slope indicates 2-e charge transfer. With a sufficiently high overpotential, accumulation of Fe^{II} occurred, and the oxidation of Fe^{II} ® Fe_3O_4 increased the slope of E-log(i). When the buffered solution had an intermediate $NaNO_3$ concentration (1 mM $NaNO_3$), the anodic current slope was about 0.111 V/decade, and the anodic current was high at E_{appl} slightly above E_{corr}, indicating that saturation of $Fe(OH)_2$ layer followed by the formation of magnetite can occur under a small overpotential. This high current and formation of magnetite results in mass transfer of ions through the oxide layer. Thus, the anodic branch will be controlled by mass transfer. Although mass transfer becomes rate controlling in intermediate nitrate concentrations, the high ionic strength of the solution provides a fast mass transfer rate that results in an overall increase in the current density. In the presence of sufficiently high nitrate concentrations (above 300 mM with higher equilibrium potential for the nitrate/nitrite reaction), the formation of $Fe(OH)_2$ occurs at a faster rate. Thus, in naturally corroding conditions, corrosion progresses to **Stage 3** (where the hydrogel layer is saturated with Fe^{II} and oxidation of $Fe^{II} \rightarrow Fe_3O_4$ occurs within the $Fe(OH)_2$ hydrogel) in less than one second. However, the anodic Tafel slope indicated a 2-electron charge transfer reaction. It was also observed that the anodic current densities in solutions with >10 mM $NaNO_3$ are almost one decade higher than

those in low and intermediate $NaNO_3$ concentrations. We can conclude that, although the interfacial region is saturated with Fe^{II} and the formation of Fe_3O_4 occurs at E_{corr} and under low positive overpotentials (in the Tafel region), the formation of Fe_3O_4 cannot limit the oxidation of Fe®Fe^{II} in such a high ionic strength medium in low overpotentials (in the Tafel region). At sufficiently high overpotentials, the current densities were limited by mass transfer of ions. The potential at which the current density reaches the mass transfer limit was higher in 10 mM $NaNO_3$ than that in 1 M $NaNO_3$. This indicates that, although the rate of charge transfer is faster in 1 M $NaNO_3$, the supersaturation of iron at the surface can occur at a lower potential.

Ferric ion is a strong oxidant, and the large cathodic current observed in the presence of ferric nitrate was due to the Fe^{3+}/Fe^{2+}reduction reaction. The results indicated that the current densities are under charge transfer control up to sufficiently high overpotentials at which current density undergoes mass transfer control. The ionic strength increases with [$Fe(NO_3)_3$]; thus, the solubility limit of Fe^{2+} at which the rate of mass transfer of metal ions from the interfacial region becomes rate-controlling increases with [$Fe(NO_3)_3$]. Although, the maximum measured anodic current increased with [$Fe(NO_3)_3$], it was reached at a lower overpotential. The electrochemical analysis in the presence of $Fe(NO_3)_3$ revealed the importance of Fe^{III} as a strong oxidant, and how it may influence the oxide on the surface and the rate of the reactions. Understanding the effect of the presence of Fe^{III} in the solution is particularly important when it is taken into account that in limited solution volumes (discussed in **Chapter 7**) and in the presence of radiation (**Chapter 8**) conditions are favourable for Fe^{III} formation.

4.5 REFERENCES

[1] B. Cottis, M. Graham, R. Lindsay, S. Lyon, T. Richardson, D. Scantlebury, S. Howard, eds., Shreir's Corrosion, Elsevier, 2010.

[2] T. Islam, H.M.M.A. Rashed, Classification and Application of Plain Carbon Steels, in: Ref. Modul. Mater. Sci. Mater. Eng., Elsevier, 2019.

[3] J.C. Wren, Steady-State Radiolysis: Effects of Dissolved Additives, in: C.M. Wai1, B.J. Mincher (Eds.), Nucl. Energy Environ., American Chemical Society, 2010: pp. 271–295.

[4] J.W.T. Spinks, R.J. Woods, An introduction to radiation chemistry, John Wiley and Sons Inc, United States, 1990.

[5] Y.G. Shin, Nonlinear Dynamics of Carbon Steel Corrosion under Gamma Radiation, PhD Thesis, The University of Western Ontario, 2020.

[6] M. Naghizadeh, Copper Corrosion Dynamics under Deep Geologic Repository Conditions, PhD Thesis, The University of Western Ontario, 2021.

[7] P.A. Yakabuskie, The Influence of Long-Term Gamma-Radiation and Initially Dissolved Chemicals on Aqueous Kinetics and Interfacial Processes, The University of Western Ontario, 2015.

[8] M. Behazin, Radiation Induced Corrosion of Stellite-6, The University of Western Ontario, 2014.

[9] R. Karimihaghighi, Non-Linear Effects of Solution Parameters and Gamma Radiation on Nickel Oxidation Dynamics, PhD Thesis, The University of Western Ontario, 2021.

[10] R.P. Morco, Gamma-Radiolysis Kinetics and Its Role in the Overall Dynamics of Materials Degradation, PhD Thesis, The University of Western Ontario, 2020.

[11] Farhataziz, M.A.J. Rodgers, eds., Radiation chemistry: principles and applications, VCH Publishers, United States, 1987.

[12] C.J. Hochanadel, Effects Of Cobalt γ-Radiation On Water And Aqueous Solutions, J. Phys. Chem. 56 (1952) 587–594.

[13] J.H. O'Donnell, D.F. Sangster, Principles of Radiation Chemistry, American Elsevier Publishing Company, 1970.

[14] X. Zhang, W. Xu, D.W. Shoesmith, J.C. Wren, Kinetics of H_2O_2 reaction with oxide films on carbon steel, Corros. Sci. 49 (2007) 4553–4567.

[15] B. Pastina, J. Isabey, B. Hickel, The influence of water chemistry on the radiolysis of the primary coolant water in pressurized water reactors, J. Nucl. Mater. 264 (1999) 309–318.

[16] F. Scenini, R.C. Newman, R.A. Cottis, R.J. Jacko, Effect of Surface Preparation on Intergranular Stress Corrosion Cracking of Alloy 600 in Hydrogenated Steam, Corrosion. 64 (2008) 824–835.

[17] I. Štefanić, J.A. LaVerne, Temperature Dependence of the Hydrogen Peroxide Production in the γ-Radiolysis of Water, J. Phys. Chem. A. 106 (2002) 447–452.

[18] B. Pastina, J.A. LaVerne, Effect of Molecular Hydrogen on Hydrogen Peroxide in Water Radiolysis, J. Phys. Chem. A. 105 (2001) 9316–9322.

[19] P.A. Yakabuskie, J.M. Joseph, C.R. Stuart, J.C. Wren, Long-Term γ-Radiolysis Kinetics of NO_3^- and NO_2^- Solutions, J. Phys. Chem. A. 115 (2011) 4270–4278.

[20] A.J. Bard, L.R. Faulkner, Electrochemical Methods: Fundamentals and Applications, 2nd Edition | Wiley, Wiley, New York. (2000) 864.

[21] V.S. Bagotsky, Fundamentals of electrochemistry, 2nd ed., John Wiley & Sons, Inc, 2006.

[22] J.C. Wren, J. Ball, LIRIC 3.2 an updated model for iodine behaviour in the presence of organic impurities, Radiat. Phys. Chem. 60 (2001) 577–596.

[23] J.M. Joseph, B.S. Choi, P. Yakabuskie, J.C. Wren, A combined experimental and model analysis on the effect of pH and O_2(aq) on γ-radiolytically produced H_2 and H_2O_2, Radiat. Phys. Chem. 77 (2008) 1009–1020.

[24] R.P. Morco, J.M. Joseph, D.S. Hall, C. Medri, D.W. Shoesmith, J.C. Wren, Modelling of radiolytic production of HNO_3 relevant to corrosion of a used fuel container in deep geologic repository environments, Corros. Eng. Sci. Technol. 52 (2017) 141–147.

[25] P. Driver, G. Glowa, J.C. Wren, Steady-state γ-radiolysis of aqueous methyl ethyl ketone (2-butanone) under postulated nuclear reactor accident conditions, Radiat. Phys. Chem. 57 (2000) 37–51.

[26] J.C. Wren, G.A. Glowa, A simplified kinetic model for the degradation of 2-butanone in aerated aqueous solutions under steady-state gamma-radiolysis, Radiat. Phys. Chem. 58 (2000) 341–356.

[27] P.A. Yakabuskie, J.M. Joseph, P. Keech, G.A. Botton, D. Guzonas, J.C. Wren, Iron oxyhydroxide colloid formation by gamma-radiolysis, Phys. Chem. Chem. Phys. 13 (2011) 7198–7206.

[28] W. Xu, K. Daub, X. Zhang, J.J. Noel, D.W. Shoesmith, J.C. Wren, Oxide formation and conversion on carbon steel in mildly basic solutions, Electrochim. Acta. 54 (2009) 5727–5738.

[29] L. Wu, D. Guo, M. Li, J.M. Joseph, J.J. Noël, P.G. Keech, J.C. Wren, Inverse Crevice Corrosion of Carbon Steel: Effect of Solution Volume to Surface Area, J. Electrochem. Soc. 164 (2017) C539–C553.

[30] K. Daub, A Study of Gamma Radiation Induced Carbon Steel Corrosion, PhD Thesis, The University of Western Ontario, 2013.

[31] Q.W. Knapp, J.C. Wren, Film formation on type-316L stainless steel as a function of potential: Probing the role of gamma-radiation, Electrochim. Acta. 80 (2012) 90–99.

[32] K. Daub, X. Zhang, J.J. Noël, J.C. Wren, Effects of γ-radiation versus H_2O_2 on carbon steel corrosion, Electrochim. Acta. 55 (2010) 2767–2776.

[33] D. Guo, Corrosion Dynamics of Carbon Steel in Used Fuel Container Environments, PhD Thesis, The University of Western University, 2018.

[34] R.P. Morco, A.Y. Musa, M. Momeni, J.C. Wren, Corrosion of carbon steel in the [P14666][Br] ionic liquid: The effects of γ-radiation and cover gas, Corros. Sci. 102 (2016) 1–15.

[35] K. Daub, X. Zhang, J.J. Noël, J.C. Wren, Gamma-radiation-induced corrosion of carbon steel in neutral and mildly basic water at 150 °C, Corros. Sci. 53 (2011) 11–16.

[36] G. van Weert, Y. Shang, Iron control in nitrate hydrometallurgy by (auto) decomposition of iron (II) nitrate, Hydrometallurgy. 33 (1993) 255–271.

[37] M. Li, Galvanic Corrosion of Carbon Steel-Stainless Steel Welds, PhD Thesis, The University of Western Ontario, 2020.

[38] M. Bahrami, Effects of Solution pH, Temperature and Redox Environment on Corrosion and Oxide Formation on Inconel X-750, PhD Thesis, The University of Western Ontario, 2021.

[39] W. Davison, G. Seed, The kinetics of the oxidation of ferrous iron in synthetic and natural waters, Geochim. Cosmochim. Acta. 47 (1983) 67–79.

[40] W. Stumm, G.F. Lee1, Oxygenation of Ferrous Iron, Ind. Eng. Chem. 53 (2002) 143–146.

[41] A.R. Ahmad, Coupled diffusion and oxidation of ferrous iron in soils. I. Kinetics of oxygenation of ferrous iron in soil suspension, 1990.

[42] E. McCafferty, Introduction to corrosion science, Springer, New York, 2010.

[43] D. Guo, M. Li, J.M. Joseph, J.C. Wren, A New Method for Corrosion Current Measurement: the Dual-Electrochemical Cell (DEC), J. Electrochem. Soc. 167 (2020) 111505.

[44] N. Perez, Electrochemistry and Corrosion Science, 1st ed., KluwerAcademic Publishers, Boston, 2004.

[45] A.Y. Musa, J.C. Wren, Combined effect of gamma-radiation and pH on corrosion of Ni-Cr-Fe alloy inconel 600, Corros. Sci. 109 (2016) 1–12.

[46] B. Beverskog, I. Puigdomenech, Revised Pourbaix diagrams for iron at 25-300°C, Corros. Sci. 38 (1996) 2121–2135.

[47] A. Anderko, P. McKenzie, R.D. Young, Computation of Rates of General Corrosion Using Electrochemical and Thermodynamic Models, Corrosion. 57 (2001) 202–213.

[48] G.E. Dima, A.C.A. De Vooys, M.T.M. Koper, Electrocatalytic reduction of nitrate at low concentration on coinage and transition-metal electrodes in acid solutions, J. Electroanal. Chem. 554–555 (2003) 15–23.

[49] J.C. Fanning, The chemical reduction of nitrate in aqueous solution, Coord. Chem. Rev. 199 (2000) 159–179.

[50] C.F. Baes Jr., R.E. Mesmer, The Hydrolysis of Cations, John Wiley & Sons, Inc, 1976.

[51] P. Taylor, Ostwald ripening in emulsions, Adv. Colloid Interface Sci. 75 (1998) 107–163.

[52] J.H. Yao, K.R. Elder, H. Guo, M. Grant, Theory and simulation of Ostwald ripening, Phys. Rev. 47 (1993) 14110–14125.

[53] J.E. Saiers, G.M. Hornberger, The influence of ionic strength on the facilitated transport of cesium by kaolinite colloids, Water Resour. Res. 35 (1999) 1713–1727.

[54] J.E. Saiers, J.J. Lenhart, Ionic-strength effects on colloid transport and interfacial reactions in partially saturated porous media, Water Resour. Res. 39 (2003) 1256.

[55] H. Strathmann, Electromembrane Processes: Basic Aspects and Applications, Compr. Membr. Sci. Eng. 2 (2010) 391–429.

[56] C. Lefrou, R.P. Nogueira, F. Huet, H. Takenouti, Electrochemistry, in: Shreir's Corros., Elsevier, 2010: pp. 13–51.

[57] R.A. Buchanan, E.E. Stansbury, Electrochemical Corrosion, in: M. Kutz (Ed.), Handb. Environ. Degrad. Mater. Second Ed., Elsevier Inc., 2012: pp. 87–125.

[58] J.C. Earthman, Corrosion, in: W.F. Gale, T.C. Totemeier (Eds.), Smithells Met. Ref. Book, 8th Ed., Butterworth-Heinemann, 2004: pp. 31.1-31.13.

[59] X.L. Zhang, Z.H. Jiang, Z.P. Yao, Y. Song, Z.D. Wu, Effects of scan rate on the potentiodynamic polarization curve obtained to determine the Tafel slopes and corrosion current density, Corros. Sci. 51 (2009) 581–587.

[60] A. Persat, R.D. Chambers, J.G. Santiago, Basic principles of electrolyte chemistry for microfluidic electrokinetics. Part I: Acid–base equilibria and pH buffers, Lab Chip. 9 (2009) 2437–2453.

[61] M. Semmler, E.K. Mann, J. Rička, M. Borkovec, Diffusional Deposition of Charged Latex Particles on Water−Solid Interfaces at Low Ionic Strength, Langmuir. 14 (1998) 5127–5132.

[62] Y. Liu, Z. Zhang, N. Bhandari, Z. Dai, F. Yan, G. Ruan, A.Y. Lu, G. Deng, F. Zhang, H. Al-Saiari, A.T. Kan, M.B. Tomson, New Approach to Study Iron Sulfide Precipitation Kinetics, Solubility, and Phase Transformation, Ind. Eng. Chem. Res. 56 (2017) 9016–9027.

[63] K. Daub, X. Zhang, J.J. Noël, J.C. Wren, Gamma Radiation-Induced Carbon Steel Corrosion, ECS Trans. 33 (2011) 15–24.

CHAPTER 5
CORROSION BEHAVIOUR OF CARBON STEEL AND STAINLESS STEELS IN NITRIC ACID SOLUTIONS

5.1 INTRODUCTION

A leak in the end shield cooling (ESC) system in Ontario Power Generation's Pickering Unit 6 nuclear reactor was subjected to an investigation. The potential issue is that the moisture from this leak could reach a location in the annular air gap, which exists around the periphery of the calandria tank assembly and its supporting structures. This region consists of two dissimilar metals (carbon steel and 304L SS), welded together using 309 SS (as the filler material). Corrosion in this region, and in particular, accelerated (galvanic) corrosion, would be problematic and needs careful evaluation.

The pH of the ESC water is 10.4, but when it condenses onto the weld region, the pH is expected to change, altering the dissolution rate. In addition, the weld is close to the reactor core and exposed to gamma radiation. The radiolysis kinetics of liquid water have been well studied using a water radiolysis model (WRM) [1–7] and validated using

experimental data as a function of pH, temperature, and initial concentrations of dissolved O_2 and nitrate. The radiolysis of humid air will produce both HNO_3 and H_2O_2, two oxidizing species [8–10], resulting in corrosive conditions in the weld region. The kinetics of charge transfer and mass transfer reactions can change considerably with not only the concentrations of redox-active species present, but also the solution ionic strength [11]. Nitric acid produced in humid air can dissolve in any condensed water and lower its pH. This can affect the solubility of metal cations produced by metal oxidation. This factor, as well as possible changes in the oxidation rate, can affect the rate of corrosion [8–10,12–16].

The effect of nitrate ions on the corrosion of carbon steel in pH 6.0 buffered solution was investigated in **Chapter 4**. The results show that depending on the concentration of nitrate and ionic strength, nitrate affects the corrosion dynamics of carbon steel by either accelerating the metal oxidation rate via NO_3^- acting as an oxidant, or by influencing the rate of mass transport of metal ions.

This chapter investigates the corrosion behaviour of carbon steel and stainless steels (304L SS and 309 SS) in nitric acid solutions. The electrochemical behaviour of CS and SS (304L SS and 309 SS) was studied in nitric acid solution using E_{corr} measurements, linear polarization (LPR) and potentiodynamic polarization (PD) tests. Solution studies were also performed using ICP-OES on the solution collected during E_{corr} measurement experiments to correlate the rates of corrosion and the rates of dissolution of iron and other elements.

5.2 EXPERIMENTAL PROCEDURES

5.2.1 Sample and Solution Preparation

The working electrodes used in this study were CS A36 (provided by Ontario Power Generation Inc. (OPG)), 304L SS and 309 SS (provided by Goodfellow). Their compositions are given in **Table 5-1**.

Table 5-1: Chemical composition of CS 36A, 304L SS, and 309 SS (in wt.%).

Material	Cr	Ni	C	Mn	Mo	Si	S	P	Fe
CS A36	0.16	0.23	0.15	0.84	0.03	0.24	0.03	0.02	bal.
SS 304L	18.8	8.2	0.02	2	-	0.35	0.003	0.02	bal.
SS 309	24	14	0.03	1.2	0.1	0.63	0.005	0.02	bal.

Prior to each test, the coupon was ground manually with a series of silicon carbide papers (100, 320, 400, 800 and 1200, and 2500 grit). This was followed by polishing on a Texmet microcloth (Buehler) with a 1 μm MetaDi Supreme diamond paste suspension (Buehler) and lastly sonication in an acetone/methanol mixture for 5 min to remove polishing residues. The polished coupons were then rinsed with Type I water and dried in flowing argon.

All solutions were prepared with water purified with a NANO pure Diamond UV ultrapure water system (Barnstead International) to give a resistivity of 18.2 MΩ.cm. Sodium nitrate (Sigma Aldrich) and nitric acid (Fisher Chemical) were used to prepare nitrate solutions. The electrochemical analyses and solution measurements presented in this chapter were performed in 10 mM NO_3^- (10 mM HNO_3) and also in 100 mM NO_3^-

(10 mM HNO_3 + 90 mM $NaNO_3$) solutions at pH 2.0. The pH of the solution was measured using an Accumet® Basic AB15 pH meter with a saturated calomel electrode (SCE).

5.2.2 Electrochemical Tests

E_{corr} measurements, linear polarization resistance (LPR), and potentiodynamic polarization (PD) measurements were carried out in order to study the corrosion behaviour of CS and stainless steels in acidic nitrate solutions. These electrochemical tests were performed using a three-compartment cell using a saturated calomel electrode (SCE, Fisher Scientific) as the reference electrode and a platinum mesh as the counter electrode. The CS or SS (304L SS and 309 SS) coupons were used as the working electrode. All electrochemical measurements were conducted using a BioLogic VMP-300 multichannel potentiostat. All experiments were performed in Ar-purged solutions. The volume of the test solution used was 100 ml. The solution was purged with argon for 30 min. prior to the test.

In all potentiodynamic polarization tests, the potential was scanned from -0.3 V to 0.4 V with respect to E_{corr}. Each experiment was repeated at least three times. The sweep rate of the PD test was 0.167 mV s^{-1}. An LPR measurement was performed after each successive 2 h of immersion. For the LPR measurements, the potential was scanned negatively from E_{corr} toward -10 mV vs. E_{corr} and then reversed to +10 $mV_{E_{corr}}$ followed by a negative scan to E_{corr}.

5.2.3 Solution Analysis

In addition to electrochemical experiments, to evaluate the anodic dissolution at

E_{corr}, ICP measurements were also performed under the same conditions. After each successive 2 h period of immersion of the coupon in solution, 1 ml of solution was taken from the test solution, and the concentration of dissolved iron was measured using ICP-OES. Prior to the solution analysis, the test samples were digested using trace analytical grade nitric acid (Fisher Chemical) to dissolve any colloidal particles present in the solution. The dissolved iron concentration in the test solution was analyzed using a Perkin Elmer Avio 200 inductively coupled plasma optical emission spectrometer (ICP-OES). The ICP measurement reports the concentration of iron, which would include any colloid particles present in the solution. ICP-OES can detect concentrations as low as 0.1 ppb.

5.3 RESULTS AND DISCUSSION

The electrochemical behaviours of CS, 304L SS and 309 SS in pH 2.0 nitrate solutions were investigated in order to understand the effect of ionic strength on the corrosion behaviour of carbon steels and stainless steels. The range of nitrate ions and the pH were chosen to reflect the potential conditions that could arise during humid air radiolysis.

5.3.1 Effect of Nitrate on Corrosion of CS in Acidic Solutions

The E_{corr} vs time and the PD curves of CS in pH 2.0 nitrate solutions are presented in **Figure 5-1**, and the extracted electrochemical parameters are listed in **Table 5-2**. It should be mentioned that a prerequisite for accurate Tafel slope measurements is finding a linear region in a range of potential far from the corrosion potential, which

should extend for at least one decade of current density [17]. In this study, finding such a linear region was difficult, and therefore the reported Tafel slopes are based on the best fit for the most linear region within ±30 mV to ±60 mV around E_{corr} (explained in **Section 4.3.2)** [18], and these Tafel slopes will be used for a comparison study on the polarizability (how easily current density changes with change in potential).

The total dissolved iron ($[Fe]_{meas}$) vs t_{corr} is shown in **Figure 5-2**. More details on the different redox reactions involved in iron oxidation can be found in **Table 5-3** and **Figure 5-4**. The E_{eq} values of redox reactions under standard conditions are presented on the left. It is worth noting that the purpose of comparing of E_{corr} with the standard equilibrium potentials of various redox reactions (E_{rxn}^{eq}), is not to determine whether the redox reaction can occur or not. It is rather because an analysis of the trends of the changes in the E_{corr} can be employed to determine the reactions happening at the steady-state and to understand the corrosion system. The redox half-reactions that involve dissolved metal cations ($Fe^{2+}_{(aq)}$) are not listed in the table because the values of E^{eq} of redox reactions of these ions depend on the dissolved concentrations of these cations, which are continuously shifting as corrosion progresses.

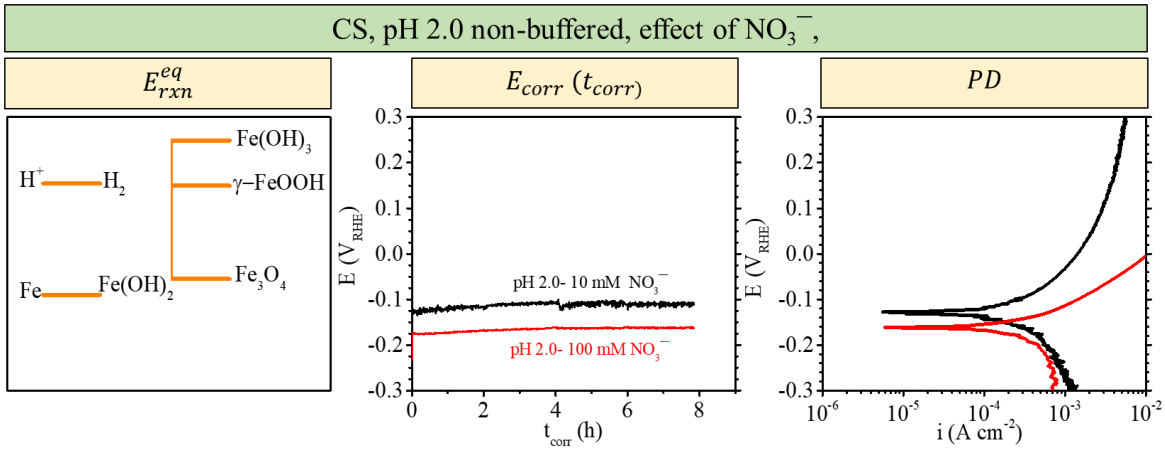

Figure 5-1: E_{corr} vs t_{corr} (plotted in log scale) and the PD curves in pH 2.0 non-buffered nitrate solutions. The standard equilibrium potentials of relevant iron and iron oxide redox reactions are shown on the left.

Table 5-2: The values of $E_{i=0}$, Tafel slopes, and corrosion current densities (i_{corr}) obtained from the PD experiment involving CS in pH 2.0 solution.

[NO_3^-]	**10 (mM)**	**100 (mM)**
E_{corr} (mV_{RHE})	-111	-163
$E_{i=0}$ (mV_{RHE})	-128	-162
b_a (mV decade^{-1})	100	75
$\|b_c\|$ (mV decade^{-1})	87	163
$i_{corr,a}$ (A cm^{-2})*	1.47×10^{-4}	2.21×10^{-4}
$i_{corr,c}$ (A cm^{-2})**	1.22×10^{-4}	2.57×10^{-4}
i_{corr} (A cm^{-2})	1.34×10^{-4}	2.45×10^{-4}

*$i_{corr,a}$ is the measured current density when the anodic Tafel line is extrapolated to $E_{i=0}$

** $i_{corr,a}$ is the measured current density when the cathodic Tafel line is extrapolated to $E_{i=0}$

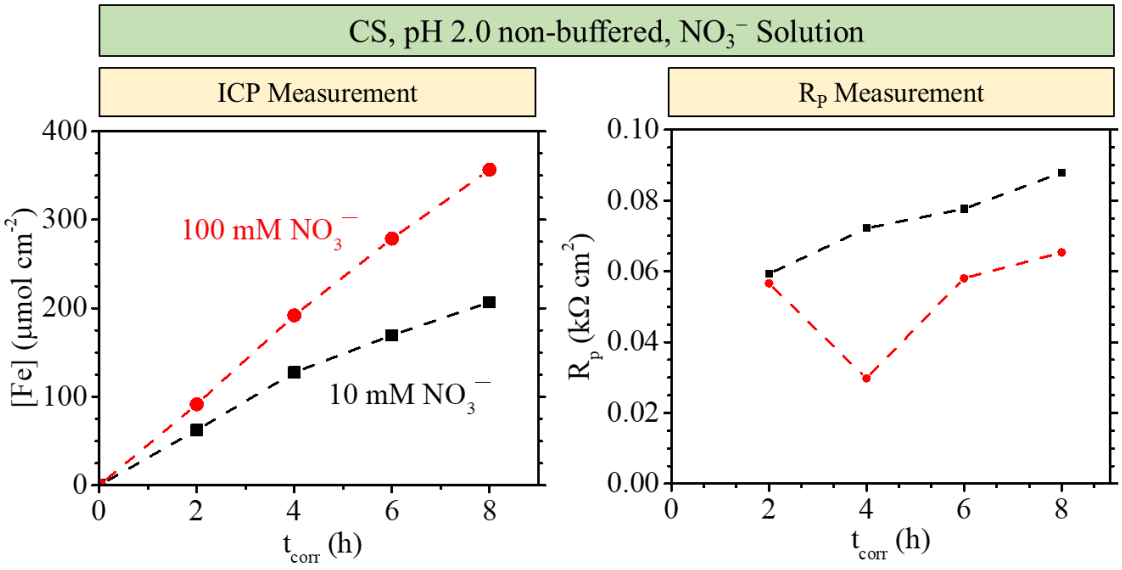

Figure 5-2: $[Fe]_{meas}$ (obtained from ICP-OES experiments) and R_P (obtained from LPR experiments) as a function of time in 10 mM and 100 mM NO_3^- pH 2.0 non-buffered solutions.

The key observations from the results presented in **Figure 5-1** to **Figure 5-4** are as follows:

- E_{corr} in the presence of 10 mM and 100 mM NO_3^- (at pH 2.0) reached its first steady-state at $t_{corr} < 1\ s$. The steady state E_{corr} values were -0.11 V_{RHE} and -0.163 V_{RHE}, for 10 mM and 100 mM NO_3^-, respectively. For the solution containing 100 mM NO_3, the first steady state E_{corr} was below $E^{eq}_{Fe \leftrightarrows Fe(OH)_2}$, while it was very close to $E^{eq}_{Fe \leftrightarrows Fe(OH)_2}$ in the 10 mM NO_3^--containing solution (see **Figure 5-1)**.
- The cathodic current in the PD curves was constant over a wide range of potentials in 100 mM NO_3^-, while it showed Tafel behaviour (apart from at large negative overpotentials) in 10 mM NO_3^- (see **Figure 5-1**).
- The anodic current Tafel slopes (b_a) differed depending on [NO_3^-]: approximately 100 mV decade^{-1} and 75 mV decade^{-1} in 10 mM NO_3^- and 100 NO_3^- respectively (see

Figure 5-1). The charge transfer region in the anodic branch was followed by a diffusion-limited current at high overpotentials (this will be discussed later and is shown in **Figure 5-3**). The charge-transfer region in the anodic branch was very narrow (30 to 60 mV>E_{corr}) and the diffusion-limited region occurred immediately above $E_{i=0}$. (see **Figure 5-3**).

$[Fe]_{meas}$ increased initially (for 4 h) almost linearly with t_{corr} in both 10 mM and 100 mM NO_3^-solutions. The rate of increase of $[Fe]_{meas}$ was 48 μmol cm^{-2} h^{-1} over 4 h corrosion in 100 mM NO_3^-. Assuming that no iron was consumed in oxide formation, this rate corresponds to a corrosion current density of 2.57×10^{-3} A cm^{-2}. The rate of increase of $[Fe]_{meas}$ was slightly lower in 10 mM NO_3^- (31.9 μmol cm^{-2} h^{-1} or 1.71×10^{-3} A cm^{-2}). (see **Figure 5-2**).

- The R_P was generally higher in 10 mM NO_3^- than in 100 mM NO_3^-.

5.3.1.1 Corrosion of CS in high ionic strength acidic solutions

In 100 mM NO_3^- solution with initial pH 2.0, the dissolved concentration of Fe^{II} increases linearly with time. This linear increase, in combination with the observation that the E_{corr} is significantly below $E^{eq}_{Fe\leftrightarrows Fe(OH)_2}$, suggests that the Fe^{II} saturation concentration is not reached within the duration of the test.

Figure 5-1 shows that in a pH 2.0 solution, the cathodic current does not change with an increase in nitrate concentration from 10^{-2} M to 10^{-1} M. Thus, increasing the nitrate concentration at pH 2.0 does not affect the CS oxidation rate, but rather increases the mass transfer rate and increases the saturation capacity for Fe^{II} near the surface, and hence delays the formation of $Fe(OH)_2$. For at least 8 h of immersion in 100 mM NO_3^-

non-buffered pH 2.0 solution, the E_{corr} remains below $E^{eq}_{Fe \leftrightarrows Fe(OH)_2}$, indicating that the saturation limit for Fe^{II} has not been reached. As discussed in **Chapter 4**, the prerequisite for $Fe(OH)_2$ formation on the surface is saturation of the interfacial region with Fe^{II} cations. Note that the corrosion potential was above the $E^{eq}_{Fe \leftrightarrows Fe^{2+}}$, considering 10^{-6} M as the corrosion criteria for $[Fe^{2+}]$. However, the equilibrium potential of Fe to Fe^{II} was not presented because the change in the iron cation concentration continuously changes it. Since the solubility of Fe^{II} at pH 2.0 is high, and mass transport is fast, the Fe^{II} cations do not saturate the interfacial region to form $Fe(OH)_2$.

In 10 mM NO_3^-, the E_{corr} approaches a value close to $E^{eq}_{Fe \leftrightarrows Fe(OH)_2}$ indicating that $Fe(OH)_2$ has formed, but has not become sufficiently saturated with Fe^{II} to form oxides.

When the potential is scanned toward positive potentials in both solutions (10 mM NO_3^- and 100 mM NO_3^-), Fe^{II} continues to accumulate at the surface while diffusing out toward the bulk solution in the acidic environment. In 10 mM NO_3^-, and at $E_{appl} > E_{corr}$, the rate of accumulation of Fe^{II} in the interfacial region is high, and mass transfer becomes limited by the presence of the $Fe(OH)_2$ layer at the surface. In fact, the corrosion rate in both solutions is partially limited by the mass transport of ions. The lower Tafel slope obtained in high ionic strength acidic solution (i.e., in the presence of 100 mM NO_3^-) indicates that a faster mass transfer rate could result in a faster oxidation rate. The PD results are consistent with the LPR and ICP results, which show that over the 8 h of measurements, the value of R_P is lower, and the rate of increase of $[Fe]_{meas}$ is higher for 100 mM NO_3^- than for 10 mM NO_3^-. Oxidation of Fe in 10 mM NO_3^- during the scanning of potentials above E_{corr} occurs mostly via $Fe(OH)_2 \rightarrow Fe_3O_4$ inside the

hydrogel and can occur via $Fe(OH)_2 \rightarrow FeOOH$ at higher potentials. In 100 mM NO_3^-, the rate of mass transfer of Fe^{2+} from the surface is fast enough to compete with the oxidation rate, which prevents the saturation of $Fe(OH)_2$. That is, the rate of oxidation is only partially limited by mass transport of ions until very high overpotentials, where the current density becomes limited by the formation of a thick oxide/hydroxide.

5.3.1.2 Corrosion of CS in nitrate solutions at pH 2.0 vs pH 6.0

To understand the effect of pH on the corrosion of CS, the E_{corr} vs time and potentiodynamic polarization curves of CS in pH 2.0 non-buffered solutions of 10 mM NO_3^- and 100 mM NO_3^- obtained in this chapter were compared to those shown and discussed in **Chapter 4** for pH 6.0 (see **Figure 5-3**).

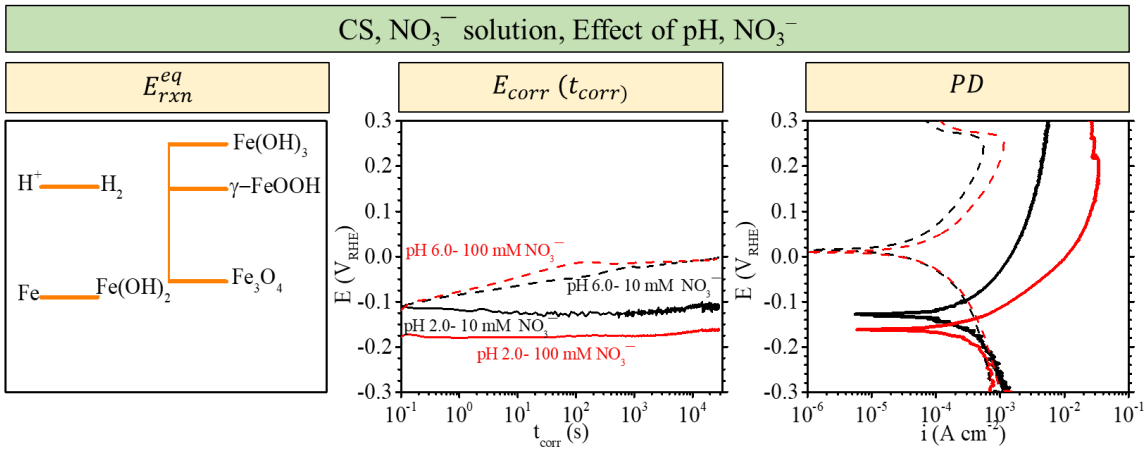

Figure 5-3: E_{corr} vs t_{corr} (plotted in log scale) and the PD curves for CS in the presence of different [NO_3^-] at different pHs. The solid line and dashed lines denote pH 6.0 and pH 2.0, respectively. The standard E_{eq} values for iron and iron oxide redox reactions are shown on the left.

The E_{corr} vs t_{corr} plots showed that, for the same concentration of NO_3^-, E_{corr} increases more rapidly and reaches a higher value at pH 6.0 than at pH 2.0. As explained

earlier in **Chapter 4**, the interfacial region is saturated with Fe ions when the bulk pH is 6.0. Thus, the formation of $Fe(OH)_2/Fe(OH)_3$ occurs immediately (in less than 0.1 s), and the corrosion progresses to **Stage 3** by 100 s where $Fe(OH)_2 \rightarrow Fe_3O_4$ oxidation can occur. For pH 2.0, in both 10 and 100 mM NO_3^- solutions, as explained earlier in this chapter, the accumulation of Fe ions in the interfacial region has not exceeded the saturation limit by 8 h, and E_{corr} remains constant at a value below $E^{eq}_{Fe \leftrightarrows Fe(OH)_2}$. For pH 2.0, 10 mM NO_3^-, the accumulation of Fe^{2+} occurs immediately after immersion; however, the concentration remains low, and progression to **Stage 3** and oxidation of $Fe(OH)_2 \rightarrow Fe_3O_4$ did not occur within the 8 h of measurements in this study.

A comparison of PD curves in solutions of pH 2.0 and pH 6.0 showed that the anodic current densities are significantly higher for pH 2.0. Even at high overpotentials, where current densities are under mass transfer control, the current is still significantly higher for pH 2.0 than for pH 6.0, indicating that a protective oxide cannot form at pH 2.0. The anodic current was one decade higher for pH 2.0 which resulted in a corrosion rate almost six times higher.

5.3.2 Effect of Nitrate on Corrosion of Stainless Steels in Acidic Solutions

In stainless steels, the redox reactions of other alloying elements (and particularly Ni and Cr) participate in the corrosion process, in addition to those of Fe. The standard potentials [19] and the equilibrium potentials of different redox reactions are listed in **Table 5-3** and also presented in **Figure 5-4**. The $E^{eq}_{Cr \leftrightarrows Cr_2O_3}$ is not shown in **Figure 5-4**.

Table 5-3: Redox half-reactions involving metal and solution species that can occur during corrosion of stainless steels [19].

Redox Reaction	Standard Potential (V_{RHE})
$Cr_2O_3 + 6\,H^+ + 6\,e^- \rightleftharpoons 2\,Cr + 3\,H_2O$	-0.59
$FeCr_2O_4 + 2\,H^+ + 2\,e^- \rightleftharpoons Fe + Cr_2O_3 + H_2O$	-0.29
$Fe(OH)_2 + 2H^+ + 2e^- \rightleftharpoons Fe + 2\,H_2O$	-0.092
$Fe_3O_4 + 2\,H^+ + 2\,e^- \rightleftharpoons Fe(OH)_2 + H_2O$	-0.055
$3\,NiFe_2O_4 + 8\,H^+ + 8\,e^- \rightleftharpoons 3\,Ni + 2\,Fe_3O_4 + 4\,H_2O$	0.074
$Ni(OH)_2 + 2\,H^+ + e^- \rightleftharpoons Ni + 2\,H_2O$	0.079
$\gamma\text{-}FeOOH + H^+ + e^- \rightleftharpoons Fe(OH)_2 + H_2O$	0.15
$Fe(OH)_3 + H^+ + e^- \rightleftharpoons Fe(OH)_2 + H_2O$	0.247
$3\,\gamma\text{-}Fe_2O_3 + 2\,H^+ + 2\,e^- \rightleftharpoons 2\,Fe_3O_4 + H_2O$	0.361
$3\,\gamma\text{-}FeOOH + H^+ + e^- \rightleftharpoons Fe_3O_4 + 2\,H_2O$	0.559

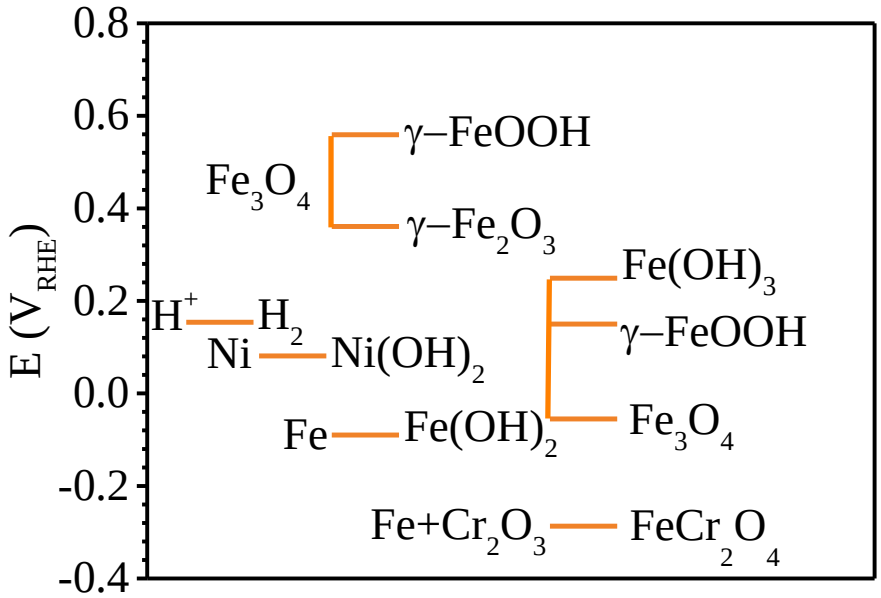

Figure 5-4: The E_{eq} values of redox reactions of metals and metal oxides that can occur on the steel alloys tested in this study at 21 °C and pH 2.0 [19].

In this section, the key observations from different experiments are given, followed by a discussion of the corrosion mechanism.

Stainless steels contain multiple alloying elements (Fe, Ni, and Cr), and each metal can also undergo different oxidation reactions coupled with solution reduction reactions. Not listed in the table are the redox half-reactions that involve dissolved metal cations ($Fe^{2+}_{(aq)}$, $Ni^{2+}_{(aq)}$, $Cr^{3+}_{(aq)}$) because the E^{eq} values of redox reactions of these ions depend on the dissolved concentrations of these cations, which are continuously shifting as corrosion progresses.

5.3.2.1 E_{corr} measurements and potentiodynamic polarization after 8 h corrosion of stainless steels

The effects of pH and NO_3^- concentration on the corrosion of 304L SS and 309 SS were investigated. The corrosion potential (E_{corr}) vs $\log t_{corr}$ plots for the corrosion of 304L SS and 309 SS in pH 2.0 Ar-purged solution are presented in **Figure 5-5**.

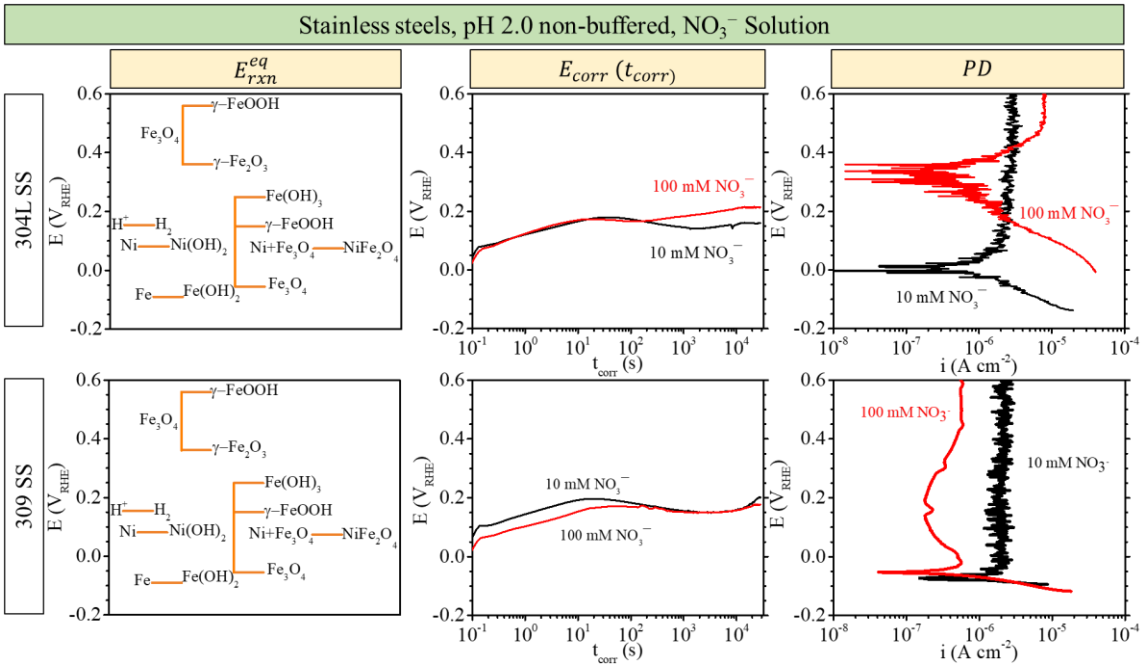

Figure 5-5: E_{corr} vs t_{corr} (plotted in log scale) and the PD curves for 304L SS and 309 SS in nitrate-containing pH 2.0 non-buffered solutions. The E^{eq} values for metal and metal oxide redox reaction are shown on the left.

The key observations from the E_{corr} measurements for 304L SS and 309 SS are as follows:

- For both 304L SS and 309 SS, E_{corr} increased with time and became stable after ~10 s at around 0.2 V_{RHE} in the presence of both 10 mM and 100 mM NO_3^-.
- The final E_{corr} values for both 304L SS and 309 SS in 10 mM HNO_3 lay above the E^{eq} values of the redox reactions Cr ⇆ Cr_2O_3 and Fe + Cr_2O_3 ⇆ $FeCr_2O_4$ (not shown in **Figure 5-5**) and Fe ⇆ $Fe(OH)_2$, $Fe(OH)_2$ ⇆ Fe_3O_4, Ni ⇆ $Ni(OH)_2$. The final E_{corr} was slightly above $E^{eq}_{Fe(OH)_2 \leftrightarrows \gamma-FeOOH}$.
- The anodic region of all PD curves showed a passive behaviour (0.4 - 8 μA cm^{-2}).

- *The* $E_{i=0}$ values for stainless steels, obtained in all conditions, were significantly different from the E_{corr} values at 8 h. For 304L SS in 10 mM NO_3^-, the $E_{i=0}$ was 200 mV below the E_{corr}, and in 100 mM NO_3^- it was about 100 mV above E_{corr}. For 304L SS the $E_{i=0}$ in 100 mM NO_3^- was about 400 mV which was close to the $E^{eq}_{Fe_3O_4 \leftrightarrows Fe_2O_3}$.
- For 309 SS in both 10 mM NO_3^- and in 100 mM NO_3^- solutions, the $E_{i=0}$ was 200 mV below the E_{corr}. $E_{i=0}$ of 309 SS was almost the same in both NO_3^- concentrations and was close to $E^{eq}_{Fe \leftrightarrows Fe(OH)_2}$.

5.3.2.2 Evolution of Linear Polarization Resistance over 8 h Corrosion

Linear polarization resistance measurements were carried out as a function of time.

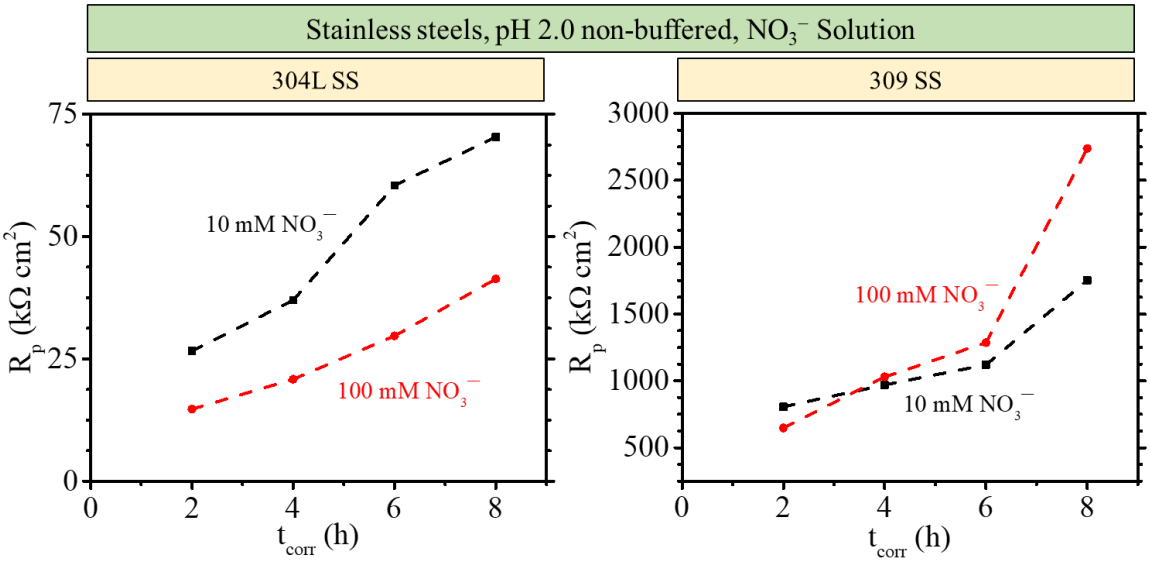

Figure 5-6: R_P as a function of time for 304L SS and 309 SS in pH 2.0 non-buffered nitrate solution

R_P vs t_{corr} was plotted for 304L SS and 309 SS in pH 2.0 non-buffered nitrate

solutions (see **Figure 5-6**). The results are as follows:

- R_P for 304L SS and 309 SS increased with time for both 10 mM NO_3^- and 100 mM NO_3^- containing solutions.
- In the presence of both 10 mM NO_3^- and 100 mM NO_3^-, R_P values for 309 SS were significantly larger than for 304L SS.
- In 10 mM NO_3^-, the R_P values for 304L SS and 309 SS were about 500 times and 15,000 times larger than for CS, respectively. These ratios remained nearly unchanged after 8 h immersion.
- In 100 mM NO_3^-, the R_P for CS and 304L SS is lower than that in 10 mM NO_3^-, while for 309 SS in 100 mM NO_3^-, it remains almost the same as the one in 10 mM NO_3^- until $t_{corr} = 6\ h$ and then increases significantly.
- The LPR results after 8 h differed from the PD results (Tafel extrapolation). For 309 SS, the corrosion rate determined via Tafel extrapolation (taken after 8 h immersion) was almost 4 times smaller for 100 mM NO_3^- than for 10 mM NO_3^-, while the rates obtained via LPR measurements showed that the polarization resistance of 309 SS in 100 mM NO_3^- is two times higher than in 10 mM NO_3^- after 8 h.

5.3.2.3 Solution Analysis over 8 h of Immersion

Each oxidation reaction produces metal cations which either form oxides or dissolve into solution. The study of the dissolved cation concentrations and the evaluation of the progression of the dissolution process aims to improve the understanding of the corrosion pathways. $[Fe]_{meas}$, $[Ni]_{meas}$, and $[Cr]_{meas}$ were determined using the ICP-OES technique as a function of time, during the corrosion of 304L SS and 309 SS in

nitrate-containing pH 2.0 non-buffered solutions (see **Figure 5-7**).

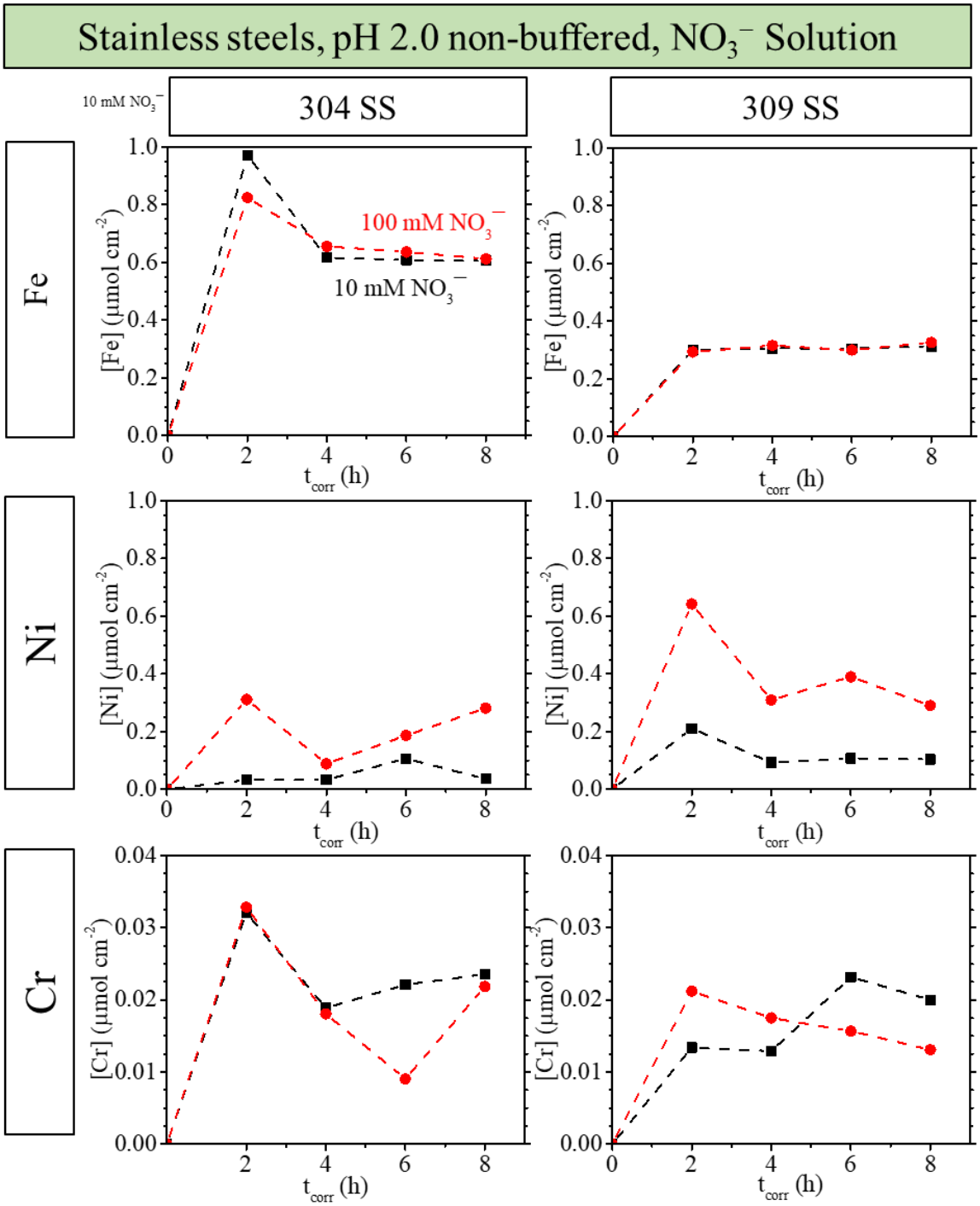

Figure 5-7: $[Fe]_{meas}$, $[Ni]_{meas}$, and $[Cr]_{meas}$ as a function of time during the corrosion of 304L SS and 309 SS in nitrate-containing pH 2.0 non-buffered solutions.

- For 304L SS in both 10 mM NO_3^- and 100 mM NO_3^- containing solutions, $[Fe]_{meas}$ decreases initially (after 2 h) and remains almost constant with t_{corr}. The $[Fe]_{meas}$ values were generally lower in 309 SS in both solutions and the initial decrease (after 2 h) was not observed. The maximum values of $[Fe]_{meas}$ were 200-300 times lower for stainless steels than that for CS.
- $[Ni]_{meas}$ for 304L SS and 309 SS had a similar trend over time as for Fe except that $[Ni]_{meas}$ was lower than $[Fe]_{meas}$. The values of $[Ni]_{meas}$ were generally higher for 304L SS than for 309 SS and were higher in 100 mM NO_3^- than in 10 mM NO_3^-. The values of $[Ni]_{meas}$ for 304L SS and 309 SS were almost the same except at 2 h, at which time the value for 309 SS was almost twice that for 304L SS.
- $[Cr]_{meas}$ for 304L SS and 309 SS had a similar trend over time as for Fe, except that $[Cr]_{meas}$ was almost 1/10 of $[Ni]_{meas}$ and 1/50 of $[Fe]_{meas}$.
- Nitrate concentration did not affect $[Fe]_{meas}$ and $[Cr]_{meas}$, but increased $[Ni]_{meas}$ for both 304L SS and 309 SS.

5.3.2.4 Corrosion of Stainless Steels in Nitrate Solutions

A similar mechanism to that proposed for Alloy 800 (an alloy containing 33 wt% Ni, 22 wt% Cr, and 45 wt% Fe) by Momeni et al. [20] (**Figure 5-8**) is applicable for stainless steels. 304L SS and 309 SS are Fe-Cr-Ni alloys similar to Alloy 800, which contain 40% Fe, 22% Cr and 33% Ni. The only difference between 304L SS, 309 SS and Alloy 800 is the difference in the ratios of the alloying elements. Therefore, we can use the same global mechanism and intermediate steps proposed for Alloy 800 for 304L SS and 309 SS. The difference in the chemical composition will result in the different rates

of each intermediate step; however, the steps themselves, and thus the overall mechanism, should be the same.

According to this mechanism, corrosion can proceed via different pathways. Some of the oxidation reactions occur in sequence and some in parallel. The corrosion pathway can vary depending on the relative rates of the different redox reactions of involved metal cations. The solution transport of metal cations can also affect the kinetics of oxidation and change the corrosion pathway. The oxidation of Fe to Fe^{II} converts the chromium oxide to iron chromate spinel oxide ($FeCr_2O_4$), and then the partial oxidation of Fe^{II} to Fe^{III} results in the formation of Fe_3O_4 (mixed Fe^{II}/Fe^{III} oxide) or FeOOH. At sufficiently high potentials, magnetite can be oxidized further to γ-Fe_2O_3. At later times and at sufficiently high potentials, where Ni oxidation to Ni^{II} is thermodynamically possible, an iron spinel oxide ($NiFe_2O_4$) and finally $NiO/Ni(OH)_2$ can form.

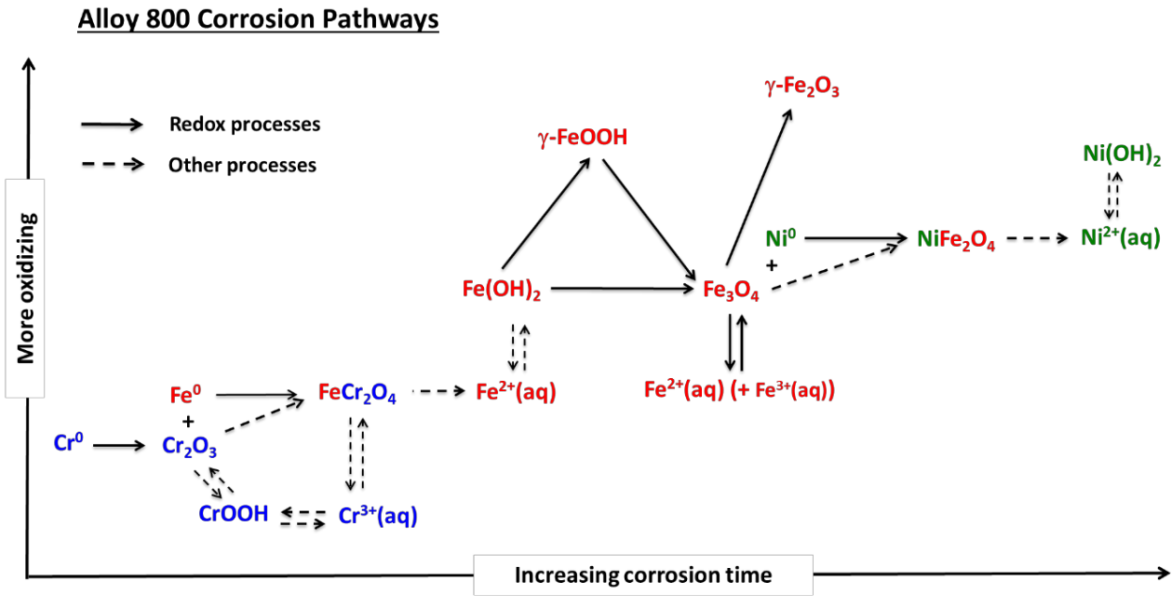

Figure 5-8: Proposed mechanism for Alloy 800 corrosion [20]

The solubility of a given metal cation depends on the pH. Each metal cation has its own pH solubility-dependence; at pHs below 6.0, the solubilities of Cr and Ni decreases with pH increase, while that of Fe^{II} is nearly independent of pH. The solubilities of different alloying elements vs. pH are shown in **Figure 5-9**.

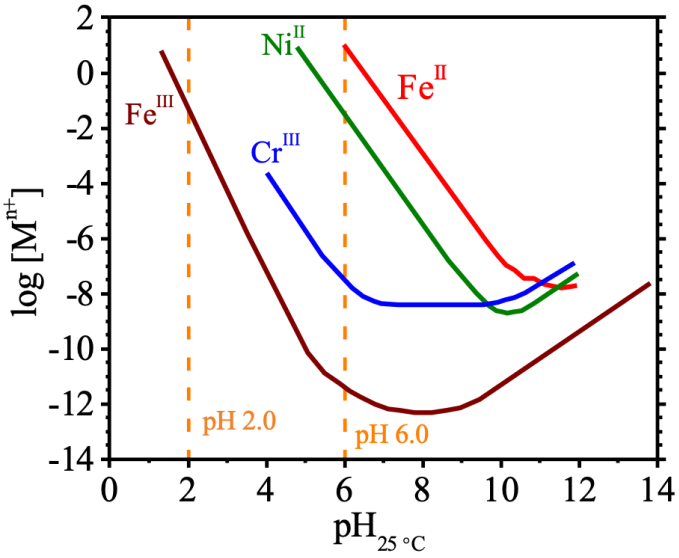

Figure 5-9: The solubilities of Fe^{II}, Fe^{III}, Cr^{III} and Ni^{III} as a function of pH at 21 °C [21–26].

In 10 mM NO_3^- or 100 mM NO_3^- pH 2.0 non-buffered solutions, the E_{corr} values of both stainless steels reached steady-state values (close to the E^{eq} values of the oxidation of $Fe(OH)_2$ to $Fe(OH)_3$) immediately after cathodic cleaning. The steady-state E_{corr} values were below $E^{eq}_{Cr^{III}\leftrightarrows Cr^{VI}}$ and were higher than $E^{eq}_{Fe_3O_4\leftrightarrows \gamma-FeOOH}$ (this value is not shown on the graph shown in **Figure 5-4**). The E_{corr} values were all above $E^{eq}_{Ni\leftrightarrows Ni^{II}\ (NiFe_2O_4 \text{ and } Ni(OH)_2)}$, indicating that 10 mM NO_3^- and 100 mM NO_3^- solutions are sufficiently oxidizing to form Ni^{II} oxide/hydroxide on stainless steel surfaces from which Ni^{2+} can dissolve out. The final values of E_{corr} were also above the E^{eq} values of

the oxidation of $E^{eq}_{Fe \leftrightarrows Fe(OH)_2}$, $E^{eq}_{Fe(OH)_2 \leftrightarrows Fe_3O_4}$, and $E^{eq}_{Fe(OH)_2 \leftrightarrows \gamma - FeOOH}$, indicating that all three iron oxides ($Fe(OH)_2$, Fe_3O_4 and γ-FeOOH) can form during corrosion of stainless steels.

The metal cations on the surfaces of the oxides are hydrated (Cr^{3+} and Fe^{2+}) and diffuse into the bulk solution phase. Dissolution of metal cations from the oxide is followed by hydration, hydrolysis and diffusion of the cation. In both solutions and both alloys, Cr quickly reaches supersaturation at the metal-solution interface and Cr_2O_3 formation occurs. Note that Cr_2O_3 can also be present on the surface as the air-formed oxide that was not reduced during cathodic cleaning. The E_{corr} observed at pH 2.0 is significantly higher for 304L SS and 309 SS than for CS. The presence of a pre-formed Cr_2O_3 layer on stainless steel can provide a large potential barrier that can significantly lower the interfacial metal oxidation rate for the oxidation of Fe⇌ Fe^{2+} and Ni ⇌ Ni^{2+}. The $[Fe]_{meas}$ was significantly lower for stainless steels than for CS at all time points, which confirms the lower rate of oxidation of Fe. The oxidation of Fe to Fe^{2+} produced Fe^{II} species that react with Cr_2O_3 to form $FeCr_2O_4$. The formation of the chromium iron oxide ($FeCr_2O_4$) is followed by the rapid oxidation of Fe^{II} to Fe^{III} to form Fe_3O_4 (mixed Fe^{II}/Fe^{III} oxide) and FeOOH. The concentration of dissolved Fe, therefore, remains very low compared to what was observed for CS. At later times, Ni oxidation to Ni^{II} is thermodynamically possible ($E_{corr} > E^{eq}$) resulting in $NiFe_2O_4$, $Ni(OH)_2$ and NiO, iron spinel oxide ($NiFe_2O_4$), and finally $NiO/Ni(OH)_2$ can form. Similar to the rate of oxidation of Fe to Fe^{2+}, the rate of oxidation of Ni to Ni^{2+} is low due to the potential barriers created by Cr_2O_3 and $FeCr_2O_4$. Thus, the concentration of all alloying elements increases initially and remains almost constant with time after the protective oxide has

formed and limits the oxidation rates. The relative solubilities are Fe^{II} > Ni^{II} > Cr^{III} at pHs below 6.0. Therefore, the concentrations of Fe^{II} and Ni^{II} that can diffuse out from the surface toward the solution increase until the saturation limit of these species is reached, and hydroxide and oxide formation become dominant. This results in $[Fe]_{meas}$, $[Ni]_{meas}$, and $[Cr]_{meas}$ remaining constant with time.

The E_{corr} of 304L SS was slightly higher in 10 mM NO_3^- than in 100 mM NO_3^- solution. This can be attributed to the higher rate of mass transfer in higher ionic strength solution, which increases the rate of oxidation of Fe (and Ni). The small increase in the E_{corr} of 309 SS in 10 mM NO_3^- after 5 h immersion can be attributed to the growth of $NiFe_2O_4$. The dissolved ions can diffuse out into the solution phase while they are in equilibrium with the oxides.

One key observation for both 304L SS and 309 SS alloys was that $E_{i=0}$ was lower than E_{corr} for both alloys in 10 mM NO_3 and was slightly above E_{corr} for 304L SS in the solution containing 100 mM NO_3^-. During the potential scan over the range of potentials below E_{corr}, the thermodynamic conditions are favourable for reduction of Fe^{III} cations to Fe^{II} and Ni^{II} to Ni, causing a partial reduction of the oxide layer on the surface. This oxide reduction shifts the $E_{i=0}$ to potentials more negative than that of E_{corr}. As was mentioned earlier, the only exception was the $E_{i=0}$ for 304L SS in 100 mM NO_3^-, which was higher than E_{corr}. The exact reason for this behaviour requires more analysis. However, it could be postulated that since the potential from which the potentiodynamic polarization test started was above the equilibrium potential for $Fe(OH)_2$ to Fe_3O_4, some of the Fe^{II} hydroxide on the surface converted to magnetite. This provides the conditions resulting in an $E_{i=0}$ slightly higher than E_{corr} for 304L SS in 100 mM NO_3^-. It is

important to mention that 304L SS has lower Ni content than 309 SS and therefore the concentration of Ni^{II} was lower during corrosion of 304L SS than 309 SS. This can be seen from the ICP-OES results. Thus, while reduction of Ni^{II} to Ni is possible (and it is believed that this happens), the low concentration of Ni^{II} could not significantly contribute to the potential distribution in the interfacial region.

5.4 SUMMARY

This chapter investigated the effect of nitrate concentration on the corrosion behaviour of carbon steel (CS A36) and stainless steels (304L SS and 309 SS) in 10 mM HNO_3 solution (i.e., pH 2.0) using electrochemical (E_{corr} vs time measurement, LPR, and PD) techniques and solution analysis (ICP-OES).

The results revealed that the addition of 90 mM NO_3^- to 10 mM HNO_3 increases the mass transport of Fe^{II} ions and prevents the accumulation of Fe ions in the interfacial region. In 100 mM NO_3^- solution at pH 2, the E_{corr} does not reach $E^{eq}_{Fe \leftrightarrows Fe(OH)_2}$, and hence corrosion does not pass **Stage 1**, in which oxidation of iron is under charge transfer control. Similarly, the effect of a decrease in solution pH (from pH 6.0, presented in **Chapter 4**) for the same [NO_3^-] was to increase the mass transfer rate via preventing Fe saturation in the interfacial region, consequently increasing the corrosion rate.

For stainless steels, the measured E_{corr} values were significantly different from the $E_{i=o}$ values obtained from the PD experiments. The difference between $E_{i=o}$ and E_{corr} could be attributed to a change in the electrode surface condition as a result of applying a potential below that of naturally corroding conditions.

Because forward scanning from negative overpotentials results in the formation of a protective chromium oxide at potentials below the corrosion potential, the cathodic and anodic currents are not representative of the rates of reactions that occur under naturally corroding conditions; thus, the application of a Tafel slope extrapolation method was not suitable for corrosion rate determination.

Unlike for CS, for types 304L and 309 stainless steel, the anodic current is lower in 100 mM NO_3^- solution than in 10 mM NO_3^-. For 304L SS (with lower Cr and Ni content than 309 SS) a higher [NO_3^-] results in faster formation of a protective oxide at very low overpotentials, that becomes unstable at potentials $>E^{eq}_{Fe(OH)_2 \leftrightarrows Fe(OH)_3}$. For 309 SS, the oxide formed at lower potential is stable over the entire range of potential scanning. The implication of these results is that when a protective oxide is stable, increasing the nitrate concentration cannot increase the rate of corrosion of stainless steels at low pHs.

The results presented in this chapter revealed that in the presence of nitrate ions (in the range expected from the humid air radiolysis) and in acidic media (which is considered to be the worst-case scenario), stainless steels (304L and 309) in the weld structure have much lower corrosion rates than CS. These results will be used in the interpretation of the corrosion behaviour of the weld joint under humid air conditions in the presence of radiation, which will be presented in **Chapter 8**.

5.5 REFERENCES

[1] J.C. Wren, J. Ball, LIRIC 3.2 an updated model for iodine behaviour in the presence of organic impurities, Radiat. Phys. Chem. 60 (2001) 577–596.

[2] J.M. Joseph, B.S. Choi, P. Yakabuskie, J.C. Wren, A combined experimental and model analysis on the effect of pH and O_2(aq) on γ-radiolytically produced H_2 and H_2O_2, Radiat. Phys. Chem. 77 (2008) 1009–1020.

[3] P. Driver, G. Glowa, J.C. Wren, Steady-state γ-radiolysis of aqueous methyl ethyl ketone (2-butanone) under postulated nuclear reactor accident conditions, Radiat. Phys. Chem. 57 (2000) 37–51.

[4] J.C. Wren, G.A. Glowa, A simplified kinetic model for the degradation of 2-butanone in aerated aqueous solutions under steady-state gamma-radiolysis, Radiat. Phys. Chem. 58 (2000) 341–356.

[5] P.A. Yakabuskie, J.M. Joseph, C.R. Stuart, J.C. Wren, Long-Term γ-Radiolysis Kinetics of NO_3^- and NO_2^- Solutions, J. Phys. Chem. A. 115 (2011) 4270–4278.

[6] P.A. Yakabuskie, J.M. Joseph, P. Keech, G.A. Botton, D. Guzonas, J.C. Wren, Iron oxyhydroxide colloid formation by gamma-radiolysis, Phys. Chem. Chem. Phys. 13 (2011) 7198–7206.

[7] R.P. Morco, Gamma-Radiolysis Kinetics and Its Role in the Overall Dynamics of Materials Degradation, PhD Thesis, The University of Western Ontario, 2020.

[8] J.W.T. Spinks, R.J. Woods, An introduction to radiation chemistry, John Wiley and Sons Inc, United States, 1990.

[9] R.P. Morco, J.M. Joseph, D.S. Hall, C. Medri, D.W. Shoesmith, J.C. Wren, Modelling of radiolytic production of HNO_3 relevant to corrosion of a used fuel container in deep geologic repository environments, Corros. Eng. Sci. Technol. 52 (2017) 141–147.

[10] Y.G. Shin, Nonlinear Dynamics of Carbon Steel Corrosion under Gamma Radiation, PhD Thesis, The University of Western Ontario, 2020.

[11] R. Karimihaghighi, Non-Linear Effects of Solution Parameters and Gamma Radiation on Nickel Oxidation Dynamics, PhD Thesis, The University of Western Ontario, 2021.

[12] Farhataziz, M.A.J. Rodgers, eds., Radiation chemistry: principles and applications, VCH Publishers, United States, 1987.

[13] J.H. O'Donnell, D.F. Sangster, Principles of Radiation Chemistry, American Elsevier Publishing Company, 1970.

[14] J.C. Wren, Steady-State Radiolysis: Effects of Dissolved Additives, in: C.M. Wai1, B.J. Mincher (Eds.), Nucl. Energy Environ., American Chemical Society, 2010: pp. 271–295.

[15] I.C. Draganic, Z.D. Draganic, The Radiation Chemistry of Water, Academic Press, 1971.

[16] M. Li, Galvanic Corrosion of Carbon Steel-Stainless Steel Welds, PhD Thesis, The University of Western Ontario, 2020.

[17] B. Cottis, M. Graham, R. Lindsay, S. Lyon, T. Richardson, D. Scantlebury, S. Howard, eds., Shreir's Corrosion, Elsevier, 2010.

[18] E. McCafferty, Introduction to corrosion science, Springer, New York, 2010.

[19] A.Y. Musa, J.C. Wren, Combined effect of gamma-radiation and pH on corrosion of Ni-Cr-Fe alloy inconel 600, Corros. Sci. 109 (2016) 1–12.

[20] M. Momeni, Gamma-Radiation Induced Corrosion of Alloy 800, PhD Thesis, The University of Western Ontario, 2017.

[21] Y.M.T. Tan, R. Winston Revie, Heterogeneous Electrode Processes and Localized Corrosion, John Wiley & Sons, Inc, 2012.

[22] B. Beverskog, I. Puigdomenech, Revised pourbaix diagrams for chromium at 25-300°C, Corros. Sci. 39 (1997) 43–57.

[23] B. Beverskog, I. Puigdomenech, Revised Pourbaix diagrams for iron at 25-300°C, Corros. Sci. 38 (1996) 2121–2135.

[24] B. Beverskog, I. Puigdomenech, Pourbaix Diagrams for the Ternary System of Iron-Chromium-Nickel, Corrosion. 55 (1999) 1077–1087.

[25] B. Beverskog, I. Puigdomenech, Revised Pourbaix diagrams for nickel at 25-300°c, Corros. Sci. 39 (1997) 969–980.

[26] M. Pourbaix, Atlas of chemical and electrochemical equilibria in Aqueous Solutions, Second ed, NACE International Cebelcor, 1974.

CHAPTER 6
CORROSION BEHAVIOUR OF CARBON STEEL AND STAINLESS STEELS IN HYDROGEN PEROXIDE SOLUTION

6.1 INTRODUCTION

During a periodic inspection of the Pickering unit 6 CANDU reactor, a leak was found in the End Shield Cooling (ESC) System. This raised concern that the moisture from this leak could reach a location in the annular air gap, which is adjacent to the periphery of the calandria tank assembly and its supporting structures. The reactor structural materials in this area are exposed to a continuous flux of γ-radiation. Radiation energy absorbed by the metals themselves dissipates mainly as heat and does not induce chemical changes [1–3]. Any water in this area, however, when exposed to γ-radiation, will be decomposed to various redox active species (as shown in **Eq. 6-1**), that can strongly influence the corrosion of materials [1–7]. These species will determine the aqueous redox conditions that determine the corrosion kinetics of materials in contact

with the solution.

Of the species produced, H_2O_2 is the most important species that can affect corrosion.

$$H_2O \rightarrow^{\gamma} \rightarrow \bullet OH, e_{aq}^-, \bullet H, H_2, H_2O_2, H^+ \quad \textbf{(Eq. 6-1)}$$

The radiolysis kinetics of liquid water have been well studied using a water radiolysis model (WRM) and validated using experimental data as a function of pH, temperature, and initial concentrations of dissolved oxygen and nitrate [8–13]. Under a continuous flux of γ-radiation, H_2O_2 is continuously produced, and removed by chemical reactions with other radiolysis products; therefore, the concentration of H_2O_2 in solution reaches a near steady-state value [6,9,14,15]. This concentration has been measured as 0.9×10^{-4} M in aerated pH 6.0 solution and 0.3×10^{-4} M and 1.4×10^{-4} M in deaerated and aerated pH 10.6 solutions, respectively [9].

Hydrogen peroxide can decompose to water and O_2, and also can act as either an oxidant or a reductant depending on the nature of the corroding surface [10,11], and can significantly change the overall metal oxidation rate by establishing a catalytic cycle between different redox reactions. In addition, because H_2O_2 is a stronger oxidant than dissolved O_2 [18], its formation and increase in its concentration due to the presence of γ-radiation in the annular gap of the ESC system of CANDU reactor could facilitate coupling between diffusion and redox reactions [3], and therefore, produce strong systemic feedback behaviours.

The effect of γ-radiation on the corrosion of carbon steel and other metals has

been previously studied under limited combination of solution redox and transport conditions using electrochemical techniques and coupon tests [3,17,19–28]. The effects of γ-radiation on the corrosion kinetics of carbon steel and different alloys have also been reported [17,19,25–27]. These studies have shown that the key radiolysis product for corrosion is H_2O_2. Daub et al. [27,29] showed that γ-radiation has a major impact on the corrosion process by increasing E_{corr} and the type of oxide which forms on the surface. They suggested that water radiolysis leads to the formation of a more passive film composed of a mixture of Fe_3O_4 and γ-Fe_2O_3 when the solution is mildly basic (pH 10.6).

Another study, also by Daub et al. [17], investigated CS corrosion under γ-radiation. By simulating of the E_{corr} behaviour in solutions containing representative concentrations of H_2O_2 at solution pH 10.6, they showed that the key radiolysis product controlling corrosion of CS is H_2O_2. Their results revealed that for $[H_2O_2] < 10^{-3}$ M, the E_{corr} of CS is a function of $[H_2O_2]$, and for $[H_2O_2] \geq 10^{-3}$ M, E_{corr} is independent of $[H_2O_2]$.

Due to the presence of γ-radiation, the temperature in the annular gap would be around 50 °C, and humidity of ~100% would be present. When humid air is exposed to γ-radiation, in addition to water radiolysis products (**Eq. 6-1)**, HNO_3 will also form via humid air radiolysis. The corrosion of carbon steel with different concentrations of NO_3^- at pH 6.0 was studied in **Chapter 4**, and corrosion of CS and stainless steels at pH 2.0 (10 mM HNO_3), was studied in **Chapter 5**. This chapter discusses the corrosion behaviour of carbon steel in the presence of different concentrations of chemically added

H_2O_2 at pH 6.0. Corrosion potential (E_{corr}) measurements, and potentiodynamic polarization (PD) measurements were employed to study the effect of hydrogen peroxide on the corrosion behaviour of CS in pH 6.0 buffered solution.

In the second part of this chapter, the effect of 10 mM H_2O_2 on corrosion of CS and stainless steels (304L SS and 309 SS) was studied in pH 2.0 nitric acid solutions. Corrosion potential (E_{corr}) measurements, linear polarization resistance (LPR), and potentiodynamic polarization (PD) measurements were employed to study the effect of hydrogen peroxide on the electrochemical behaviour of CS and stainless steels in acidic solutions. Additionally, the amounts of dissolved metal ions (Fe, Cr, and Ni) were measured using ICP-OES. The radiolytic corrosion of CS in small solution volumes and under different cover gases in the presence of γ-radiation is discussed in **Chapter 8**.

6.2 EXPERIMENTAL PROCEDURE

6.2.1 Sample and Solution Preparation

The working electrodes used in this study were CS A36, 304L SS, and 309 SS (provided by the Ontario Power Generation Inc. (OPG)). The alloy compositions of the tested carbon steels and stainless steels are given in Table 6-1.

Table 6-1: Elemental compositions of various steels tested in this chapter.

Alloy	Cr (wt.%)	Ni (wt.%)	Fe (wt.%)
Carbon Steel A36 (CS)	0.16	0.23	98
Weld Metal Stainless Steel 309 (W)	24	14	60
Stainless Steel 304L	19	8	71

Prior to the experiment, the coupons were ground manually with a series of fine silicon carbide papers (400, 600 and 1200, and 2500 grit), followed by polishing on a Texmet microcloth (Buehler) with a 1 μm MetaDi Supreme diamond paste suspension (Buehler) and lastly sonication in an acetone/methanol mixture for 5 min to remove polishing residues. The polished coupons were then rinsed with Type I water and dried in flowing argon.

All solutions were prepared with water purified with a NANO pure Diamond UV ultrapure water system (Barnstead International) to give a resistivity of 18.2 MΩ.cm. Sodium nitrate (Sigma Aldrich) and nitric acid (Fisher Chemical) were used to prepare the nitrate solutions.

For the experiments performed in pH 6.0 buffered solution, the borate buffered solution was prepared using $Na_2B_4O_7.H_2O$ (0.01 M) and H_3BO_3 (0.3 M) all purchased from Caledon Laboratories Ltd. Hydrogen peroxide (3 wt.%, purchased from Fisher Scientific) was added to the buffered solution at different concentrations.

For the experiments performed in solution at pH 2.0, the electrochemical analyses and solution measurements were performed by adding 10 mM H_2O_2 to 10 mM $NaNO_3$ or 100 mM $NaNO_3$ (10 HNO_3 + 90 mM $NaNO_3$) solutions. The pH of the solution was measured using an Accumet® Basic AB15 pH meter using a saturated calomel electrode (SCE).

6.2.2 Electrochemical Tests

The electrochemical tests were conducted using a BioLogic VMP-300 multichannel potentiostat. All electrochemical measurements were performed using a

three-compartment cell using a saturated calomel electrode (SCE, Fisher Scientific) as the reference electrode, and a platinum mesh as the counter electrode (CE). The working electrodes (WE) were CS, 304L SS, or 309 SS. All experiments were performed in Ar-purged solutions. The solution volume was 100 ml.

After cathodic cleaning at -0.23 V_{RHE} for 5 min, the E_{corr} was measured for 8 h in pH 6.0 buffered solution pH 6.0, containing different concentrations of H_2O_2. Each E_{corr} measurement was followed by a potentiodynamic polarization (PD) experiment at a sweep rate of 0.167 mVs^{-1}. E_{corr} measurements and PD experiments were performed in 10 mM HNO_3 and in 10 mM HNO_3 + 90 mM $NaNO_3$ (100 mM NO_3^-) pH 2.0 solutions with and without 10 mM H_2O_2, to investigate the corrosion behaviour of CS and stainless steels in the presence of H_2O_2 in acidic nitrate-containing solutions. During 8 h E_{corr} measurements the LPR measurements were performed for every 2 h of immersion. For the LPR measurements, the potential was scanned negatively from E_{corr} toward -10 $mV_{E_{corr}}$ and then reversed to +10 $mV_{E_{corr}}$, followed by a negative scan to E_{corr}. Another set of PD tests was performed immediately after cleaning.

In all PD tests, the potential was scanned from -0.3 V with respect to E_{corr} to 1 V_{RHE}. The PD test sweep rate was 0.167 mV s^{-1}. Each experiment was repeated at least three times. For each experiment, a freshly prepared solution was used to ensure minimal decomposition of H_2O_2. Also, for the same purpose, the test flasks and experimental cells were covered with aluminum foil. The polarization experiments were repeated for stainless steels in acidic solutions.

6.2.3 Solution Analysis

In addition to electrochemical experiments, to evaluate the anodic dissolution at E_{corr}, ICP-OES measurement were also performed for acidic solutions. Every 2 h, during the immersion of the coupon in solution, 1 mL of solution was taken from the test solution, and the amount of iron in solution was measured using ICP-OES. Prior to the solution analysis, the test solution was digested using trace analytical grade nitric acid (Fisher Scientific) to dissolve any colloidal particles present. The dissolved iron concentration in the test solution was analyzed using a Perkin Elmer Avio 200 inductively coupled plasma optical emission spectrometer (ICP-OES). The ICP-OES measurement reports the concentration of iron, which may include any colloid particles, if present in the solution. ICP-OES can detect concentrations of iron as low 0.1 ppb, chromium as low as 0.1 ppb, and nickel as low as 0.1 ppb.

6.3 RESULTS AND DISCUSSION

6.3.1 Effect of H_2O_2 on Corrosion of CS in Low Ionic Strength Solutions (pH 6.0 buffered solution)

It is necessary to study both E_{corr} evolution and PD curves to understand the effect of H_2O_2 on the corrosion behaviour of CS. The evolutions of corrosion potentials of CS in H_2O_2 solutions in pH 6.0 buffered solutions over time are presented in two different time scales in **Figure 6-1.** The polarization behaviour of CS in pH 6.0 buffered solution was investigated in solutions with different $[H_2O_2]_0$ immediately after cleaning and then after 8 h E_{corr} measurement (see Figure 6-1**c** and Figure 6-1**d).**

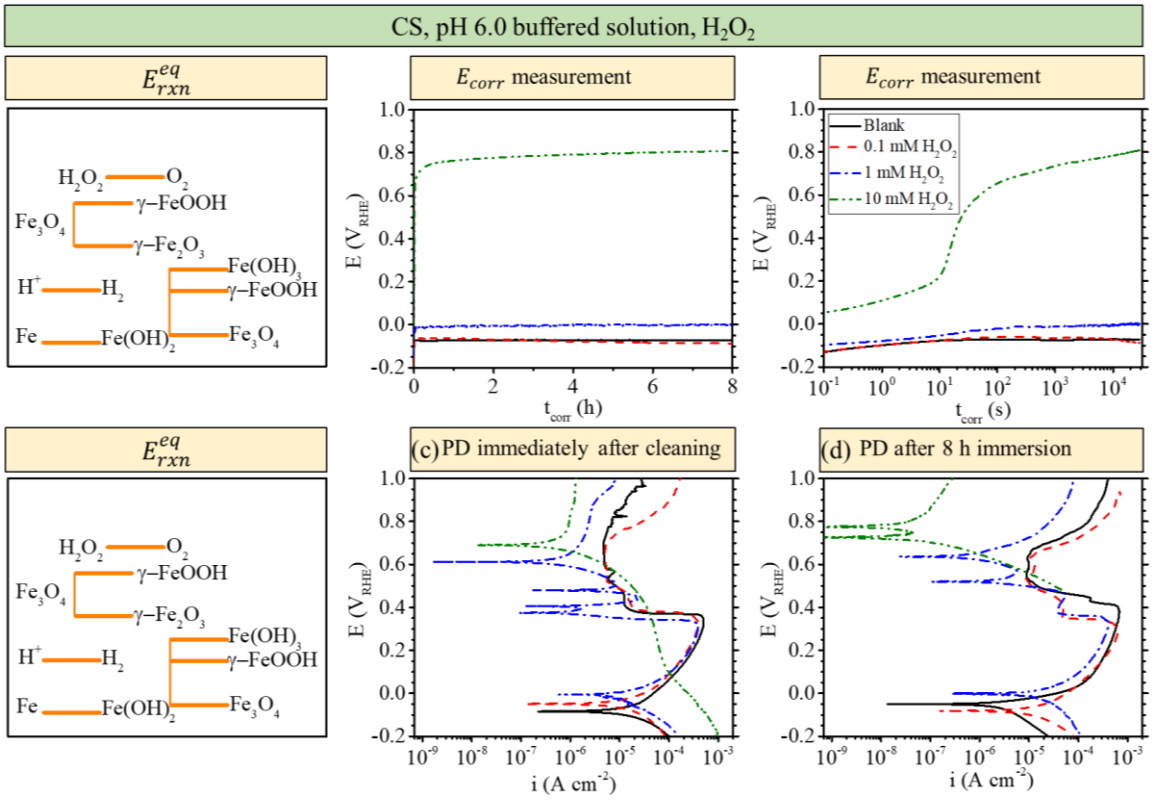

Figure 6-1: Corrosion behaviour of CS in pH 6.0 buffered solution containing different concentrations of H_2O_2. (a) E_{corr} of CS as a function of t_{corr}, (b) E_{corr} of CS as a function of t_{corr} (plotted in log scale); (c) PD experiments performed immediately after cathodic cleaning; (d) PD experiments performed after 8 h immersion. The E_{eq} of redox reactions in the potential range between -0.2 V and 1 V are presented on the left graph.

The key observations from the results presented in **Figure 6-1** are as follows:

- The E_{corr} vs t_{corr} curves in the blank (free of H_2O_2) solution and in the presence of 0.1 mM H_2O_2 were almost the same. The steady state E_{corr} values were close to $E^{eq}_{Fe^0 \rightleftharpoons Fe(OH)_2}$ and below the $E^{eq}_{Fe(OH)_2(\text{sat'd}) \rightleftarrows Fe_3O_4}$.
- Addition of 1 mM H_2O_2 resulted in a slight increase in both the initial and steady state E_{corr}. The initial E_{corr} and steady state values of E_{corr} were close to and above $E^{eq}_{Fe(OH)_2(\text{sat'd}) \rightleftarrows Fe_3O_4}$, respectively.

- In the presence of 10 mM H_2O_2, the initial E_{corr} was approximately 0.2 V higher than the initial E_{corr} in other solutions and gradually increased to 0.2 V_{RHE} until it jumped above 0.6 V_{RHE} and continued to increase. The E_{corr} in 10 mM H_2O_2 was about 0.8 V_{RHE} after 8 h which is above $E^{eq}_{Fe_3O_4 \rightleftarrows Fe_2O_3}$ and $E^{eq}_{\gamma-FeOOH \rightleftarrows Fe_2O_3}$, and also above $E^{eq}_{H_2O_2 \rightleftarrows O_2}$.
- In blank solution, the cathodic current at very negative potentials is generated by water reduction. The current density obtained from the PD after 8 h E_{corr} was 5 times smaller than from the PD performed immediately after 0 h E_{corr}.
- The addition of 0.1 mM H_2O_2 to pH 6.0 buffered solution did not affect the cathodic current density which indicates that the 0.1 mM H_2O_2 solution is not an effective oxidant.
- When 1 mM H_2O_2 was added to the solution, the redox overpotential for H_2O_2 was sufficiently high for the reduction of hydrogen peroxide slightly increased the cathodic current.
- At t_{corr}= 8 h the PD behaviours of CS in 0.1 mM and 1 mM H_2O_2 solutions are almost unchanged (see Figure 6-1**c**) and the only change over time was a slightly decreased cathodic current, and a slightly lower $E_{i=0}$ than those obtained from PD performed immediately after cleaning.
- In blank solution and 0.1 mM H_2O_2 solution, the $E_{i=0}$ obtained from the PD test immediately after cathodic cleaning, and after 8 h immersion were close to the values of E_{corr} at t_{corr}= 0 and at t_{corr}= 8 h, respectively.

- The anodic current density at very high overpotentials (at potentials above $E^{eq}_{H_2O_2 \rightleftarrows O_2}$) was higher in the 0.1 mM H_2O_2 than in the blank solution. However, a further increase in $[H_2O_2]_0$ (1 mM and 10 mM H_2O_2) decreased the anodic current density.
- In 1 mM H_2O_2 solution, multiple $E_{i=0}$ values were observed.
- In the PD curve immediately after cathodic cleaning in 10 mM H_2O_2 solution, only one $E_{i=0}$ was observed, located above $E^{eq}_{H_2O_2 \rightleftarrows O_2}$.
- In the PD curve obtained after 8 h E_{corr} measurement in 10 mM H_2O_2 solution, two $E_{i=0}$ was observed, located near and above $E^{eq}_{H_2O_2 \rightleftarrows O_2}$, respectively.
- The net anodic current density generally decreases with an increase in $[H_2O_2]_0$.

Hydrogen peroxide became the main oxidant for $[H_2O_2]_0$=10 mM. The current density of cathodic branch increased almost one decade when 10 mM H_2O_2 was present.

The Tafel analysis of PD curves for CS in buffered solution pH 6.0 containing different concentrations of H_2O_2 is presented in more detail in **Figure 6-2** for further discussion on the effect of hydrogen peroxide. The evolution of E_{corr} with t_{corr}, and PD curves obtained after 0 h and after 8 h of E_{corr} measurement are also presented for the purpose of comparison.

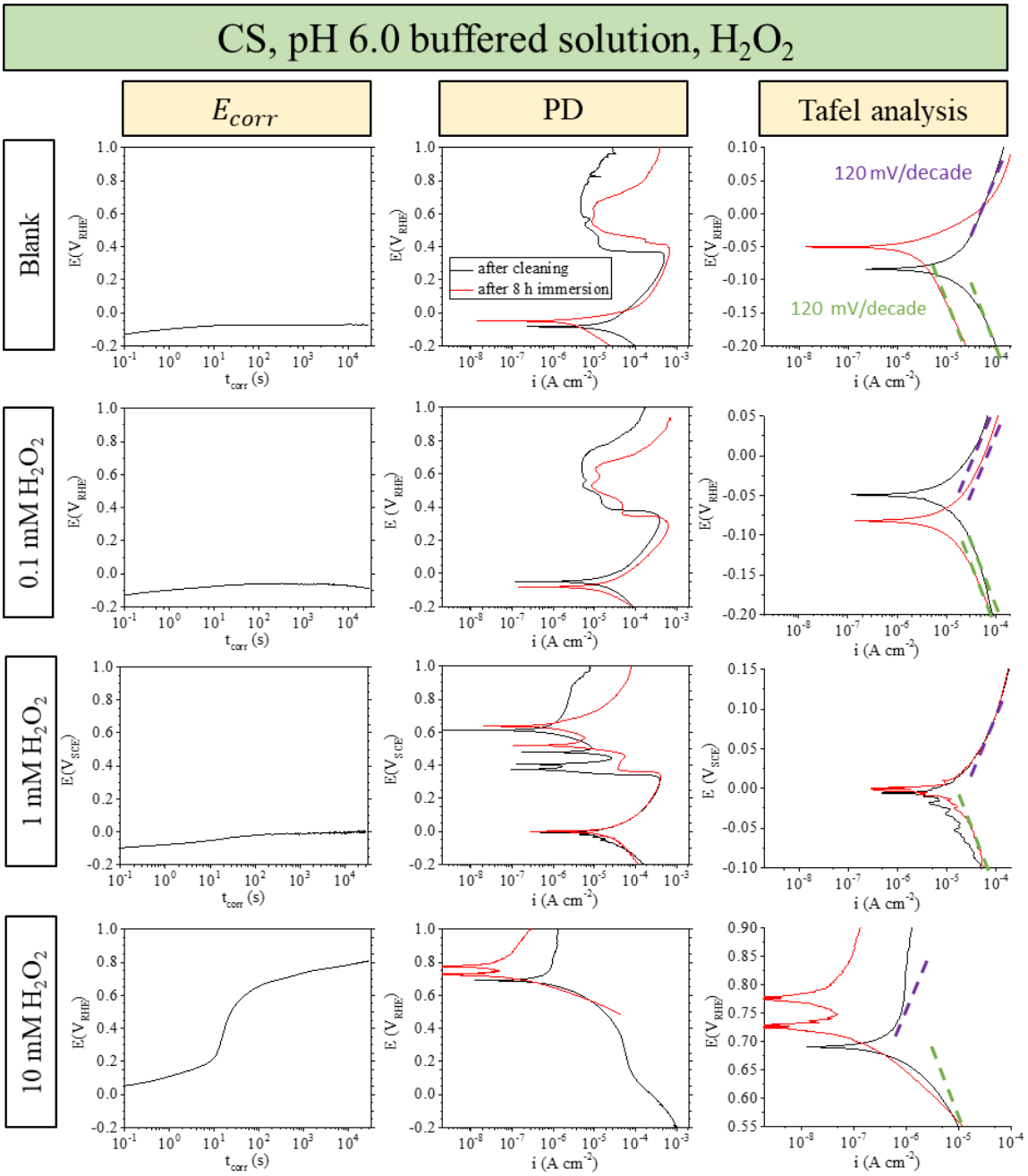

Figure 6-2: The evolution of E_{corr} with t_{corr}, PD curves after cathodic cleaning and after 8 h of E_{corr} measurment, and Tafel analysis of PD curves for CS in pH 6.0 buffered solution containing different H_2O_2 concentrations. The purple and green dashed lines are representative of anodic Tafel slope of 120 mV/decade and cathodic Tafel slope of 120 mV/decade, respectively.

This section discusses the corrosion behaviour of CS in H_2O_2-containing pH 6.0 buffered solutions.

The ionic strength of the solution does not have a direct influence on the interfacial charge transfer (i.e., on the redox half-reactions, metal oxidation and solution reduction in the near surface region) but rather affects the mass transport properties of the solution through its effect on ion mobility [30–34]. The low concentration gradients of redox-active species in buffered solution pH 6.0 with 10^{-4} M H_2O_2 arise from low mass transport conditions.

The dynamics of corrosion in the blank solution and the changes in E_{corr} with t_{corr} are discussed in **Chapter 4.** In blank solution, E_{corr} reached its 1st steady state close to $E^{eq}_{Fe^0 \rightleftharpoons Fe(OH)_2}$ and below $E^{eq}_{Fe(OH)_2(\text{sat'd}) \rightleftarrows Fe_3O_4}$ after 10 s and CS corrosion progressed towards **Stage 1,** where $Fe(OH)_2$ hydrogel forms. When PD is performed immediately after cleaning, corrosion is still in **Stage 0** (discussed in details in **Chapter 7)**, where the $Fe \rightarrow Fe^{2+}$ oxidation is followed by the transfer of metal cations, and the surface is free of hydroxide/oxide. Formation of a hydroxide gel layer, during 8-h E_{corr} measurement, can provide the conditions to limit the rate of water reduction.

At potentials above $E_{i=0}$, the anodic current densities obtained after 0 h and 8 h E_{corr} measurement showed a slope of ≈120 mV/decade, indicating a 1-electron transfer reaction ($Fe^{2+} \rightarrow Fe^{3+} + e^-$). During the positive scan, the oxidation of Fe^{II} to Fe^{III} results in the formation of $Fe(OH)_3$ within the $Fe(OH)_2/Fe(OH)_3$ solution, which limits the transfer of Fe cations, but further promotes the oxidation of Fe^{II} to Fe^{III}.

$E^{eq}_{H_2O_2 \leftrightarrow H_2O}$ in pH 6.0 in the presence of 10 mM H_2O_2 is 1.71 V_{RHE}. In 1 mM and

0.1 mM, the values of $E^{eq}_{H_2O_2 \leftrightarrow H_2O}$ are 1.68 V_{RHE} and 1.66 V_{RHE}, respectively (**Eq. 6-2**) [35]. Thus, the overpotential for the reduction of H_2O_2 is very large for the measured E_{corr} range in all tested solutions.

$$H_2O_2 + 2\ H^+ + 2\ e^- \leftrightarrows 2\ H_2O,\ E_{eq} = 1.77 + 0.03 \log [H_2O_2]\ (V_{RHH}) \qquad \textbf{(Eq. 6-2)}$$

Hydrogen peroxide can also be oxidized at lower potentials. Assuming the dissolved oxygen to be 0.1% in Ar-purged solution, the E^{eq} of the O_2/H_2O_2 reaction (**Eq. 6-3**) [35] is 0.65 V_{RHE} for 10 mM H_2O_2, 0.68 V_{RHE} 1 mM H_2O_2, and 0.71 V_{RHE} for 0.1 mM.

$$O_2 + 2\ H^+ + 2\ e^- \leftrightarrows H_2O_2,\ E_{eq} = 0.68 + 0.03 \log (P_{O2}/[H_2O_2])\ (V_{RHE}) \qquad \textbf{(Eq. 6-3)}$$

Hydrogen peroxide could undergo oxidation at potentials between $E^{eq}_{H_2O_2 \leftrightarrow H_2O}$ and $E^{eq}_{O_2 \leftrightarrow H_2O_2}$. It also has a negligible effect on the ionic strength; thus, the transfer process is not influenced by the addition of H_2O_2.

The results showed that 0.1 mM H_2O_2 is not an effective oxidant and has a negligible effect on the E_{corr} vs t_{corr}, PD behaviour and the current densities observed after 0-h E_{corr} measurement. However, the PD results performed after 8-h E_{corr} measurement showed that, when CS is polarized to negative potentials (when hydrogel has already formed at the surface), the cathodic current is comparable to the PD curve after 0-h E_{corr} measurement. The results indicate that hydrogen peroxide can be reduced at the hydrogel layer formed during the E_{corr} measurement which produces a current as large as in the PD after 8-h E_{corr} measurement, while the reduction of water on the hydrogel layer generates only a small current density.

In 1 mM H_2O_2 solution, the initial E_{corr} was slightly higher than for 0 and 0.1 mM H_2O_2 which indicates that hydrogen peroxide is an effective oxidant even for the oxidation of Fe to Fe^{II} when the surface is clean, and that oxidation of Fe is under 2-electron charge transfer. The accelerated oxidation of Fe to $Fe(OH)_2$ by H_2O_2, and consequently the formation of a $Fe(OH)_2/Fe(OH)_3$ hydrogel, provides the conditions for the oxidation of $Fe(OH)_2$ to $Fe(OH)_3$. For longer t_{corr} periods in 1 mM H_2O_2 solution, the E_{corr} approached a value above $E^{eq}_{\mathrm{Fe}(OH)_2 \rightleftarrows Fe_3O_4}$ while it remained in a potential range below $E^{eq}_{\mathrm{Fe}(OH)_2 \rightleftarrows Fe_3O_4}$ in blank and 0.1 mM H_2O_2 solutions. The decrease in the net anodic current density in 1 mM H_2O_2 relative to that in 0.1 mM H_2O_2 is associated with the reduction reaction. Solutions containing higher $[H_2O_2]_0$ have higher values of $E^{eq}_{H_2O_2 \rightleftarrows O_2}$. Thus, the sum of iron oxidation and H_2O_2 reduction is smaller in solutions containing higher $[H_2O_2]_0$, which results in lower net anodic current density.

A high concentration of H_2O_2 (10 mM H_2O_2) provides a sufficiently oxidizing environment to rapidly convert the hydrolyzed Fe^{II} and Fe^{III} into solid mixed Fe^{II}/Fe^{III} oxides. The formation of solid oxide shifts the E_{corr} toward the 2nd steady state, where the E_{corr} is closer to the $E^{eq}_{\mathrm{Fe}(OH)_2 \rightleftarrows Fe_3O_4}$ reaction, and the thermodynamic conditions for the conversion of Fe_3O_4 to Fe_2O_3 are met at potentials above $E^{eq}_{Fe_3O_4 \rightleftarrows Fe_2O_3}$ (0.361 V_{RHE}). γ-Fe_2O_3 is a semiconductor and limits the oxidation rate by generating a potential barrier for charge transfer reactions. The net current at significantly high potentials in the PD indicates the formation of a protective oxide at potentials close to the 2nd steady-state E_{corr} of CS in 10 mM H_2O_2.

In the PD curve obtained after the 0-h E_{corr} measurement in 10 mM H_2O_2

solution, unlike in the one for the 8-h E_{corr} measurement, only one $E_{i=0}$ was observed. However, at a potential lower than E_{corr}, a slight decrease in the cathodic current was observed. Although the net rates of the oxidation and reduction reactions are negative near E_{corr}, the rate of oxidation is high enough to provide the conditions for the rapid formation of the solid oxide, which results in a decrease in the oxidation rate. Because the rate of oxidation in the presence of an oxide barrier is very low, the current density remained negative until the potential reached values higher than $E^{eq}_{H_2O_2 \rightleftarrows O_2}$. Thus, only one $E_{i=0}$ was seen in the PD curve. The rate of CS corrosion in 10 mM H_2O_2 is the sum of the oxidation of H_2O_2 to O_2, reduction of H_2O_2 to H_2O, and oxidation of Fe.

The anodic and cathodic slopes in all solutions, except for 10 mM H_2O_2, was 120 mV decade^{-1}. This Tafel slope is indicative of 1-electron transfer reactions (H_2O/OH^- and Fe^{II}/Fe^{III} for reduction and oxidation reaction). For 10 mM H_2O_2, the oxidation reactions are predominantly H_2O_2 oxidation and Fe^{II} oxidation. The slope of the cathodic branch was close to 60 mV decade^{-1} which is an indication of the H_2O_2/H_2O 2-electron charge transfer reaction.

6.3.2 Effect of H_2O_2 on the Corrosion of CS in High Ionic Strength Solutions (H_2O_2 solution of pH 2.0)

The effect of H_2O_2 on the corrosion of CS in high ionic strength (10 mM NO_3^- and 100 mM NO_3^- nitrate at initial pH 2.0) was investigated using electrochemical techniques (E_{corr} measurements, PD tests, and LPR measurement) and solution analysis (ICP-OES). The results are presented in **Figure 6-3** and **Figure 6-4**.

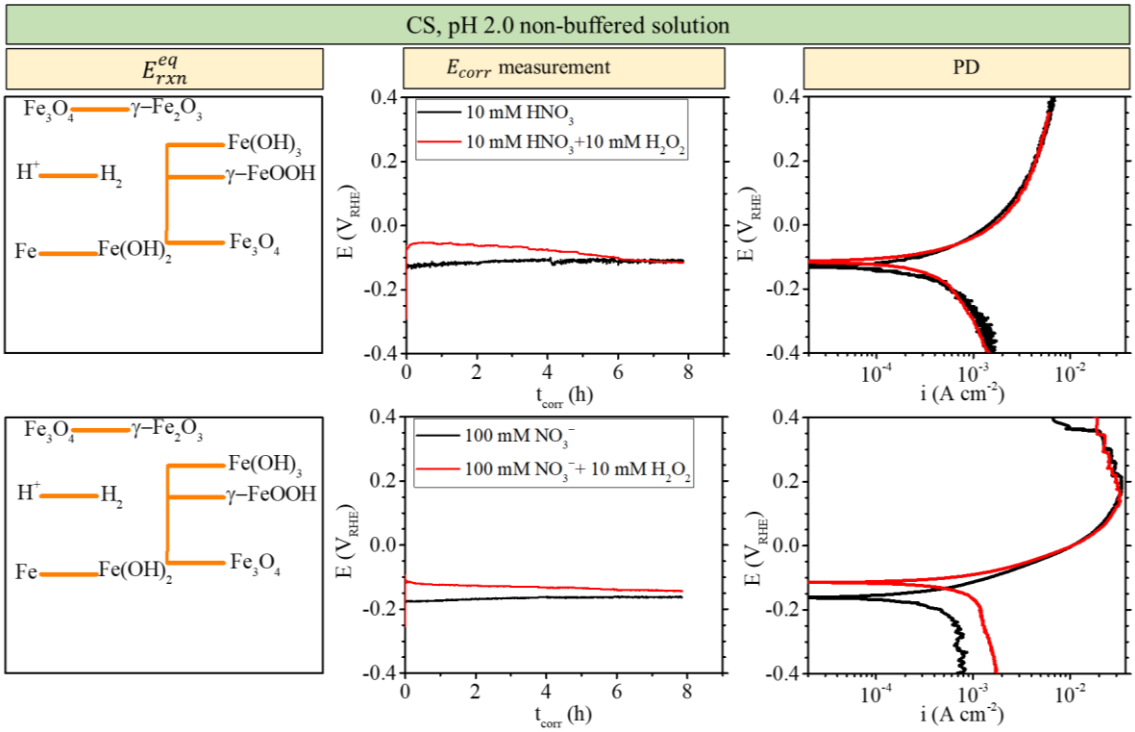

Figure 6-3: E_{corr} as a function of log(t_{corr}) and the PD curves for CS in 10 mM NO_3^- and 100 mM NO_3^- solution with initial pH 2.0, in the absence and presence of 10 mM H_2O_2: curves taken immediately after cathodic cleaning

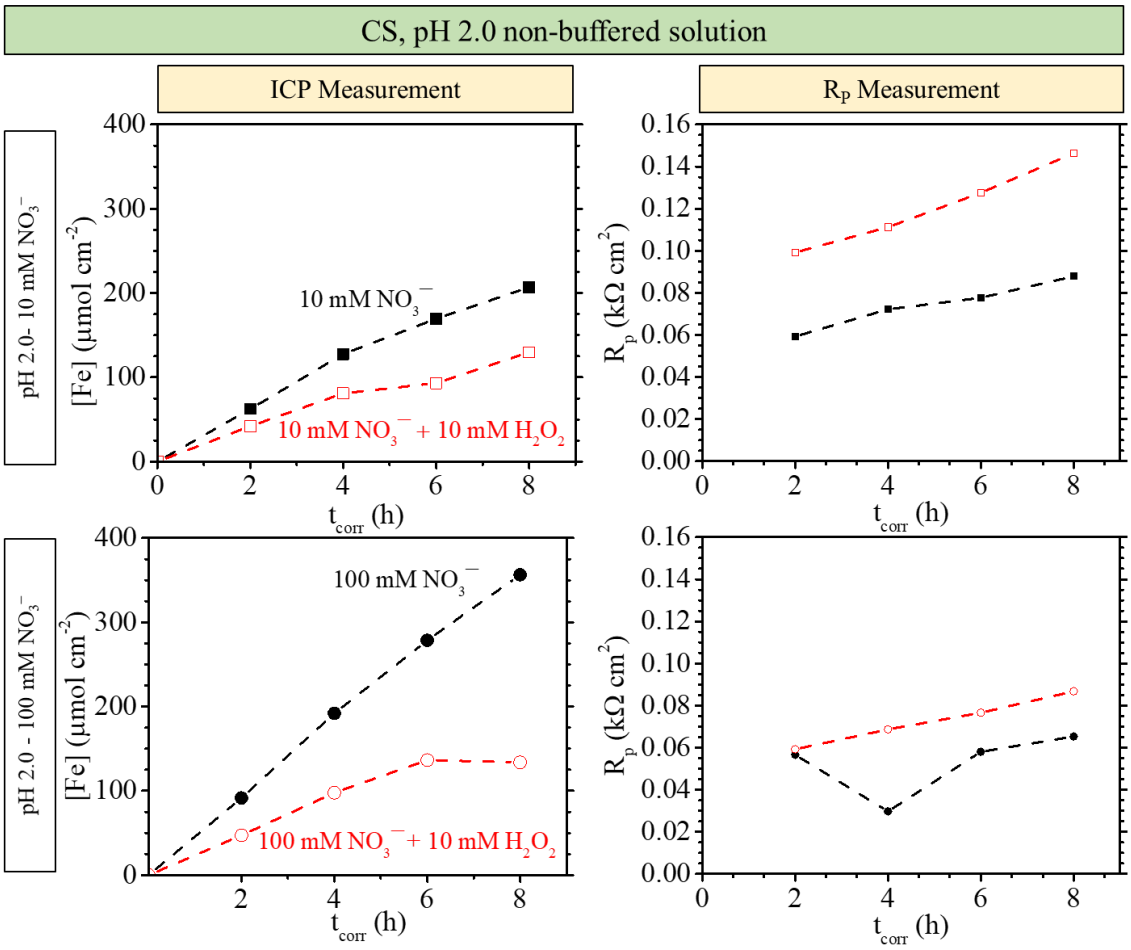

Figure 6-4: $[Fe]_{meas}$ and R_p as function of t_{corr} during corrosion of CS in 10 mM or 100 mM NO_3^- solution with initial pH 2.0 in the absence and presence of 10 mM H_2O_2.

The key observations from these experiments (presented in **Figure 6-3** and **Figure 6-4**.) are as follows:

In 10 mM NO_3^-:

- The steady state E_{corr} was -0.11 V_{RHE} in the presence and absence of H_2O_2 and was close to $E^{eq}_{Fe \leftrightarrows Fe(OH)_2}$. The E_{corr} after 8 h was close to the $E_{i=0}$ observed in the PD curves.

- In the absence or presence of H_2O_2, both the anodic and cathodic currents have the same values. The anodic Tafel slope was less than 120 mV/decade with and without H_2O_2.
- $[Fe]_{meas}$ increased almost linearly with t_{corr} in all solutions. The dissolution rates in the first 4 h were 31.9 μmol cm^{-2} h^{-1} and 20.3 μmol cm^{-2} h^{-1}, corresponding to 1.71×10^{-3} A cm^{-2} in solution without H_2O_2 and 1.09×10^{-3} A cm^{-2} in solution with H_2O_2.
- The values of R_P were generally higher in the presence of H_2O_2. R_P slightly increased with corrosion time in both solutions.

<u>In 100 mM NO_3^-:</u>

- The steady state E_{corr} values were -0.163 and -0.144 V_{RHE} in the absence and the presence of H_2O_2, respectively. These E_{corr} values were slightly below the value of E_{corr} in 10 mM nitrate solution and slightly below $E^{eq}_{Fe \leftrightarrows Fe(OH)_2}$. The values of $E_{i=0}$ were approximately 50 mV higher in the presence of H_2O_2.
- Addition of 10 mM H_2O_2 did not change the anodic branch, while it increased the cathodic current almost 2 times. The anodic Tafel slope was 120 mV $decade^{-1}$ in both the presence and absence of H_2O_2. Current densities plateaued above 100 mV.
- $[Fe]_{meas}$ increased almost linearly with t_{corr} in all solutions. The dissolution rates in first 4 h were 48.0 μmol cm^{-2} h^{-1} and 24.4 μmol cm^{-2} h^{-1} in the absence and presence of H_2O_2, respectively, corresponding to 2.57×10^{-3} A cm^{-2} and 1.31×10^{-3} A cm^{-2}. In the presence of H_2O_2, in the last 4 h of E_{corr} measurements, the dissolution rate slowed down.

- The value of R_P increased with t_{corr} (except for the decrease observed after 2 h in the absence of H_2O_2,) and was generally higher in the presence of H_2O_2. The R_P values in 100 mM NO_3^- were lower than those obtained in 10 mM NO_3^-.

6.3.2.1 Effect of hydrogen peroxide on corrosion of CS in nitric acid solutions

As discussed in **Chapter 4**, during corrosion of CS in 10 mM NO_3^-, the E_{corr} approaches a value close to $E^{eq}_{Fe \leftrightarrows Fe(OH)_2}$ suggesting that $Fe(OH)_2$ has formed, but the hydrogel at the interface has not become sufficiently saturated with Fe^{II} to form oxides. In 100 mM NO_3^- solutions, the E_{corr} is significantly below $E^{eq}_{Fe \leftrightarrows Fe(OH)_2}$, which suggests that the Fe^{II} saturation concentration in the interfacial region is not reached within the duration of the test.

An increase in $[NO_3^-]$ from 10^{-2} M to 10^{-1} M did not change the magnitude of the cathodic current but significantly increased the anodic current and decreased the anodic Tafel slope. Thus, an increase in the $[NO_3^-]$ at pH 2.0 does not affect the reduction rate, but rather increases the rate of oxidation via increasing the mass transfer rate of metal species, and increases the saturation capacity for Fe^{II} near the surface, which delays the formation of $Fe(OH)_2$. The results of these experiments showed that although H_2O_2 slightly increases the initial E_{corr}, the E_{corr} approaches the same value as in the absence of H_2O_2. The experiments performed in lower ionic strength (solutions of pH 6.0) suggested that 10 mM H_2O_2 is effective as an oxidant, and results in fast formation of a protective oxide, which consequently limits the oxidation of Fe and decreases the Fe oxidation current. However, the results at pH 2.0 indicated that, even in the presence of 10 mM H_2O_2, the mass transport in 10 mM NO_3^- and 100 mM NO_3^- is fast, and the

corrosion products can rapidly transport away from the metal surface into the bulk solution, preventing their accumulation and the formation of an extensive hydrogel network; Thus, in the absence of a dense hydrogel layer, the presence of 10 mM H_2O_2 cannot further increase the E_{corr} to the potentials where the formation of a protective oxide limits the oxidation to the extent that the E_{corr} is controlled mainly by the oxidation and reduction of hydrogen peroxide (as observed in pH 6.0 buffered solution).

The PD tests showed that hydrogen peroxide increases the cathodic current in 100 mM NO_3^-, indicating that H_2O_2 is reduced to H_2O under negative applied potentials. However, when CS is naturally corroding during E_{corr} measurements, hydrogen peroxide reduction cannot be effectively coupled with the oxidation of iron unless iron cations can accumulate at the surface and form a solid phase. When the potential was scanned toward positive potentials in 10 mM NO_3^- and 100 mM NO_3^-, Fe^{II} continued to diffuse out towards the bulk solution in the acidic environment; thus, conditions for the formation of a dense gel layer could not be met.

While oxide formation is negligible under naturally corroding conditions, when H_2O_2 is present, the rate of change of $[Fe]_{meas}$ is lower than in the solution without H_2O_2 and decreases with t_{corr}, due to continuous oxide formation inside the hydrogel. The lower slope of $[Fe]_{meas}$ vs t_{corr}, and higher R_p in the presence of H_2O_2 can be attributed to the formation of $Fe(OH)_2/Fe_3O_4/FeOOH$.

6.3.3 Effect of H_2O_2 on Corrosion of Stainless Steels in High Ionic Strength Acidic Solutions

The effect of H_2O_2 on the electrochemical behaviour of 304L SS and 309 SS

(10 mM NO_3^- and 100 mM NO_3^- nitrate at initial pH 2.0) was investigated using electrochemical techniques (E_{corr} measurements, PD tests, and LPR measurement) and solution analysis (ICP-OES). The results are presented in **Figure 6-5** and Figure 6-6. To investigate the effect of H_2O_2 on the corrosion of 304L SS, and 309 SS, $[Fe]_{meas}$, $[Ni]_{meas}$ and $[Cr]_{meas}$ as function of t_{corr}, in 10 mM NO_3^- and 100 mM NO_3^-, were compared for solutions with and without H_2O_2 (**Figure 6-7)**.

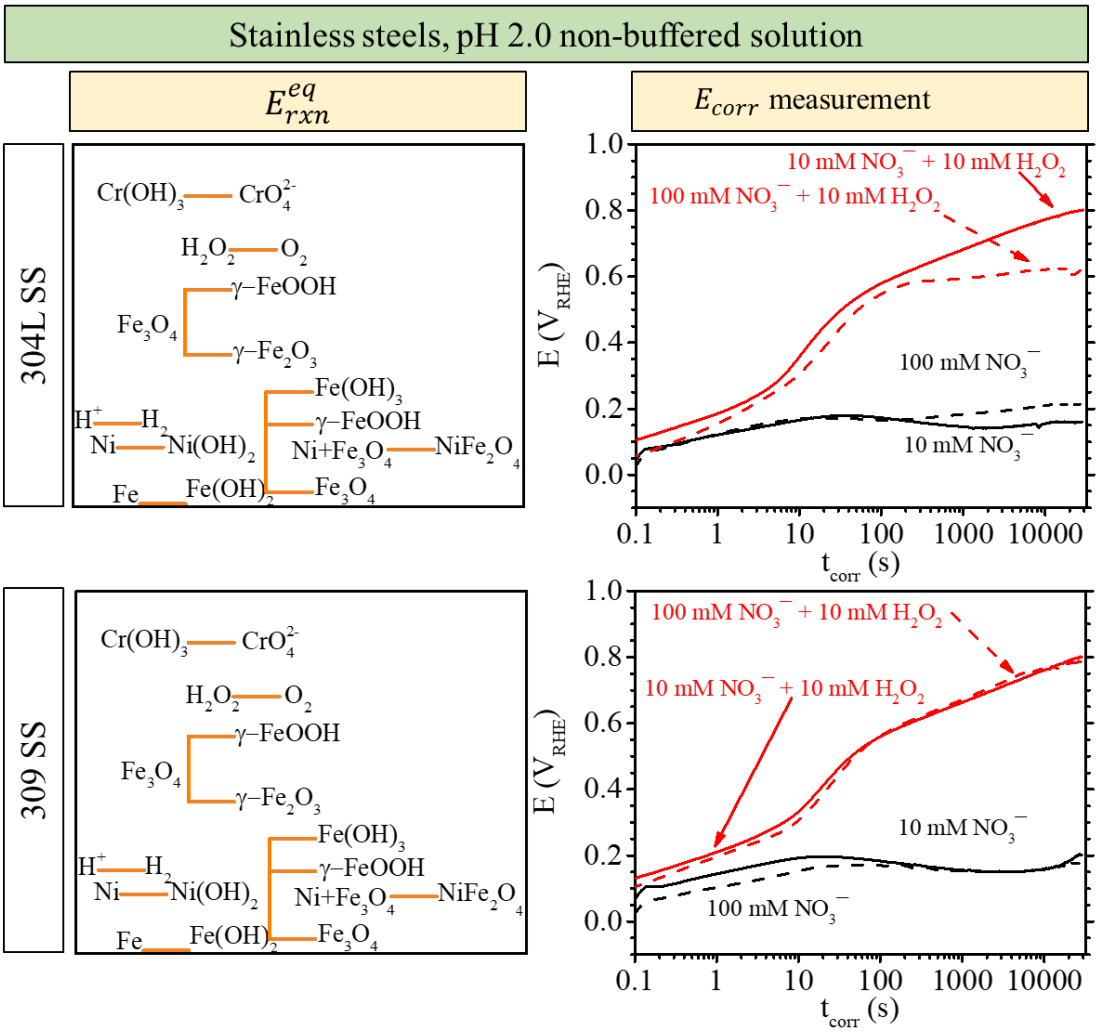

Figure 6-5: E_{corr} as a function of log(t_{corr}) for 304L SS and 309 SS in NO_3^- -containing pH 2.0 buffered solutions, in the absence and the presence of 10 mM H_2O_2. Tests taken immediately after cathodic cleaning.

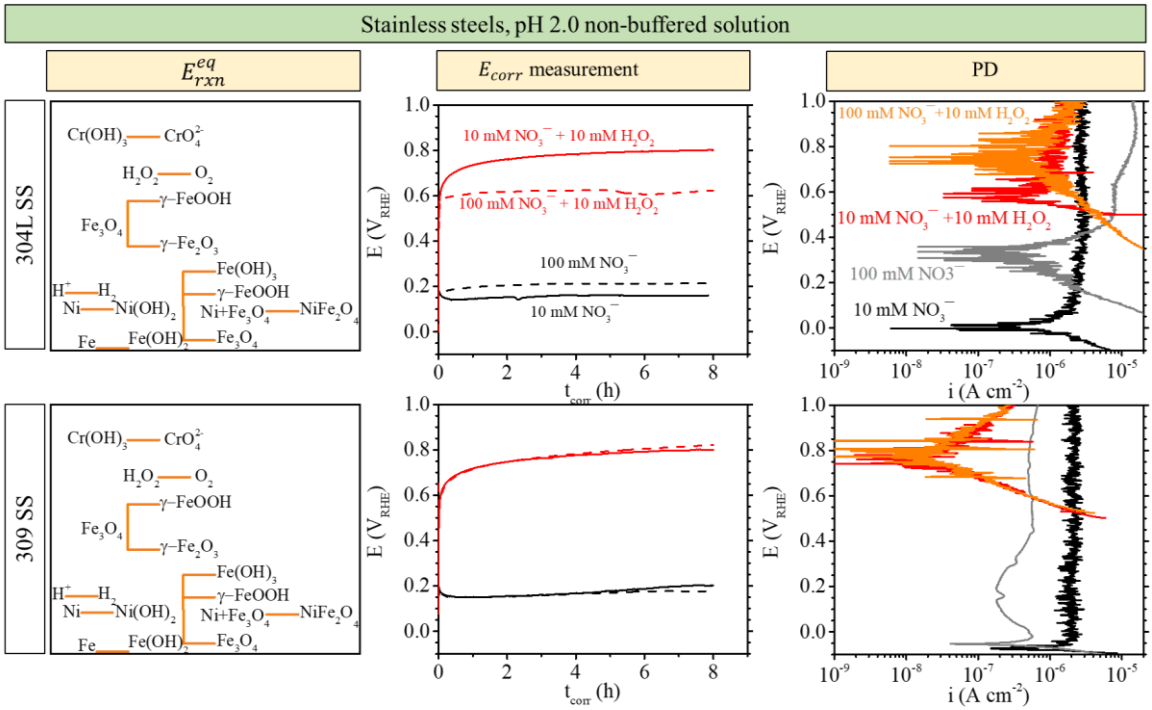

Figure 6-6: E_{corr} of as a function of t_{corr} and PD for 304L SS and 309 SS in nitrate-containing pH 2.0 non-buffered solution, in the absence and the presence of 10 mM H_2O_2. Tests were performed immediately after 8 h E_{corr} measurement.

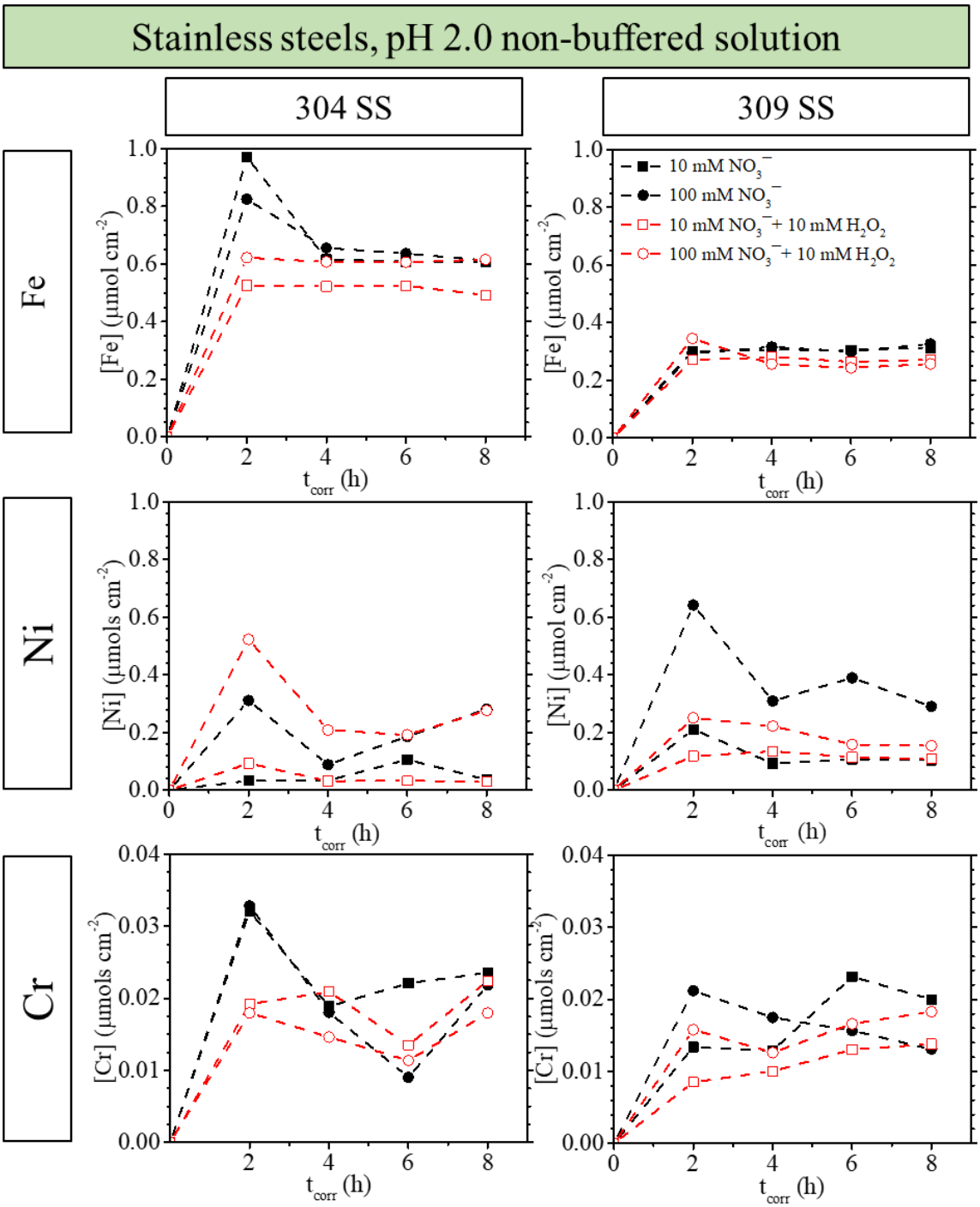

Figure 6-7: $[Fe]_{meas}$, $[Ni]_{meas}$, and $[Cr]_{meas}$ as a function of t_{corr} during corrosion of 304L SS and 309 SS in NO_3^--containing pH 2.0 non-buffered solutions, in the presence and absence of 10 mM H_2O_2.

The key observations from the results of these E_{corr} measurements, PD

measurements, and ICP-OES results (presented in **Figure 6-5**, **Figure 6-6**, and **Figure 6-7**) are as follows:

- For both 304L SS and 309 SS, the E_{corr} vs log (t_{corr}) curves were initially similar in all solutions. It should be noted that the initial $E_{corr}$was slightly higher in the presence of H_2O_2.
- In the absence of H_2O_2, E_{corr} approached $E^{eq}_{Ni \leftrightarrows Ni(OH)_2}$ and $E^{eq}_{Fe(OH)_2 \leftrightarrows \gamma-FeOOH}$ but remained below $E^{eq}_{Fe(OH)_2 \leftrightarrows Fe(OH)_3}$.
- For 304L SS, the presence of 10 mM H_2O_2 resulted in a rapid increase in the E_{corr}. The E_{corr} reached its 2nd steady-state after 100 s in 100 mM NO_3^- (close to the $E^{eq}_{Fe_3O_4 \leftrightarrows \gamma-FeOOH}$), while approaching the higher value of 0.8 V_{RHE} (close to the $E^{eq}_{Cr(OH)_3 \leftrightarrows CrO_4^{2-}}$) in 10 mM NO_3^-.
- For 309 SS in 100 mM NO_3^-, the addition of 10 mM H_2O_2 increased the initial E_{corr} to a value above $E^{eq}_{Fe_3O_4 \leftrightarrows \gamma-FeOOH}$. The E_{corr} then dropped more than 200 mV within 20 s, and increased again to a value close to that observed for 304L SS.
- For both alloys in 10 mM HNO_3 + 10 mM H_2O_2,, and for 309 SS in 100 mM HNO_3+10 mM H_2O_2, E_{corr} increased to a potential above $E^{eq}_{H_2O_2 \leftrightarrows O_2}$, at which the oxidation of H_2O_2 becomes the dominant oxidation reaction. For 304L SS, in 100 mM HNO_3+10 mM H_2O_2, mass transfer of cations is sufficiently fast that E_{corr} remains at a potential below $E^{eq}_{H_2O_2 \leftrightarrows O_2}$.
- For both 304L SS and 309 SS, the anodic regions of all PD curves showed passive behaviours. The passive region in the presence of H_2O_2 is smaller than in its absence. For 309 SS the anodic current density for10 mM nitrate solution (~2×10^{-6} A cm^{-2}) is

the highest among all the solutions. The addition of 90 mM nitrate or 10 mM H_2O_2 decreased the current density.

- For 309 SS in the presence of H_2O_2 the $E_{i=0}$ was the same as E_{corr}, whereas the $E_{i=0}$ values were 200 mV lower (in 10 mM NO_3^-) or higher (in 100 mM NO_3^-) than E_{corr} for 304L SS. Note that the results in the absence of hydrogen peroxide were previously discussed in **Chapter 5**.
- For both concentrations of nitrate and for both stainless steels, hydrogen peroxide had a negligible effect on the trend of changes in $[Fe]_{meas}$, $[Ni]_{meas}$ and $[Cr]_{meas}$.
- For 309 SS, the concentrations of dissolved metals were not affected by H_2O_2 addition. However, over 2 h of corrosion, H_2O_2 slightly increased the rate of change of $[Ni]_{meas}$ and slightly decreased the rates of change of $[Fe]_{meas}$ and $[Cr]_{meas}$. The plot of $[Cr]_{meas}$ vs. time remained almost unchanged upon addition of H_2O_2.
- For 309 SS, the concentrations of dissolved metals were not affected by H_2O_2 addition except in the case of $[Ni]_{meas}$.

6.3.3.1 Effect of hydrogen peroxide on the corrosion of stainless steels in nitric acid solutions

The corrosion of stainless steels in 10 mM and 100 mM NO_3^- pH 2.0 non-buffered solutions without H_2O_2 was discussed in detail in **Chapter 5**. A mechanism proposed for Alloy 800 corrosion [36] was used to describe the oxidation of stainless steels in nitrate solution. The effect of hydrogen peroxide on the rates of each intermediate step is discussed here; however, the steps themselves, and therefore the overall mechanism, should be the same.

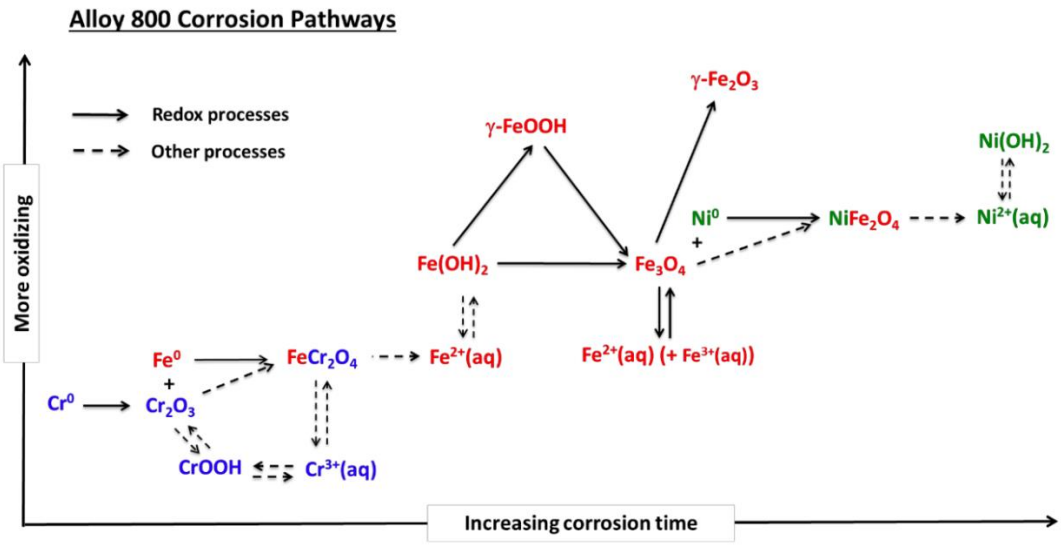

Figure 6-8: Proposed mechanism for Alloy 800 corrosion [36].

Immediately after cathodic cleaning in 10 mM NO_3^- or 100 mM NO_3^- pH 2.0 non-buffered solutions, the E_{corr} values of both stainless steels approached a steady state value close to $E^{eq}_{Fe(OH)_2 \leftrightarrows \gamma-FeOOH}$, which is below $E^{eq}_{Cr^{III} \leftrightarrows Cr^{VI}}$, and above $E^{eq}_{Fe_3O_4 \leftrightarrows \gamma-FeOOH}$ and $E^{eq}_{Ni \leftrightarrows Ni^{II}\ (NiFe_2O_4 \text{ and } Ni(OH)_2)}$, indicating that 10 mM NO_3^- and 100 mM NO_3^- solutions are sufficiently oxidizing to form Ni^{II} oxide/hydroxide on stainless steel surfaces from which Ni^{2+} can dissolve out. All three iron (hydr)oxides ($Fe(OH)_2$, Fe_3O_4 and γ-FeOOH) are also thermodynamically stable at the final values of E_{corr}. Addition of 10 mM H_2O_2 to nitric acid solutions does not affect the initial E_{corr} of stainless steels. However, in the presence of H_2O_2, the E_{corr} of 304L SS and 309 SS shifts toward a higher value.

For both alloys, in all solutions, oxidation of metal cations from the surface is followed by hydration, hydrolysis, and diffusion of the cations. Chromium oxide (Cr_2O_3) can remain on the surface as the previously air-formed oxide. The presence of Cr_2O_3 can

provide a large potential barrier that can significantly lower the interfacial metal oxidation rate for the oxidation of $Fe \rightleftharpoons Fe^{2+}$ and $Ni \rightleftharpoons Ni^{2+}$. The oxidation of Fe produces Fe^{II} species which react with Cr_2O_3 to form $FeCr_2O_4$. The formation of this iron chromate oxide is followed by the rapid oxidation of Fe^{II} to Fe^{III} to form Fe_3O_4 and FeOOH. In the presence of H_2O_2, the rate of oxidation is increased, and the maximum $[Fe]_{meas}$ (occurring at 2 h) was lower than in its absence, indicating that oxide formation was accelerated by H_2O_2. The increase in the E_{corr} in H_2O_2 solution provides the conditions for Ni to Ni^{II} oxidation to be thermodynamically possible, which leads to the formation of an iron spinel oxide ($NiFe_2O_4$), and finally $NiO/Ni(OH)_2$. The dissolved ions can diffuse out into the solution phase while they are in equilibrium with the oxides. When hydrogen peroxide was present, the slope of $[Ni]_{meas}$ vs t_{corr} in the first 2 h was higher than in its absence, which could indicate faster oxidation of Ni to Ni^{II}. The further increase in the E_{corr} of stainless steels in the presence of hydrogen peroxide relative to in nitric acid solutions can be attributed to the growth of $NiFe_2O_4$.

Dissolved cations can diffuse out from the interfacial region toward the solution. Thus, the concentration of metal cations increases until the saturation limit of these species is reached, and hydroxide and oxide formation become dominant. This results in $[Fe]_{meas}$, $[Ni]_{meas}$, and $[Cr]_{meas}$ remaining constant with t_{corr}.

6.4 SUMMARY

The electrochemical behaviours of CS, 304L SS and 309 SS were investigated by initial addition of hydrogen peroxide in pH 6.0 buffered and pH 2.0 nitric acid solutions.

The corrosion of these alloys was then assessed using solution analysis methods. The results presented in this chapter have improved the understanding of how hydrogen peroxide (key product of water radiolysis) can affect carbon steel and stainless steels corrosion.

The corrosion study of CS, 304L SS, and 309 SS in the combined presence of nitrate and hydrogen peroxide gives us insight into their corrosion in the presence of water and humid air radiolysis products. This analysis also demonstrates the role of hydrogen peroxide concentration as a potential oxidant when the ionic strength of the solution is low, and mass transport is slow, as well as in conditions where the ionic strength is high and another oxidant (nitrate) is present.

In pH 6.0 buffered solutions, the addition of a small amount of 10^{-4} M H_2O_2 does not change the corrosion potential and the PD behaviour of CS. A more oxidizing environment (10^{-3} M H_2O_2), however, significantly increases the E_{corr} and changes the electrochemical behaviour of CS. In the presence of high concentrations of hydrogen peroxide (10 mM H_2O_2), the corrosion potential is controlled by the redox reaction of H_2O_2 rather than by the metal oxidation and solution species redox reactions.

It was concluded that for $[H_2O_2]_0<10^{-2}$ M, E_{corr} is determined by the cathodic current of the H_2O_2/OH^- reduction reaction, coupled with the anodic current of the iron oxidation half-reaction. On the other hand, for $[H_2O_2]\geq10^{-2}$ M, E_{corr} is likely to be determined primarily by the cathodic half-reactions of H_2O_2, coupled with the anodic half-reactions of H_2O_2.

In acidic solutions, CS corrosion is not influenced by the addition of H_2O_2 to nitric

acid solutions, except for the fact that it decreases the rate of change of $[Fe]_{meas}$, which indicates that it accelerates oxide formation while not affecting the net rate of oxidation. This finding revealed the role of mass transport in the corrosion process. While hydrogen peroxide was identified as an effective oxidant in low ionic strength solutions, when mass transport is fast, in the high ionic solutions with the same concentration of hydrogen peroxide, oxide formation does not occur, as observed in the buffered solutions.

The corrosion of the tested stainless steels is highly affected by the addition of hydrogen peroxide. Unlike in nitric acid solutions, in more oxidizing solutions at the same ionic strength (i.e., when 10 mM hydrogen peroxide solution was added to nitric acid), the saturation of the surface can immediately occur, which limits surface oxidation by limiting the mass transfer of metal ions to the solution phase. This oxide formation shifts the E_{corr} to the equilibrium potential of the H_2O_2 oxidation reaction. The difference between CS corrosion and stainless steel corrosion in a similar environment was attributed to the different oxides that form on the surface.

Although addition of 10 mM H_2O_2 to the non-buffered pH 2.0 solution containing 10 mM and 100 mM NO_3^- increases the E_{corr} of both 304L SS and 309 SS, it has no significant effect on $[Fe]_{meas}$, $[Ni]_{meas}, and\ [Cr]_{meas}$ despite the difference in the composition of these two types of stainless steels.

The results presented in this chapter demonstrate how corrosion of CS, 304L SS and 309 SS are affected by hydrogen peroxide concentration, the combination of hydrogen peroxide and nitrate and the role of ionic strength. It was concluded that while hydrogen peroxide is a strong oxidant and its influence on the corrosion, metal dissolution and oxide formation on both stainless steels is marked, for CS ion transfer plays a more

important role in the corrosion pathway. These results will be particularly important for interpreting the results presented in **Chapter 7** and **Chapter 8** where the corrosion of CS, 304L SS and 309 SS, and the CS-309 SS weld joint are studied in the presence of gamma radiation. In the following chapters, and based on the results presented in this chapter and **Chapter 4** and **Chapter 5**, the role of radiolytic hydrogen peroxide and nitric acid on the corrosion pathways can be explained as a function of time and cover gas composition.

6.5 REFERENCES

[1] J.W.T. Spinks, R.J. Woods, An introduction to radiation chemistry, John Wiley and Sons Inc, United States, 1990.

[2] R.P. Morco, J.M. Joseph, D.S. Hall, C. Medri, D.W. Shoesmith, J.C. Wren, Modelling of radiolytic production of HNO_3 relevant to corrosion of a used fuel container in deep geologic repository environments, Corros. Eng. Sci. Technol. 52 (2017) 141–147.

[3] Y.G. Shin, Nonlinear Dynamics of Carbon Steel Corrosion under Gamma Radiation, PhD Thesis, The University of Western Ontario, 2020.

[4] Farhataziz, M.A.J. Rodgers, eds., Radiation chemistry: principles and applications, VCH Publishers, United States, 1987.

[5] J.H. O'Donnell, D.F. Sangster, Principles of Radiation Chemistry, American Elsevier Publishing Company, 1970.

[6] J.C. Wren, Steady-State Radiolysis: Effects of Dissolved Additives, in: C.M. Wai1, B.J. Mincher (Eds.), Nucl. Energy Environ., American Chemical Society, 2010: pp. 271–295.

[7] I.C. Draganic, Z.D. Draganic, The Radiation Chemistry of Water, Academic Press, 1971.

[8] J.C. Wren, J. Ball, LIRIC 3.2 an updated model for iodine behaviour in the presence of organic impurities, Radiat. Phys. Chem. 60 (2001) 577–596.

[9] J.M. Joseph, B.S. Choi, P. Yakabuskie, J.C. Wren, A combined experimental and model analysis on the effect of pH and O_2(aq) on γ-radiolytically produced H_2 and H_2O_2, Radiat. Phys. Chem. 77 (2008) 1009–1020.

[10] P. Driver, G. Glowa, J.C. Wren, Steady-state γ-radiolysis of aqueous methyl ethyl ketone (2-butanone) under postulated nuclear reactor accident conditions, Radiat. Phys. Chem. 57 (2000) 37–51.

[11] J.C. Wren, G.A. Glowa, A simplified kinetic model for the degradation of 2-butanone in aerated aqueous solutions under steady-state gamma-radiolysis, Radiat. Phys. Chem. 58 (2000) 341–356.

[12] P.A. Yakabuskie, J.M. Joseph, C.R. Stuart, J.C. Wren, Long-Term γ-Radiolysis Kinetics of NO_3^- and NO_2^- Solutions, J. Phys. Chem. A. 115 (2011) 4270–4278.

[13] P.A. Yakabuskie, J.M. Joseph, P. Keech, G.A. Botton, D. Guzonas, J.C. Wren, Iron oxyhydroxide colloid formation by gamma-radiolysis, Phys. Chem. Chem. Phys. 13 (2011) 7198–7206.

[14] P.A. Yakabuskie, J.M. Joseph, J. Clara Wren, The effect of interfacial mass transfer on steady-state water radiolysis, Radiat. Phys. Chem. 79 (2010) 777–785.

[15] O. Roth, J.A. Laverne, Effect of pH on H_2O_2 production in the radiolysis of water, J. Phys. Chem. A. 115 (2011) 700–708.

[16] K. Daub, A Study of Gamma Radiation Induced Carbon Steel Corrosion, PhD Thesis, The University of Western Ontario, 2013.

[17] K. Daub, X. Zhang, J.J. Noël, J.C. Wren, Effects of γ-radiation versus H_2O_2 on carbon steel corrosion, Electrochim. Acta. 55 (2010) 2767–2776.

[18] J.R. Rumble, T.J. Bruno, M.J. Doa, CRC handbook of chemistry and physics : a ready-reference book of chemical and physical data, 2020.

[19] M. Behazin, J.J. Noël, J.C. Wren, Combined effects of pH and γ-irradiation on the corrosion of Co-Cr alloy stellite-6, Electrochim. Acta. 134 (2014) 399–410.

[20] W. Xu, K. Daub, X. Zhang, J.J. Noel, D.W. Shoesmith, J.C. Wren, Oxide formation and conversion on carbon steel in mildly basic solutions, Electrochim. Acta. 54 (2009) 5727–5738.

[21] A.Y. Musa, J.C. Wren, Combined effect of gamma-radiation and pH on corrosion of Ni-Cr-Fe alloy inconel 600, Corros. Sci. 109 (2016) 1–12.

[22] R.P. Morco, A.Y. Musa, M. Momeni, J.C. Wren, Corrosion of carbon steel in the [P14666][Br] ionic liquid: The effects of γ-radiation and cover gas, Corros. Sci. 102 (2016) 1–15.

[23] D. Guo, Corrosion Dynamics of Carbon Steel in Used Fuel Container Corrosion Dynamics of Carbon Steel in Used Fuel Container Environments Environments, PhD Thesis, The University of Western University, 2018.

[24] L. Wu, D. Guo, M. Li, J.M. Joseph, J.J. Noël, P.G. Keech, J.C. Wren, Inverse Crevice Corrosion of Carbon Steel: Effect of Solution Volume to Surface Area, J. Electrochem. Soc. 164 (2017) C539–C553.

[25] M. Behazin, M.C. Biesinger, J.J. Noël, J.C. Wren, Comparative study of film formation on high-purity Co and Stellite-6: Probing the roles of a chromium oxide layer and gamma-radiation, Corros. Sci. 63 (2012) 40–50.

[26] Q.W. Knapp, J.C. Wren, Film formation on type-316L stainless steel as a function of potential: Probing the role of gamma-radiation, Electrochim. Acta. 80 (2012) 90–99.

[27] K. Daub, X. Zhang, J.J. Noël, J.C. Wren, Gamma-radiation-induced corrosion of carbon steel in neutral and mildly basic water at 150 °C, Corros. Sci. 53 (2011) 11–16.

[28] M. Behazin, Radiation Induced Corrosion of Stellite-6, The University of Western Ontario, 2014.

[29] K. Daub, X. Zhang, J.J. Noël, J.C. Wren, Gamma Radiation-Induced Carbon Steel Corrosion, ECS Trans. 33 (2011) 15–24.

[30] M. Rousseau, L. Di Pietro, R. Angulo-Jaramillo, D. Tessier, B. Cabibel, Preferential Transport of Soil Colloidal Particles: Physicochemical Effects on Particle Mobilization, Vadose Zo. J. 3 (2004) 247–261.

[31] C. Wang, R. Wang, Z. Huo, E. Xie, H.E. Dahlke, Colloid transport through soil and other porous media under transient flow conditions—A review, Wiley Interdiscip. Rev. Water. 7 (2020) e1439.

[32] J.E. Saiers, J.J. Lenhart, Ionic-strength effects on colloid transport and interfacial reactions in partially saturated porous media, Water Resour. Res. 39 (2003) 1256.

[33] J. Won, S.E. Burns, Influence of Ionic Strength on Clay Particle Deposition and Hydraulic Conductivity of a Sand Medium, J. Geotech. Geoenvironmental Eng. 143 (2017) 04017081.

[34] J.E. Saiers, G.M. Hornberger, The influence of ionic strength on the facilitated transport of cesium by kaolinite colloids, Water Resour. Res. 35 (1999) 1713–1727.

[35] J.O.M. Bockris, L.F. Oldfield, The oxidation-reduction reactions of hydrogen peroxide at inert metal electrodes and mercury cathodes, Trans. Faraday Soc. 51 (1955) 249–259.

[36] M. Momeni, Gamma-Radiation Induced Corrosion of Alloy 800, PhD Thesis, The University of Western Ontario, 2017.

CHAPTER 7
CORROSION DYNAMICS OF CARBON STEEL IN SMALL VOLUME SOLUTIONS

7.1 INTRODUCTION

The annular air gap around the periphery of the calandria tank assembly and its supporting structures in the nuclear CANDU reactor are exposed to a continuous flux of γ-radiation (which has the largest penetration depth of the three types of ionizing radiation (α- γ-, and β-rays) [1]) and could contain small volumes of stagnant water or be exposed to humid air. When ionizing radiation is present, water is decomposed to redox-active species such as H_2O_2 and •OH [1,2] (**Eq. 7-1**), and humid air radiolysis produces HNO_3, which eventually dissolves into the small volume stagnant water layer [3,4] (**Eq. 7-2**).

$$H_2O \xrightarrow{\gamma} \bullet OH, \bullet e_{aq}^-, \bullet H, H_2, H_2O_2, H^+ \qquad \textbf{(Eq. 7-1)}$$

$$N_2, O_2, H_2O \rightarrow^{\gamma}\rightarrow \bullet H, \bullet OH, \bullet N, \bullet O, H_2, O_2, H_2O_2, O_3, NO_x, HNO_3 \qquad \textbf{(Eq. 7-2)}$$

These species can participate in the corrosion process and affect the corrosion behaviour of CS [5,6].

Corrosion involves many electrochemical and chemical reactions, which are coupled with interfacial transfer and solution transport of metal cations [7,8]. The overall corrosion rate is determined by the rates of the elementary steps involved in the corrosion process, and the solution parameters affecting the rates of the elementary processes [9–11]. In previous chapters, the effect of chemically added HNO_3 and H_2O_2 on the corrosion behaviour of CS was studied using electrochemical methods. The small solution volumes are expected to be rapidly saturated with the initial corrosion products, and the subsequent reactions of dissolved metal cations and metal hydroxide/oxide formation and growth can be complex. These chemical processes can strongly affect the corrosion dynamics. In this chapter, the oxide growth and corrosion evolution were investigated via coupon exposure studies in solutions initially containing different concentrations of chemically added radiolysis products (i.e., HNO_3 or H_2O_2). The coupling between the charge transfer reactions and the diffusion kinetics was studied by monitoring the dissolved concentration of iron using inductively coupled plasma-optical emission spectroscopy (ICP-OES). The evolution of the surface during corrosion was studied using optical and scanning electron microscopy. The chemical composition of the oxide was characterized using Raman spectroscopy. All experiments in this chapter were performed in small volume solutions (150 μL and 89 μL for carbon steel and pure iron coupons, respectively), with different initial concentrations of nitric acid or hydrogen

peroxide. The small water volumes were chosen because they represent the conditions that carbon steel in annular gap in the calandria tank assembly will experience in the presence of humid air.

7.2 EXPERIMENTAL PROCEDURES

7.2.1 Sample and Solution Preparation

Coupons of pure iron (purchased from Goodfellow) with a diameter of 0.77 cm and Grade 36A carbon steel (CS) (provided by OPG) (composition in wt.%: 0.15 C, 0.84 Mn, 0.024 P, 0.03 S, 0.24 Si, 0.16 Cr, 0.23 Cu, 0.03 Mo, 0.23 Ni, balance Fe), with a diameter of 1 cm, were used in this study. The coupons were manually polished with a series of fine silicon carbide papers (400, 600 and 1200, and 2500 grit), followed by polishing on a Texmet microcloth (Buehler) with a 1 μm MetaDi Supreme diamond paste suspension (Buehler) and sonication in an acetone/methanol mixture for 5 min to remove polishing residues. The polished coupons were then rinsed with Type I water and dried in flowing argon.

All solutions were prepared with water purified with a NANO pure Diamond UV ultrapure water system (Barnstead International) to give a resistivity of 18.2 MΩ.cm. The test solutions used in this chapter were 10^{-2} M HNO_3 (with an initial pH of 2.0), 10^{-3} M HNO_3 (with an initial pH of 3.0), 10^{-4} M HNO_3 (with an initial pH of 4.0) and 10^{-4} M H_2O_2 with an initial pH of 6.0. The nitric acid test solution was prepared by diluting concentrated nitric acid (Caledon Laboratories Ltd). A hydrogen peroxide test solution (10^{-4} M) was prepared prior to each experiment by dilution from a 3.5 wt.%, stock H_2O_2 solution (Fisher Chemical).

7.2.2 Droplet Studies

The freshly polished and argon-dried coupons were placed in individual vials. A 150 µL drop of the solution was placed on the CS surface using a micropipette. In order to have the same volume/surface area ratio, the droplet volume used for pure iron coupons was 89 µL. The water droplets spread to the edges of the coupons, covering the entire surface of these coupons, and forming dome shapes, as shown in **Figure 7-1**.

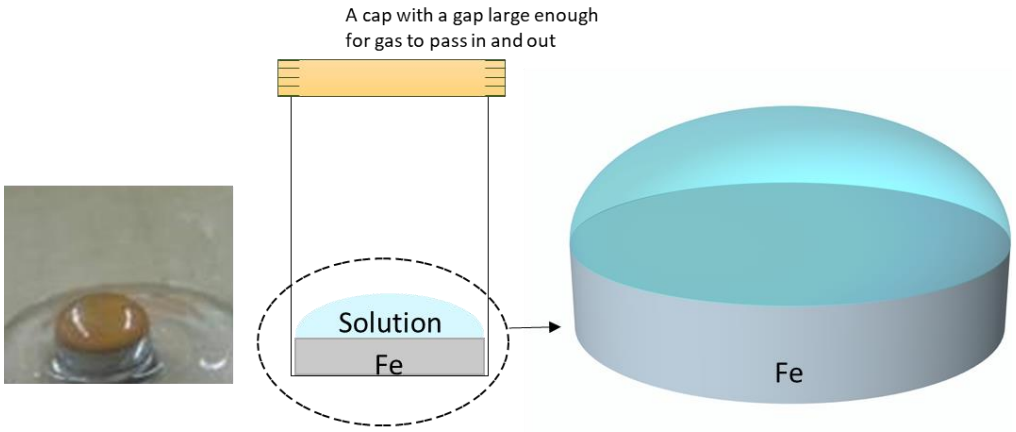

Figure 7-1: The droplet study set up; a 150 µL water droplet on the surface of a circular carbon steel coupon surface.

The coupon surfaces were exposed to the test solution for periods of time ranging from 15 min to 72 h. The solutions were naturally aerated by having been prepared under air, and no additional aerating gases were used. To suppress decomposition of H_2O_2 in the presence of light, all the test vials were covered with aluminum foil for the experiments performed in the presence of 10^{-4} M H_2O_2. After the experiment, each coupon was washed with 6 mL of NANOpure water to collect all the loose particles formed on the surface, and then dried in flowing argon.

7.2.3 Post-Test Analyses

7.2.3.1 Solution Analysis

The dissolved iron concentration ($[\mathrm{Fe}]_{meas}$) in the test solution was analyzed using ICP-OES. Prior to the solution analysis, pure nitric acid (trace analytical grade, Fisher Scientific) was added to the collected solutions to dissolve any colloidal particles present. Therefore, the concentration of dissolved metal measured using ICP includes any colloid particles that were present in the solution. The detection limit for iron using this technique was determined to be 0.1 ppb.

7.2.3.2 Surface Analysis

The coupon surfaces were imaged using a Leica DVM6 optical microscope. Scanning electron microscopy (SEM) images and energy-dispersive x-ray spectroscopy (EDX) were obtained using a Hitachi S-4500 field emission scanning electron microscope equipped with a Quartz XOne EDX system or using an LEO (Zeiss) 1540XB SEM/EDX. Raman spectroscopy was used to determine the composition of oxides, comparing the Raman spectra obtained with those of standard compounds. The Raman spectra were obtained using a Renishaw model 2000 spectrometer with a laser excitation wavelength of 633 nm and spatial resolution of ~1 μm.

7.3 RESULTS AND DISCUSSION

Iron oxides and hydroxides are known to have characteristic colours. The colours in the low-magnification optical micrographs thus provide analytical information on the types of oxide present and their spatial distributions on the corroded surface. In this

chapter and in **Chapter 8**, optical images are shown, which show the progression through the dynamic stages. It is therefore useful here to describe the characteristic colours of iron oxides and hydroxides prior to a detailed discussion of the dynamic stages. Oxide colours and morphologies are already well established from previously published work, in which detailed analyses were performed using Raman, XPS, and optical and scanning electron microscopy [10,40,146,179,180]. Hydrated ferrous species ($Fe^{II}_{(aq)}$ and $Fe(OH)_2$) are green; $Fe(OH)_3$ and its dehydrated form (amorphous FeOOH) are yellow to brown; magnetite (Fe_3O_4) and maghemite (γ-Fe_2O_3) are black; hematite (α-Fe_2O_3) is red; and lepidocrocite (γ-FeOOH) is orange [43]. The colours of iron oxide powder samples (supplied by Alfa Aesar) observed under the optical microscope are presented in **Figure 7-2**.

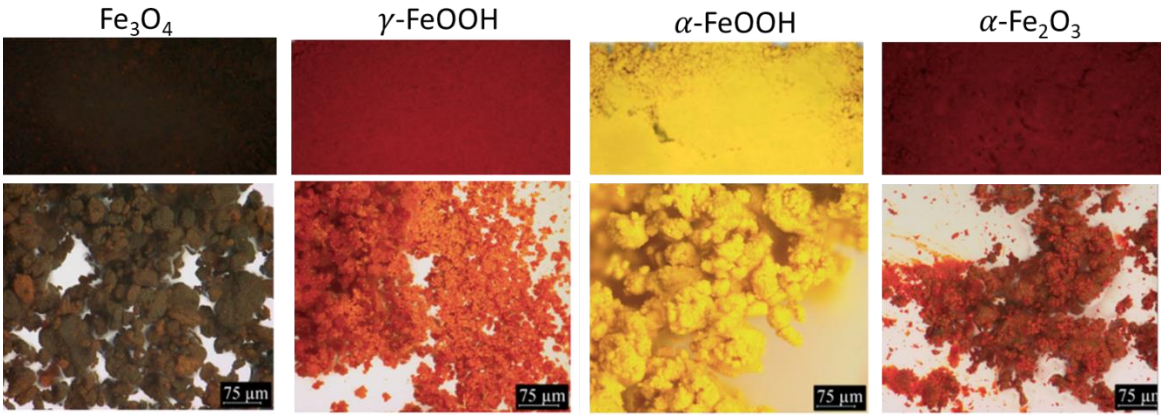

Figure 7-2: Colours of different iron oxides (supplied by Alfa Aesar) observed using optical microscopy [40].

Studying the time-dependent behaviour of the corrosion of metals in small volume solution droplets allows the rate-determining step(s) that control(s) the overall corrosion rate to be identified. It also provides information on the effect of solution parameters on

the nature and duration of the different dynamic stages. To study the evolution of the corrosion dynamics of CS, the overall yields of metal oxidation products (i.e., the total dissolved metal cations and hydroxides/oxides) were measured as a function of corrosion duration (t_{corr}), and the changes over time in the morphology and elemental and chemical composition of the surface were studied.

Figure 7-3 presents the optical images of the surfaces and the dissolved iron concentrations ($[Fe]_{\boldsymbol{meas}}$) as a function of corrosion duration for CS in a 150 μL solution initially containing different concentrations of HNO_3. The $[Fe]_{\boldsymbol{meas}}$ vs. time is plotted in different scales to allow the corrosion behaviour over short and long timescales to be observed. The durations of the distinct kinetic stages identified are indicated on the top of the plots.

The surface evolution and the $[Fe]_{meas}$ values exhibited three distinct stages, each with its own characteristic dependence on t_{corr}. These will be referred to henceforth as "dynamic stages." It should be noted that the droplet forms a dome shape, and the solution does not have a uniform thickness over the coupon surface. As discussed later, corrosion progression to subsequent stages is faster for smaller solution depths.

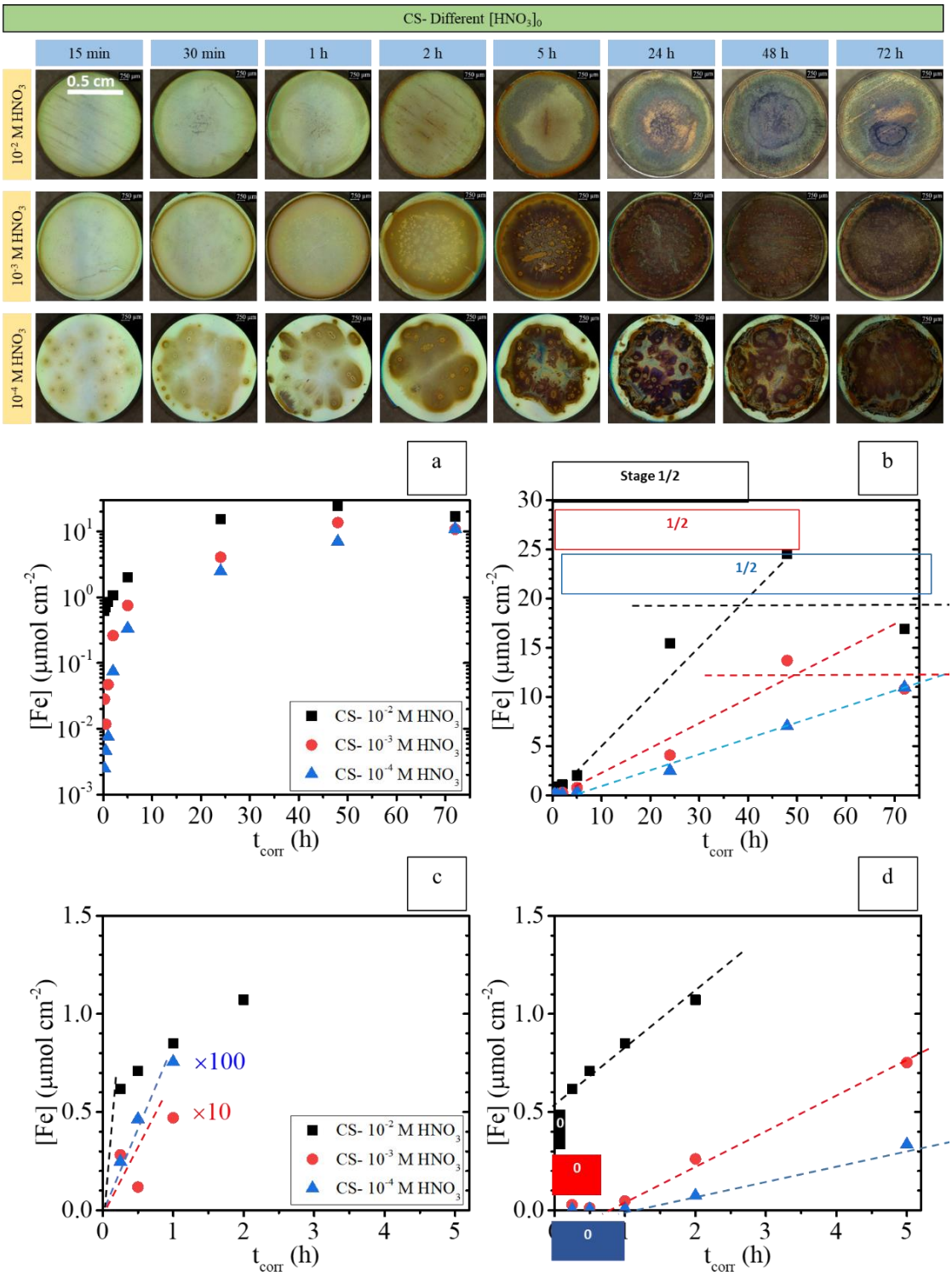

Figure 7-3: Optical images of surfaces and dissolved iron ($[Fe]_{meas}$) obtained as a function of corrosion duration in 150 µL droplets, initially containing different concentrations of HNO_3, a) log $[Fe]_{meas}$ vs t_{corr} b) $[Fe]_{meas}$ vs t_{corr}, c) $[Fe]_{meas}$ within first 5 h of corrosion ($[Fe]_{meas}$ for 10^{-3} M HNO_3 and 10^{-4} M HNO_3 was multiplied by 10 and 100, respectively), and d) $[Fe]_{meas}$ within 5 h of corrosion).

Figure 7-4 shows high magnification optical images and SEM images of the CS coupon surfaces in 10^{-2} M HNO_3 solution. These images can be used along with **Figure 7-2** to study the corrosion progression with time.

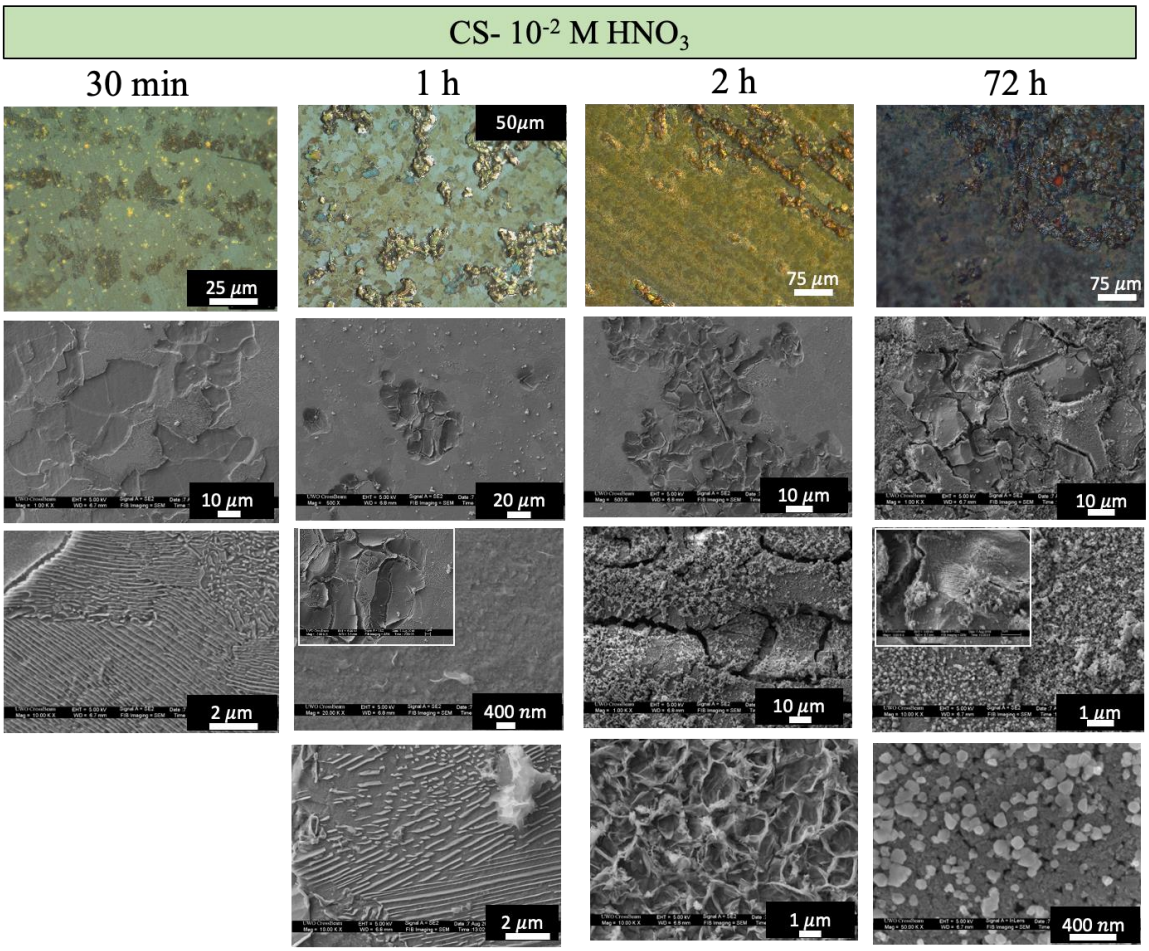

Figure 7-4: High magnification optical images and different magnification SEM images of the central area of a CS surface corroded in 10^{-2} M HNO_3 solution for different durations.

The data presented in **Figure 7-3a** show that the $[Fe]_{meas}$ at very early times has a linear dependence on $[HNO_3]_0$. At longer times, $[Fe]_{meas}$ approaches the same limiting value of ~15 µmol cm^{-2}, independent of $[HNO_3]_0$; however, the rate of approach to this value is faster for a higher $[HNO_3]_0$.

The general characteristics of the different dynamic stages in the presence of different $[HNO_3]_0$ values are as follows (a more detailed description of these stages will be given later in the chapter):

- **Stage 0:** The total amount of dissolved metal increased approximately linearly with time. The rate of metal dissolution (the slope of $[Fe]_{meas}$ vs time) in this stage was approximately proportional (within a factor of 2) to $[HNO_3]_0$. However, the duration of this stage appeared to be shorter for higher $[HNO_3]_0$ values. Note that the concentration fluctuated about the average value that increased linearly with time. The fluctuation is due to the nature of the corrosion process, because it involves interfacial transfer of metal species from solid to liquid and liquid to solid phase, which results in a decreased or increase in total dissolved iron concentration at a certain t_{corr}. The macroscopic dissolution rates for different $[HNO_3]_0$ values are presented in **Table 7-1**:

$$\text{Rate} \approx k_0 \times [HNO_3]_0 \qquad \textbf{(Eq. 7-3)}$$

Table 7-1: Dissolution rates and reaction constants for Fe dissolution in solutions containing different $[HNO_3]_0$. The data were obtained from Figure 7-3c. The ratio of solution volume (V) to surface area (A) was 0.191 cm ($\frac{V}{A}$ =0.191 cm)

$[HNO_3]_0$ (M)	$Rate_{(t_{corr}<1h)}$ (μmol cm^{-2} h^{-1})	k_0 (s^{-1})
10^{-2}	1.49±0.05	2.2×10^{-4}
10^{-3}	0.053±0.002	7.7×10^{-5}
10^{-4}	0.006±0.003	8.7×10^{-5}

- **Stage 1b/2**: This period in time is referred to as **Stage 1b/2** (**Stage 1b/Stage 2)** because corrosion progresses at different rates depending on the solution depths across the metal surface, and the stage reached depends on the solution depth. The perimeter of the droplet, where the solution is shallower, will progress to **Stage 2** faster than the centre of the droplet. The total amount of dissolved metal continued to increase approximately linearly with time. The rate of metal dissolution in this stage had a very weak dependence on $[HNO_3]_0$. **Eq. 7-4** shows that the rate of dissolution has a logarithmic dependence with the square of $[HNO_3]_0$. It increased by approximately a factor of 2 for one order of magnitude increase in $[HNO_3]_0$. The duration of this stage is also shorter for higher $[HNO_3]_0$ (discussed in detail below). The macroscopic dissolution rates for different $[HNO_3]_0$ for t_{corr} <5 h and t_{corr} > 5 h are presented in **Table** 7-2:

$$\text{Rate} \approx -k_1 \times \log([HNO_3]_0)^2 \qquad \textbf{(Eq. 7-4)}$$

Table 7-2: Dissolution rates and reaction constants for Fe dissolution in different $[HNO_3]_0$. Data were obtained from Figure 7-3b and Figure 7-3d for different corrosion durations ($A = 0.785\ cm^2$).

$[HNO_3]_0$ (M)	$Rate_{(t_{corr}<5h)}(1)$ (μmol cm^{-2} h^{-1})	$k_{1_{(t_{corr}<5h)}}(1)$ (mol h^{-1})	$Rate_{(t_{corr}>5h)}(2)$ (μmol cm^{-2} h^{-1})	$k_{1_{(t_{corr}>5h)}}(2)$ (mol h^{-1})
10^{-2}	0.22+0.02	0.044×10^{-6}	0.50±0.03	0.098×10^{-6}
10^{-3}	0.14±0.03	0.018×10^{-6}	0.24±0.00	0.031×10^{-6}
10^{-4}	0.08±0.02	0.007×10^{-6}	0.14±0.01	0.014×10^{-6}

(1) The rate and k_1 for 10^{-2} M HNO_3 were calculated for 15 min < t_{corr} < 5 h.
(2) The end of **Stage 1b/2** was $t_{corr} > 30\ h$ for 10^{-2} M HNO_3, $t_{corr} > 50\ h$ for 10^{-3} M HNO_3 and $t_{corr} > 72\ h$ for 10^{-4} M HNO_3.

- **Stage 2/3**: The total amount of dissolved metal stopped increasing and fluctuated around an average value that remained nearly constant with time. That is, no net dissolution/precipitation was observed over large surface areas and over long durations, but over shorter time scales, the overall process cycles from net dissolution to net precipitation.

These dynamic stages were observed for CS corroding in solutions of the same volume but containing different initial nitric acid concentrations. The nitric acid concentration affected the duration rather than the nature of the dynamic stages, as will be discussed later in **Section 7-3-2.**

7.3.1 Corrosion Progression in Small Volumes of 10^{-2} M Nitric Acid Solution

In 10^{-2} M HNO_3, by 15 min the total amount of dissolved metal was increasing approximately linearly with time. The slope of $[Fe]_{meas}$ vs time was approximately 1.49 μmol cm^{-2} h^{-1}. Surface images are not available for this duration, but the surface analysis after 1 h indicated that the surface remained almost free of oxide or hydroxide until the subsequent stage. The high magnification optical and SEM images of the central areas of the coupon corroded for 30 min clearly show that the surface of CS is highly etched at this early time. The SEM images show the lamellar morphology of cementite layers within the pearlite grains. The iron in the cementite phase is known to be strongly coordinated to carbon and inert to oxidation. Thus, in the early stages of corrosion, iron dissolution will occur preferentially at the active α-Fe phase regions. This preferential oxidative dissolution of ferrite will leave cementite layers on the surfaces of the pearlite grains but smooth surfaces on the pure α-Fe grains [146].

HNO_3 affects the pH as well as the nitrate concentration. Thus, the change in pH as well as in $[NO_3^-]$ must be considered. In addition, the water droplet solutions are exposed to air. For CS, the proton is also an effective oxidant. That is, there is more than one oxidant present (H^+, O_2 and NO_3^-), and which one is dominant depends on their concentrations as well as their standard redox activities. From previous work in our group [11,17], we know that in this stage, the formation of Fe ions via oxidation is accompanied by the production of OH^- (or consumption of H^+) by solution reduction reactions. The oxidation of iron is followed by the transport of metal cations from the surface to the bulk solution. In this stage, while a proportion of the iron ions are transported to the solution phase, metal cations also accumulate near the surface. The rate of accumulation of cations near the surface depends on the relative rates of oxidation and mass transport of ions, which are not independent, and is also a function of solution parameters such as redox potential of oxidants and their solubility. In the presence of oxygen and nitrate ions, the interfacial metal charge transfer reaction and the possible reduction half reactions at the metal surface are as follows:

Oxidation half-reaction: $Fe_{(m)} \rightarrow Fe^{2+} + 2\ e^-$ (**Eq. 7-5a**)

Reduction half-reaction of oxygen: $O_2 + 4\ H^+ + 4\ e^- \rightarrow 2\ H_2O$ (**Eq. 7-5b**)

Reduction half reaction of nitrate: $NO_3^- + 2\ H^+ + 2\ e^- \rightarrow NO_2^- + H_2O$ **(Eq. 7-5c)**

Reduction half reaction of hydrogen: $2\ H^+ + 2\ e^- \rightarrow H_2$ **(Eq. 7-5d)**

Overall charge transfer reaction for oxidation via oxygen:

$2\ Fe_{(m)} + O_2 + 4\ H^+ \rightarrow 2\ Fe^{2+} + 2\ H_2O$ (**Eq. 7-5e**)

Overall charge transfer reaction for oxidation via nitrate:

$$Fe_{(m)} + NO_3^- + 2\,H^+ \rightarrow Fe^{2+} + NO_2^- + H_2O \qquad \textbf{(Eq. 7-5f)}$$

Overall charge transfer reaction for oxidation via H^+ reduction:

$$Fe_{(m)} + 2\,H^+ \rightarrow Fe^{2+} + H_2 \qquad \textbf{(Eq. 7-5g)}$$

where the subscript (m) denotes the solid metal.

The interfacial mass transfer reactions and the transport of solution oxidants to the surface are as follows:

Mass transport of metal cations: $Fe^{2+}|_{x=0} \longrightarrow\!\!\!\!\rightarrow Fe^{2+}|_{x=sol}$ **(Eq. 7-6a)**

Mass transport of oxygen: $O_2|_{x=sol} \longrightarrow\!\!\!\!\rightarrow O_2|_{x=0}$ **(Eq. 7-6b)**

Mass transport of hydroxide ions: $OH^-|_{x=0} \longrightarrow\!\!\!\!\rightarrow OH^-|_{x=sol}$ **(Eq. 7-6c)**

Mass transport of nitrate ions: $NO_3^-{}_{x=sol} \longrightarrow\!\!\!\!\rightarrow NO_3^-|_{x=0}$ **(Eq. 7-6d)**

Mass transport of nitrite ions: $NO_2^-|_{x=0} \longrightarrow\!\!\!\!\rightarrow NO_2^-|_{x=sol}$ **(Eq. 7-6e)**

where **x** represents the distance of species from the surface, and "sol" denotes the solution phase.

After 1 h, and up to about 48 h, the rate of increase of $[Fe]_{meas}$ was linear and was proportional to log $([HNO_3]_0)^2$. The second row image of the 2-h corroded surface in **Figure 7-4** shows an area with a thin hydrogel layer that was formed above cementite bridges and collapsed during drying or some turbulence during corrosion. A hydrogel consists of a semi-stationary phase of loosely-connected mixed hydroxide colloidal particles and a mobile phase of the solution containing ferrous ions at a concentration near saturation level. Hydrogel, composed of aggregates of colloids of mainly $Fe(OH)_2$ (with $Fe(OH)_3$ at an impurity level), forms a smooth layer in this stage. The smooth

surface over a wide area indicates it is a hydrogel, and not granular/crystalline oxide/hydroxide. Once the interfacial region is saturated with Fe^{2+} ions (by 2 h in 10^{-2} M HNO_3, see **Figure 7-5**), the formation of this $Fe(OH)_2$ gel layer starts at the surface. The formation of a viscous hydroxide layer (the greenish gel) through hydrolysis and hydrogel formation occurs as follows:

$$Fe^{2+} + n\ OH^- \rightleftharpoons Fe(OH)_m^{2-m} + (n-m)\ OH^- \text{ where } m = 1, 2, \text{ or } 3 \qquad \textbf{(Eq. 7-7a)}$$

$$n\ Fe(OH)_2 + m\ H_2O \rightleftarrows Fe_m(OH)_{2n}(H_2O)_{m(gel)} \qquad \textbf{(Eq. 7-7b)}$$

Transition metal ions easily form hydroxides, which are hygroscopic and grow in colloidal forms and/or a hydrogel network [11,18–20]. This hydrogel network provides a slow transport medium in which the oxidation/precipitation reactions and the solution transport processes can be strongly coupled, resulting in feedback processes. The formation of a hydrogel layer slows down the transport of metal ions from the metal/solution interface to the bulk solution. In a study conducted by Shin [11], concentric rings were observed in **Stage 2** during corrosion of CS in a low ionic strength solution. These bands of metal oxides, Shin [11] postulated, result from chemical waves established as a result of chemical oscillation in a low ionic strength medium. The work presented here confirms that these concentric rings occur only in low ionic strength solutions (10^{-4} M HNO_3 and 10^{-4} M H_2O_2), as discussed in detail in **Section 7.2.2.**

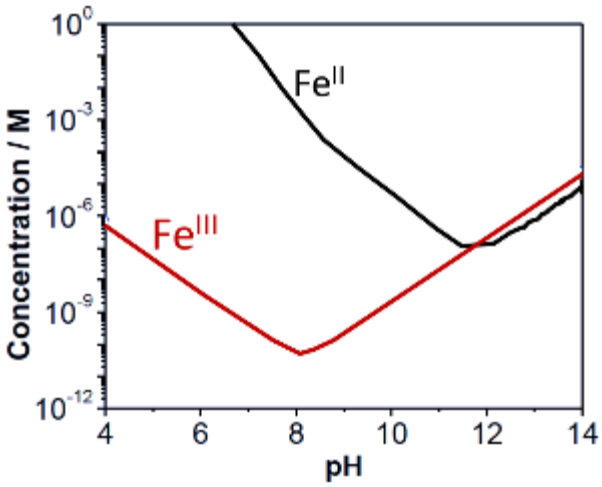

Figure 7-5: pH-dependent solubility of Fe^{II}, Fe^{III} at 25 °C [49].

From SEM images, it appears that the granular oxide growth (**Stage 3**) begins at 72 h. The 4th row image of 2-h corroded surfaces (**Figure 7-4**) shows that corrosion has progressed to **Stage 3**. In the 3rd row image (**Figure 7-4**) the coupon surface is bluish-green to greenish-yellow or brown, which indicates a thicker hydrogel and also higher ferric content in the hydroxide hydrogel layer. The mixed Fe^{II}/Fe^{III} hydroxides will slowly convert to magnetite or FeOOH by Ostwald ripening [19–21]. The images of the 72-h corroded surface show that mixed hydroxide in the hydrogel layer is slowly converting to magnetite. It takes longer to see these magnetite crystals in octahedral shapes in a solution of initial pH 2.0. Magnetite formation occurs in the beginning of **Stage 3**. Some oxide deposits are present on top of the cementite and α-Fe grains. The following redox reactions occur within the hydrogel layer in **Stage 2**.

Oxiation half-reaction of Fe^{II}: $2\ Fe(OH)_2 + 2\ OH^- \longrightarrow 2\ Fe(OH)_3 + 2\ e^-$ **(Eq. 7-8a)**

Reduction half-reaction of nitrate: $NO_3^- + 2\ H^+ + 2\ e^- \longrightarrow NO_2^- + H_2O$ **(Eq. 7-8b)**

Reduction half-reaction of oxygen: $O_2 + 4\ H^+ + 4\ e^- \longrightarrow 2\ H_2O$ **(Eq. 7-8c)**

Overall charge transfer reaction with oxygen as oxidant:

$$4\ Fe(OH)_2 + O_2 + 2\ H_2O \longrightarrow 4\ Fe(OH)_3 \qquad \textbf{(Eq. 7-8d)}$$

Overall charge transfer reaction with nitrate as oxidant:

$$2\ Fe(OH)_2 + NO_3^- + H_2O \longrightarrow 2\ Fe(OH)_3 + NO_2^- \qquad \textbf{(Eq. 7-8e)}$$

Electron transfer between Fe^{II} and Fe^{III} is faster in the hydrogel than in the aqueous solution [40,149–151]. Thus, **Eq. 7-8d** occurs more rapidly once the hydrogel has formed.

The iron oxide starts to form via the reactions below:

Magnetite Formation:

$$Fe(OH)_2 + 2\ Fe(OH)_3 \rightarrow\rightarrow Fe_3O_4 + 4\ H_2O \qquad \textbf{(Eq. 7-9a)}$$

FeOOH Formation:

$$Fe(OH)_3 \rightarrow\rightarrow FeOOH + H_2O \qquad \textbf{(Eq. 7-9b)}$$

In small-volume solutions, when nitrate is consumed in the gel layer, the $[NO_2^-]$:$[NO_3^-]$ ratio becomes high enough for Fe^{III}/Fe^{II} reduction to couple with the oxidation of nitrite. Thus, in addition to **Eq. 7-8**, oxide formation can occur through the iron reduction via oxidation of nitrite to nitrate (**Eq. 7-10b**) inside the gel layer. It should be noted here that the coupling between the reduction half-reaction of Fe^{III} to Fe^{II} and the oxidation half-reaction of hydroxide ions to oxygen is not as effective as that involving nitrite/nitrate due to the very high activation energy of oxidation of OH^- to O_2. Thus, although $[OH^-]$ also increases with time in the interfacial region, it diffuses out into the bulk solution rather than reducing ferric ion.

In conclusion, when nitrate has been reduced to nitrite, and [NO_2^-] and [Fe^{3+}] are high enough for oxidation of nitrite to nitrate to be thermodynamically possible, Fe^{III} to Fe^{II} reduction can couple with NO_2^-/NO_3^- oxidation in the gel network. The concentration of Fe^{III} in the hydrogel in **Stage 1/2b** is low; thus, the rate of the $Fe(OH)_3 \rightarrow Fe(OH)_2$ reduction half reaction (in the $Fe(OH)_3 \leftrightarrows Fe(OH)_2$ redox reaction) in **Stage 1/2b** is far lower compared to the rate of oxidation of $Fe \rightarrow Fe^{II}$. In S**tage 3**, [Fe^{III}] in the hydrogel layer is sufficient for its reduction reaction to Fe^{II} to effectively couple with the oxidation of NO_2^- to NO_3^-. Hence, the elementary steps will include both oxide crystal or particle growth (**Eq. 7-9**) and redox coupling reactions (**Eq. 7-10**):

Redox coupling in the hydrogel network:

Red half-reaction of Fe^{II}: $2\ Fe(OH)_3 + 2\ e^- \leftrightarrows 2\ Fe(OH)_2 + 2\ OH^-$ **(Eq. 7-10a)**

Ox half-reaction of nitrite: $NO_2^- + H_2O \leftrightarrows NO_3^- + 2\ H^+ + 2\ e^-$ **(Eq. 7-10b)**

Overall charge transfer reaction with nitrite as reductant:

$2\ Fe(OH)_3 + NO_2^- \leftrightarrows 2\ Fe(OH)_2 + NO_3^- + H_2O$ **(Eq. 7-10c)**

Because the net oxidation of $Fe^{2+}/Fe(OH)_2$ to $Fe^{3+}/Fe(OH)_3$ is negligible in **Stage 3**, $[Fe]_{meas}$ remains constant with time**.** Metal oxide growth (i.e., magnetite and/or lepidocrocite) depends on the relative production rates of $Fe^{2+}/Fe(OH)_2$ and $Fe^{3+}/Fe(OH)_3$. The net result is a hydroxide gel layer of constant thickness and significant granular oxide growth.

7.3.2 Effect of Initial Concentration of Nitric Acid on the Corrosion of CS in Small Solutions

The rates of chemical and redox reactions in the interfacial region (**Eq. 7-5**) depend on the concentration of both oxidants and the concentrations of Fe^{II} and Fe^{III} species in the interfacial region. Thus, the overall corrosion process is affected significantly not only by the transport of oxidants from the bulk to the interfacial region, but also the transport of metal cations from the interfacial region into the solution phase. As mentioned earlier, corrosion in various concentrations of nitric acid followed the same dynamic stages as observed for 10^{-2} M HNO_3. The difference was that the duration of the stages was different. This section discusses how the concentration of HNO_3 affects the dynamic stages of corrosion.

Corrosion of CS in a Droplet Solution Initially Containing 10^{-3} M HNO_3

The $[Fe]_{meas}$ vs time graph and optical images of corroded surfaces as a function of t_{corr} in small solution volume droplets initially containing 10^{-3} M HNO_3 are presented in **Figure 7-3**. The main differences observed for corrosion of CS in 10^{-3} M HNO_3, as opposed to 10^{-2} M HNO_3, are described below:

- In **Stage 0,** during which the rate of $[Fe]_{meas}$ increase was linear, the slope of $[Fe]_{meas}$ vs time was ~10 times lower in 10^{-3} M HNO_3 than in 10^{-2} M HNO_3.
- The duration of **Stage 0** was longer (1 h) in 10^{-3} M HNO_3 than in 10^{-2} M HNO_3 (15 min).
- In **Stage 1b/2** ($1\ h < t_{corr}$ <50 h), $[Fe]_{meas}$ was generally lower in 10^{-3} M HNO_3 than in 10^{-2} M HNO_3. However, similar to what was observed for 10^{-2} M HNO_3, $[Fe]_{meas}$

increased linearly with time. The rate of increase of $[\mathrm{Fe}]_{meas}$ was almost 2 times lower in 10^{-3} M HNO_3 than in 10^{-2} M HNO_3. Similar to what was observed for 10^{-2} M HNO_3, $[\mathrm{Fe}]_{meas}$ reached a maximum (by 48 h) and decreased after that.

  - Except for the formation of a darker ring at the edges of the coupon corroded in 10^{-3} M HNO_3, the oxide was generally uniform across the entire surface, whereas in 10^{-2} M HNO_3, large circular rings formed.
- Some locally corroded spots (small circular rings) were observed on the surface of the coupon corroded in 10^{-3} M HNO_3 during the first hour of corrosion, while the surface was entirely covered with oxide at longer times.
- The area near the edges was covered with a yellow-brown oxide/hydroxide after 15 min.

The main conclusion that can be drawn from these results is that the corrosion pathways in solutions with 10^{-3} M and 10^{-2} M HNO_3 are the same, and regardless of the concentration of oxidant (i.e., the $[HNO_3]$) and initial pH, corrosion progresses through the same dynamic stages.

In **Stage 0**, the rate of increase of $[\mathrm{Fe}]_{meas}$ was 10 times lower than in 10^{-2} M HNO_3. In this stage, the rate of oxide/hydroxide formation is negligible, and the rate of oxidation and dissolution are therefore almost the same. The oxidation rate in this stage has a linear dependence on $[HNO_3]_0$.

At lower $[HNO_3]_0$ (i.e., 10^{-3} M compared to 10^{-2} M), the ionic strength of the solution is lower. Fe^{2+}, Fe^{3+}, H^+, NO_3^- and NO_2^- are all ionic species that contribute to the ionic strength. Although one known effect of ionic strength is on the double layer thickness (the square root of the ionic strength ($\sqrt{I_s}$) is inversely proportional to double

layer thickness (δ_{dl}) [10,25–27]), its main effect is via its influence on the transport of metal ions [28,29]. While a lower mass transport rate is expected in 10^{-3} M HNO_3 than in 10^{-2} M HNO_3, the rate of oxidation is 10 times lower in 10^{-3} M HNO_3 solution. During **Stage 0**, HNO_3 is consumed, and Fe cations accumulate at the surface. In 10^{-3} M HNO_3, the mass transport of ions through a lower ionic strength solution and the rate of oxidation are slow. The net result is that the time at which corrosion is under complete mass transport control, due to the formation of a hydrogel, is longer than for solutions with initial pH 2. The lower observed slope of $[Fe]_{meas}$ vs time for **Stage 1b/2** in 10^{-3} M HNO_3 (than in 10^{-2} M HNO_3) can be explained based on the lower rate of mass transport of ions in low ionic strength solutions. When a hydrogel is formed, the oxidation of Fe metal to Fe^{II} occurs at the metal gel interface while Fe^{II} is oxidized to Fe^{III} inside the gel layer. The overall rate of corrosion is controlled by the rate at which Fe^{II} transfers from the interfacial region to the solution phase. The lower mass transfer rate in 10^{-3} M HNO_3 solution results in the lower rate of transport of Fe^{II} to the bulk solution and consequently a dissolution rate 2 times smaller than in 10^{-2} M HNO_3.

The other observation was the oxide ring at the surface edges. Fe^{III} has very low solubility compared to Fe^{II} (see **Figure 7-5**). The formation of Fe^{III} hydroxide/oxide at the edges of the coupon occurs because of rapid saturation of Fe^{III} in the early stages of corrosion, within a few minutes or earlier. The oxidation of Fe becomes slower due to the formation of this diffusion barrier near the edges of the coupon. Thus, there will be less Fe^{II} available to participate in magnetite formation at the edges of the coupon surface. The Fe^{III} oxide/hydroxide was loose and washed off and does not appear in images of the surface.

One interesting observation for 10^{-3} M HNO_3 was the formation of the circular oxide rings that disappear after 5 h corrosion (covered with oxide at longer times). The formation of these rings will be discussed in detail when the 10^{-4} M HNO_3 results are discussed.

Depending on the steady-state concentration of Fe^{II} and Fe^{III} and also on the concentration of oxygen or other oxidants in the interfacial region, the oxidation rate of Fe^{II} to Fe^{III} will be different.

Corrosion of CS in Droplet Solutions Initially Containing 10^{-4} M HNO_3

Figure 7-3 also shows the $[Fe]_{meas}$ vs time and the optical images of surfaces observed as a function of corrosion duration in 10^{-4} M HNO_3. The surface of coupons prior to collecting the water droplet and after collecting the water (and prior to drying) are also shown in **Figure 7-6** to discuss some oxides that may not have been observed under optical microscopy.

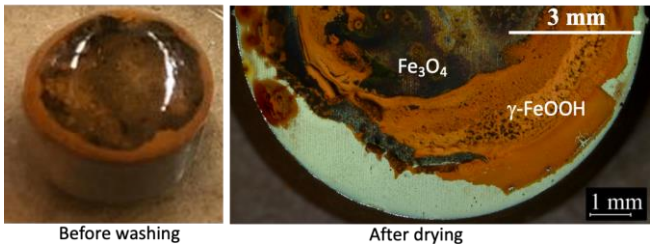

Figure 7-6: The left image shows the coupon surface under the water droplet and the right-side image shows the two-layer structure of oxides indicating growth of magnetite at the γ-FeOOH/Fe metal interface – coupon surfaces corroded for 72 h in 10^{-3} M HNO_3.

Based on the relative production rates of $Fe^{2+}/Fe(OH)_2$ and $Fe^{3+}/Fe(OH)_3$, metal oxide grows preferentially as magnetite (black) and/or lepidocrocite (orange). It was

observed that, in the top layer, $Fe(OH)_2$ starts to convert into ferric hydroxide and γ-FeOOH (the orange oxide). γ-FeOOH forms at the top and magnetite (the black oxide) from Fe^{II}/Fe^{III} lower down. This can be clearly seen in the optical images of the surface corroded in 10^{-4} M HNO_3. The results obtained in 10^{-4} M HNO_3 will be discussed later. The rate of mass transport of ions to the solution is low, and Fe^{II} is consumed in the gel layer to form Fe^{III}. The formation of γ-FeOOH from $Fe(OH)_3$ is favoured at the top of the gel layer, where the Fe^{II}:Fe^{III} ratio is low. The formation of Fe_3O_4, which is a mixed Fe^{II}/Fe^{III} oxide, is predominant underneath the orange γ-FeOOH oxide where the Fe^{II}:Fe^{III} ratio is high.

The key observations in the corrosion of CS in 10^{-4} M HNO_3 (initial pH 4.0) small volume solutions are described below:

- In **Stage 0** (t < 1h), the maximum $[Fe]_{meas}$ was very low (<0.008 μmol cm^{-2}). These values were ≈ 0.05 μmol cm^{-2} and ≈ 0.6 μmol cm^{-2} in 10^{-3} M HNO_3 and 10^{-2} M HNO_3, respectively.
- In **Stage 0,** the slope of $[Fe]_{meas}$ vs time was ~10 times lower in 10^{-4} M HNO_3 than in 10^{-3} M HNO_3.
- The duration of **Stage 0** was 1 h (i.e., almost the same as observed in 10^{-3} M HNO_3).
- In **Stage 1b/2** ($1\ h < t_{corr}$), the $[Fe]_{meas}$ was generally lower than in 10^{-2} M and 10^{-3} HNO_3. Similar to what was observed for 10^{-2} M HNO_3, $[Fe]_{meas}$ increased linearly with time. The rate of increase of $[Fe]_{meas}$ was almost 2 times lower than in 10^{-3} M. However, unlike what was observed for 10^{-2} and 10^{-3} M HNO_3, $[Fe]_{meas}$ did not reach a maximum (by 72 h).

- By 15 min, yellowish-brown oxides had formed in Liesegang patterns. These patterns were observed for 10^{-3} M HNO_3, but the rings were not as clear and large as they were for 10^{-4} M HNO_3. These circular rings were found mostly on the central areas of the surface rather than the edge areas.
- By 1 h, the general colour of these circular rings had become darker brown.
- With time, the circular rings merged and formed larger rings. By 2 h, the entire surface was covered with a brown oxide, while a small hole at the centre of each of these rings could still be clearly seen.
- The areas near the edges were clean and shiny on the optical images. However, when the droplet was on the coupon surface (before it was washed, as shown in the bottom row in **Figure 7-6**), the outer part of the surface was covered with a thick yellow oxide the entire time, even after 15 min.

The difference in corrosion progression between 10^{-4} M HNO_3 and 10^{-3} M HNO_3 is very similar to the differences observed between 10^{-3} M HNO_3 and 10^{-2} M HNO_3. The decrease in ionic strength decreases the rate of diffusion of metal ions. The key observation was that the slow-diffusion environment of 10^{-4} M HNO_3, due to its low ionic strength, provides the conditions for the formation of oxide patches in the shape of Liesegang rings. Additional high-resolution optical images of surface circular features presented in **Figure 7-7** show the progression of the Liesegang rings with corrosion time. The formation of concentric ring patterns such as these is a well-known phenomenon in geology [21,30]. Liesegang rings are formed when dissolved species continuously diffuse through a slow transport medium such as gel or porous rock, causing solid products to periodically precipitate and re-dissolve. In CS corrosion, this phenomenon

arises from systemic feedback between the chemical reactions and transport processes of $Fe^{2+}_{(aq)}$ and OH^- ions in solution. Depending on the relative metal oxidation and ion transport rates, the oxide particles can grow and aggregate in Liesegang patterns 11,31–34].

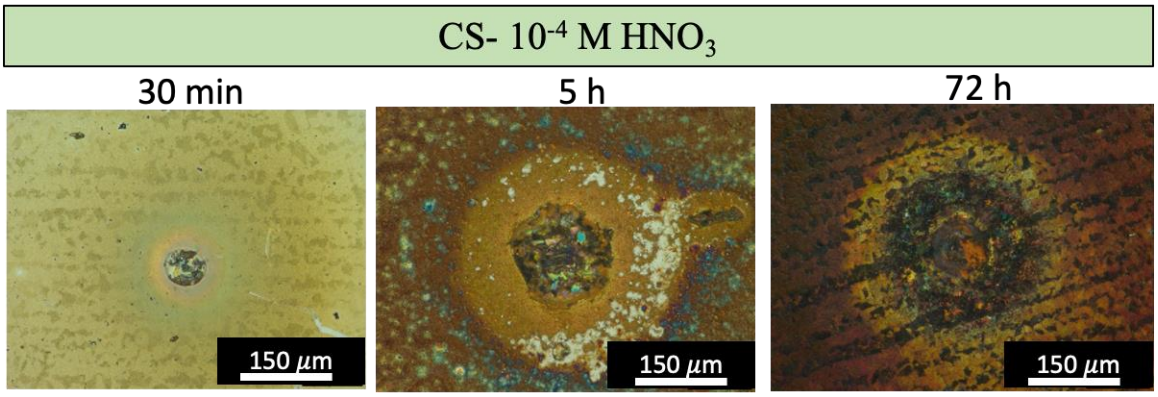

Figure 7-7: High magnification optical images of CS surfaces corroded for different durations in 10^{-4} M HNO_3 solution, showing the evolution of concentric rings.

As shown in **Figure 7-8**, the oxidation of iron occurred randomly across the surface. Not all circular features were examined. However, from the study of several sites, MnS inclusion sites were defined as one of the preferential sites of formation for these rings [35,36]. Note that, although MnS sites can act as favoured oxidation sites, the formation of Liesegang ring can also occur independently of these inclusions. In 10^{-4} M HNO_3, relatively large concentric rings form on the CS surface. The colour of the surface adjacent to the preferentially dissolved areas was orange, and small needle-like particles were present mostly around the centre of the rings. Oxide wave propagation in the radial direction far beyond the dissolved area around the inclusion site, in perfect circular shapes and not in the shape of the MnS grain, further support that the oxide growth patterns are not due to metallurgical structure patterns or through solid-state

diffusion of metal cations.

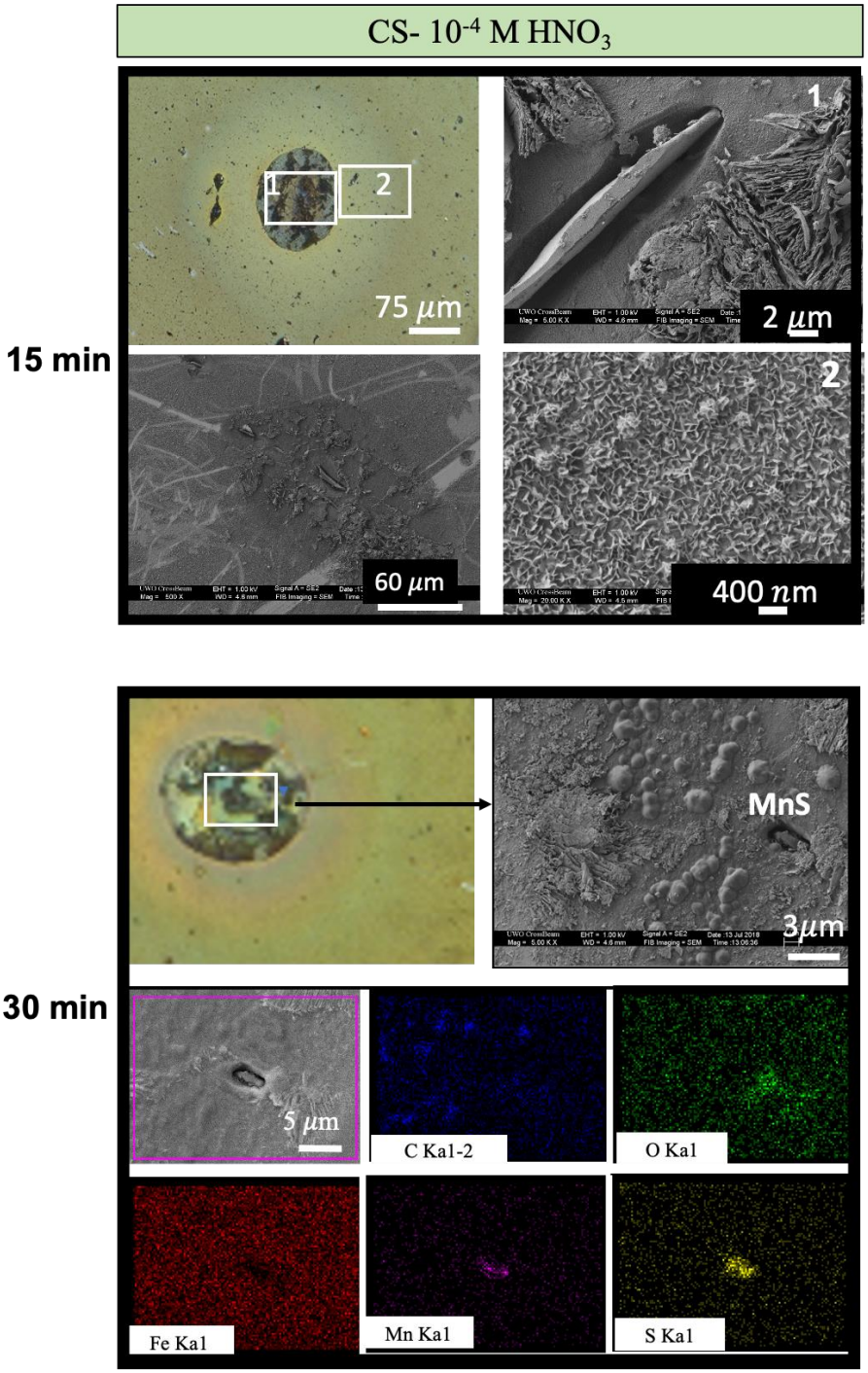

Figure 7-8: High magnification optical images and SEM images of CS surfaces corroded in 10^{-4} M HNO_3 small volume solutions for different durations, showing the MnS inclusion at the centre of Liesegang rings on CS surfaces. The bottom row (30 min corrosion) shows the SEM image and EDS elemental mappings of an MnS inclusion at the centre of one of the newly developed circular features.

Further surface analysis to identify the oxides on the surface

The Raman spectra of oxides at different surface locations (**Figure 7-9**) indicate that the black and yellow oxides are magnetite and lepidocrocite, respectively. The Raman spectrum of the orange area in the central region shows four major peaks at 250, 380, and 530, and 650 cm^{-1} corresponding to the four main peaks of γ-FeOOH (lepidocrocite), whereas the spectrum of the area near the edges (**Area 2**) shows no iron oxide peaks. In the optical micrographs, no oxide was observed at the edges of the samples. However, when studying the microstructure of the surface oxides, it is important to consider what oxides were present under the droplet prior to collecting the water and drying the coupon surface. Optical images taken from the sample under the droplet (see **Figure 7-6)** show that an orange oxide is present near the edges, but it was very loose and washed off into the solution when the sample was rinsed with water. The Raman results showed that, after 5 h, most of the surface is covered with magnetite. The remaining yellow oxides (**Area 3**) were γ-FeOOH. The optical image of the sample under the droplet after 72 h shows that the whole sample is covered with a mixture of orange oxide (γ-FeOOH) and black oxide (Fe_3O_4). The Raman spectrum of the black oxide on the outer ring of the coupon (**Area 6**) and the brown oxides (the central area, **Area 7**) indicates the presence of both magnetite and maghemite in addition to lepidocrocite. However, since the main Raman peak for magnetite (Fe_3O_4), is located at a wavenumber close to the major peaks of maghemite, and has a low Raman scattering probability, the presence of magnetite in these areas could not be confirmed using Raman spectroscopy.

It is should be noted that Raman spectroscopy was performed on all samples, and no nitrate-containing complexes were found on the coupon surfaces for the conditions

studied in this chapter.

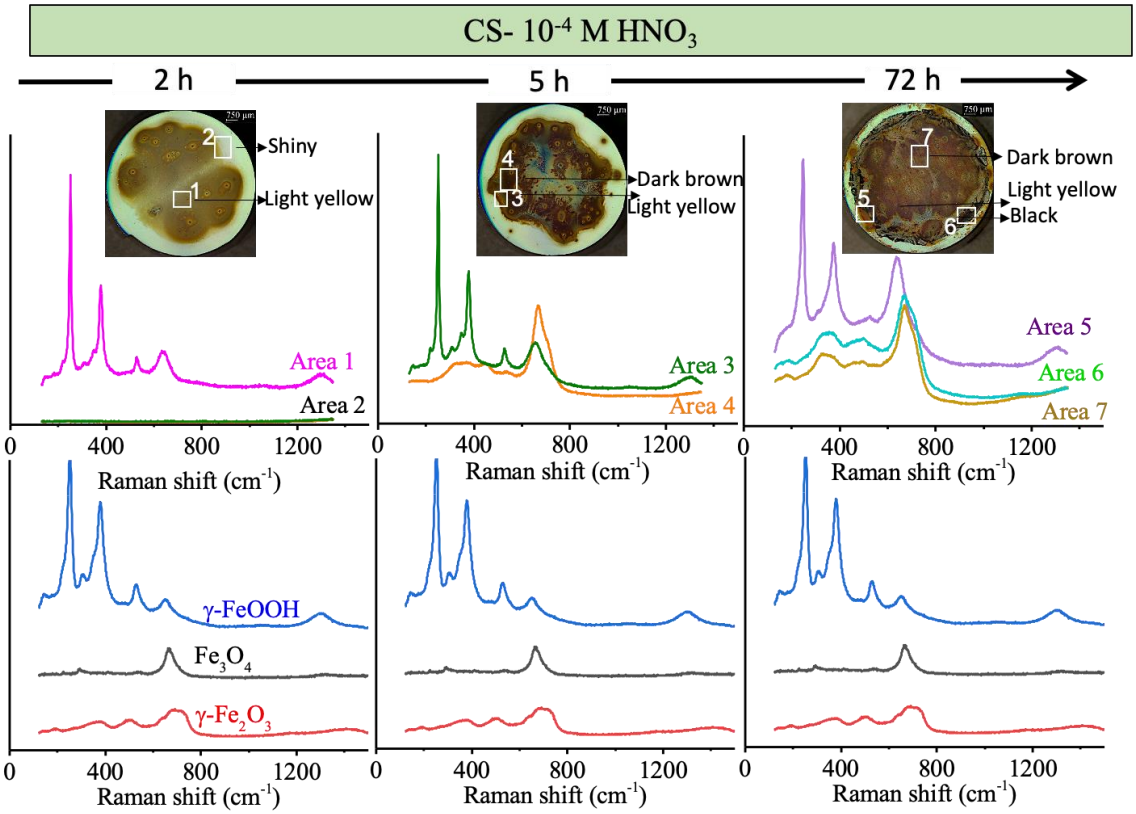

Figure 7-9: Optical and Raman spectra of oxides formed on CS surfaces corroded for different durations in solutions initially containing 10^{-4} M H_2O_2. The Raman spectra of Fe_3O_4, γ-Fe_2O_3, and γ-FeOOH powder samples are shown for reference.

7.3.3 Corrosion of CS vs Pure Iron in Small Volume Nitric Acid Solutions

Figure 7-10 compares the corrosion evolution of pure iron and CS in small volume 10^{-2} M HNO_3 solutions.

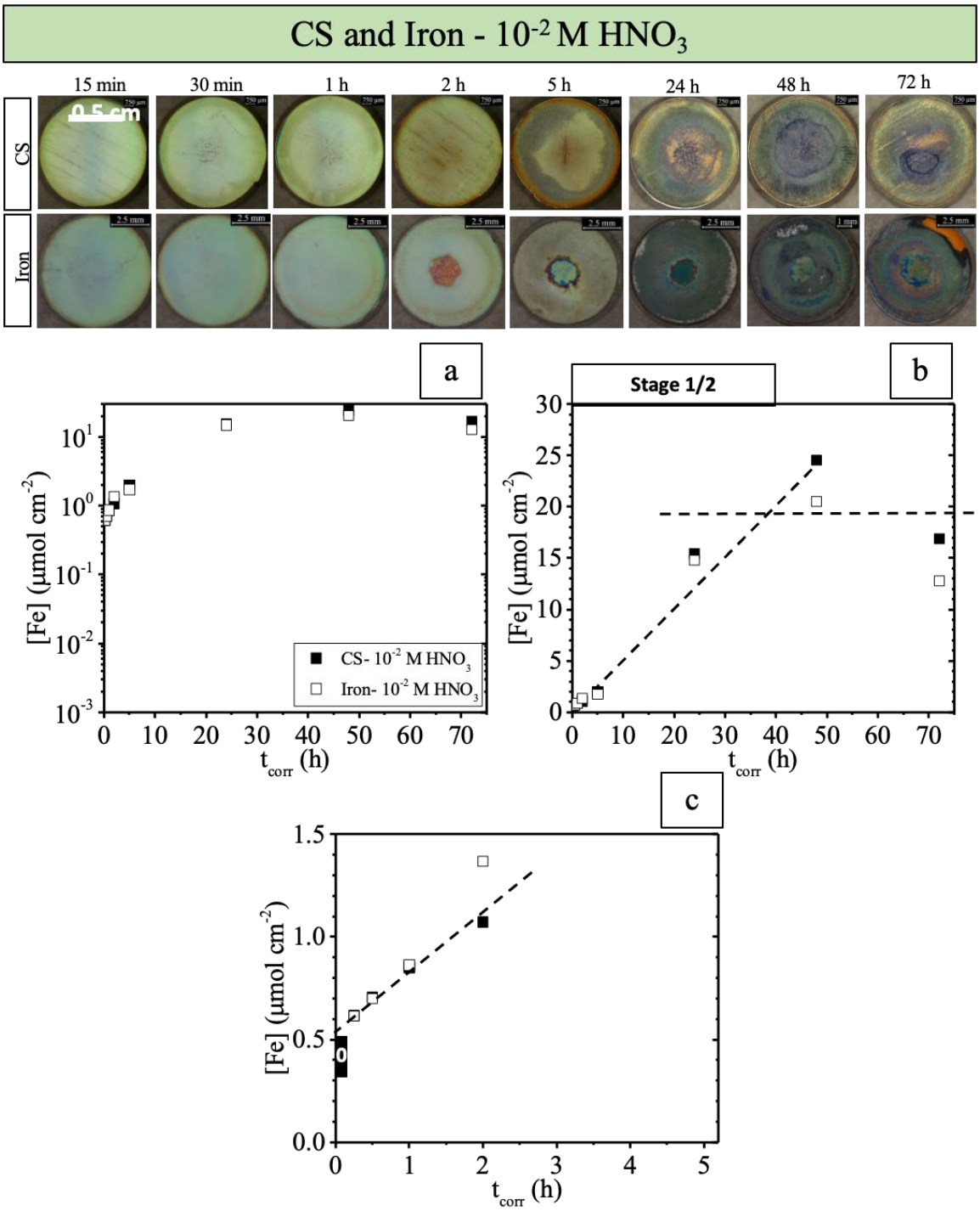

Figure 7-10: Optical images of surfaces and dissolved iron ($[Fe]_{meas}$) obtained as a function of corrosion duration for corrosion of CS and pure iron in a 150 µL solution initially containing 10^{-4} M H_2O_2, a) log $[Fe]_{meas}$ vs t_{corr}, b) $[Fe]_{meas}$ vs t_{corr}, and c) $[Fe]_{meas}$ within first 5 h of corrosion.

The oxide pattern on the surface of pure iron is very similar to that observed for CS. In addition, the amount of dissolved iron at a given time was similar. The results show that regardless of microstructural differences (such as the presence of inclusions) and differences in metal composition (pure metal vs. a solid solution of iron and alloying elements) corrosion of both metals progresses in the same way in solutions with high ionic strength.

7.3.4 Corrosion of CS in Small Volume H_2O_2 Solutions

Figure 7-11 shows the $[Fe]_{meas}$ and the optical images of CS surfaces as a function of corrosion duration in small volume (150 µL) 10^{-4} M H_2O_2 solutions.

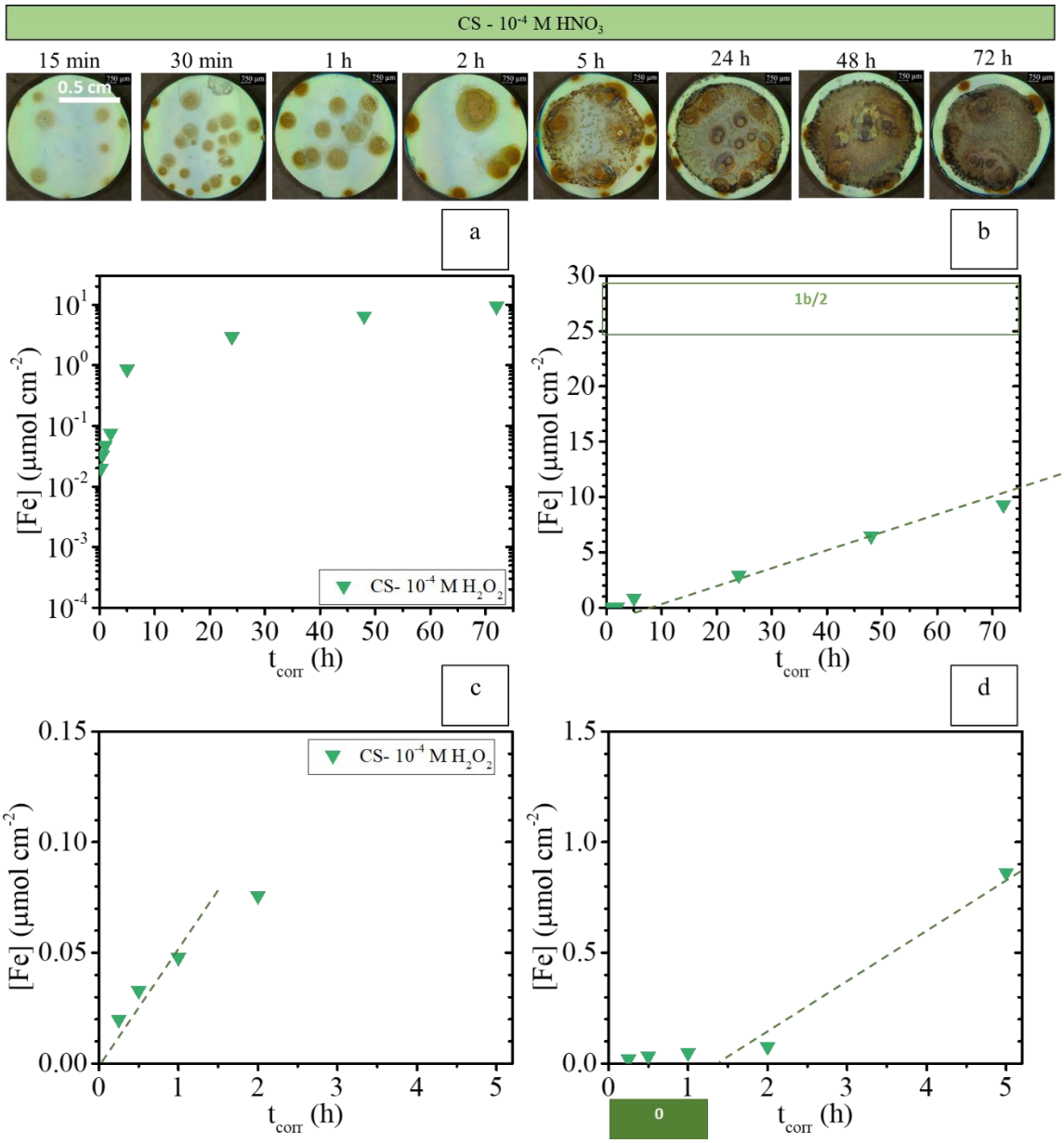

Figure 7-11: Optical images of surfaces and dissolved iron ($[Fe]_{meas}$) obtained as a function of corrosion duration for CS corrosion in 150 µL initially containing 10^{-4} M H_2O_2, a) log $[Fe]_{meas}$ vs t_{corr}, b) $[Fe]_{meas}$ vs t_{corr}, c and d)$[Fe]_{meas}$ within first 5 h of corrosion in different scales.

- In **Stage 0** (t_{corr} < 1 h), the slope of $[Fe]_{meas}$ vs time was ~0.05 µmol cm^{-2} which is similar to that observed in 10^{-3} M HNO_3.
- The duration of **Stage 0** was ~1 h (i.e., almost the same as was observed in 10^{-3} M

HNO_3).

- In **Stage 1b/2** ($1\ h < t_{corr}$), the $[Fe]_{meas}$ was generally lower than in 10^{-2} M and 10^{-3} M HNO_3. $[Fe]_{meas}$ increased linearly with time, similar to what was observed for 10^{-4} M HNO_3. The rate of increase of $[Fe]_{meas}$ was almost 2 times lower than in 10^{-3} M HNO_3. $[Fe]_{meas}$ did not reach a maximum (by 72 h), similar to what was observed for 10^{-4} M HNO_3.
- In H_2O_2 solution, the evolution of oxide formation with time is very similar to that in 10^{-4} M HNO_3, except that the oxide coverage is less extensive in H_2O_2 solution.

Hydrogen peroxide can act as both an oxidizing and a reducing reagent. For H_2O_2, the redox half-reaction is:

$$H_2O_2 + 2\ e^- \leftrightarrows 2\ OH^- \qquad \textbf{(Eq. 7-11)}$$

Initially, the oxidation rate is high, and the hydrolyzed Fe^{2+} and Fe^{3+} are rapidly converted into solid mixed Fe^{II}/Fe^{III} oxides, which facilitates the solvent-mediated conversion of hydroxides to oxides so that conversion of hydrolyzed Fe species into solid oxides is fast enough to progress to **Stage 1b/2** by 1 h. After 1 h, corrosion continues in **Stage 1b/2** and $[Fe]_{meas}$ increases with t_{corr} with the same slope as observed for 10^{-4} M HNO_3. Although hydrogen peroxide is known to be a stronger oxidant than dissolved oxygen [13], and can accelerate the oxidation of Fe to Fe^{II}, it can also serve as a reductant, depending on the nature of the corroding surface [5,37]. It can therefore establish a catalytic cycle between different redox reactions. The iron redox half-reaction is also reversible. The oxidation of hydrogen peroxide to oxygen on the surface of solid Fe^{III} or Fe^{II} oxide is coupled with the kinetically reversible conversion between Fe^{II} and

Fe^{III} on Fe_3O_4 [5,37,38]. The redox reactions (redox coupling) in **Stage 1b/2** (**Eq. 7-12a** to **7-12c**) are as follows:

Red half-reaction: $2\ Fe(OH)_3 + 2\ e^- \rightarrow 2\ Fe(OH)_2 + 2\ OH^-$ (**Eq. 7-12a**)

Ox half-reaction: $H_2O_2 \rightarrow O_2 + 2\ H^+ + 2\ e^-$ (**Eq. 7-12b**)

Overall reaction: $2\ Fe(OH)_3 + H_2O_2 \rightarrow 2\ Fe(OH)_2 + O_2 + 2\ H_2O$ (**Eq. 7-12c**)

Magnetite formation occurs via **Eq. 7-12**.

Magnetite Formation: $Fe(OH)_2 + 2\ Fe(OH)_3$ ®® $Fe_3O_4 + 4\ H_2O$ **(Eq. 7-13)**

In summary, the surface and $[Fe]_{meas}$ analysis revealed similar dynamic stages to those of HNO_3. The rates of reactions in the presence of 10^{-4} M H_2O_2 were mostly similar to those observed with 10^{-3} M HNO_3. Similar rates in the presence of lower hydrogen peroxide concentration is consistent with the greater oxidation power of H_2O_2 than that of HNO_3.

7.4 SUMMARY

In this chapter the effects of HNO_3 and H_2O_2 on the evolution of CS corrosion were investigated. The CS corrosion dynamics were studied in small solutions (solution droplets) by analyzing the average bulk concentrations of dissolved iron and the morphology of the corroded surface as a function of corrosion time. HNO_3 and H_2O_2 were investigated because they are water and humid air radiolysis products in the presence of ionizing radiation and participate in the corrosion process. CS corrosion progresses through the same dynamic stages, for both HNO_3 and H_2O_2. **Stage 0** involves

the oxidation of Fe to solvated $Fe^{2+}_{(aq)}$ in the interfacial region, followed by transport of $Fe^{2+}_{(aq)}$ to the bulk solution. Once the surface solubility limit is reached, the Fe^{II} in the interfacial region precipitates as $Fe(OH)_2$ hydrogel on the surface. In **Stage 1b/2** electron hopping between Fe^{II} and Fe^{III} is faster in the hydrogel network, resulting in faster oxidation. The nitrate concentration affects the rate of progression through individual stages and the overall corrosion rates in individual stages. The linear dependence of reaction rate on the concentration of $[HNO_3]_0$ implies that a first-order reaction occurs in **Stage 0**. The duration of this stage is shorter in solution with higher $[HNO_3]_0$ due to a higher oxidation rate and a higher mass transfer rate, resulting in faster saturation of Fe^{II} in the interfacial region. In **Stage 1b/2,** the corrosion rate was proportional to log $[HNO_3]_0$. In this stage, particularly in solutions of higher $[HNO_3]_0$, the distribution of oxides/hydroxides is not uniform across the coupon surface and depends on the solution thickness, which is not uniform because of the dome shape of the solution droplet. The area exposed to the shallower solution approaches subsequent stages faster.

The time-dependent behaviours of CS corrosion in 10^{-4} M H_2O_2 were similar to those observed in HNO_3 solutions. For 10^{-4} M hydrogen peroxide, the rate of **Stage 0** was 10 times larger than for 10^{-4} M HNO_3, indicating that hydrogen peroxide is a more effective oxidant than 10^{-4} HNO_3 for iron oxidation when the surface is not saturated with iron. However, in **Stage 1b/2**, hydrogen peroxide acts as an oxidant for the oxidation of Fe^{II} to Fe^{III}, while also acting as a reductant, participating in oxide formation through the reduction of Fe^{III} to Fe^{II} in a low ionic strength solution.

The evolution of the surface and solution with time for pure iron in 10^{-2} M HNO_3 showed that regardless of microstructural differences and differences in metal

composition, corrosion of both metals progresses in the same way in solutions of high ionic strength. This implies that, in high ionic strength, the effect of microstructure on corrosion of CS is negligible.

This chapter has demonstrated the dynamic stages of CS corrosion in the presence of chemically added HNO_3 and H_2O_2. These two oxidants are the main products of humid air radiolysis. The presented results and the dynamic stages identified will be used in interpreting CS corrosion in small volume solutions in the presence of radiation in **Chapter 8**.

7.5 REFERENCES

[1] J.W.T. Spinks, R.J. Woods, An introduction to radiation chemistry, John Wiley and Sons Inc, United States, 1990.

[2] W.A. Van Hook, Handbook of Nuclear Chemistry, 2nd ed., Springer, 2011.

[3] J.C. Wren, Steady-State Radiolysis: Effects of Dissolved Additives, in: C.M. Wai1, B.J. Mincher (Eds.), Nucl. Energy Environ., American Chemical Society, 2010: pp. 271–295.

[4] R.P. Morco, J.M. Joseph, D.S. Hall, C. Medri, D.W. Shoesmith, J.C. Wren, Modelling of radiolytic production of HNO_3 relevant to corrosion of a used fuel container in deep geologic repository environments, Corros. Eng. Sci. Technol. 52 (2017) 141–147.

[5] A.Y. Musa, J.C. Wren, Combined effect of gamma-radiation and pH on corrosion of Ni-Cr-Fe alloy inconel 600, Corros. Sci. 109 (2016) 1–12.

[6] M. Momeni, Gamma-Radiation Induced Corrosion of Alloy 800, PhD Thesis, The University of Western Ontario, 2017.

[7] V.S. Bagotsky, Fundamentals of Electrochemistry: Second Ed., Wiley Blackwell, 2005.

[8] A.J. Bard, L.R. Faulkner, Electrochemical Methods: Fundamentals and Applications, 2nd Edition | Wiley, Wiley, New York. (2000) 864.

[9] M. Naghizadeh, Copper Corrosion Dynamics under Deep Geologic Repository Conditions, PhD Thesis, The University of Western Ontario, 2021.

[10] R. Karimihaghighi, Non-Linear Effects of Solution Parameters and Gamma Radiation on Nickel Oxidation Dynamics, PhD Thesis, The University of Western Ontario, 2021.

[11] Y.G. Shin, Nonlinear Dynamics of Carbon Steel Corrosion under Gamma Radiation, PhD Thesis, The University of Western Ontario, 2020.

[12] D. Fu, J.C. Wren, Preparation and characterization of ferric oxyhydroxide and ferric oxide thin films by direct-hydrolysis deposition, J. Nucl. Mater. 374 (2008) 116–122.

[13] K. Daub, A Study of Gamma Radiation Induced Carbon Steel Corrosion, PhD Thesis, The University of Western Ontario, 2013.

[14] R.P. Morco, A.Y. Musa, M. Momeni, J.C. Wren, Corrosion of carbon steel in the [P14666][Br] ionic liquid: The effects of γ-radiation and cover gas, Corros. Sci. 102 (2016) 1–15.

[15] S.M. Cambier, D. Verreault, G.S. Frankel, Raman Investigation of Anodic Undermining of Coated Steel During Environmental Exposure, Corrosion. 70 (2014) 1219–1229.

[16] R.M. Cornell, U. Schwertmann, The Iron Oxides, Wiley-VCH Verlag GmbH & Co. KGaA, Weinheim, FRG, 2003.

[17] D. Guo, Corrosion Dynamics of Carbon Steel in Used Fuel Container Corrosion Dynamics of Carbon Steel in Used Fuel Container Environments Environments, PhD Thesis, The University of Western University, 2018.

[18] C.F. Baes Jr., R.E. Mesmer, The Hydrolysis of Cations, John Wiley & Sons, Inc, 1976.

[19] P. Taylor, Ostwald ripening in emulsions, Adv. Colloid Interface Sci. 75 (1998) 107–163.

[20] J.H. Yao, K.R. Elder, H. Guo, M. Grant, Theory and simulation of Ostwald ripening, Phys. Rev. 47 (1993) 14110–14125.

[21] Y. Wang, M.A. Chan, E. Merino, Self-organized iron-oxide cementation geometry as an indicator of paleo-flows, Sci. Rep. 5 (2015) 1–15.

[22] W. Davison, G. Seed, The kinetics of the oxidation of ferrous iron in synthetic and natural waters, Geochim. Cosmochim. Acta. 47 (1983) 67–79.

[23] A.R. Ahmad, Coupled diffusion and oxidation of ferrous iron in soils. I. Kinetics of oxygenation of ferrous iron in soil suspension, 1990.

[24] W. Stumm, G.F. Lee1, Oxygenation of Ferrous Iron, Ind. Eng. Chem. 53 (2002) 143–146.

[25] A. Persat, R.D. Chambers, J.G. Santiago, Basic principles of electrolyte chemistry for microfluidic electrokinetics. Part I: Acid–base equilibria and pH buffers, Lab Chip. 9 (2009) 2437–2453.

[26] M. Semmler, E.K. Mann, J. Rička, M. Borkovec, Diffusional Deposition of Charged Latex Particles on Water−Solid Interfaces at Low Ionic Strength, Langmuir. 14 (1998) 5127–5132.

[27] Y. Liu, Z. Zhang, N. Bhandari, Z. Dai, F. Yan, G. Ruan, A.Y. Lu, G. Deng, F. Zhang, H. Al-Saiari, A.T. Kan, M.B. Tomson, New Approach to Study Iron Sulfide Precipitation Kinetics, Solubility, and Phase Transformation, Ind. Eng. Chem. Res. 56 (2017) 9016–9027.

[28] M. Xu, K. Sullivan, G. Vanness, K.G. Knauss, S.R. Higgins, Dissolution kinetics and mechanisms at dolomite-water interfaces: effects of electrolyte specific ionic strength, Environ. Sci. Technol. 47 (2013) 110–118.

[29] J. Wang, J. Wang, E.H. Han, Influence of Conductivity on Corrosion Behavior of 304 Stainless Steel in High Temperature Aqueous Environment, J. Mater. Sci. Technol. 32 (2016) 333–340.

[30] H.J. Krug, H. Brandtstädter, K.H. Jacob, Morphological instabilities in pattern formation by precipitation and crystallization processes, Int. J. Earth Sci. 85 (1996) 19–28.

[31] H. Nabika, M. Itatani, I. Lagzi, Pattern Formation in Precipitation Reactions: The Liesegang Phenomenon, Langmuir. 36 (2020) 481–497.

[32] E. Nakouzi, O. Steinbock, Self-organization in precipitation reactions far from the equilibrium, Sci. Adv. 2 (2016).

[33] H.K. Henisch, Liesegang ring formation in gels, J. Cryst. Growth. 76 (1986) 279–289.

[34] K.H. Stern, The Liesegang Phenomenon., Chem. Rev. 54 (2002) 79–99.

[35] S. Li, L.H. Hihara, In situ Raman spectroscopic identification of rust formation in Evans' droplet experiments, Electrochem. Commun. 18 (2012) 48–50.

[36] S. Li, L.H. Hihara, In situ Raman Spectroscopic Study of NaCl Particle-Induced Marine Atmospheric Corrosion of Carbon Steel, J. Electrochem. Soc. 159 (2012) C147–C154.

[37] P.A. Yakabuskie, J.M. Joseph, C.R. Stuart, J.C. Wren, Long-Term γ-Radiolysis Kinetics of NO_3^- and NO_2^- Solutions, J. Phys. Chem. A. 115 (2011) 4270–4278.

[38] D. Fu, X. Zhang, P.G. Keech, D.W. Shoesmith, J.C. Wren, An electrochemical study of H_2O_2 decomposition on single-phase γ-FeOOH films, Electrochim. Acta. 55 (2010) 3787–3796.

CHAPTER 8
GAMMA RADIATION-INFLUENCED CORROSION OF CARBON STEEL AND STAINLESS STEEL

8.1 INTRODUCTION

As nuclear power plants age, assessment of the integrity of their structural materials becomes increasingly important. In CANDU reactors, the annular air gap around the periphery of the calandria tank assembly and its supporting structures is a possible location for corrosion. The shield tank materials (carbon steel) and end shield (304L stainless steel) are welded to each other using 309 stainless steel as the filler material. This dissimilar metal joint will be exposed to a continuous flux of γ-radiation and, potentially, small volumes of stagnant water or humid air.

Corrosion rates of metal alloys are controlled by the concentrations of redox-active species in the solution. Gamma-radiolysis of water and humid air results in redox-active species such as H_2O_2 and HNO_3, respectively. The concentrations of these redox-

active species affect the corrosion rates of metals. Because these radiolysis products can affect the corrosion kinetics, it is important to understand the corrosion performance of structural materials in the presence of γ-radiation. Radiolysis of humid air produces nitric acid, which is easily absorbed by water in contact with the humid air and lowers its pH [1] (See **Figure 8-1**).

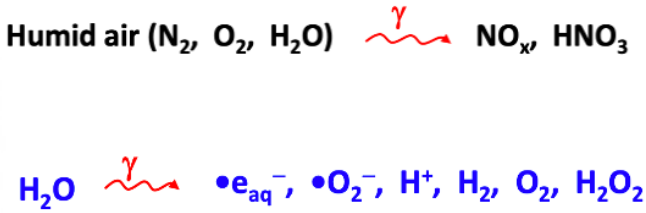

Figure 8-1: Humid air and water radiolysis products.

Nitric acid is a powerful oxidant [2]. It is one of the main humid air radiolysis products continuously produced under γ-radiation, and makes the solution system complex [3,4]. Not only can the continuous introduction of nitric acid into solution affect the metal solution redox reactions, but it also changes the solution pH, and consequently metal solubility [5]. Nitrate ions also complex with Fe^{3+}, which further affects Fe^{3+} solubility and hinders production of protective Fe^{3+} oxides [2].

The kinetics of water radiolysis have been well studied under a wide range of solution conditions using radiolysis kinetics modelling and experiments [4,6–11]. A humid-air radiolysis model (HARM) has been developed and used to calculate time-dependent concentrations of radiolysis products [1,4]. These calculations were performed as a function of temperature, relative humidity in air and radiation dose rate. The model calculation results show that HNO_3 is the dominant oxidizing species formed during humid air radiolysis. These results were analyzed by R.P. Morco [1,4] to formulate the

overall radiolytic production rate of nitric acid that may be absorbed in the water in contact with the supporting structure steels. There has also been extensive research on the corrosion of carbon steel and stainless steels in the presence of γ-radiation [12–19].

The corrosion kinetics of an alloy depend not only on the metallurgical properties of the metal, but also on the solution redox and electrolyte properties, including the concentrations of redox active species present, pH and temperature. Therefore, in order to understand the performance of these metals in nuclear environments it is essential to understand the effect of water radiolysis on their corrosion kinetics.

The effect of chemically added nitric acid (HNO_3), as the main oxidant produced in humid air and hydrogen peroxide (H_2O_2), as the main product of water radiolysis, were studied in **Chapters 4-7** of this thesis. This chapter studies the effect of a continuous flux of γ-radiation on the corrosion of CS and SS under small solution droplets and in humid air environments. The first section of this chapter discusses the evolution of CS corrosion under a water droplet in the presence and absence of γ-radiation. To understand the effect of γ-radiation in different environments, the surface evolution was studied using an optical microscope and the amount of dissolved iron was measured as a function of time. The cover gases studied in this section were hydrocarbon-free (HC-free) air (21% oxygen + 79% nitrogen), 21% oxygen + 79% argon, and pure argon. The second section of this chapter discusses the results of the investigation on the effect of cover gas composition on the radiation-influenced humid air corrosion of CS, and SS.

8.2 EXPERIMENTAL PROCEDURES

8.2.1 Procedure for Corrosion Studies in Small Volume Solutions

Time-dependent droplet studies were performed in the presence and absence of γ-radiation. In the experiments presented in the first section of this chapter, the coupon material was carbon steel and the test solution used was pure water. Each coupon was placed in its own separate vial and the vial was sealed using an aluminum crimp cap fitted with a PTFE silicon septum (Agilent Technologies). Then, vials containing the coupons and those containing the solution were all purged with the cover gas being used for 30 min. Finally, using a syringe, a 150 µL drop of the test solution was placed on the surface of the coupon in the test vial. The water droplets spread right to the edges of the coupons, forming dome shapes, as shown in Figure 8-2.

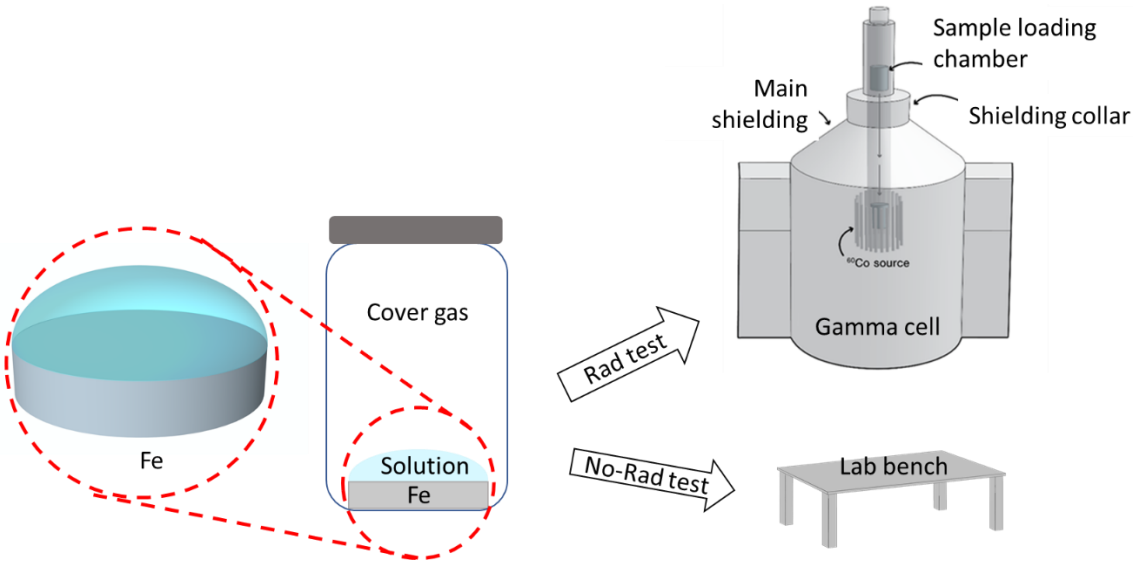

Figure 8-2: Experimental set-up for droplet studies in the presence and absence of γ-radiation.

After the test period, the vials were uncapped, and the coupon surfaces were washed with 6 mL of NANOpure water to collect all the solution and any loose particles on the surface. The coupon surfaces were dried under vacuum to ensure the adhered oxide layer was not removed during drying, which would occur under Ar gas drying. The coupons were then stored in a desiccator under vacuum to await surface analysis.

One set of experiments was performed under γ-radiation. Radiation experiments were performed in a ^{60}Co gamma cell irradiator (220 Excel, MDS Nordion). The absorbed radiation dose rate in the irradiation chamber during the experiments was 2.8 $kGyh^{-1}$, where 1 Gy = 1 J absorbed per kg of water. All vials were irradiated in a custom-made circular sample holder to assure that all coupons received the same dose rate during the exposure time.

8.2.2 Procedure for Humid Air Exposure Tests

A carbon steel-stainless steel weld joint block was provided by Ontario Power Generation. A rectangular (10 mm by 5 mm) coupon was cut from the carbon steel CS/W joint, as shown in **Figure 8-3.** The elemental compositions of CS, 304L SS (SS), and 309 SS (W) are shown in **Table 6-1**.

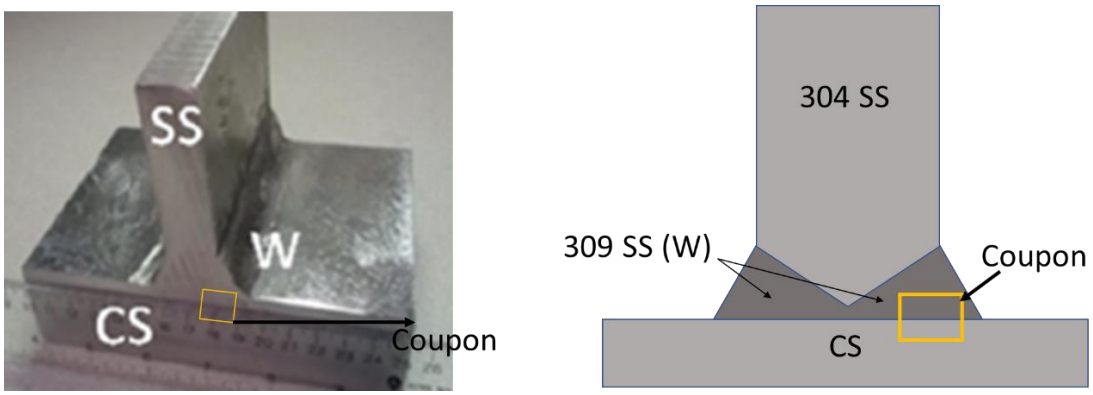

Figure 8-3: The carbon steel-stainless steel weld joint block provided by Ontario Power Generation, and the location from which the coupon was cut.

Table 8-1: Elemental composition of various steels presented in Figure 8-3.

Material	Cr (wt.%)	Ni (wt.%)	Fe (wt.%)
Carbon Steel A36 (CS)	0.16	0.23	98
Weld Metal Stainless Steel 309 (W)	24	14	60
Stainless Steel 304L (SS)	19	8	71

The humid air experiments were performed only under γ-radiation. A separate vial was used for each coupon. Each coupon was placed in a vial and water was added. The set-up for the test coupon (Figure 8-4**)** shows that the coupons are not immersed and are exposed only to the humid air contained within the vial. Each vial was sealed using an aluminum crimp cap fitted with a PTFE silicon septum (Agilent Technologies), and then purged with the cover gas. The temperature in the gamma cell naturally rose to 50 °C, which provided the conditions required for the 100% humidity during the exposure period.

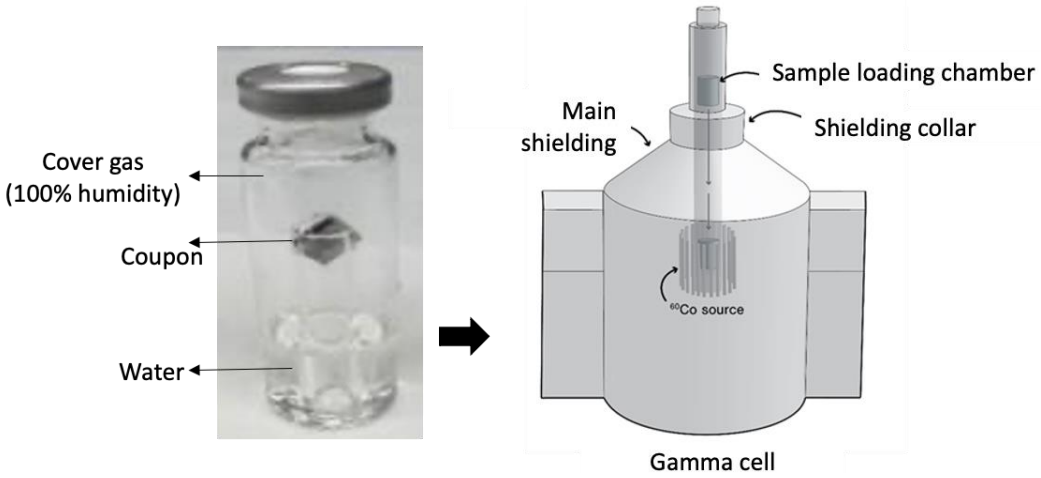

Figure 8-4: Experimental set-up for humid air corrosion under γ-radiation.

The procedure for the experiments in the gamma cell was the same as for the droplet studies, as described in **section 8.2.1**.

8.2.3 Irradiation

All radiation exposure tests were performed using a ^{60}Co gamma cell irradiator (220 Excel, MDS Nordion). The absorbed radiation dose rate in the irradiation chamber during the experiments was 2.8 kGy h^{-1}, where 1 Gy = 1 J absorbed per kg of water. The individual vials containing the CS coupons were placed in a circular sample holder to ensure that all samples received the same dose during the exposure time.

8.2.4 Post-Test Analysis

After each test, the solution was collected and transferred to a glass vial. After reaching room temperature the pH of the solution was measured and the concentration of dissolved Fe ions (including dissolved species and solid oxide particles dispersed in the solution, was determined by ICP-OES. The metal coupon was removed, washed with Type 1 water, and dried with argon gas. The surface morphology and composition of oxides on the coupons were then investigated by optical and scanning electron microscopy (SEM), and X-ray spectroscopy (EDX). The optical microscope used was a Leica DVM 6A digital microscope and high-resolution images were obtained using a LEO 1540XB field emission SEM.

8.3 RESULTS AND DISCUSSION

The first section of the results and discussion deals with CS corrosion studies in small volume solutions in the presence and absence of radiation and under different cover gases, and the second section presents the results of humid air corrosion of the CS-W joints under different cover gases in the presence of γ-radiation.

8.3.1 Corrosion Studies in Small Volume Solutions

8.3.1.1 Effect of γ-Radiation on Corrosion of CS in Small Water Volumes under Ar

The evolution of the CS surface as function of t_{corr} during the corrosion of CS in a 150 μl pure water droplet under Ar, in the presence and absence of γ-radiation, is presented in Figure 8-5**.**

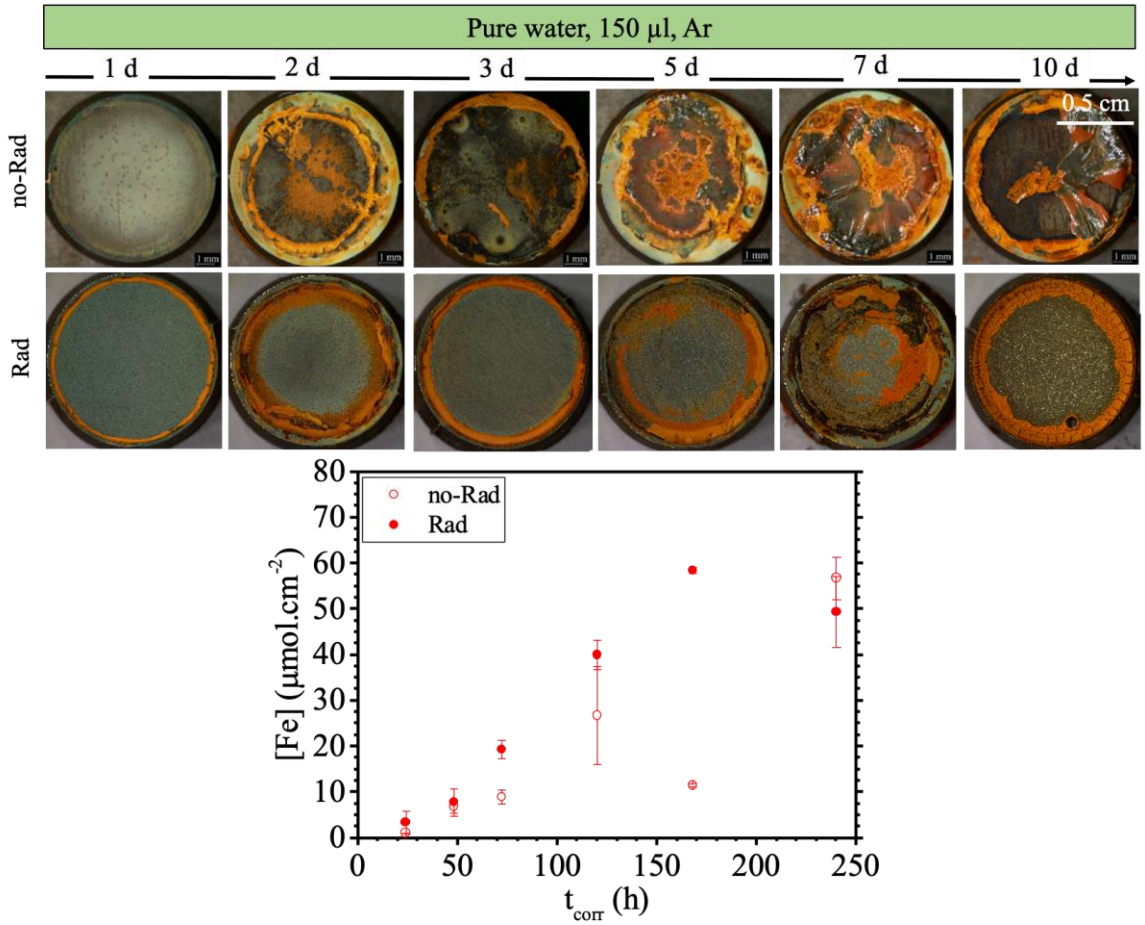

Figure 8-5: Evolution of the surface and $[Fe]_{meas}$ vs t_{corr} for CS corroded under a 150 µL pure water droplet in the presence ("Rad") and absence ("no-Rad") of γ-radiation. The cover gas was Ar.

Corrosion Progression in the Absence of γ-Radiation

In the absence of γ-radiation, $[Fe]_{meas}$ fluctuated with t_{corr} in the earlier periods of corrosion (before 7 d) and increased to higher values afterward. The CS surface was covered with a very thin black oxide after 1 d, with the coupon edge areas appearing darker than the central area. It should be noted that the droplet does not have uniform thickness across the coupon surface. As discussed later, corrosion progression to advanced stages is faster for smaller solution depths. Thus, it should be noted here that the stages described in this chapter are considered the dynamic stages for the central area

of the coupon surface, and do not correspond to the coupon edge progression. The difference in corrosion progression for the coupon edge areas will be explained later for the cases where significant differences were observed.

The appearance of the double layer oxide observed at longer times of exposure suggests that it consists of a γ-FeOOH outer layer, and a magnetite sublayer. This double layer is shown for coupons surfaces corroded for 7 d under droplets, in the absence of γ-radiation.

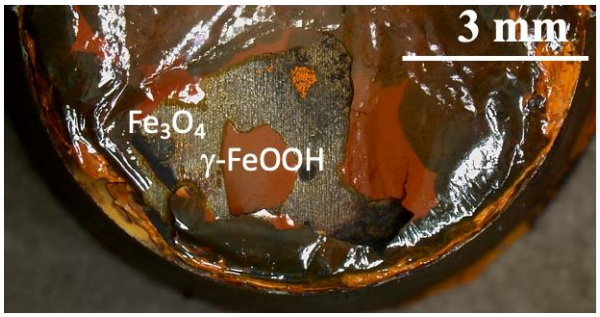

Figure 8-6: Optical microscope images of a CS surface corroded under a 150 µL pure water droplet in the absence of γ-radiation for 7 d, showing the top layer and underlying oxides. The cover gas was Ar.

The type of surface oxides remained the same and the surface remained covered with oxide for at least 240 h, which was the longest exposure time in this study. Quantifying the thickness of magnetite, which was underneath the γ-FeOOH, was not performed. However, the optical microscopy of the corroded samples suggested that the magnetite oxide became thicker with t_{corr}.

The edge areas of the surface were covered mostly with $Fe(OH)_3$ during the tests. This hydroxide was loose (see **Figure 8-6**) and was washed off in some cases, such as for the 2 d, 5 d, and 7 d coupons; thus, they are not observed in the optical microscopy

images of the surfaces. The explanation for the preferential formation of Fe^{III} at the edge areas of coupons due to the early supersaturation of the shallower solution is presented in detail in **Chapter 7**.

As explained in **Chapter 7**, In **Stage 1**, in the absence of oxygen, the interfacial charge transfer reactions at the metal surface are as follows:

Oxidation half-reaction: $Fe_{(m)} \rightarrow Fe^{2+} + 2\ e^-$ (**Eq. 8-1a**)

Reduction half-reaction of water: $2\ H_2O + 2\ e^- \rightarrow H_2 + 2\ OH^-$ (**Eq. 8-1b**)

Overall charge transfer reaction:

$Fe_{(m)} + 2\ H_2O \rightarrow Fe^{2+} + 2\ OH^- + H_2$ (**Eq. 8-1c**)

where the subscript (m) denotes the solid metal.

The interfacial mass transfer reactions and the transport of solution oxidants to the surface are as follows:

Mass transport of metal cations: $Fe^{2+}|_{x=0} \longrightarrow\!\!\!\!\!\rightarrow Fe^{2+}|_{x=sol}$ **(Eq. 8-2a)**

Mass transport of OH^-: $OH^-|_{x=sol} \longrightarrow\!\!\!\!\!\rightarrow OH^-|_{x=0}$ **(Eq. 8-2b)**

Once the interfacial region is saturated with Fe^{2+} ions, a viscous $Fe(OH)_2$ hydroxide layer starts to form at the surface. The corrosion of CS in a small droplet of pure water has progressed to **Stage 2** after 1 d. While reactions **Eq. 8-1** and **Eq. 8-2** continue to occur, hydrogel formation occurs as follows:

$Fe^{2+} + n\ OH^- \rightleftharpoons Fe(OH)_m^{2-m} + (n-m)\ OH^-$ where m = 1, 2, or 3 **(Eq. 8-3a)**

$n\ Fe(OH)_2 + m\ H_2O \rightleftarrows Fe_m(OH)_{2n}(H_2O)_{m(gel)}$ **(Eq. 8-3b)**

The formation of a hydrogel layer slows down the transport of metal ions from the metal/solution interface to the bulk solution. Electron transfer between Fe^{II} and Fe^{III} is faster in the hydrogel than in an aqueous solution [40]. Thus, **Eq. 8-4c** occurs more rapidly once the hydrogel has formed. The following redox reactions occur within the hydrogel layer in **Stage 2**.

Ox half-reaction of Fe^{II}: $2\ Fe(OH)_2 + 2\ OH^- \longrightarrow 2\ Fe(OH)_3 + 2\ e^-$ **(Eq. 8-4a)**

Red half-reaction of water: $2\ H_2O + 2\ e^- \longrightarrow 2\ OH^- + H_2$ **(Eq. 8-4b)**

Overall charge transfer reaction with water as oxidant:

$2\ Fe(OH)_2 + 2\ H_2O \longrightarrow 2\ Fe(OH)_3 + H_2$ (**Eq. 8-4c**)

Ferrous ions are continuously produced by metal oxidation but also consumed continuously by hydrolysis reactions and $Fe(OH)_2$ precipitation. Because the Fe ions that are being produced are consumed to grow the gel layer, the net production rate of Fe^{2+} is negligible.

The corrosion of CS in small volume solutions under Ar progressed to **Stage 3** by 5 d. In **Stage 3**, reactions (**Eq. 8-1**) to (**Eq. 8-4**) occur and iron oxides start to form via the reactions below (**Eq. 8-5**):

Magnetite formation: $Fe(OH)_2 + 2\ Fe(OH)_3 \rightarrow\rightarrow Fe_3O_4 + 4\ H_2O$ **(Eq. 8-5a)**

γ-FeOOH formation: $Fe(OH)_3 \rightarrow\rightarrow FeOOH + H_2O$ **(Eq. 8-5b)**

Depending on the steady-state concentrations of Fe^{II} and Fe^{III} and also on the concentration of oxygen or other oxidants in the interfacial region, the oxidation rate of

Fe^{II} to Fe^{III} will be different. In **Stage 3**, the rate of oxide formation inside the gel layer is equal to the rate of oxidation and the rate of $[Fe]_{meas}$ increase is almost zero. Based on the relative production rates of $Fe^{2+}/Fe(OH)_2$ and $Fe^{3+}/Fe(OH)_3$, metal oxide grows preferentially as magnetite (black) and/or lepidocrocite (orange). It was observed (see Figure 8-6) that in the top layer, $Fe(OH)_2$ starts to convert into ferric hydroxide and γ-FeOOH (the orange oxide). The formation of magnetite from Fe^{II}/Fe^{III} (the black oxide) occurred between the CS surface and the outer solution/oxide interface where γ-FeOOH formed. The formation of γ-FeOOH from $Fe(OH)_3$ is favoured at the top of the gel layer, where the Fe^{II}:Fe^{III} ratio is low. The formation of Fe_3O_4, which is a Fe^{II}/Fe^{III} oxide is predominant below where the orange γ-FeOOH oxide forms, where the Fe^{II}:Fe^{III} ratio is high. The total $[Fe]_{meas}$ increased almost linearly until 124 h. Once it had reached its maximum, the total $[Fe]_{meas}$ fluctuated around a constant value.

Corrosion Progression in the Presence of γ-Radiation

The hydrogen peroxide redox half-reaction in the presence of radiation (and therefore continuous replenishment of H_2O_2) is:

$$H_2O_2 + 2\ e^- \leftrightarrows 2\ OH^- \qquad \textbf{(Eq. 8-6)}$$

Shin [5] showed that under γ-radiation, $[H_2O_2]$ reaches a steady-state concentration of $\sim 2\times10^{-4}$ M in 6 h with a dose rate of 2.5 kGy h^{-1}. The fast rate of iron oxidation is initially provided by the high concentration of H_2O_2. The fast rate of iron oxidation provides the conditions for saturation of Fe^{II}. The hydrolyzed Fe^{2+} and Fe^{3+} are rapidly converted into mixed solid $Fe^{II/}Fe^{III}$ oxides. The magnetite that forms in the presence of γ-radiation is uniform and is adhered to the surface. Hydrogen peroxide can act as both an oxidizing

[14] and a reducing reagent, depending on the nature of the corroding surface [10,20] and it facilitates the solvent-mediated conversion of Fe^{II} hydroxides to Fe^{II}/Fe^{III} or Fe^{III} oxides so that the conversion of hydrolyzed Fe species into solid oxides is fast enough to progress to **Stage 3** by <1 d. After 1 d, corrosion continues in **Stage 3** and $[Fe]_{meas}$ increases with t_{corr} with the same slope as observed in the absence of radiation.

Because hydrogen peroxide can act both as an oxidizing and as a reducing agent, a catalytic cycle between different redox reactions can be established. The iron redox half-reaction is also reversible. The oxidation of hydrogen peroxide to oxygen on the surface of solid Fe^{III} or Fe^{II} oxide can couple with the kinetically reversible conversion between Fe^{II} and Fe^{III} on Fe_3O_4 [10,20,21].

The redox reactions (redox coupling) in **Stage 3** (**Eq. 8-7a** to **8-7c**) are as follows:

Red half-reaction: $2\ Fe(OH)_3 + 2\ e^- \rightarrow 2\ Fe(OH)_2 + 2\ OH^-$ (**Eq. 8-7a**)

Ox half-reaction: $H_2O_2 \rightarrow O_2 + 2\ H^+ + 2\ e^-$ (**Eq. 8-7b**)

Overall reaction: $2\ Fe(OH)_3 + H_2O_2 \rightarrow 2\ Fe(OH)_2 + O_2 + 2\ H_2O$ (**Eq. 8-7c**)

Magnetite formation occurs via **Eq. 8-8**.

Magnetite Formation: $Fe(OH)_2 + 2\ Fe(OH)_3$ ®® $Fe_3O_4 + 4\ H_2O$ **(Eq. 8-8)**

The evolution of the magnetite oxide layer during corrosion in the presence and absence of γ-radiation is presented in Figure 8-7.

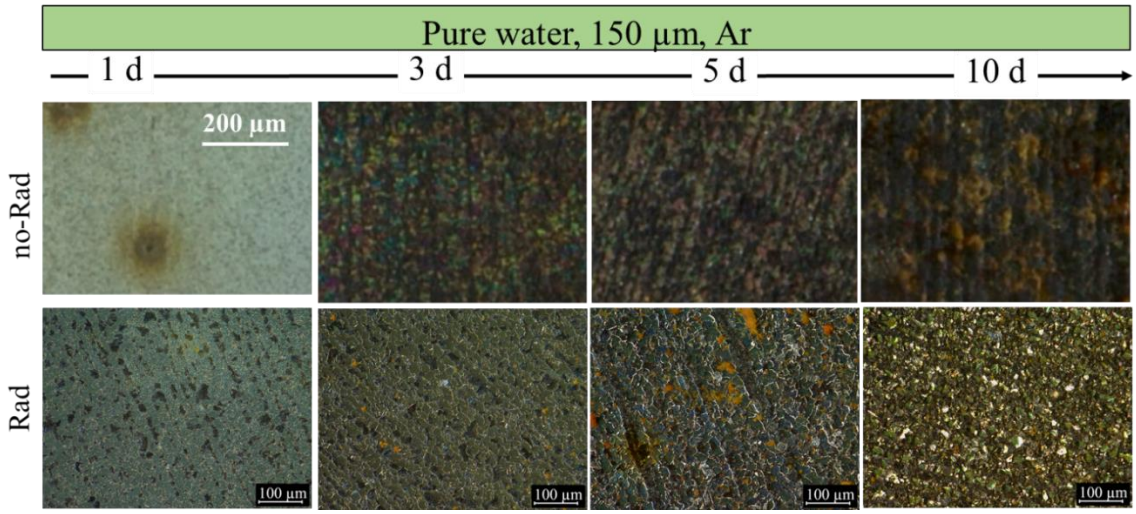

Figure 8-7: The evolution of the magnetite oxide layer during corrosion under a 150 µL pure water droplet under Ar, in the presence and absence of γ-radiation.

Although in the presence of γ-radiation corrosion has progressed to **Stage 3** in less than 1 d, the formation of a uniform magnetite layer in the early stages of corrosion results in more uniform progression of oxide formation and a more uniform magnetite oxide in later times in **Stage 3** where redox coupling is less effective (less Fe^{III} is available to participate in $Fe^{II} \leftrightarrows Fe^{III}$ reduction).

The surfaces corroded under γ-radiation were covered with orange γ-FeOOH while Fe^{III} was converted to Fe^{II} oxide underneath the γ-FeOOH layer. The magnetite oxide layer thickens in both the presence and absence of γ-radiation. However, it increases more rapidly under radiation, where there is continuous production of H_2O_2. The continuous generation of hydrogen peroxide continues to oxidize Fe to Fe^{II} and Fe^{II}/Fe_3O_4 to Fe^{III}/FeOOH, resulting in the continuous formation of FeOOH on top and Fe_3O_4 underneath the FeOOH.

Under γ-radiation, magnetite formed at the coupon edge areas, where it was covered with Fe^{III} oxide. This was different from the observation in non-irradiated conditions, where the surface underneath Fe^{III} oxide at the edges was magnetite free. Early deposition of Fe^{III} oxide at the irradiated coupon edge areas also occurs in the presence of γ-radiation, just like in its absence. However, the formation of magnetite under the Fe^{III} hydroxide via redox coupling between Fe^{III}/Fe^{II} and H_2O_2/O_2 is possible under radiation, which can increase the rate at which magnetite forms under the FeOOH layer.

In summary, it was observed that the progression of CS corrosion in pure water under γ-radiation is more influenced by the early formation of Fe^{III} cations and redox coupling between Fe^{III}/Fe^{II} and H_2O_2/O_2, which facilitate the formation of magnetite and results in a faster progression to **Stage 3** than that observed without radiation.

8.3.1.2 Effect of Cover Gas on the Corrosion Behaviour of CS in Small Volume Solutions in the Absence of γ-Radiation

The evolution of the surface and $[Fe]_{meas}$ as a function of t_{corr} during the corrosion of CS under a small water droplet (150 μL), in the presence of different cover gases and in the absence and presence of γ-radiation, are presented in Figure 8-8**.**

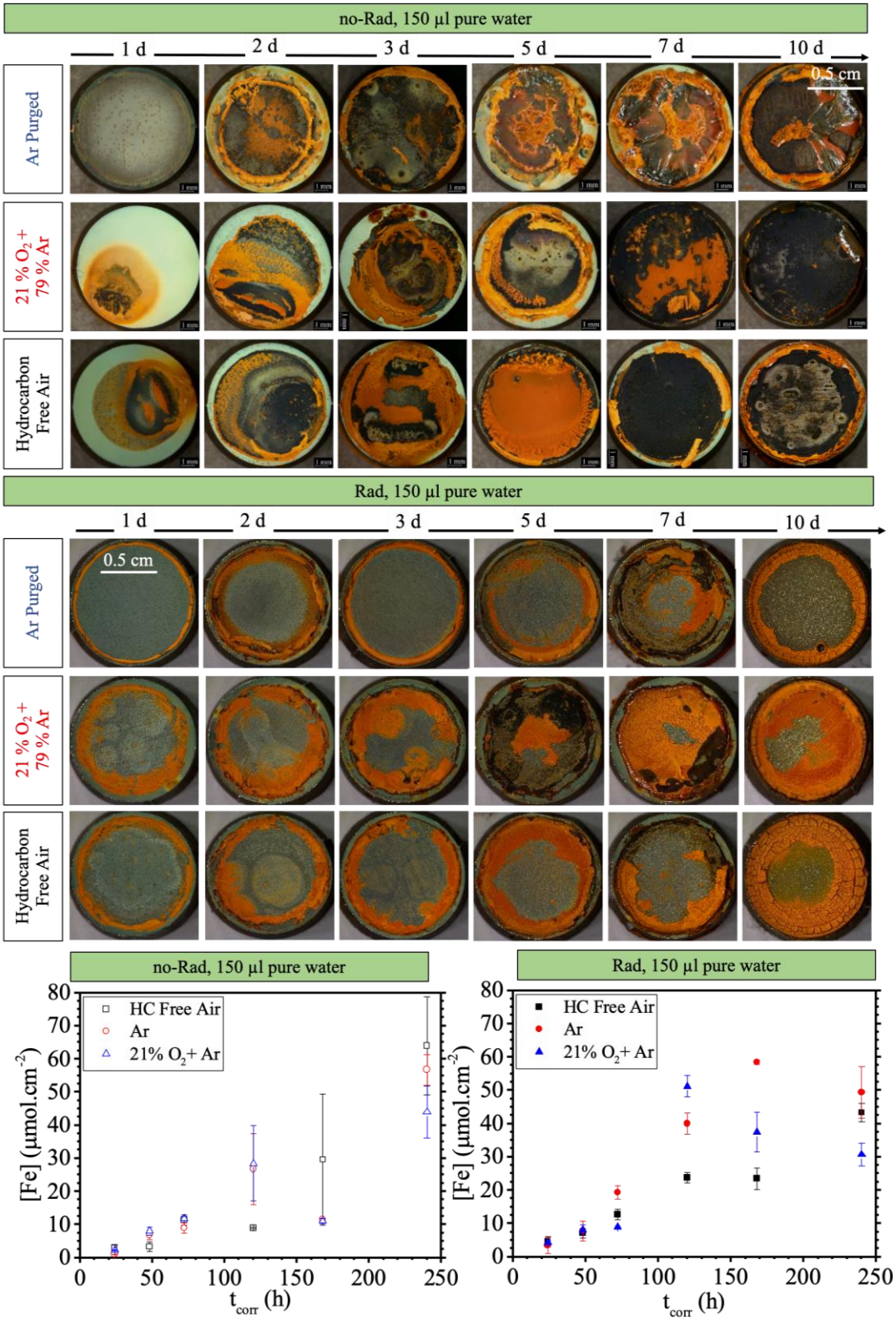

Figure 8-8: The evolution of the surfaces and $[Fe]_{meas}$ vs t_{corr} for CS corroded under a 150 µL pure water droplet under Ar, HC-free air, and 21% oxygen balance Ar gas in the presence and absence of γ-radiation.

The key observations on the effect of different cover gases on the corrosion progression of CS in a 150 µL pure water droplet in the absence of γ-radiation (shown in **Figure 8-8**) are as follows:

- Under all cover gases, the evolution of oxide formation and $[Fe]_{meas}$ vs t_{corr} was very similar.
- At 5 d, $[Fe]_{meas}$ obtained under HC-free air was slightly lower than under Ar and 21% O_2+Ar.
- $[Fe]_{meas}$ vs t_{corr} became almost constant with t_{corr} after 5 d immersion, and slightly decreased (after 7 d) prior to the subsequent sharp increase at 10 d.
- After 1 d corrosion under Ar, the oxide was significantly thinner than for other cover gasses. Under cover gases containing O_2, the surface was locally covered with γ-FeOOH and Fe_3O_4.
- After 72 h, because of the significant variation in surface oxide (formation of a non-uniform oxide) and because the surface oxide becomes loose with time, no accurate comparison of the evolution of the surface oxide can be drawn.
- In all cover gases, Fe_3O_4 formed at the metal surface and γ-FeOOH formed on top of the Fe_3O_4 oxide layer.

The results of experiments under different cover gases indicate that the presence of oxygen results in earlier progression of corrosion to **Stage 3**. The oxidation of Fe to Fe^{II} can be accelerated by the oxygen reduction reaction in the presence of oxygen (reaction **Eq. 8-9**). As we have seen, **Stage 2** has already been reached after 1 d corrosion under oxygen and HC free air.

Reduction half-reaction of oxygen: $O_2 + 2\ H_2O + 4\ e^- \rightarrow 4\ OH^-$ (**Eq. 8-9a**)

Overall reaction:

$2\ Fe_{(m)} + O_2 + 2\ H_2O \rightarrow 2\ Fe^{2+} + 4\ OH^-$ (**Eq. 8.9-b**)

The results also showed that oxygen and nitrogen have negligible effects on the corrosion dynamics during **Stage 3**.

8.1.1.1 Effect of Cover Gas on the Corrosion Behaviour of CS in Small Volume Solutions in the Presence of γ-Radiation

$[Fe]_{meas}$ vs t_{corr} and the evolution of the surface of CS in a 150 µL pure water droplet in the presence of γ-radiation were studied (See Figure 8-8)

The key observations for $[Fe]_{meas}$ and the surface are as follows:

- For all cover gases, up to 48 h corrosion, $[Fe]_{meas}$ vs t_{corr} was close to that measured in the absence of γ-radiation. After 48 h, $[Fe]_{meas}$ continued to increase in the presence of γ-radiation, while it plateaued in its absence. When the cover gas contained nitrogen (HC-free air), the rate of increase of $[Fe]_{meas}$ with time was lower than with the other cover gases.
- $[Fe]_{meas}$ increased up to a certain value (60 µmol cm^{-2} after 5 d in Ar, and 50 µmol cm^{-2} after 7 d in Ar + 21% O_2). The increase in $[Fe]_{meas}$ was followed by a subsequent drop (42 µmol cm^{-2} in Ar, and 36 µmol cm^{-2} in Ar + 21% O_2 after 10 d). When the cover gas was HC-free air, $[Fe]_{meas}$ increased continuously during the timeframe of this experiment and reached 47 µmol cm^{-2} after 10 d.
- For all cover gases, the surface was entirely covered with magnetite after 1 d except

for the edge areas of the surface which were covered with $Fe(OH)_3$.

The results of the solution analysis and surface study for humid air exposure under radiation showed that cover gas composition has a negligible effect on the corrosion dynamics of CS. The main effect of oxygen is on how long it takes [H_2O_2] to reach its steady-state concentration. Based on the results obtained from the studies under all the cover gas compositions in the presence of radiation, it is apparent that an increase in iron concentration occurs earlier than observed in the absence of radiation.

8.3.2 Humid Air Corrosion of CS-W Joints under Different Cover Gases in the Presence of γ-Radiation

Corrosion of the CS-W interface was studied by evaluating surfaces exposed to humid air under different cover gases and a continuous flux of γ-radiation.

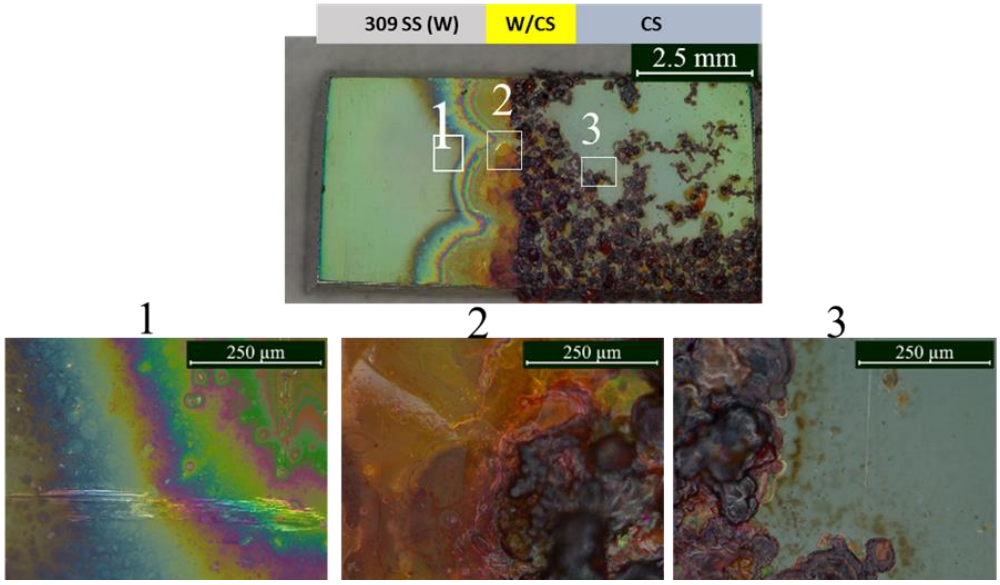

Figure 8-9: The evolution of the surface of the W-CS joint exposed to 100% humidity under γ-radiation at a dose rate of 2.8 kG/h under Ar. The solution was non-buffered, with initial pH 6.0. The images are taken from the upward faces of the coupons.

Figure 8-9 shows the low and high magnification optical microscopy images of surfaces corroded under Ar gas, after 10 d of exposure. The main observations are as follows:

- The CS surface was partially covered with thick non-uniform black oxides (Fe_3O_4), whereas the stainless steel was covered with a light green layer (a thin hydroxide layer: $Fe(OH)_2$).
- Oxide formation on the CS at the CS/W joint was not different from the rest of the CS surface.
- Oxide formation on CS was non-uniform, and was in the form of localized granular oxide patches.
- A particular rainbow-like pattern was observed on SS at the CS/W joint.

The effect of cover gas on the corrosion of the CS/W joint was investigated by evaluation of the upward face and side faces of corroded coupons with two different exposure times (10 d and 20 d) under 100% humid air and in the presence of γ-radiation (See **Figure 8-10** and **Figure 8-11**).

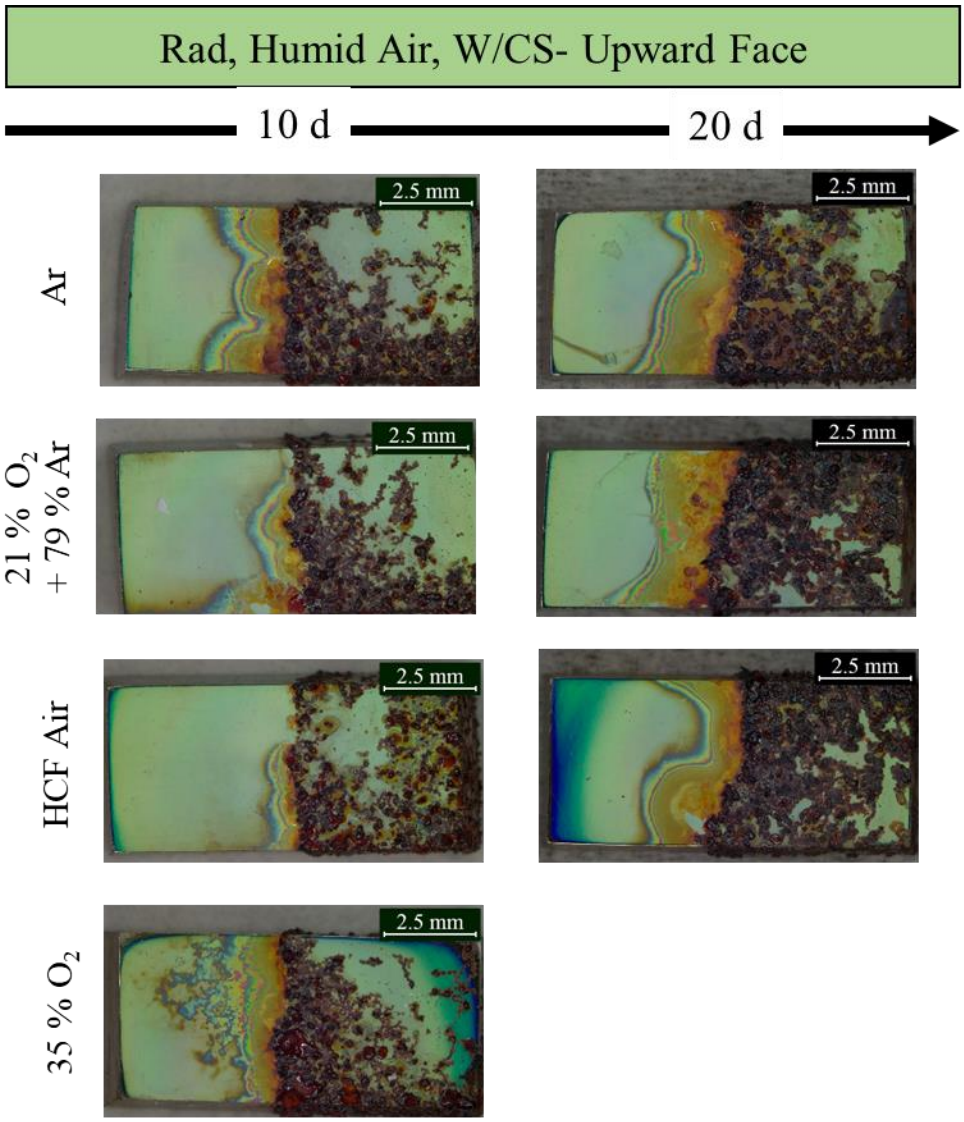

Figure 8-10: Optical microscope images of the surface of the W-CS joint exposed to 100% humidity for 10 h and 20 h, under γ-radiation at a dose rate of 2.8 kG/h and under different cover gases. The solution was non-buffered with initial pH 6.0. The images are taken from the upward face.

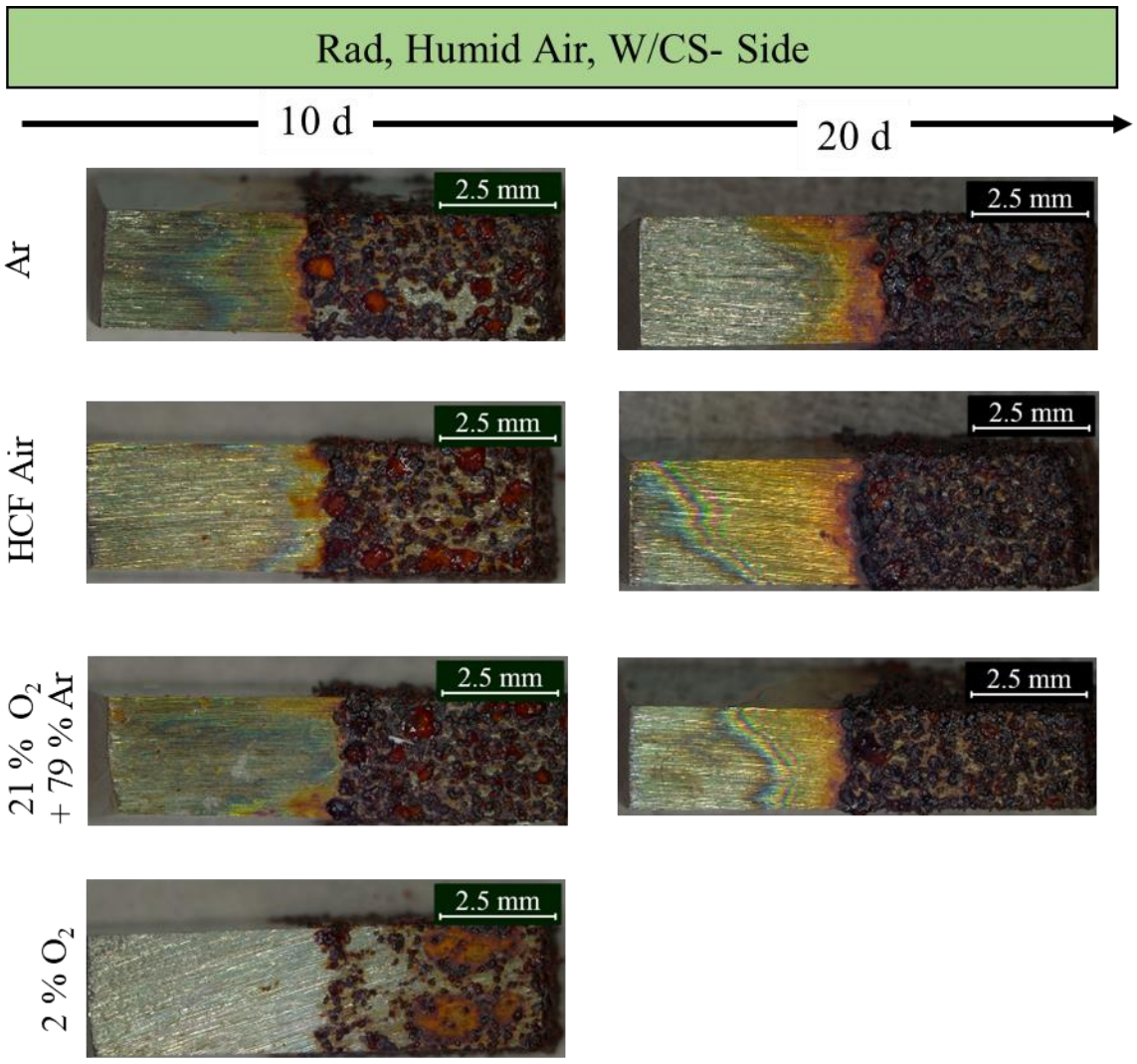

Figure 8-11: Optical microscope images of the surface of the W-CS joint exposed to 100% humidity for 10 h and 20 h, under γ-radiation at a dose rate of 2.8 kG/h and under different cover gases. The solution was non-buffered with initial pH 6.0. The images are taken from the sides of the coupons.

The key observations with regard to the morphology of oxides on different faces of CS/W joints after exposure for 10 d and 20 d to humid air under γ-radiation and under different cover gases (shown in **Figure 8-10** and **Figure 8-11**) are as follows:

- The cover gas composition had negligible or no effect.
- Magnetite coverage on the CS surface was greater after 20 d than after 10 d.

- Relative to the upward coupon face, the magnetite on the sides of the coupons was thicker and the CS oxide coverage was higher. Almost all the CS surface was covered on the coupon sides.
- The periodic pattern had progressed further towards the SS on the 20-h corroded surface than on the 10-h corroded surface.

In order to further investigate corrosion at the interface of CS-W, the samples were examined using SEM, and the images are shown in **Figure 8-12**.

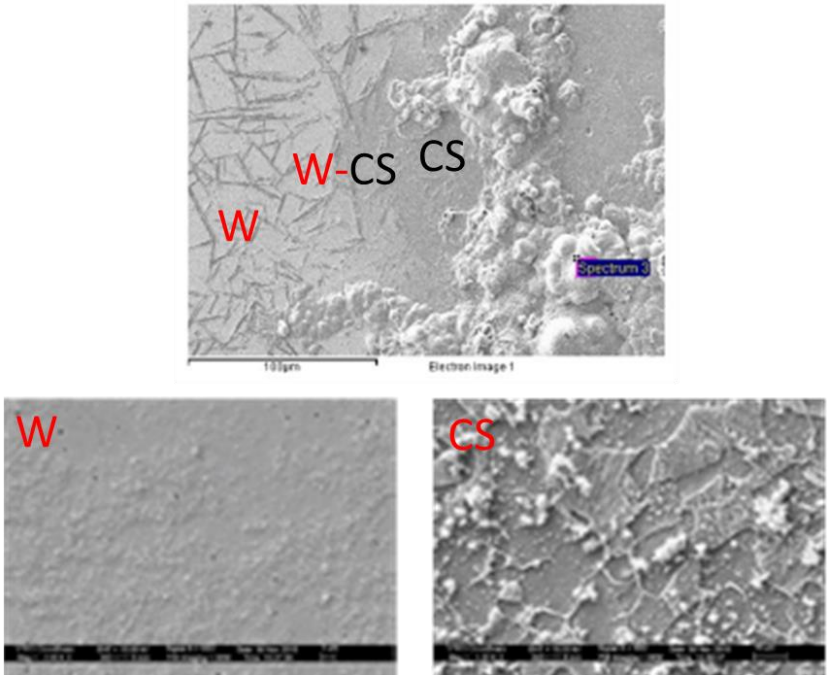

Figure 8-12: Low magnification image and high magnification SEM images of the weld, W-CS, and CS surfaces after corrosion under humid air under HC-free air for 10 d.

The SEM images of different areas show that the oxide is thicker on the CS surface than on the SS surface. The SEM analysis also confirmed the presence of a thicker oxide on the CS side while there was no oxide coverage on the SS surface or the

interface of SS and CS. Moreover, no localized attack was observed at the interfacial region.

The corrosion of the CS-W joint under humid air can be explained using the data presented in the first section of this chapter where corrosion of CS under a small droplet with and without radiation was investigated, as well as the results previously presented in **Chapters 4-7**. To use the previously presented data in this explanation, it will be useful here to briefly summarise the main differences between the experiments of the previous chapters, and first section of this chapter with the humid air studies. The main differences are the corrosion electrolyte volume and the initial concentrations and evolution of the concentrations of oxidants during corrosion. In the previously presented results, the initial electrolyte volume (solution volume in the electrochemical studies and droplet volume in the droplet studies) was known and controlled. The concentration of the oxidant was determined and known at the beginning of the experiments. While oxidation and reduction of corrosion products and solution species continuously changed the oxidant concentrations, there was no other source for the addition of oxidants to the solution. These factors are not known in the humid air radiolysis corrosion. On one hand, the size of the droplets is not the same, and may vary from site to site and influence the corrosion behaviour. The effect of electrolyte thickness (and therefore droplet size) on the dynamics of corrosion has previously been studied and well documented [5,22]. On the other hand, the radiolysis of humid air continuously introduces oxidants into the solution. Therefore, while corrosion reactions consume and produce oxidants, they are also being constantly injected into the solution via water radiolysis. While these two main differences affect the corrosion kinetics and possibly therefore the corrosion progression of CS, the overall

corrosion mechanism is expected to remain the same. With these two main differences in mind, we can use the results presented in the previous chapters to discuss the corrosion of the CS-W joint under humid air radiolysis.

The droplet studies presented in the first section of this chapter showed that after 1 d, corrosion of CS had progressed through **Stage 3** where oxidation of $Fe \rightarrow Fe^{II}$ and $Fe^{II} \rightarrow Fe^{III}$ and the dehydration of $Fe(OH)_2$ and $Fe(OH)_3$ leads to the formation of magnetite. The droplets that form through condensation of humid air are significantly smaller than those used in section one. This may explain the smaller oxide patches, with each perhaps representing the oxide formed under a small droplet. With time, there is more water condensation on the surface and an extended surface area is covered by magnetite under thin water droplets.

The types of oxides which formed on the CS, CS-W, and W surfaces (**Figure 8-10** and **Figure 8-11**) were the same after 10 d and 20 d of exposure. However, the oxide coverage increased with t_{corr}, while the stainless steel surface remained almost clean and protected by a thin surface oxide during the entire exposure time. The rainbow-like pattern between the joint and the SS area (see optical microscopy image of area 1 in **Figure 8-9**) is a classic thin film interference pattern, which indicates the presence of a thin film on the surface, which is probably a hydroxide gel layer. The progression of the thin layer shows that Fe species diffuse through the gelatinous layer towards the weld. As explained earlier, Fe ions can continuously form on the CS surface and diffuse radially towards areas of lower concentration (W). The observation of oxide deposits is evidence of a thin layer of iron hydroxide hydrogel formed on the CS, spreading over the surface of W with time.

Under different cover gases, the type and coverage of surface oxides were similar. For oxygen, no significant effect was identified. Also, the comparison of the surfaces under hydrocarbon free air (O_2 + N_2) and under other cover gases (N_2-free gases) showed that nitric acid, as the main radiolytic product in humid air, does not affect oxide formation within 10-20 d of exposure time period. These results can be explained based on the previous findings from the electrochemical studies and solution analysis presented in **Chapters 4-6** which elucidated the mechanism of CS and stainless steel corrosion in the presence of H_2O_2 and HNO_3, by studying the effects of different oxidant concentrations, solution pH, and ionic strength. The droplet studies presented in **Chapter 7** also revealed that the mechanism of corrosion under a small volume solution can be explained using the electrochemical test results. The previously presented results demonstrated that in the absence of a protective oxide (in the case of CS corrosion), ionic strength plays a major role in the corrosion progression. The oxidant concentration mainly influences the rate of reduction reactions, which in turn affects the dissolved metal cation concentration. However, progression of corrosion to a new stage and therefore formation of a different oxide on the surface requires that the interface where corrosion occurs meets certain conditions. These conditions are dictated by the concentration of oxidant, pH and ionic strength. Therefore, it is possible to say that in the time frame of this test and based on the assumed size of most of the droplets formed on the CS-W joint test samples, the conditions for corrosion progression to a stage beyond formation of magnetite were not met. For SS, however, the pre-existing protective oxide on the surface facilitated progression of corrosion to the next stage, where more insulating oxides form on the surface (as shown in **Chapter 6**), and the rate of cathodic

reactions on the SS surface is slow. This low rate of reduction reactions, in combination with the low probability of formation of a droplet at the interface where it covers both the SS and CS surfaces (and thus no possibility of galvanic corrosion), has led to the absence of any corrosion acceleration in the humid air environment.

In summary, no acceleration of corrosion at the CS-W interface, which could suggest a significant effect of galvanic coupling, was observed under any of the conditions studied in this chapter. Therefore, it is reasonable to assume that the corrosion of CS in the joint area will not be significantly different from that of CS on its own under humid air conditions in the presence of radiation. In other words, under the conditions studied in this thesis, the accelerated corrosion rate of CS (The corrosion current density due to galvanic coupling between the CS and weld material) will be close to that of CS on its own. It should be noted that galvanic corrosion of the whole sample (CS welded to 304L SS using 309 SS as the filler material) was not studied under humid air conditions. Because the more noble materials (309 SS welded to 304L SS) have a larger surface area in this case, this could significantly affect the accelerated corrosion rate of CS. In addition, galvanic corrosion between CS and 304L SS and 309 SS on the microscale, and also in the heat affected zone (HAZ), still need to be investigated.

8.4 SUMMARY

The first section of this chapter discussed the evolution of CS corrosion under a 150 μl water droplet in the presence and absence of γ-radiation and under HC-free air, 21% O_2+79% Ar, and pure Ar, studied between 1 d and 10 d of corrosion time. In the

absence of radiation, where the only oxidant present is O_2 or H^+ (depending on the cover gas), the dissolved iron concentration increases linearly with t_{corr} in all environments. The surface of CS became covered with a double layer oxide comprising a magnetite layer (first layer) and a FeOOH oxide (outer layer), and the effect of cover gas was negligible. In the presence of radiation, regardless of type of cover gas, the CS corrosion was influenced by early formation of Fe^{III} cations and redox coupling between Fe^{III}/Fe^{II} and H_2O_2/O_2 which facilitates formation of magnetite and results in the formation of a uniform magnetite layer and also the observation of a constant iron concentration in the bulk solution after 120 h corrosion.

The second section of this chapter discussed the effect of cover gas composition on the radiation-influenced humid air corrosion of CS, CS-W, and SS. The type of oxide formed on the CS surface was the same for both exposure times. However, a greater surface area was covered with time. The stainless steel surface remained clean, protected by a thin surface oxide. However, the Fe species were able to diffuse through a gelatinous layer of $Fe(OH)_2$ towards the weld area. The results showed no preferential oxidation at the CS/W interface. The results showed that Fe ions continuously form on the CS surface and diffuse radially towards areas of lower concentration (i.e., the weld region). The observation of oxide deposits on the weld region is evidence of a thin layer of iron hydroxide hydrogel formed on CS spreading over the surface of W with over time. The effect of cover gas on oxide formation during 20 d corrosion was negligible. The analysis of the results revealed that humid air corrosion of the CS-W region occurs in a similar manner to that of CS on its own. That is, in the presence of γ-radiation, the corrosion of CS is not accelerated due to welding to 304L SS with 309 SS as the filler material and

galvanic corrosion can be disregarded. Therefore, a simple assessment of CS corrosion on its own can be used to estimate the service life of 304L SS/W in the annular gap of the calandria tank supporting structures.

8.5 REFERENCES

[1] R.P. Morco, Gamma-Radiolysis Kinetics and Its Role in the Overall Dynamics of Materials Degradation, PhD Thesis, The University of Western Ontario, 2020.

[2] G. van Weert, Y. Shang, Iron control in nitrate hydrometallurgy by (auto) decomposition of iron (II) nitrate, Hydrometallurgy. 33 (1993) 255–271.

[3] R.S. Wittman, Radiolysis Model Sensitivity Analysis for a Used Fuel Storage Canister, 2013.

[4] R.P. Morco, J.M. Joseph, D.S. Hall, C. Medri, D.W. Shoesmith, J.C. Wren, Modelling of radiolytic production of HNO_3 relevant to corrosion of a used fuel container in deep geologic repository environments, Corros. Eng. Sci. Technol. 52 (2017) 141–147.

[5] Y.G. Shin, Nonlinear Dynamics of Carbon Steel Corrosion under Gamma Radiation, PhD Thesis, The University of Western Ontario, 2020.

[6] J.C. Wren, J. Ball, LIRIC 3.2 an updated model for iodine behaviour in the presence of organic impurities, Radiat. Phys. Chem. 60 (2001) 577–596.

[7] J.M. Joseph, B.S. Choi, P. Yakabuskie, J.C. Wren, A combined experimental and model analysis on the effect of pH and O_2(aq) on γ-radiolytically produced H_2 and H_2O_2, Radiat. Phys. Chem. 77 (2008) 1009–1020.

[8] P. Driver, G. Glowa, J.C. Wren, Steady-state γ-radiolysis of aqueous methyl ethyl ketone (2-butanone) under postulated nuclear reactor accident conditions, Radiat. Phys. Chem. 57 (2000) 37–51.

[9] J.C. Wren, G.A. Glowa, A simplified kinetic model for the degradation of 2-butanone in aerated aqueous solutions under steady-state gamma-radiolysis, Radiat. Phys. Chem. 58 (2000) 341–356.

[10] P.A. Yakabuskie, J.M. Joseph, C.R. Stuart, J.C. Wren, Long-Term γ-Radiolysis Kinetics of NO_3^- and NO_2^- Solutions, J. Phys. Chem. A. 115 (2011) 4270–4278.

[11] P.A. Yakabuskie, J.M. Joseph, P. Keech, G.A. Botton, D. Guzonas, J.C. Wren, Iron oxyhydroxide colloid formation by gamma-radiolysis, Phys. Chem. Chem. Phys. 13 (2011) 7198–7206.

[12] W. Xu, K. Daub, X. Zhang, J.J. Noel, D.W. Shoesmith, J.C. Wren, Oxide formation and conversion on carbon steel in mildly basic solutions, Electrochim. Acta. 54 (2009) 5727–5738.

[13] L. Wu, D. Guo, M. Li, J.M. Joseph, J.J. Noël, P.G. Keech, J.C. Wren, Inverse Crevice Corrosion of Carbon Steel: Effect of Solution Volume to Surface Area, J. Electrochem. Soc. 164 (2017) C539–C553.

[14] K. Daub, A Study of Gamma Radiation Induced Carbon Steel Corrosion, PhD Thesis, The University of Western Ontario, 2013.

[15] Q.W. Knapp, J.C. Wren, Film formation on type-316L stainless steel as a function of potential: Probing the role of gamma-radiation, Electrochim. Acta. 80 (2012) 90–99.

[16] K. Daub, X. Zhang, J.J. Noël, J.C. Wren, Effects of γ-radiation versus H_2O_2 on carbon steel corrosion, Electrochim. Acta. 55 (2010) 2767–2776.

[17] D. Guo, Corrosion Dynamics of Carbon Steel in Used Fuel Container Corrosion Dynamics of Carbon Steel in Used Fuel Container Environments Environments, PhD Thesis, The University of Western University, 2018.

[18] R.P. Morco, A.Y. Musa, M. Momeni, J.C. Wren, Corrosion of carbon steel in the [P14666][Br] ionic liquid: The effects of γ-radiation and cover gas, Corros. Sci. 102 (2016) 1–15.

[19] K. Daub, X. Zhang, J.J. Noël, J.C. Wren, Gamma-radiation-induced corrosion of carbon steel in neutral and mildly basic water at 150 °C, Corros. Sci. 53 (2011) 11–16.

[20] A.Y. Musa, J.C. Wren, Combined effect of gamma-radiation and pH on corrosion of Ni-Cr-Fe alloy inconel 600, Corros. Sci. 109 (2016) 1–12.

[21] D. Fu, X. Zhang, P.G. Keech, D.W. Shoesmith, J.C. Wren, An electrochemical study of H_2O_2 decomposition on single-phase γ-FeOOH films, Electrochim. Acta. 55 (2010) 3787–3796.

[22] M. Naghizadeh, Copper Corrosion Dynamics under Deep Geologic Repository Conditions, PhD Thesis, The University of Western Ontario, 2021

Chapter 9
THESIS SUMMARY AND FUTURE WORK

9.1 SUMMARY

In this thesis, the effects of γ-radiation and chemically added water and humid air radiolysis products (H_2O_2 and HNO_3) on the corrosion of carbon steel, 304L stainless steel, and stainless steel weld (309 SS) were investigated. The results will be used in the development of a corrosion dynamics model that can be used to accurately assess the long-term integrity of CANDU nuclear reactor structural materials. The parameters studied in this thesis project were pH, nitrate concentration, hydrogen peroxide concentration, the cover gas composition, and the presence or absence of γ-radiation. The effects of ionic strength and effects of other oxidants in the presence of nitrate ions were also studied.

The experimental approach used in this thesis involved the use of electrochemical methods (corrosion potential measurement, potentiodynamic polarization, and linear polarization) and coupon exposure tests, followed by post-test surface and solution

analysis.

In **Chapter 4**, the effect of NO_3^- ions on the corrosion of CS in Ar-purged pH 6.0 buffered $NaNO_3$ and $Fe(NO_3)_3$ solutions was studied using electrochemical techniques. These results showed that, depending on the concentration of nitrate and ionic strength, nitrate can affect the dynamics of corrosion by either accelerating the rate of iron oxidation via the NO_3^-/NO_2^- reduction reaction or by influencing the rate of mass transport of metal ions. At pH 6.0, due to the high solubility of Fe in solutions containing high concentrations of nitrate, the major corrosion pathway for CS is metal dissolution and the faster charge transfer rate in nitrate solutions combined with a fast reduction rate results in a higher corrosion rate for $[NaNO_3] \geq 10$ mM. When sodium nitrate is replaced by $Fe(NO_3)_3$, the anodic charge transfer reaction becomes even faster, and the main reduction reaction is the diffusion-controlled reduction of ferric ions. Based on the PD results, the main oxidation pathway in $Fe(NO_3)_3$ solution is metal dissolution. The formation of an oxide that can suppress the anodic dissolution of metal occurs at potentials significantly higher than in $NaNO_3$ solutions. The results also indicate that in $NaNO_3$ solutions, because of the contribution of mass transfer in the anodic branch of PD curves and the contribution of iron oxidation in the cathodic branch of PD curves, the requirements for establishing a valid Tafel region are not met. Thus, Tafel extrapolation is inaccurate for determining the corrosion rate at E_{corr} for the conditions studied in this thesis.

In **Chapter 5**, the effect of nitrate concentration on the corrosion behaviour of carbon steel (CS A36) and stainless steels (304L SS and 309 SS) in HNO_3 solutions at pH 2.0 was investigated using E_{corr} vs time measurements, LPR, and PD techniques and

by analyzing the dissolved alloying elements as a function of time using ICP-OES. The results showed that, for the same [NO_3^-], the corrosion rate of CS at pH 2.0 is greater than at pH 6.0, due to the higher mass transfer rate. When 100 mM NO_3^- is present in pH 2.0 solution, the ionic strength is high enough to prevent Fe saturation in the interfacial region. E_{corr} remains below $E^{eq}_{Fe \leftrightarrows Fe(OH)_2}$ where the oxidation of iron is under charge transfer control. For stainless steels, because forward scanning from negative overpotentials results in the formation of a protective Cr-rich oxide at potentials below the corrosion potential, the application of a Tafel slope extrapolation method was not suitable for corrosion rate determination. Unlike for CS, for types 304L and 309 stainless steels, the anodic current is lower in 100 mM NO_3^- solution than in 10 mM NO_3^-. For 304L SS a higher [NO_3^-] results in faster formation of a protective oxide at very low overpotentials, which becomes unstable at potentials $>E^{eq}_{\mathrm{Fe(OH)_2 \leftrightarrows Fe(OH)_3}}$. For 309 SS, the oxide formed at lower potential is stable over the entire range of potential scanning. The implication of these results is that when a protective oxide is stable, increasing the nitrate concentration cannot increase the rate of corrosion of stainless steels at low pHs.

The corrosion studies of CS, 304L SS, and 309 SS in the combined presence of nitrate and hydrogen peroxide has given us insight into the corrosion behaviours of these alloys in the presence of water and humid air radiolysis products.

In **Chapter 6**, the electrochemical behaviours of CS, 304L SS and 309 SS were investigated by the initial addition of hydrogen peroxide in pH 6.0 buffered solutions and in pH 2.0 nitric acid solutions. The corrosion of these alloys in pH 2.0 was then assessed using solution analysis. The results presented in this chapter have improved the understanding of how hydrogen peroxide, as the key water radiolysis product, can affect

the corrosion carbon steel and stainless steels. This analysis has also demonstrated the role of hydrogen peroxide as a potential oxidant when the ionic strength of the solution is low, and mass transport is slow, as well as in conditions where the ionic strength is high and nitrate is present as an additional oxidant.

In pH 6.0 buffered solutions, the addition of a small amount of 10^{-4} M H_2O_2 does not change the corrosion potential and the PD behaviour of CS. A more oxidizing environment (10^{-3} M H_2O_2), however, significantly increases the E_{corr}. It was concluded that for $[H_2O_2]_0<10^{-2}$ M, E_{corr} is determined by the cathodic current of the H_2O_2/OH^- reduction reaction, coupled with the anodic current of the iron oxidation half-reaction. On the other hand, for $[H_2O_2] \geq 10^{-2}$ M, E_{corr} is likely to be determined primarily by the cathodic half-reactions of H_2O_2, coupled with the anodic half-reactions of H_2O_2.

In acidic solutions, CS corrosion is not influenced by the addition of H_2O_2 to nitric acid solutions, except for the fact that it decreases the rate of change of $[Fe]_{meas}$, which indicates that it accelerates oxide formation while not affecting the net rate of oxidation. This finding revealed the role of mass transport in the corrosion process. While hydrogen peroxide was identified as an effective oxidant in low ionic strength solutions, when mass transport is fast, in the high ionic strength solutions with the same concentration of hydrogen peroxide, oxide formation does not occur, as observed in the buffered solutions.

The corrosion of the tested stainless steels is strongly affected by the addition of hydrogen peroxide. Unlike in nitric acid solutions, in more oxidizing solutions at the same ionic strength (i.e., when 10 mM hydrogen peroxide solution was added to nitric

acid), saturation of the surface can immediately occur, which limits surface oxidation by limiting the mass transfer of metal ions to the solution phase. Oxide formation shifts the E_{corr} to the equilibrium potential of the H_2O_2 oxidation reaction. The difference between CS corrosion and stainless steel corrosion in a similar environment was attributed to the different oxides that form on the surface.

In **Chapter 7** the corrosion dynamics of CS in small solution volumes were studied in the presence of 10^{-4} H_2O_2 and different concentrations of HNO_3 (as the key products of humid air radiolysis products) in small-volume solutions (150 µL solution droplets) by analyzing the average bulk concentrations of dissolved iron and the morphology of the corroded surface as a function of corrosion time. CS corrosion progresses through the same dynamic stages for both HNO_3 and H_2O_2. **Stage 0** involves the oxidation of Fe to solvated $Fe^{2+}_{(aq)}$ in the interfacial region, followed by the transport of $Fe^{2+}_{(aq)}$ to the bulk solution. Once the surface solubility limit is reached, the Fe^{II} in the interfacial region precipitates as $Fe(OH)_2$ hydrogel on the surface. In **Stage 1b/2,** electron hopping between Fe^{II} and Fe^{III} is faster in the hydrogel network, resulting in faster oxidation. The nitrate concentration affects the rate of progression through individual stages and the overall corrosion rates in individual stages. The linear dependence of reaction rate on the concentration of $[HNO_3]_0$ implies that a first-order reaction occurs in **Stage 0**. The duration of this stage is shorter in solutions with higher $[HNO_3]_0$ due to a higher oxidation rate and a higher mass transfer rate, resulting in faster saturation of Fe^{II} in the interfacial region. In **Stage 1b/2,** the corrosion rate was proportional to $\log [HNO_3]_0$. In this stage, and particularly in solutions with higher $[HNO_3]_0$, the distribution of oxides/hydroxides is not uniform across the coupon surface and depends

on the solution thickness, which is not uniform because of the dome shape of the solution droplet. The area exposed to the shallower solution approaches subsequent stages faster.

The time-dependent behaviours of CS corrosion in 10^{-4} M H_2O_2 were similar to those observed in 10^{-4} M HNO_3 solutions. For 10^{-4} M hydrogen peroxide, the rate of metal oxidation in **Stage 0** was 10 times larger than for 10^{-4} M HNO_3, indicating that hydrogen peroxide is a more effective oxidant than 10^{-4} M HNO_3 for iron oxidation when the surface is not saturated with iron. However, in **Stage 1b/2**, the corrosion rate was similar to that of 10^{-4} M HNO_3, indicating that hydrogen peroxide acts as an oxidant for the oxidation of Fe^{II} to Fe^{III}, while also acting as a reductant, participating in oxide formation through the reduction of Fe^{III} to Fe^{II} in a low ionic strength solution.

The evolution of the surface and solution with time for pure iron in 10^{-2} M HNO_3 showed that, regardless of microstructural differences and differences in metal composition, corrosion of both metals progresses in the same way in solutions of high ionic strength. This implies that, in high ionic strength, the effect of microstructure on the corrosion of CS is negligible.

In **Chapter 8**, the effect of γ-radiation and different cover gases (HC-free air, 21% O_2+79% Ar, and pure Ar) on the evolution of CS corrosion with time was studied in a 150 μl water droplet. In the absence of radiation, the dissolved iron concentration increases linearly with t_{corr} in all environments. In the presence of radiation, however, the oxidation of H_2O_2 can couple with the oxidation of Fe^{III}/Fe^{II} reduction, and the dissolved iron concentration remains constant with time for t_{corr}>120 h. When radiation is present, CS corrosion is influenced by the early formation of Fe^{III} cations and redox coupling between Fe^{III}/Fe^{II} and H_2O_2/O_2, which facilitate the formation of magnetite. This

chapter also discusses the effect of cover gas composition on the radiation-influenced humid air corrosion of CS, CS-W, and SS. The results showed that CS becomes covered with magnetite. Fe ions continuously form on the CS surface. The type of oxide formed on CS surface remained the same with exposure time. However, a greater surface area was covered as time progressed. Stainless steel remains clean, protected by a thin surface oxide. The results showed no preferential oxidation at the CS/W interface. The effect of cover gas on oxide formation during 20 d corrosion was negligible. The analysis of the results revealed that humid air corrosion of the CS-W region occurs in a similar manner to that of CS on its own. That is, in the presence of γ-radiation and under the conditions studied in this thesis, the corrosion of CS is not significantly accelerated due to being welded to 304L SS with 309 SS as the filler material. Therefore, to estimate the service life of the CS/304L SS/W in the annular gap of the calandria tank supporting structures, it is sufficient to assess the independent corrosion of the CS component.

The results presented in this thesis have improved the understanding of how the presence of radiolysis products (H_2O_2 and HNO_3) can affect the corrosion of carbon steel and stainless steels. These results will be used to develop a mechanistic model that can be used to predict the long-term corrosion behaviours of reactor structural materials with confidence.

9.2 FUTURE WORK

The main objective of this thesis was to develop a mechanistic understanding of the corrosion of the structural materials of the end shield cooling (ESC) tank and its supporting structures in humid air and the presence of a continuous flux of γ-radiation.

This will contribute to the development of a mechanism that can explain how nitric acid and hydrogen peroxide (the main radiolytic products in humid air) impact the corrosion of CS and different stainless steels under the conditions anticipated inside the calandria tank and adjacent to its supporting structures.

An investigation of the effect of different [NO_3^-] and [H_2O_2] in buffered solutions in the pH range 2 to 6 is needed for future work.

A study of galvanic corrosion between CS, 304L SS, and 309 SS with different surface areas and in different solution volumes and the presence of different concentrations of radiolytic products (H_2O_2 and HNO_3) is also recommended. The effect of periodic additions of radiolytic products to the test solution could also be carried out to better simulate the continuous production of these products due to a flux of γ-radiation.

The long-term goal of this continuing project is to develop a high-fidelity corrosion

dynamic model for the independent and galvanically coupled corrosion of steels. The results presented in this thesis will eventually be incorporated into this dynamic model, which is still under development. To achieve this, it will be necessary to formulate individual processes as a function of solution parameters, such as the interfacial electrochemical reactions and mass transport processes.

Appendix A

CURRICULUM VITAE

Masoud Zakeri

LIST OF PUBLICATIONS

1. **M. Zakeri**, J. M. Joseph, O. Yong, J. C. Wren, "*Effect of Chemically Added Radiolytic Products on The Corrosion of Carbon Steel*", under preparation.
2. **M. Zakeri**, J. M. Joseph, O. Yong, J. C. Wren, "*Humid air corrosion of Carbon Steel and Stainless Steel under γ-radiation*", under preparation.
3. **M. Zakeri**, M. Momeni, M. Li, J. Joseph, O. Yong, J.C. Wren, *Humid air corrosion of carbon steel – stainless steel welds in the presence of γ-radiation,* 41th Annual CNS-CNA Student Conference
4. **M. Zakeri**, M. Naghizadeh, D. Nakhaie, M. H. Moayed, "*Pit transition potential and repassivation potential of stainless steel in thiosulfate solution*", Journal of The Electrochemical Society, 163(2016): C275-C281.
5. M. Naghizadeh, D. Nakhaie, **M. Zakeri**, M. H. Moayed, "*The effect of dichromate ion on the pitting corrosion of AISI 316 stainless steel. Part II: pit initiation and transition to stability*", Corrosion Science, 94 (2015), 420-427.
6. **M. Zakeri**, D. Nakhaie, M. Naghizadeh, M. H. Moayed, "*The effect of dichromate ion on the pitting corrosion of AISI 316 stainless steel. Part I: Critical pitting temperature",* Corrosion Science, 93 (2015), 234-241.
7. A. Abbasi Aghuy, **M. Zakeri**, M. H. Moayed, M. Mazinani, "*Effect of grain size on pitting corrosion of 304L austenitic stainless steel*", Corrosion Science, 94 (2015), 368-376.
8. D. Nakhaie, **M. Zakeri**, M. Naghizadeh, M. H. Moayed, "*Effect of Thiosulfate on Pitting Corrosion of 316SS: II. Metastable Pitting and Transition to Stability*", Journal of The Electrochemical Society, 162 (2015), C121-C127.

9. M. Naghizadeh, D. Nakhaie, **M. Zakeri**, M.H. Moayed, "*Effect of Thiosulfate on Pitting Corrosion of 316SS: I. Critical Pitting Temperature and Pit Chemistry*", Journal of The Electrochemical Society, 162 (2015), C71-C77.
10. **M. Zakeri**, M. H. Moayed, *"Investigation on the effect of nitrate ion on the critical pitting temperature of 2205 duplex stainless steel along a mechanistic approach using pencil electrode",* Corrosion Science, 85 (2014), 222-231.
11. N. Ebrahimi, M. Momeni, A. Kosari, **M. Zakeri**, M. H. Moayed, "*A Comparative Study of Critical Pitting Temperature (CPT) of Stainless Steels by Electrochemical Impedance Spectroscopy (EIS), Potentiodynamic and Potentiostatic Techniques*", Corrosion Science, 59 (2012), 96-102.
12. A. Kosari, M. Momeni, R. Parvizi, **M. Zakeri**, M. H. Moayed, A. Davoodi, H. Eshghi, "*Theoretical and Electrochemical Assessment of Inhibitive Behaviour of Some Thiophenol Derivatives on Mild Steel in HCl",* Corrosion Science, 53 (2011), 3058-3067.

LIST OF CONFERENCES

1- O- **M. Zakeri**, R.C. Newman, "*Investigation on the possibility of UPD of lead on copper at near-neutral pH, as a model for impurity effects in groundwater*", ORF Meeting, Western University, London, Canada, Dec 2021.

2- O- **M. Zakeri**, J. M. Joseph, O, Yong, J. C. Wren, "*An Evaluation of Carbon Steel Corrosion in Nitrate Solution Using Electrochemical and Solution Analysis Methods",* 237th ECS Meeting with the 18th International Meeting on Chemical Sensors (IMCS 2020), May 10-14, 2020), Montreal, QC, Canada.

3- P- **M. Zakeri**, M. Momeni, J. M. Joseph, O, Yong, J. C. Wren, "*Humid Air Corrosion of Carbon Steel – Stainless Steel Welds in The Presence of γ-Radiation",* 41th Annual CNS-CNA Student Conference, June 2017, Niagara Falls, ON.

4- O- **M. Zakeri**, M. Momeni, J. M. Joseph, O, Yong, J. C. Wren, "*Investigation of Humid Air Corrosion of Carbon Steel Stainless Steel Welds in the Presence of γ-Radiation*", 100th Canadian Chemistry Conference and Exhibition, May 28 - June 1, 2017, Toronto, ON.

5- P. **M. Zakeri**, M. Momeni, J. M. Joseph, O, Yong, J. C. Wren, "*Investigation of Humid Air Corrosion of Carbon Steel – Stainless Steel Welds in the Presence of γ-Radiation"*, UNENE, 14-14 December, 2016, Waterloo, Canada.

6- P. **M. Zakeri**, M. Momeni, J. M. Joseph, O, Yong, J. C. Wren, "*Investigation of Humid Air Corrosion of Carbon Steel – Stainless Steel Welds int he Presence of γ-Radiation*", NACE Northern Area Eastern Conference, October 31– November 2, 2016, Toronto, Canada.

7- P- **M. Zakeri**, M. H. Moayed, "*A Justification on Critical Pitting Temperature (CPT) Mechanism Proposed by Salinas-Bravo and Newman Using Pencil Electrode/Effect of Nitrate Ion Addition*", 223rd ECS Meeting, 12-16 May 2013, Toronto, Canada.

8- O- **M. Zakeri**, M. H. Moayed, *"Investigation on The Effect of Nitrate Ion on The Critical Pitting Temperature (CPT) Of Duplex Stainless Steel Using Pencil Electrode*", 223rd ECS Meeting, 12-16 May 2013, Toronto, Canada.

9- P- M. Abooie Mehrizi, M. Naghizadeh, **M. Zakeri,** A. Davoodi, M. H. Moayed, "*Investigation on The Inhibition Effect of Jujube as a Green Inhibitor on Mild Steel in HCl Media*", 13th National Iranian Corrosion Association Conference, 15-17 May 2012, University of Tabriz, Tabriz, Iran.

10- P- E. Kheradmand, A. Kiani Rashid, A. Babakhani, **M. Zakeri**, A. Ronaghi, "*The Influence of Nucleation Agent and Cooling Rate on Graphitization in Cast Iron"*, 4th Joint Conference of Iranian Society of Metallurgical Engineers and Casting Society of Iran, 24-25 November 2010, Iran University of Science and Technology, Tehran, Iran.

11- O- A. Kosari, M. Momeni, R. Parvizi, **M. Zakeri**, M. H. Moayed, Ali Davoodi, "*Electrochemical Impedance Spectroscopy for Investigating the Inhibitor Behavior on Mild Steel*", Iranian Electrochemical Society (Iran ECS), 9-11 October 2010, Kish, Iran.

ACADEMIC EXPERIENCE

* Radiation Assisted Materials Performance Science Group

- Research Assistant (Apr 2021 – Present)

University of Toronto, Toronto, Canada

- Ph.D. Candidate/Researcher, RAMPS* (May 2016 – 2021)

Western University, London, Canada

- M.Sc. Candidate/Research Assistant (Sep. 2010 - Feb 2013)

Ferdowsi University of Mashhad, Mashhad, Iran

- Teacher Assistant (2011-2012)

Corrosion and Oxidation of Materials, Department of chemistry Ferdowsi University of Mashhad, Iran.

FORMAL EDUCATION

- Ph.D., Physical Chemistry (May 2016 – 2021)

Western University, London, Canada

- M.Sc., Materials Science and Engineering, Corrosion and Protection of Materials (September 2010 - Feb 2013)

Ferdowsi University of Mashhad, Mashhad, Iran

- B.Sc. in Materials Engineering / Industrial Metallurgy (Sep 2005 – Sep 2010)

Ferdowsi University of Mashhad, Mashhad, Iran

RELEVANT EXPERIENCE

- Metallurgical and Corrosion Engineer (May. 2013- May. 2016)

Techinco, Tehran, Iran

- Metallurgical Engineer and Welding Inspector (Sep 2010- May 2013) (Part-time)

Toos Joosh Gostar. Co, Mashhad, Iran

- CO-OP, (Jun. 2010- Sep. 2010)

Tigh Arreh Toos (TAT), Mashhad, Iran

SCHOLARSHIPS

- NACE Foundation Graduate Student Book Award
- Ontario Trillium Scholarship (OTS), University of Western Ontario, 2016-2020

EXECUTIVE MEMBERSHIPS AND VP POSITIONS

- Executive member of NACE SOSS, London, ON, Canada, (2017– 2019)

STUDENT MEMBERSHIPS

- Electrochemical Society (ECS)
- NACE INTERNATIONAL
- Ontario Society of Professional Engineers (OSPE)
- The Canadian Society for Chemistry (CSC)
- The Royal Society of Chemistry (RSC)
- Canadian Nuclear Society (CNS)
- Canadian Institute of Mining, Metallurgy and Petroleum (CIM)
- The Centre for Advanced Materials and Biomaterials Research (CAMBR)

VOLUNTEER WORK AND COMMITTEE INVOLVEMENT

- Judge in the Canada Wide Science & Engineering Fair (CWSF), 2021-2022.
- Judge in the Thames Valley Science & Engineering Fair (TVSF), London, ON, Canada, 2018-2022.
- Member of S election committee for the "Ontario Remembrance Scholarship in honour of the victims of flight PS752", University of Western Ontario, 2021.
- Executive member of NACE SOSS, Western University, London, ON, 2017-2019
- Member of Financial Committee, Society of Graduate Students (SOGS), Western University, London, ON, 2018-present
- Member of Organizing Committee for Honoring the Victims of Flight PS 752, Western University, London, ON, Canada, 2020
- Member of Graduate Students' Issues Committee, Western University, London, ON, 2018-present
- Volunteer of Food Bank, London, ON, Canada, 2020
- Member of International Graduate Students' Issues Committee, Western University, London, ON, Canada, 2018 – 2020
- Member of Graduate Peer Support, Western University, London, ON, Canada, 2018– Present
- Member of Organizing Committee of 50th anniversary of SOGS, Western University, London, ON, Canada, 2018
- Member of Orientation and Social Committee, Western University, London, ON, Canada, 2018 – 2019
- Science Rendezvous, the annual festival, London, ON, Canada, May, 2018

- Judg in Mystery Solutions Event-Science Olympics, Western University, London, ON, Canada, May, 2019
- Volunteer of organizing for NACE SOSS conference, Western University, Western University, London, ON.
- Member of organizing committee for 10th conference in metallurgy and materials, Ferdowsi University of Mashhad, Iran, 2006